Comparative study of beam-induced carbonaceous deposits in helium-ion and scanning electron microscopes.

Robert O'Connell

A thesis submitted for the degree of
Doctor of Philosophy

Supervised by Prof. Hongzhou Zhang
Nanofabrication and Ultramicroscopy
School of Physics
Trinity College Dublin

May 1, 2018

To my parents

DECLARATION

I declare that this thesis has not been submitted as an exercise for a degree at this or any other university and it is entirely my own work.

I agree to deposit this thesis in the University's open access institutional repository or allow the library to do so on my behalf, subject to Irish Copyright Legislation and Trinity College Library conditions of use and acknowledgement.

Elements of this work that have been carried out jointly with others or by collaborators have been duly acknowledged in the text wherever included.

Robert O'Connell

ABSTRACT

In this work, the phenomena of beam-induced contamination in charged beam microscopes (i.e. the scanning electron microscope (SEM) and helium ion microscope (HIM)) was investigated in order to determine its influence on specimen characterisation. This was achieved through a comparative study on the secondary electron (SE) generation mechanisms in both microscopes, which is key contamination formation process.

Deposited contamination structures formed by electron and He^+ ion irradiation were assessed in relation to specimen properties and beam parameters. Characterised in terms of morphology and composition, their effect on SE image contrast was evaluated. This revealed that the He^+ induced contamination behaves initially like electron-induced contamination, depending almost linearly on irradiation dose. However, for larger dose values, the nature of the beam-specimen-hydrocarbon interaction precludes comparison between HIM and SEM due to ion sputtering and implantation.

Various specimens were used to evaluate the SE contrast mechanisms. Firstly, image contrast of Ga^+ implanted regions in an n-type silicon specimen was analysed. This revealed a similar relationship between, image contrast, Ga^+ density and the imaging parameters. The quantification of SE contrast was also significantly influenced by dynamic charging effects. Secondly, SE imaging of a graphene surface was used to provide sub-nanometer information on the morphology of contaminants there on. The contrast of contaminants, i.e. their apparent lateral dimensions, varied with imaging conditions however, a quantitative method to determine the physical size of surface features, regardless of contrast variation, was derived. The HIM was evaluated as a superior SE imaging technique, in terms of image fidelity, due to the finite size of its primary beam probe. Thirdly, a quantitative method for the extraction of graphene work function was determined from SE images of layered graphene specimens. A model based on illumination by both the primary beam and backscattered particles was established to explain the observed layer-dependent SE contrast and work function.

Complimentary to the SE imaging study, and to further enhance the specimen characterisation function of HIM, a SE energy filter device was designed and fabricated for use in both HIM and SEM. It was quantified in terms of filtering

efficiency and used to generate image based SE energy spectra of electron and He^{+}-ion irradiated specimens.

Finally, a dedicated study to understand Raman enhancement of electron-induced carbonaceous deposits was conducted. Its focus was to determine the influence of electron beam energy on the bonding structure of the carbon layers and its effect on their optical properties.

PUBLICATION

1. Hu Luo, **Robert O' Connell**, Rongming Wang, Yanhui Chen, Daniel Fox, Jing Jing Wang, and Hongzhou Zhang*. Enhanced photoluminescence from SiO_x-Au nanostructures. *CrystEngComm*, 15:10116–10122, 2013.

2. Yangbo Zhou, **Robert O'Connell**, Pierce Maguire, Hongzhou Zhang*. High throughput secondary electron imaging of organic residues on a graphene surface. *Nature Scientific Reports*, 4:7032, 2014.

3. Yanhui Chen, **Robert O'Connell**, Junfeng Zhou, Daragh Mullarkey, Robert O'Connell, Wolfgang Schmitt, M. Venkatesan, Michael Coey, and Hongzhou Zhang*. Synthesis, characterization and magnetic properties of ultrafine Co_3O_4 octahedra. American Institute of Physics, *AIP Advances*, 5:087122, 2015.

4. Yangbo Zhou, **Robert O'Connell**, Daniel S. Fox, Pierce McGuire, Robert Masters, Cornelia Rodenburg, Hanchun Wu, Maurizio Dapor, Ying Chen & Hongzhou Zhang*. Quantitative secondary electron imaging for work function extraction at atomic level and layer identification of graphene. *Nature Scientific Reports*, 6:21045, 2016.

5. Yanhui Chen, **Robert O'Connell**, Junfeng Zhou, Felim Vajda, Pierce Richard Maguire, Wolfgang Schmitt, Yonghe Li, Zheng-Guang Yan, Yue-Fei Zhang and Hongzhou Zhang*. Enhancing capacitance behaviour of CoOOH nanostructures using transition metal dopants by ambient oxidation. *Nature Scientific Reports*, 6:20704, 2016.

6. Yanhui Chen, **Robert O'Connell**, Junfeng Zhou, Felim Vajda, Pierce Richard Maguire, Wolfgang Schmitt, Yonghe Li, Zheng-Guang Yan, Yue-Fei Zhang and *Hongzhou Zhang. Multi-metallic Hydrate Hollow Structures in Cobalt Hydrate Based Systems. *Crystal Growth & Design*, 4:1568-1573, 2017.

7. **Robert O'Connell**, Yanhui Chen, Yangbo Zhou, Daniel Fox, Pierce Richard Maguire, Jing Jing Wang, Cornelia Rodenburg, Hongzhou Zhang*. Comparative study of image contrast in scanning electron microscope and helium ion microscope *Journal of Microscopy*, 3:313-320, 2017.

8. Nicola Stehling, Robert Masters, Yangbo Zhou, **Robert O'Connell**, Chris Holland, Hongzhou Zhang and Cornelia Rodenburg*. New perspectives on nano-engineering by secondary electron spectroscopy in the helium ion and scanning electron microscope *MRS Communications*, mrc.2018.75

9. **Robert O'Connell**, Yangbo Zhou, Pierce Richard Maguire, Daniel Fox, Tatiana Perova, Niall McEvoy, Jing Jing Wang and Hongzhou Zhang*. Optical properties of electron beam induced amorphous carbon deposits. *In Preparation*

ACKNOWLEDGEMENTS

To my supervisor, Prof. Hongzhou Zhang. Thank you for your support, kindness and guidance on all matters of science and life.

Thanks to the Irish Research Council and Intel Ireland for co-funding my research.

To my research family members, thank you one and all for your individual contributions to my work and for allowing me to be part of yours. Dr. Yanhui Chen, Dr. Yangbo Zhou, Dr. Daniel Fox, Mr. Abbas Khalid, Mr. Pierce Maguire, Mr. Junfeng Zhou, Mr. Jakub Jadwiszczak, Mr. Darragh Keane, Mr. Fei Gao and Mr. Gen Li.

Thanks to all the staff at CRANN and the Advanced Microscopy Laboratory, with special thanks to Mr. Dermot Daly, Mr. Cathal McAuley, Mr. Clive Downing and Dr. Colm Faulkner.

Thanks to Dr. Eoin McCarthy, Dr. Allan Bellew and Dr. Shaun Mills for their support with atomic force microscopy experiments and analysis. To Prof. Tatiana Perova, Dr. Niall McEvoy and Dr. Jing Jing Wang for their generous assistance with Raman experimentation and analysis. Also sincere thanks to Prof. Cornelia Rodenburg and Dr. Robert Masters for their collaboration on the secondary electron energy filter work.

Thanks to the members of the Intel Ireland research team for their support and encouragement over the duration of my PhD, including, Dr. Juan Perez-Camacho, Mr. Peter Gleeson, Mr. Chris Murray, Dr. Gavin D'Arcy, Dr. Alan Bell and Mr. Bernard Capraro.

Sincere thanks to the management and staff of School of Physics, for their time and assistance, with a special note of thanks to the Prof. Louise Bradley and Prof. James Luney. Thanks to all of the professors, whose postgraduate modules I attended, for their enthusiasm and availability for questions and discussion, including, Prof. Graham Cross, Prof. John Donegan, Prof. Valeria Nicilosi, Prof. Paul Eastman, Prof. Martin Hegner and Prof. Graham Harper. Special thanks also to Dr. Anna Drury, Mr. Ken Concanon and Mr. Alan O'Meara.

Finally, to my parents, brothers and dear friends. Thank you for all your support.

CONTENTS

Declaration of Authorship i

Abstract iii

Publication v

Acknowledgments vii

List of Figures xiii

List of Tables xix

List of Abbreviation xxi

1 Introduction 1
- 1.1 Motivation 1
- 1.2 Thesis Outline 4

2 Imaging and beam-induced contamination in charged-particle microscopes 5
- 2.1 A review on SEM/HIM imaging and spectroscopy 5
  - 2.1.1 Signal generation and imaging modes in SEM and HIM . . . 6
  - 2.1.2 SE spectroscopy 10
  - 2.1.3 SE imaging of two-dimensional materials 15
    - 2.1.3.1 Organic residues on a graphene surface 15
    - 2.1.3.2 Work function extraction and layer identification of graphene 16
- 2.2 Carbon contamination in charged particle microscopes 18
  - 2.2.1 Formation of beam-induced contamination in SEM 18
  - 2.2.2 Effects of contamination on the imaging 21
  - 2.2.3 Current technology to mitigate contamination formation . . 23
  - 2.2.4 Applications of beam-induced carbon contamination 24

3 Raman Spectroscopy and its application to the characterisation of carbonaceous materials 29
- 3.1 Raman spectroscopy 29
  - 3.1.1 Raman scattering 30
  - 3.1.2 Raman spectra 32
- 3.2 Raman characterisation of carbon materials 33
  - 3.2.1 Raman spectroscopy of crystalline carbon 33

3.2.2 Raman spectroscopy of amorphous carbon 34
3.2.3 Raman characterisation of electron beam induced carbonaceous deposits 40
3.3 Enhanced Raman Spectroscopy 42
3.3.1 The Raman enhancement effect 42
3.3.2 Enhancement mechanisms 43
3.3.2.1 Electromagnetic theory 43
3.3.2.2 Chemical theory 47
3.3.3 Raman enhancing surfaces and materials 48
3.3.4 Applications for enhanced Raman spectroscopy techniques . 51
3.3.5 Raman enhancement effect of amorphous carbon 51
3.3.6 Summary of Raman enhancement 51

4 Experimental methods 53
4.1 Contamination formation 53
4.1.1 Specimen preparation 53
4.1.2 Beam parameters for contamination formation 56
4.2 Characterisation of carbonaceous contamination 59
4.2.1 Atomic force microscopy 59
4.2.2 Chemical characterisation 62
4.2.2.1 Energy dispersive X-ray spectroscopy 62
4.2.2.2 Electron energy loss spectroscopy 63
4.2.3 Electrical characterisation 64
4.3 SE imaging of two-dimensional materials 65
4.3.1 Optimization of the probe size for SE imaging 65
4.3.2 SE contrast analysis 68
4.3.3 Collection of SE image and spectrum from graphene samples 69
4.3.4 Evaluation of graphene SE yield 70
4.3.5 Statistics of graphene SE contrast 71
4.4 Raman investigation of carbonaceous contamination 73
4.4.1 Raman mapping 73
4.4.2 Correlative Raman-AFM analysis 75

5 A comparative study: contamination formation, imaging and SE spectroscopy in SEM and HIM 79
5.1 Contamination formation in HIM and SEM 80
5.1.1 Morphology of Contamination 80
5.1.2 The effect of sample treatment 83
5.1.3 Composition of contamination 83
5.1.4 Summary of contaminaiton formation in HIM and SEM . . . 85
5.2 SE imaging in SEM and HIM: Imaging modes 86
5.2.1 Sample preparation and imaging modes 86

5.2.2 General morphology of the Si sample 87
5.2.3 Comparison of image contrast 88
5.2.4 Contrast reversal in SE imaging 91
5.2.5 Summary of the effects of imaging parameters on image contrast 94
5.3 High throughput secondary electron imaging of organic residues on a graphene surface 95
5.3.1 Graphene sample and characterisation methods 95
5.3.2 Comparison between SE imaging, optical microscopy and AFM: general features 96
5.3.3 Visibility of graphene in the SE imaging 98
5.3.4 Typical features in SE images of graphene with polymer residues 101
5.3.5 SE imaging of polymer residues in HIM and SEM 103
5.3.6 The effect of probe size on resolution of SE graphene imaging 106
5.3.7 A contrast model of SE graphene imaging in HIM and SEM 107
5.3.8 Summary of imaging organic residues on a graphene surface 110
5.4 Quantitative SE imaging for work function extraction and layer identification of graphene 111
5.4.1 Graphene preparation 111
5.4.2 Optimisation of the SE imaging conditions in SEM 112
5.4.3 Layer dependence of graphene SE contrast and work function extraction 113
5.4.4 Summary of quantitative SE imaging for work function extraction and layer identification of graphene. 123
5.5 Fabrication and application of a SE energy filter in HIM and SEM . 123
5.5.1 SE energy filter design and fabrication 123
5.5.2 SE energy filter calibration 126
5.5.2.1 Initial evaluation 126
5.5.2.2 SE energy calibration 130
5.5.2.3 Spatial electric field characterisation 133
5.5.2.4 Comparative evaluation in SEM 140
5.5.2.5 Summary of SE energy filter calibration 150
5.5.3 Application of the SE energy filter device: SE Image spectroscopy in HIM 151
5.5.3.1 HOPG Specimen preparation 152
5.5.3.2 Image acquisition and SEED generation parameters 153
5.5.3.3 Assessment of the HOPG surface condition 153
5.5.3.4 HOPG SEED generation 154
5.5.3.5 Discussion and analysis of HOPG SEED generation 161
5.5.3.6 Measurements of graphene SE spectra in SEM and HIM 163

5.5.4 Summary of fabrication and application of a SE energy filter in HIM and SEM 166
5.6 Summary of the comparative study on contamination formation, imaging and SE spectroscopy in SEM and HIM 167

6 Raman enhancement of electron-beam induced carbon layers 171
6.1 Characterisation of the carbon layers 171
6.1.1 General morphology 173
6.1.2 Chemical Analysis of the carbon layers 174
6.1.3 Electrial property of the carbon layers 176
6.2 Raman mapping and correlative study 177
6.3 Raman spectral analysis of the carbon layers 182
6.3.1 Collective spectra 182
6.3.1.1 Peak position and intensity 183
6.3.2 Individual spectra 184
6.3.2.1 5 keV Carbon Layer 184
6.3.2.2 1 keV Carbon Layer 188
6.3.2.3 3 keV Carbon Layer 191
6.3.2.4 12 keV Carbon Layer 192
6.3.2.5 20 keV Carbon Layer 198
6.3.2.6 30 keV Carbon Layer 199
6.4 Exploring the mechanisms of enhancement 205
6.4.1 The effect of excitation energy 205
6.4.2 The influence of deposition energy 214
6.4.3 Discussion on the mechanisms of enhancement 217
6.5 Summary of Raman enhancement properties of electron-beam induced carbon layers. 220

7 Conclusion and future work 221
7.1 Conclusion for the comparative SE study. 221
7.2 Conclusion for the Raman enhancement of electron-beam induced carbon layers. 229
7.3 Future work 231

A TEM lamella preperation 235

Bibliography 239

LIST OF FIGURES

2.1 A sketch of the image forming optics SEM and HIM. 5
2.2 Probe size comparison between SEM and HIM. 8
2.3 Simulated beam-specimen interactions in SEM and HIM. 8
2.4 Relationship between SE yield and primary beam energy in SEM . 9
2.5 A comparision of electron and ion induced SE energy spectra. . . . 12
2.6 Determination of specimen workfuction by the F(Ese) dependence . 14
2.7 The factors influencing contamination formation. 20
2.8 The influence hydrocarbon ionisation and electron scattering in contamination formation. 22

3.1 A Jablonksi diagram for Raman and Rayleigh scattering. 31
3.2 Raman spectra of crystalline and amorphous carbons. 33
3.3 Vibrational motions of the carbon Raman modes. 34
3.4 sp^2 cluster and crystallite size to I_D/I_G ratio. 35
3.5 Mapping the the structural changes in a-C. 37
3.6 Calculating the sp^3 fraction in a-C. 37
3.7 Calculating the sp^3 fraction in a-C:H. 39
3.8 The optical gap in a-C:H relative to G peak width. 40
3.9 Raman characterisaiton of an e-beam induced contamination layer. 40
3.10 Raman spectra of carbonaceous deposits formed from organic precursors. 41
3.11 LSPR in excited nanoparticles. 44
3.12 Extinction efficiency in an Ag nano-particle. 45
3.13 Energy level diagram for a molecule adsorbed on a metal surface. . 48

4.1 Optical and SEM images of the Si wafer specimen 54
4.2 Irradiation array layout for carbon layer deposition. 58
4.3 SEM overview images of the deposited carbon layers 58
4.4 Schematic diagram of an AFM instrument setup. 60
4.5 Carbon layer electrical characterisation apparatus. 65
4.6 Evaluation of image astigmatism. 66
4.7 HIM SE image focus series of a graphene edge. 67
4.8 Evaluation of beam probe size. 68
4.9 Determining SE yield of freestanding graphene. 71
4.10 Contrast statistics of different graphene flakes. 72
4.11 Schematic overview and labratory set-up of the Raman mapping instrument. 74
4.12 Raman intensity maps of a 3 keV - 5 nC·μm^{-2} EBID carbon layer with its corresponding AFM height profile. 77
4.13 Raman intensity maps of a 3 keV - 3 nC·μm^{-2} EBID carbon layer with its corresponding AFM height profile. 78

5.1 3D AFM height profiles of contamination generated by 30 keV He^+ ion irradiation and 1 keV electron irradiation. 80
5.2 SEM images of contamination layers formed in HIM and SEM, and the observed changes in SE contrast as a function of layer thickness. 82
5.3 SEM SE contrast of samples undergone chemical cleaning treatment, prior to contamination formation by He^+-ion and electron irradiation. 84
5.4 EDX spectra and analysis of the carbon and oxygen content in the contamination regions. 85
5.5 Characterising the morphology of the Ga doped Si regions by AFM, EDX and Raman spectroscopy 88
5.6 Images of the doping contrast and the relationships between image contrast an Ga density 89
5.7 Monte Carlo simulations of the electron and ion trajectories in the Ga implanted region and the BSE yield of a 5 keV electron beam as a function of implanted Ga density. 89
5.8 SEM-InLens images and SE contrast as a function of Ga density and e-beam energy 91
5.9 SE contrast as a function of the dwell time for SEM-InLens and HIM ET images 93
5.10 The SE yield as a function of the primary electron beam, and the charging effects in the implanted regions. 93
5.11 Low magnification images of the measured substrate supported graphene sample 97
5.12 High resolution images of graphene edges. 98
5.13 The visibility of graphene in SE contrast. 99
5.14 SE images of substrate supported graphene. 102
5.15 Measurement of the dark dot size. 103
5.16 Comparison of other graphene surface features. 104
5.17 High magnification SE images of freestanding graphene. 105
5.18 The relationship between the beam probe size and the dark dot size 108
5.19 The PMMA nanoparticle stacking model for SE contrast. 109
5.20 The influence varying WD on SEM SE imaging 113
5.21 SE image of a graphene flake under different scanning speeds. . . . 114
5.22 The effect of scan time and beam current on graphene SEM SE contrast. 114
5.23 Layer dependence of graphene SE contrast. 115
5.24 Layer dependence of graphene SE contrast for thicker layers. 116
5.25 Graphene layer identification from SE contrast. 117
5.26 Extraction of graphene work function from the SE contrast. 118
5.27 Validity of the SE contrast model and work function extraction. . . 122
5.28 The design and in-situ placement of the SE energy filter in the HIM. 124

5.29 Components of the SE energy filter assembly and its mounting within the HIM. 125
5.30 Energy filter external control, biasing, electrical set-up 126
5.31 HIM SE images of an un-biased Ta (110) specimen acquired during the initial testing of the SE energy filter. 127
5.32 The effect of the energy filter bias on SE image intensity, from an unbiased Ta(110) specimen. 128
5.33 The homogeneous filtering effect of the energy filter retarding grid. . 129
5.34 He^+ ion induced SE intensity profile of an unbiased Ta (110) test specimen, and corresponding SE energy distribution. 130
5.35 The logarithmic transform of the SEED shape collected from an unbiased Ta(110) test specimen. 132
5.36 The SEED of the unbiased Ta (110) test specimen fitted to a non-linear curve. 132
5.37 The *F(Ese)* dependence plotted as a function of SE energy (eV), used to determine the work function of the Ta (110) test specimen. 133
5.38 He^+ ion induced SE intensity profiles of a Ta (110) test specimen, biased at 0, -1, -3 and -5 V, and corresponding SE energy distributions. 134
5.39 The logarithmic transform, fitted SEED and *F(Ese)* dependence, of a Ta(110) test specimen biased at -1 V. 135
5.40 The logarithmic transform, fitted SEED and *F(Ese)* dependence, of a Ta(110) test specimen biased at -3 V. 136
5.41 The logarithmic transform, fitted SEED and *F(Ese)* dependence, of a Ta(110) test specimen biased at -5 V. 137
5.42 Onset corrected SEEDs of a Ta (110) test specimen, biased at -1, -3 and -5 V. 138
5.43 SE image intensity profiles and SEEDs of an un-biased Ta (110) test specimen irradiated with He^+ ion energies of 10, 20 and 30 keV. 139
5.44 The logarithmic transform, fitted SEED and *F(Ese)* dependence of an unbiased Ta (110) test specimen irradiated with He^+ ion energy of 10 keV. 141
5.45 The logarithmic transform, fitted SEED and *F(Ese)* dependence, of an unbiased Ta (110) test specimen irradiated with He^+ ion energy of 20 keV. 142
5.46 The logarithmic transform, fitted SEED and *F(Ese)* dependence, of an unbiased Ta (110) test specimen irradiated with He^+ ion energy of 30 keV. 143
5.47 Onset corrected SEEDs of an unbiased Ta (110) test specimen, irradiated with He^+ ion energies of 10, 20 and 30 keV. 144
5.48 Electron beam induced SE image intensity profile from an unbiased Ta (110) test specimen, and corresponding SE energy distribution. . 145
5.49 Onset corrected electron beam induced SEED and *F(Ese)* dependence, of an unbiased Ta (110) specimen. 147

5.50 Energy adjusted SEED data and replotted *F(Ese)* dependence, of an unbiased Ta (110) specimen. 147
5.51 HIM and SEM SEED data, and HIM *F(Ese)* dependence plot, of an Mo specimen. 148
5.52 A comparison of fitted electron and He^+ ion induced SEEDs of an unbiased Ta (110) specimen. 149
5.53 SEM SE Image intensity profiles of a Ta (110) specimen for stage bias settings of 0, -1, -2, and -3 V, with corresponding SE energy distributions. 149
5.54 HOPG test specimen prior to mechanical exfoliation. 153
5.55 HIM SE image of the features observed on the surface freshly cleaved HOPG specimen. 154
5.56 A SEED progression generated by four energy filtered imaging sequences from a Type-A HOPG surface area. 156
5.57 The fitted SEED from the first imaging sequence of the Type-A surface area, confirming EF filtering efficiency. 157
5.58 The first part of a SEED progression from a Type-B HOPG surface area. 158
5.59 The second part of a SEED progression from a Type-B HOPG surface area 160
5.60 SE images of a typical Type-C area, acquired prior to and during the surface cleaning scans 161
5.61 A SEED progression from a 'pre-cleaned' Type-C HOPG surface area. 162
5.62 SE Spectra of a freestanding monolayer graphene. 165
5.63 Determination of index n for multilayer graphene. 165
5.64 SE energy spectrum of monolayer graphene in HIM. 166

6.1 Overview images on the 1 - 30 keV carbon layers. 172
6.2 EDX analysis of the carbon layers. 174
6.3 EELS analysis of the carbon layers. 175
6.4 Carbon layer electrical characterisation results 176
6.5 Raman intensity maps of the carbon layers. 178
6.6 Carbon-Raman correlation study. 181
6.7 Collective Raman spectra for a 3 keV carbon layer. 182
6.8 Fitted Raman spectral peaks from the 3 keV and 5 keV carbon layers. 183
6.9 Raman spectra for individial points 5 keV carbon volume. 186
6.10 Si and carbon Raman parameters as a function of increasing 5 keV carbon layer volume. 187
6.11 Raman spectra for individial points 1 keV carbon volume 189
6.12 Si and carbon Raman parameters as a function of increasing 1 keV carbon layer volume. 190
6.13 Raman spectra for individial points 3 keV carbon volume. 193

6.14 Si and carbon Raman parameters as a function of increasing 3 keV carbon layer volume. 194
6.15 Raman spectra for individial points 12 keV carbon volume. 196
6.16 Si and carbon Raman parameters as a function of increasing 12 keV carbon layer volume. 197
6.17 Raman spectra for individial points 20 keV carbon volume. 200
6.18 Si and carbon Raman parameters as a function of increasing 20 keV carbon layer volume. 201
6.19 Raman spectra for individial points 30 keV carbon volume. 203
6.20 Si and carbon Raman parameters as a function of increasing 30 keV carbon layer volume. 204
6.21 Raman enhancing characteristics of a 3 keV carbon layer 206
6.22 Thickness-dependent Raman enhancement of a 3 keV carbon layer. 207
6.23 Raman enhancing characteristics of a 1 keV carbon layer. 209
6.24 Thickness-dependent Raman enhancement of a 1 keV carbon layer. 209
6.25 Raman enhancing characteristics of a 5 keV carbon layer. 210
6.26 Thickness-dependent Raman enhancement of a 5keV carbon layer. . 210
6.27 Raman enhancing characteristics of a 12 keV carbon layer. 211
6.28 Thickness-dependent Raman enhancement of a 12 keV carbon layer. 211
6.29 Raman enhancing characteristics of a 20 keV carbon layer. 212
6.30 Thickness-dependent Raman enhancement of a 20 keV carbon layer. 212
6.31 Raman enhancing characteristics of a 30 keV carbon layer. 213
6.32 Thickness-dependent Raman enhancement of a 30 keV carbon layer. 213
6.33 Enhancement observed accross all carbon layers. 214
6.34 Volume normalised enhancement observed across all carbon layers. . 215
6.35 Maximum normalised enhancement occurring at each e-beam deposition energy. 216

A.1 SEM images of the 3 keV carbon layer, prior to TEM lamella preperation 236
A.2 SEM and FIB images of the TEM lamellas, for the 3 keV and 30 keV carbon layers, in the lift-out stage. 237
A.3 SEM images of the TEM lamellas, for the 3 keV and 30 keV carbon layers, post final thinning to ~60nm. 238

LIST OF TABLES

4.1 A list of microscope specifications for HIM and SEM. 56
4.2 Irradiation parameters for carbon layer formation. 59
4.3 AFM probe specifications. 61
4.4 Carbon layer deposition paramaters for electrical characterisation. . 64
4.5 Contrast measurement of the same graphene flakes in two different SEMs (Carl Zeiss Ultra and FEI Strata DB 235). 73
4.6 Contrast measurement of graphene flakes in HIM. 73

6.1 Results of the statistical correlation study. 180
6.2 A comparison of the carbon D and G intensities (*Charge-Coupled Device* (CCD) counts), intensity ratios, and peak positions from the fitted Raman profiles displayed in Figure 6.8 184

LIST OF ABBREVIATIONS

2D *Two-Dimensional*. 2, 3, 15, 17, 226

3D *Three-Dimensional*. 177, 179, 180

AFM *Atomic Force Microscope*. 15, 16, 24, 25, 28, 59–61, 75, 76, 79, 80, 84, 86, 87, 96, 107, 108, 110, 161, 167, 171, 173, 177, 179, 180, 220, 230

ASIN *Architecture and Synthesis of Integrated Nanostructures*. 74

BNC *Bayonet Neil-Concelman*. 125, 126

BS *Back Scattered*. 7, 26, 164, 226

BSE *Back Scattered Electrons*. 26, 70, 89, 90, 100, 169

CCD *Charge-Coupled Device*. xix, 74, 75, 184

CM *Chemical Mechanism*. 43, 49

DVM *digital volt-meter*. 125

EBID *Electron Beam-Induced Deposition*. 3, 24, 27

EDX *Energy Dispersive X-ray Spectroscopy*. 2, 62, 63, 75, 79, 83, 86, 87, 167, 171, 174, 220, 229

EELS *Electron Energy Loss Spectroscopy*. 25, 38, 42, 62, 63, 75, 171, 174, 175, 219, 220, 229, 232

EF *Energy Filter*. 3, 124–128, 131, 133, 139, 148–151, 153, 155, 166, 169, 227–229

EM *Electron Microscope*. 1, 2, 43

EM-M *Electromagnetic Mechanism*. 43, 49, 52

ER *Enhanced Raman*. 45

EsB *Energy Selective Backscattered*. 87–90, 94, 95, 223

ET *Everheart-Thornley*. 79, 86–88, 90, 91, 94, 95, 123, 223

FFT *Fast Fourier Transformation*. 65, 66
FIB *Focused Ion Beam*. 27, 86, 87, 94, 223, 235–237
FOV *field of view*. 58, 64, 74, 103, 127, 128, 130, 140, 153, 179, 228, 236
FSE *Forward Scattered Electrons*. 26
FTIR *Fourier transform infra-red*. 232
FWHM *full width half maximuim*. 63, 102, 103, 134, 148, 150

HIM *Helium Ion Microscope*. 1–11, 13–18, 24, 53, 56, 57, 59, 66, 69–71, 79–83, 85–91, 94–98, 100–107, 110, 113, 115, 116, 121, 124, 127, 128, 130, 131, 134, 145, 146, 148–151, 153–155, 162, 163, 166–169, 221–228, 231
HOMO *Highest Occupied Molecular Orbital*. 47, 50
HOPG *highly ordered pyrolytic graphite*. 11, 79, 140, 152–163, 166, 169, 227, 228

ICP *Inductively Coupled Plasma*. 53
IMFP *inelastic mean free path*. 12, 115, 119, 226
IPA *Isopropyl Alcohol*. 83, 96, 111, 126

LSPR *Local Surface Plasmon Resonances*. 43
LUMO *Lowest Unoccupied Molecular Orbital*. 47, 50

MCP *Micro-Channel Plate*. 86, 88–90, 94, 95, 223
MIM *Metal-Insulator-Metal*. 27

NIR *Near Infra-Red*. 28, 232
NMR *Nuclear Magnetic Resonance*. 38

OM *Optical Microscope*. 98, 100, 116

PEEM *Photoelectron Emission Spectroscopy*. 17

PMDA *Pryomellitic dianhydride*. 50
PMMA *polymethyl methacrylate* . 95, 96, 101, 107–111
PTSM *Photon Scanning Tunnelling Microscopy*. 28

RF *Radio Frequency*. 56
RIE *Reactive-Ion Etching*. 53
RMS *root mean square*. 87
RNA *ribonucleic acid*. 51

SE *Secondary Electron*. 1–18, 21, 22, 26, 53, 54, 57, 65, 68–72, 79–83, 85, 86, 90, 92, 94–98, 100–104, 106–108, 110–113, 115, 116, 118–131, 133–146, 148–156, 158–164, 166–169, 173, 178–180, 221–229, 231, 232
SEED *Secondary Electron Energy Distribution*. 11–14, 130–151, 154–163, 166, 167, 169, 227, 228, 231
SEM *Scanning Electron Microscope*. 1–7, 9–11, 13, 14, 16–18, 21, 23, 26–28, 41, 53–57, 59, 62, 64, 67–72, 79–83, 85–92, 94–98, 100–107, 110, 112, 113, 115, 116, 118, 120, 126, 140, 145, 146, 148, 149, 151–153, 163, 166–169, 171, 173, 176, 177, 180, 220–223, 225–229, 232, 236–238
SERS *Surface Enhanced Raman Scattering*. 42, 46–49, 51, 52
SP *Surface Plasmons*. 43
SRIM *Stopping Range of Ions in Matter*. 87
STEM *Scanning Transmission Electron Microscope*. 63, 174
STM *Scanning Tunneling Microscope*. 15, 16, 42

TEM *Transmission Electron Microscope*. 1, 26, 55, 62, 63, 75, 124, 126, 171, 174, 235–238
TERS *Tip Enhanced Raman Scattering*. 42, 43, 48–52

TES *Terahertz Emission Spectroscopy* . 16

UHV *Ultra High Vacuum*. 125, 162
UV *Ultra-Violet*. 38, 47, 49

VDOS *Vibrational Density of States*. 36

WD *working distance*. 62, 71, 112, 127

XPS *X-ray Photoelectron Spectroscopy* . 16

ZLP *Zero Loss Peak*. 63, 174

Chapter 1

Introduction

1.1 Motivation

The *Electron Microscope* (EM), including the *Transmission Electron Microscope* (TEM) and the *Scanning Electron Microscope* (SEM), have been powerful characterisation and analytical tools to investigate materials. Advances in EM instrumentation are driven by the demands for higher resolution, which in turn enable breakthroughs in relevant fields and initiate novel research topics that seek higher resolution. For example, the spherical-aberration corrected TEM has been indispensable for recent achievements in the study of two-dimensional materials [1]. Nevertheless, there are still many characterisation challenges yet to be met by present EM technology, for example that of automated, sub-nanometer surface characterisation of insulating samples, which is of extreme importance to the continued development of semiconductor devices [2]. As a recent addition to the family of charged-particle microscopes [3], the *Helium Ion Microscope* (HIM) is a complementary tool to EM and has the potential to address these characterisation challenges. Compared with SEM, the HIM imaging has several advantages, such as a better lateral resolution, a larger depth of field, better surface sensitivity and material contrast, and a unique charging compensation mechanism [4–6]. A wide range of samples have been imaged using HIM, such as cancer cells [7], graphene [8–10], polymers [11, 12], etc. In terms of semiconductor applications, *Secondary Electron* (SE) dopant contrast imaging has been demonstrated in a SEM [13, 14], particularly by using a low-voltage scanning electron microscope [15, 16]. HIM imaging has also been used in efforts to quantify dopant concentration and a direct correlation between dopant concentration and SE intensity has been reported [17–19].

In these charged-particle microscopes (especially SEM and HIM), SE imaging is the most common imaging mode and SE images are rich in surface topographical

information, which can be interpreted intuitively. The SE imaging in HIM shows some unique features, for example, surface sensitivity and efficient charging compensation [3, 20, 21]. HIM delivers better spatial resolution than SEM, particularly for sensitive samples such as *Two-Dimensional* (2D) materials and biological tissues. However, the unique HIM contrast has yet to be fully understood. One of the most challenging problems for high-resolution imaging in charged-particle microscopy is the beam-induced contamination, arising from the interaction between the energetic particles involved with beam-specimen interaction and the hydrocarbon materials present on the specimen surface [22]. Beam-induced contamination may not only prevent correct characterisation (reduced accuracy, artefacts, etc.) but even alter the physical properties of the specimen surface. For example, SE images can be dramatically modified by the contamination induced during image acquisition [23, 24]. This issue is aggravated when seeking higher surface sensitivity and spatial resolution, since the image of a contaminated sample reflects the morphology of contamination rather than that of the sample. For optimal surface characterisation conditions, it is crucial to understand contamination formation in order to evaluate and mitigate its adverse effects.

In terms of the formation of beam-induced contamination, SEs have the highest yield for the cross-linking of hydrocarbon molecules [25], since by definition the kinetic energy of SEs is $\leq$ 50eV [26]. This means the SE yield, spatial distribution and energy spectrum have significant impacts to contamination formation. The SE energy spectrum in HIM is quite different from that in SEM. It shows a narrower peak and a lower average energy [27, 28]. Although carbonaceous contamination in EM is well documented [22, 29–31], it has rarely been investigated for HIM. To further evaluate and extend the imaging capabilities of the HIM tool, it is imperative to clarify the generation of He^{+}-induced contamination.

In addition, by understanding SE generation in beam-specimen interaction certain material properties can be revealed, e.g. work function. This has a particular importance to extending the analytical capability of the HIM tool. In SEM, *Energy Dispersive X-ray Spectroscopy* (EDX) is a well-established and powerful method for chemical analysis of materials, but characteristic X-rays are not available in HIM [32]. SE spectroscopy and energy filtered imaging techniques may provide an alternative method to EDX. This has been demonstrated in SEM to resolve polymer phases [33] and may be superior to EDX for analysis of light materials since EDX can lead to significant specimen damage due to the high doses required

for X-ray generation [34]. It is expected to find even more important applications in HIM, because HIM is an ideal instrument for imaging light materials [11, 35] and HIM SE images are formed from the signals which originate precisely from the beam-specimen interaction point. However, little in the way of He^+ ion induced SE spectroscopy has been conducted so far and the instrumentation of SE spectrum needs to be further developed.

Knowledge of beam-induced contamination will also facilitate the exploitation of *Electron Beam-Induced Deposition* (EBID). Indeed, EBID of residual hydrocarbons in SEM has many uses in microscopy [36], spectroscopy [37, 38], lithography [39], and nano-science [40, 41]. For example, a study on electron beam induced contamination reported a significant increase in Raman G band intensity [42], suggesting new applications for carbon contamination. However, the mechanism of the enhancement is not clear and the effects of beam parameters on the enhancement are not explored. This knowledge is crucial to maximise the phenomena and realize controllable enhancement for further applications.

Based on existing knowledge of electron-induced contamination in SEM, the main focus of this thesis is to investigate the formation of He^+-induced contamination in HIM and the influence of surface contaminants on specimen characterisation. Key to this is to study the SE characteristics in HIM. This will be achieved by comparing SE generation and energy spectrum in SEM and HIM, as the SE generation mechanism is of critical significance to the contamination formation process. An *Energy Filter* (EF) device is thus designed and built for operation in HIM and SEM. Upon quantification of the EFs filtering efficiency, it can be used to generate image based SE energy spectra of electron and He^+-ion irradiated specimens. The aim of this part of the thesis is to understand the significance of the beam-induced charging effects on SE emission and develop HIM SE imaging for the quantitative characterisation of 2D materials. The other primary aim of this thesis is to understand Raman enhancement of electron-induced carbonaceous deposits. The individual bonding structure of a series of carbon layers, generated over a broad range of electron beam energies, were characterised. It details the influence of electron beam energy on the bonding structure of the carbon layers and its effect on their optical properties.

1.2 Thesis Outline

This thesis begins in Chapter 2 with an introduction to charged particle microscopes and a brief review of the contamination formation mechanism. The effects and benefits of the resultant carbonaceous (contamination) deposits are also given.

Chapter 3 gives an overview on the theory of Raman spectroscopy and its application towards the analysis of amorphous carbonaceous materials.

The experimental methods used to induce and characterise the contamination profiles for studying their effect on SE contrast in SEM and HIM, and the carbon layers for studying their Raman enhancing properties, are detailed in Chapter 4.

Chapter 5 is the first of the experimental-result chapters. It starts with a comparative study between contamination formed by He^+ ion and electron irradiation. This is initially followed by a comparison study of image contrast between the two microscopes for their available imaging modes, and is subsequently followed by a systematic study on SE imaging of graphene specimens. This chapter is concluded with results on the development and application of SE energy spectra generation.

Chapter 6 is the second experimental results chapters and details the characterisation of the electron beam induced carbon layers. The Raman enhancing properties of the layers are characterised in terms of deposition energy, deposition volume and carbon sp^2:sp^3 bonding ratio.

In Chapter 7, the conclusions of the work undertaken in this thesis are outlined. The future work which still remains is discussed, along with the challenges that need to be overcome.

Chapter 2

Imaging and beam-induced contamination in charged-particle microscopes

This chapter starts with a brief review on the fundamentals of charged-particle microscopes, including its basic structures and principles. We then outline background knowledge in SE imaging that is relevant to the work in this thesis. This is followed by a discussion on the formation and effects of beam-induced contamination in SEM

2.1 A review on SEM/HIM imaging and spectroscopy

The SEM and the HIM are surface characterisation tools with a high throughput and the ability to investigate large bulk samples (up to tens of centimetres),

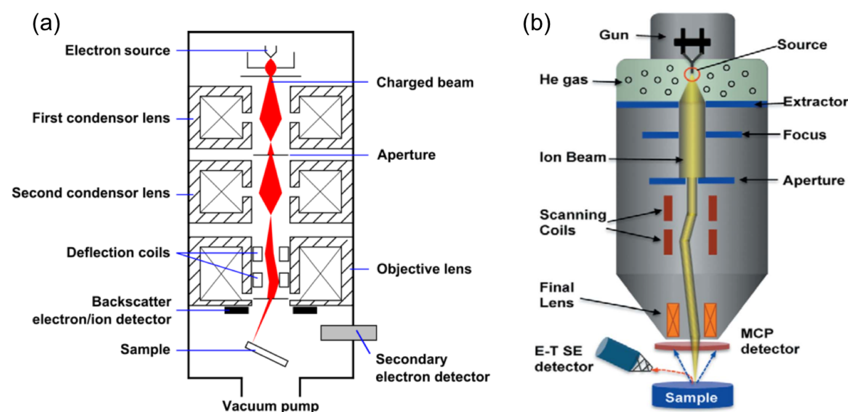

FIGURE 2.1: Sketch of (a) a scanning electron microscope (b) a helium ion microscope.

exhibiting a similar structure and working principle.The helium-ion microscope (HIM) was introduced as a surface imaging tool and made available to the research community in 2006, aiming to address the challenges of critical dimension measurement in the semiconductor industry [43]. HIMs operate on similar working principles to those of SEMs [3, 20, 21]. As shown in Figure 2.1, the major components consist of beam source, optical column, sample chamber, detectors, vacuum system, computer and electronic systems. The beam source generates the charged particles and accelerates them to the working energy. There are electromagnetic lenses (electrostatic lenses for ions), beam-limiting apertures, and scan coils in the optical column. The optical column can focus the charged particles into a fine probe (< 1 nm) and raster the probe across the specimen surface. Several detectors are used to collect a range of signals (e.g. SEs, beam-induced photons, and backscattered primary particles). A computer controls the electronic system, which regulates the beam scan and position the sample stage. A series of pumps maintain a high vacuum ($\sim 10^7$ torr) in the sample chamber. It is worth mentioning that to form a helium ion beam, the HIM uses a gas field ionisation source, which is very bright ($\sim 4 \times 10^9 A \cdot cm^{-2} \cdot sr^{-1}$) and extremely small (about the size of a single atom) [44]. This means that the He^+ beam can be focused into an ultrafine probe (~ 0.25 nm) while still having a reasonable level of beam current (1 fA to 100 pA).

2.1.1 Signal generation and imaging modes in SEM and HIM

As the primary particle (i.e. electrons in SEM and helium ions in HIM) enters the specimen, it interacts with specimen atoms and is scattered by the Coulomb potential. The interaction allows transfer of primary particle energy to the specimen, causing the excitation of specimen electrons due to inelastic scattering. The excited electrons may gain enough energy to diffuse towards the sample surface, overcome the surface barrier and escape into the vacuum. The energy of escaped electrons normally peaks at several eV and SEs are defined as escaped electrons in the energy the range of 0 to 50 eV. SE generation, diffusion and escape are determined by the primary particle (species and energy), the material (composition, structure and geometry, etc.) and the surface interface (surface potential). SE images show strong topographical information of the sample surface, while other

contrasts arising from the aforementioned beam and sample parameters may be manifested (sometimes dominant) in the SE image. The scattering of the beam particle and the sample atoms can drastically bend the particle's trajectory (especially through elastic scattering) and produce the so-called *Back Scattered* (BS) particles. To collect SEs and form images, HIM and SEM are equipped with either an Everhart-Thornley (ET) detector or an annular InLens detector [45]. To collect the backscattered particles, an energy selective backscattered (EsB) detector [46] and a microchannel plate detector (MCP) detector can be used in SEM and HIM respectively.

Lateral resolution in SEM and HIM is limited by its probe diameter (d_p), which is mainly determined by the size of the source image (d_I) and the contributions due to diffraction (d_A), spherical aberration (d_S) and chromatic aberration (d_c). The diameter of the probe containing 50% of the probe current is given by equation 2.1 [44]

$$d_p = \sqrt{d_c^2 + (d_I^{1.3} + (d_A^4 + d_S^4)^{1.3/4})^{2/1.3}} \tag{2.1}$$

where $d_I \propto (B\alpha)^{-1}$, $d_A \propto \alpha^{-1}$, $d_S \propto \alpha^3$ and $d_c \propto \alpha$ (α the semi-angle of the beam on the image side and B the brightness of the source. In an SEM, as shown in Figure 2.2 (a) lens aberrations require an α significantly below $\pi/2$ and as a result the practical probe size is diffraction-limited. In HIM however, a significantly increased particle mass ($\times$ 7300) reduces the wavelength of the He^+ ions to 1/46th of that of electrons of equal energy (keV). This reduced λ allows a much smaller α and an optical system less prone to aberrations (see Figure 2.2 (b)), enables a probe size significantly closer to its theoretical limit and on the order of $\sim$0.25 nm [47].

The backscattered particles also cause the excitation of SEs. SEs are labelled SE1 if they are excited directly by the primary beam and SE2 if excited by the backscattered particles [26]. Figure 2.3 (a) and (b) are the Monte Carlo simulation of the particle trajectories in the sample and the red lines indicate the BS particles. It is evident that the BS yield in HIM is much lower than that of SEM, which results in a narrow distribution of the interaction volume close to the sample surface. Since the BS particles can also excite SEs, the narrower BS distribution of He^+ ions indicates that SEs in the HIM are more localized at the probe location. The combination of a significantly smaller probe diameter, higher SE yield and a narrow particle distribution at the specimen surface, ultimately empowers the

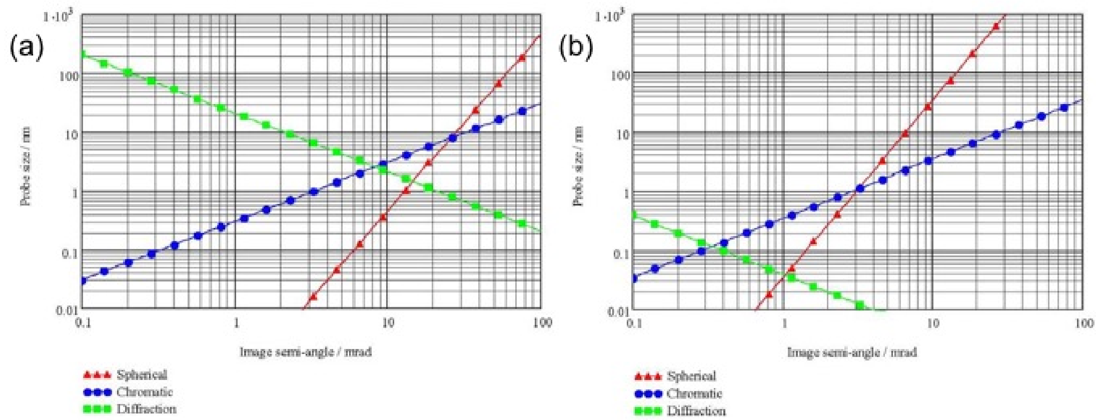

FIGURE 2.2: Probe size vs. image semi angle (a) SEM (b) HIM [44]

HIM with an increased lateral resolution, surface sensitivity and material contrast [5, 6].

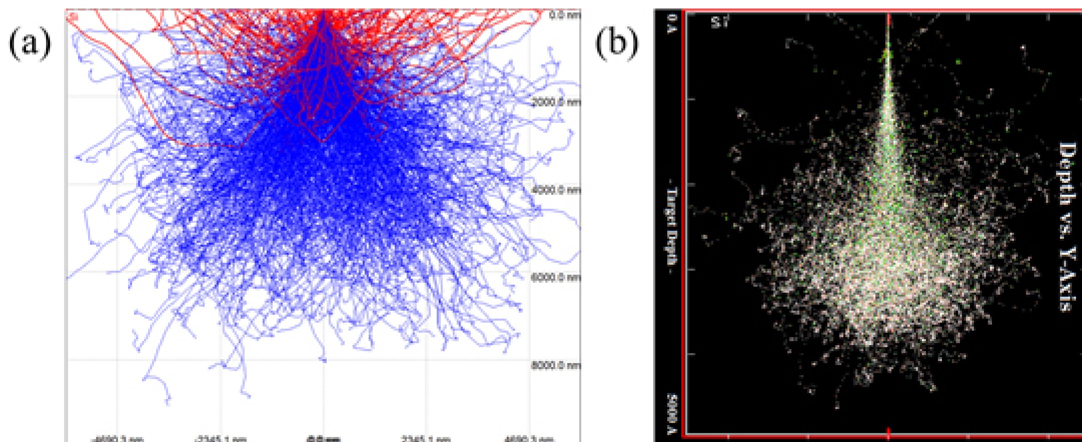

FIGURE 2.3: (a) The simulated trajectories of 500 electrons with 30 keV kinetic energy into a silicon substrate (Casino). The blue and red trajectories represent the primary and back-scattered electrons respectively. (b) The simulated trajectories of 500 helium ions with 30 keV kinetic energy into a silicon substrate (SRIM). Considerably fewer helium ions are back-scattered compared to electrons.

The SE yield, which is defined as the number of SEs generated by one incident particle, depends on the beam energy. Figure 2.4 (a) shows the SE yield as a function of the energy of the electron beam. There are normally two critical beam energies for which the yield is 1 (i.e. E_P^I and E_P^{II} in Figure 2.4(a)). The unity SE yield corresponds to the charge balance condition in the sample if there is no leakage current allowed through the sample stage, i.e. one injected charge being

compensated by an exiting SE. Typical SE yield in SEM is close to 1. In HIM, the beam is usually operating at a fixed beam energy ($\sim$ 30keV). It has been found that the SE yield in HIM is quite high ($3-9$ electrons/ion) [43, 48]. The material dependency of HIM SE yield is more significant than that of SEM.

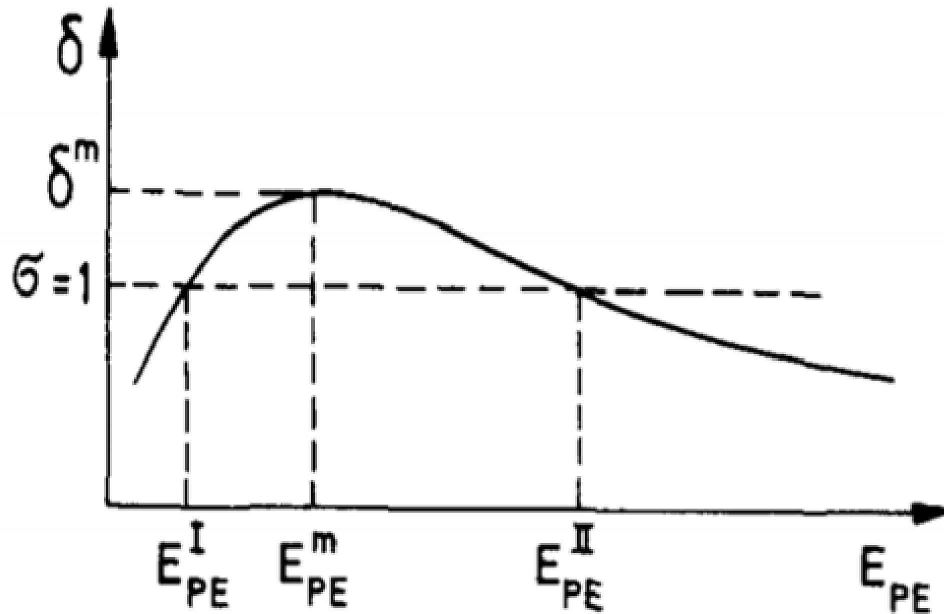

FIGURE 2.4: The relationship between the SE yield and primary beam energy.

The imaging of insulating materials in SEM will result in the accumulation of a negative surface charge, if the SE yield is not unity. This serves to alter trajectory of the primary electron beam and influence SE emission. It is well documented that charging has significant effects on image contrast in SEM and may cause contrast reversal [49]. It can be mitigated by reducing beam energy, and beam current, or by coating the specimen with a fine conductive layer ($\sim$nm) prior to irradiation. However, the specimen can be either positively or negatively charged, depending on the SE yield which can be affected by a range of factors (e.g. beam energy, sample geometry, sample materials, vacuum conditions, etc.). The charging mitigation is thus a challenging issue in SEM imaging.

In the HIM, impinging He^+ ions generate a positive surface charge on insulating materials. This serves to increase the potential barrier of the irradiated region that reduces SE emission and produces darkened images. A charge compensator can be

used to mitigate such charging by synchronous flooding of the helium irradiated region with a beam of low energy electrons (< 1000 V). By tuning the energy and pulse duration of the electron irradiation, with the scanning of the He^+ ion beam, the surface can be neutralised and high-resolution images from charging specimens obtained. However, the effects of imaging parameters and sample charging on the HIM image contrast have rarely been explored in detail. This is a crucial issue for further development and application of HIM imaging in semiconductor metrology. In chapter 5, we compare images of Ga-implanted Si samples taken with different HIM and SEM imaging modes and investigate the effects of imaging parameters (beam energy, dwell time, etc.) on the image contrast.

2.1.2 SE spectroscopy

Although not frequently used for chemical analysis, SE spectroscopy in a SEM has successfully been used for the identification of inorganic materials, i.e. the separation of metals, semiconductors and insulators along with the differentiation of compound semiconductor types [50]. Studies that utilised controlled SE detection for imaging in the SEM have enabled the characterisation of semiconductor materials further, by differentiating regions relative to charge-carrier type and dopant concentration [51–55]. While other studies have used this a method to overcome the effects of surface contamination [56, 57]. Recent studies on imaging polymer-fullerene photovoltaics revealed that filtered SE images enabled the differentiation of mixed phases from pure phases [33] and a doubling of image resolution in comparison to non-filtered SE imaging [11]. As the SE generation mechanism in SEM limits spatial resolution, the next step in optimising energy filtered SE imaging, and spectroscopy, lies in an alternative SE inducing technique.

In comparison to SEM, the HIM offers significantly higher spatial resolution and SE yield. As discussed in previous sections, the optimised spatial resolution in the HIM is due to its finite specimen probe diameter (∼0.25 nm) and higher SE yield. The higher SE yield is due to the increased stopping power a material has on impinging He^+ ions, which results in a significantly higher rate of energy transfer from the ions to the material atoms. This coupled with a negligible backscattering effect ultimately produces specimen images from SE signals that originate precisely from the beam-specimen interaction site. These attributes make the HIM an ideal instrument for imaging carbon based materials such as organic

electronics [11] and biological materials [35]. Similarly, to SEM, the HIM has also been used for semiconductor material characterisation [17–19, 58], without the use SE energy filtration. Further HIM research utilising energy filtered SEs successfully determined the work-function of a number of metals (Mo, Ni, Pt) and minimised the effect of surface contamination [59]. However the type of energy filter used in this work limited the microscopes operation and did not consider the effect of SE emission angle on spectral resolution. A study on characterising the SE emission from *highly ordered pyrolytic graphite* (HOPG) by He^+ ion (5 keV) irradiation reported clear peaks at 1 eV and 3 eV and were shown to be linked to its electronic structure [60]. The SE energy filter device used in this study is not suitable for integration into a HIM however its findings have set a benchmark for qualifying an alternative SE energy filter design. For high resolution energy-filtered SE imaging and quantitative SE spectroscopy in a HIM, an instrument-specific energy filter was required. By applying a retarding electric field between a semi-spherical grid and an Everhart-Thornley detector in HIM, a high-pass filter has been built to investigate the dependence of material contrast of the filtered images [27, 28]. Nevertheless, a new design of SE energy analyser (filter) is required to meet the operation specifications of the microscope, a Carl Zeiss Nano-Fab, which has the flexibility to analyse multiple specimens of different type simultaneously, and provide an optimised and homogeneous biasing field for maximum spectral and imaging resolution.

SE energy-spectra have been investigated theoretically. As shown in Figure 2.5 (a), the energy distribution of HIM SEs has a peak at a lower energy than that of the SEM SEs [61]. This may be due to the missing of SE2 due to the low yield of backscattered ions and Auger neutralisation may contribute to the SE emission. Such a theoretical prediction has been experimentally verified for molybdenum samples by using the semispherical analyser as shown in Figure 2.5 (b) [59]. The unique SE spectra in HIM indicates that the effects of surface potential are more prominent in HIM SE imaging compared with SEM, e.g. static capacitive contrast. The HIM imaging therefore exhibits high surface sensitivity and suitable for the characterisation of light materials and nanostructures.

To describe the shape of the *Secondary Electron Energy Distribution* (SEED) generated in HIM, a modified Chung-Everhart model [62] was proposed by Petrov and Vyvenko [59]. Thier model employed the same formulation used to describe the transport and escape of SEs, but included a function to describe the energy

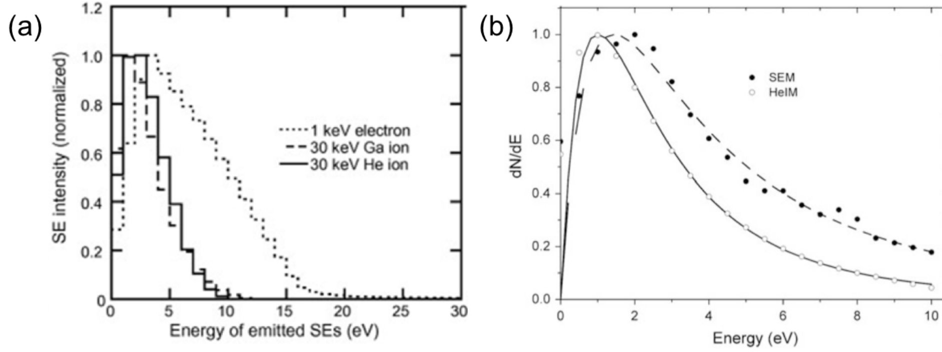

FIGURE 2.5: (a) numerical simulation, adopted from [61].(b) experimental results, Mo sample [59]

transfer from the primary He^+ ion to the SE. It was derived by the authors as follows.

The SEED is obtained by integrating the product S(E, z) P(E, θ, z) over all possible θ and z where, S(E, z) is the number of SEs excited per unit energy in the energy interval between E and E + dE at a depth of z from the surface, and P(E, θ, z) is the probability of an SE reaching the surface moving in the direction θ to the normal. This is given by Equation 2.2 where λ(E) is the *inelastic mean free path* (IMFP) of the electron in the solid.

$$P(E, \theta, z) = exp\left\{-\frac{z}{\lambda(E)\ cos\ \theta}\right\} \tag{2.2}$$

SEs will escape the surface if their energy (measured from the bottom of the conduction band) exceeds a critical value of E_{cr} = Ef + Φ, where Ef is the Fermi energy and Φ the surface work function. The momentum (p) of an electron is realised by the relationship $\theta < \arccos(p_{cr}/p)$, where p_{cr} is the critical momentum and is defined as $p_{cr} = \sqrt{2mE_{cr}}$.

As the majority of SEs have an energy of 5 - 7 eV above Fermi level, $\lambda(E)$ is estimated to be between 1 - 5 nm [63]. In most metals the He^+ ion stopping power remains at a constant value of 100 - 300 eV/nm for the first 50nm from the surface [64], as a result the He^+ ion energy losses at the maximum SE escape depth are approximately ~5% of the initial ion energy. As these losses are considered as

constant within $\lambda(E)$, the number of electrons excited per unit energy is therefore independent of depth, i.e. S(E, z) = S(E).

An explicit form of S(E) for excitation by He^+ ion irradiation is not known. However, as $\lambda(E)$ does not depend on the excitation mechanism, the SEED shape could be determined from experimental data. The function S(E) is defined in [59] as,

$$S(E) \sim \frac{dN}{dE} \frac{(E_{se} + \Phi)^2}{E_{se}} \tag{2.3}$$

where, E_{se} is the SE energy in vacuum (E_{se} = E - Ef - Φ). The experimental data of the S(E) dependence showed a linear behaviour in double logarithmic scale, reflecting a power dependence of:

$$S(E) \sim \frac{1}{(E_{se} + \Phi)^a} \tag{2.4}$$

The SEED shape for He^+ ion irradiation is derived from Equations 2.3 and 2.4 and is given as,

$$\frac{dN}{dE} \sim \frac{E_{se}}{(E_{se} + \phi)^n} \tag{2.5}$$

where n = a +2.

From the findings of [59], a good correspondence between the experimental data and the approximated formula is evident. The authors suggest that the model can be used to elicit SE spectra from other (non-metallic) He^+ ion irradiated specimens, due to its simple yet explicit analytical form.

As the S(E) dependence includes the parameter Φ, which is unknown as it depends on the state of the specimen surface, it is therefore possible to obtain specimen work function from the SEED data generated in either SEM or HIM. This is achieved by the introduction of the *$F(E_{se})$* function, which is obtained by a simple transformation of the appropriate SEED shape. It is a linear function upon the

SE energy, measured from the Fermi level. For SEM is given by,

$$F(E_{se}) = \left(\frac{E_{se}}{\frac{dN}{dE}}\right)^{1/4} \sim (E_{se} + \phi) \quad (2.6)$$

and for HIM by,

$$F(E_{se}) = \left(\frac{E_{se}}{\frac{dN}{dE}}\right)^{1/n} \sim (E_{se} + \phi) \quad (2.7)$$

By plotting the *F(E_{se})* dependence from experimental SEED data, apparent specimen work function can be determined after extrapolation to a zero SE energy value. The experimental data for electron irradiated molybdenum revealed an extrapolated zero SE energy value of -4.2 ± 0.2 eV [59]. The plotting gave good correspondence to the text book value for molybdenum work function and is displayed in Figure 2.6.

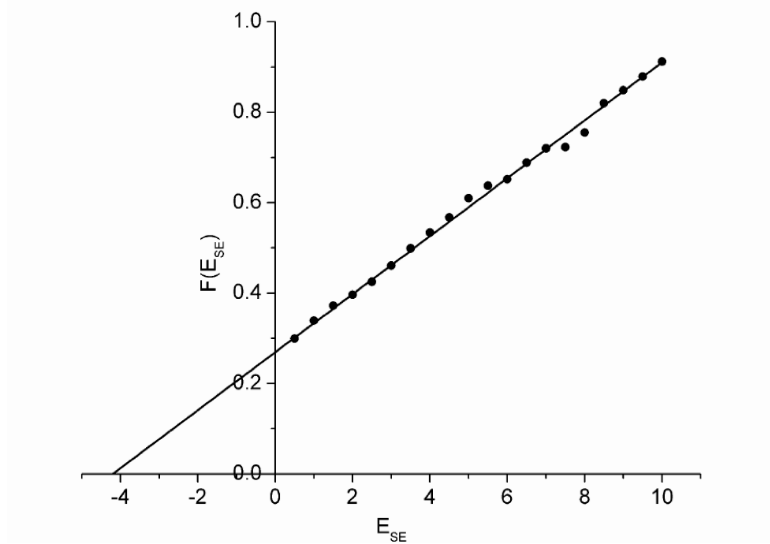

FIGURE 2.6: Experimental *F(E_{se})* data presented in [59] for the electron irradiated molybdenum. Accurate specimen work function is revealed (4.2 ± 0.2 eV) by extrapolation to the zero SE energy value.

2.1.3 SE imaging of two-dimensional materials

In this section, we will discuss application of HIM imaging in 2D materials characterisations. We focus on two examples: (1) resolve polymer contamination on graphene and (2) extract workfunction of 2D materials using SE imaging.

2.1.3.1 Organic residues on a graphene surface

Graphene is a single sheet of two-dimensional material composed of hexagonally-arranged sp^2 carbon atoms [65]. For the past decade, a vast amount of research has been conducted to understand graphene's characteristics, exemplified by its high carrier mobility [66, 67], and to establish its applications, such as graphene terahertz plasmon oscillators [68]. To investigate the properties of graphene, especially its functions in high-performance electronics, pristine graphene needs to be formed, manipulated and fabricated into a myriad of device structures ranging from the micrometer to the nanometer-scale. The process of such device fabrication normally involves several organic chemicals, for instance, polymer photoresists in electron beam lithography. This fabrication technique is known to introduce foreign species to the graphene lattice or to its surface as contaminants, which may adversely alter the intrinsic properties of graphene [69, 70]. In many research papers, it is presumed that the presence and effect of residual chemicals (e.g. polymers introduced during the graphene transfer process) can be reduced by annealing [71–73], chemical [72] and mechanical cleaning [74]. While annealing is considered to be the most effective method to "eliminate" the residues, a recent study casts doubts on the cleanliness of the processed graphene [75]. The characterization of graphene contaminants is of importance for the development of fabrication techniques for graphene-based devices.

To date *Atomic Force Microscope* (AFM) and *Scanning Tunneling Microscope* (STM) have been widely employed to study the surface of graphene and to characterize the extent of the residual contamination [71, 72]. AFM can effectively reveal the morphology and concentration of a 2 nm thick residue film and STM can determine the effect of contaminants at the atomic scale. Both techniques suffer from a very low throughput and difficulties in the interpretation of results. Given the vast diversity of geometries and fabrication methods for graphene-based devices, AFM and STM may not be suitable for the imaging of a graphene surface

in many cases, especially those involved in large-volume fabrication. Analytical techniques such as Raman spectroscopy [76], *X-ray Photoelectron Spectroscopy* (XPS) [73, 75] and *Terahertz Emission Spectroscopy* (TES) [77] have served to characterise the changes in graphene's properties induced by contaminants. These techniques have a high throughput, however their application will be limited by their spatial resolution and the ability to determine the nature of the contamination. A rapid and effective method is required to study graphene cleanliness as well as determine the effectiveness of any actions taken to clean the graphene surface.

SE imaging in the SEM is an established characterization method for surface morphology, which is superior to AFM and STM in terms of image acquisition time, magnification range, and image interpretation. In a SEM, SEs are excited by the irradiation of an energetic electron beam and collected from an image which reveals the morphology of the sample surface. Similarly, the relatively new HIM utilizes a helium ion beam to excite SEs [11, 78]. It has been demonstrated that HIM imaging is more surface sensitive with better spatial resolution, compared to SEM [8]. Both SEM and HIM have been employed to reveal the geometry of graphene nanostructures [65] and SE contrast in the SE images of graphene has been related to sample roughness, thickness [79, 80] and intrinsic doping [81]. The formation mechanism of the SE contrast is still subject to some debate [79, 82]. Reliable image interpretation as well as methods for quantitative analysis needs to be firmly established.

In addition, the ability of SE imaging to identify residues and contaminants on a graphene surface is rarely explored. One of the major challenges in resolving organic residues on graphene is caused by the absence of materials contrast, since both the contaminants and the graphene are carbon-based materials. The topographic contrast due to the non-uniformity of the contaminants does exist, but the ultrathin nature of the sample leads to a small interaction volume and small SE intensity. Nevertheless, it is imperative to clarify these issues for the application of SE imaging in graphene characterization.

2.1.3.2 Work function extraction and layer identification of graphene

Work function plays an important role in high-performance electronic devices such as transistors [83], gas sensors [84], solar cells[85] and field emitters[86]. It needs

to be tailored to particular device applications for optimised performance (e.g. efficiency in solar cells), therefore work function engineering is an important step in the transition from lab-scale devices to industrial applications [87]. In 2D few-layer materials (e.g. graphene) the work function is tuneable by varying the number of layers (thickness). A change in thickness of just one atomic layer can result in variations of several tens of meV [70, 88–90] . Other important parameters in work function engineering in such materials are chemical doping, self-assembled monolayer (SAM) treatment and strain [87, 91–93] and the substrate material, including its local crystalline orientation or local oxidation and contaminants [94]. Therefore a simple method to detect the work function of graphene with high speed and atomic level accuracy is important. Several techniques have already been demonstrated for the characterisation of the work function of graphene [88, 89]. However, the application of these techniques appears to be limited by various environmental factors and specimen interactions in scanning probe techniques [90], such as low throughput/low spatial resolution for *Photoelectron Emission Spectroscopy* (PEEM) [95]. Thus their applications are heavily restricted.

SE contrast is promising in surmounting these barriers to work function characterisation. They are exploited for surface imaging in charged particle beam scanning microscopes, such as the scanning electron microscope SEM and helium ion microscope HIM [11, 33, 96, 97]. These microscopes provide quantitative measurement of surface dimensions with sub-nanometer resolution and intuitive image interpretation. The generation, emission, and detection of SEs varies with sample properties and the electromagnetic environment around the sample. These dependencies may offer mechanisms to evaluate sample properties in addition to lateral dimensions. For example, SEs need to overcome the surface potential in order to escape into vacuum, i.e., the work function. Since the work function limits the SE escaping from the sample, it is intuitive that SE imaging could be used to extract the work function. However, this is an extremely challenging task, since the image contrast may also be affected by other factors, such as beam parameters, beam-induced contamination, specimen electric potential, SE collection efficiency, etc. Quantitative measurements of work function based on SE imaging have been scarcely reported [98, 99], especially for graphene and other 2D materials. The attempt to extract their properties (e.g. thickness) from SE imaging has been reported and a thickness-dependent SE contrast has been confirmed [79, 100, 101]. However, inconsistency exists in these works (e.g. the layer-dependence for the SE contrast) and a quantitative approach to extract work function is still absent.

2.2 Carbon contamination in charged particle microscopes

The characteristics of SE emission discussed above, contribute to SE imaging and determine the contrast mechanisms, and it also has a significant role in the contamination formation process. Although extensive knowledge of contamination in SEM has been attained, little research has been conducted in the HIM. It has been shown that contamination in the HIM persists and detrimentally affects the HIM characterisation and fabrication [102]. To be able to further evaluate and extend the HIM's capabilities, it is imperative to clarify the generation and effects of the contamination in HIM. In this section, we will briefly review the mechanism of beam-induced contamination and its effects on SE imaging in SEM.

2.2.1 Formation of beam-induced contamination in SEM

Beam-induced contamination was first studied to understand deposition on beam-limiting apertures, the colour change in the discharge tubes and poisoning of targets for research on nuclear reactions [29]. It has also been a common and inevitable problem in electron-optical instruments, particularly the electron microscope. Efforts on identifying and limiting contamination sources has led to many theoretical and experimental advances [103]. On the positive side, beam-induced contamination has been utilized to fabricate a range of nanostructures, while electron-beam induced deposition has become an important method for nanofabrication [104]. In this section, we review the formation mechanism of the contamination proposed in SEM literatures.

The contamination results from a cross-linking of adsorbed hydrocarbon molecules under the electron irradiation, i.e. the hydrocarbon molecules are polymerized by the electrons and deposited onto the sample surface. Energetic electrons can ionise hydrocarbon molecules to form free radicals. These radicals will link and become long-chain polymer contamination. Since the polymer has a low vapour pressure and a low surface mobility, the contamination increases in thickness if the polymerisation process continues. To sustain polymerisation, hydrocarbon molecules

must be continuously fed into the electron beam irradiated area through adsorption and/or surface diffusion. This indicates that the kinetics of contamination formation may be limited by the supply of molecules or electrons.

Sources of hydrocarbons include the residual molecules present within the microscope vacuum chamber and those adsorbed during sample preparation. The residual vacuum molecules arise from, the degasing of the inner chamber walls, the degasing of sealing gaskets and internal microscope components (e.g., nitrile rubber, plastics and PVC), and the molecular back-streaming of non-fluorinated mineral oils from the pumping system [105–108]. The molecules adsorbed during preparation arise from exposure to the ambient conditions prior to insertion of the sample into the microscope and from the impurities present in the materials used to mount the specimen. Typical hydrocarbon molecules present in ambient include, propene, propane, isopentane, n-hexane, acetylene, methane and ethane [109], and those in the preparatory substances are listed as, ethyl-acetate, ethanol, isopropanol, and acetone [110]. As contamination deposition occurs in a high vacuum environment, surface diffusion is the primary mode of transport for the adsorbed hydrocarbon molecules [103, 111].

Hirsch proposed an analytical model to describe the time-dependent contamination formation process [22]. The contamination is calculated through the variation of the local concentration of hydrocarbon molecules. The local concentration of molecules, $n(x, t)$, is given by

$$\frac{\partial n(x,t)}{\partial t} = N_a - \frac{n(x,t)}{\tau_0} + D\nabla^2 n(x,t) - \frac{\sigma j}{e} n(x,t) \tag{2.8}$$

where $N_a = p/\sqrt{2}\pi mkT$ is the adsorption rate of the molecules (p is the partial pressure of the molecule); the second term on the right, n/τ_0, describes the desorption of the molecule with a time constant τ_0; diffusion is represented as $D\nabla^2 n$ (with D, the diffusion constant); the rate of irradiation-induced molecule dissociation is given by the last term $(\sigma j/e)n$ with σ being the cross section of molecule dissociation. For the one-dimensional case, i.e. a stripe area being irradiated, the mass thickness $x_c = \rho d$ of the contamination layer (density $\rho \cong 1$ g/cm^3 and thickness, d) is

$$x_c(x,t) = \bar{m}\frac{\sigma j}{e}\int_0^t n(x,t)dt \tag{2.9}$$

where $\bar{m}$ is the mean mass of cross-linked molecules.

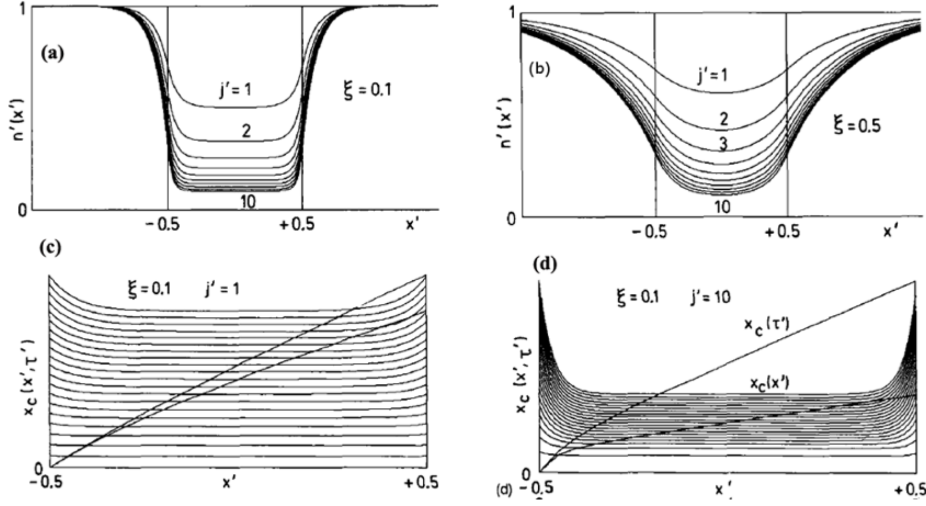

FIGURE 2.7: Calculated steady-state surface concentration influence of (a) beam current and cross section (b) molecular diffusion. Note j' = $(\sigma\tau_0 j)/e$, $\xi^2 = D\tau_0/a^2$, $x' = x/a$ and a is the length of the irradiated strip [22].

Figure 2.7 (a) and (b) outline the steady-state solution of Equation 2.8, showing the influence of the diffusion, the current density and the dissociation cross section. The larger the beam current density (j) and the cross section (σ), the lower the concentration within the irradiated area. The time-dependent numerical solutions in Figure 2.7(c) and (d) shows the evolution of thickness with respect to time for two values of j'. For large j' (Figure 2.7 d), the growth rate of contamination is nonlinear at the start of the irradiation. The boundaries of the irradiated area exhibit wall-like features, and the wall height increases with increasing j'. The effect of the diffusion can be seen from the comparison of Figure 2.7(a) and (b). The larger diffusion constant (hence the larger ξ) results in a less uniform profile of the molecular concentration in the irradiated area. The theory indicates that the profile of the contamination depends on the dose of the charges (i.e. jt) while the current density and the diffusion can also control the profile. This is because the steady-state concentration and the profile of the molecule residue inside the irradiated area also depends on the two parameters. Hirsch's model can explain some experimental results, however it is oversimplified. For example, the contributions of the primary and secondary electrons are not distinguished; the finite probe size and the beam spreading are not considered; and the effects of the grown contamination on the subsequent growth are ignored.

Since the first step in the formation of the beam-induced contamination involves

ionisation of hydrocarbon molecules, the probability of the ionisation for the electron scattering must be clarified to understand the role of SEs in the contamination formation. Simple hydrocarbons normally include methane (CH_4), ethane (C_2H_6), cyclopropane (C_3H_6), propane (C_3H_8), benzene (C_6H_6) and propene (C_3H_6), etc. Kwitnewski et.al. evaluated the total ionization cross section for electron scattering from simple hydrocarbons [25]. As shown in Figure 2.8 (a), it is clear that the ionisation cross section has a maximum value for electrons with an energy in the range of $50 - 100$ eV. Compared with the primary beam (> 1 keV), SEs have larger ionisation cross section and thus more efficiently polymerise hydrocarbon molecules. On the other hand, since the SE yield is about 1, it is expected that SEs contribute to the contamination formation at least as much as the primary beam.

In SEM, the SEs may exit several micrometres away from the probe-sample interaction point due to the extended distribution of the backscattered electrons (see Figure 2.3 a). This means that beam-induced contamination will not be confined within the probe, which has been observed experimentally by using atomic force microscopy [111]. A dynamic Monte Carlo simulation, which includes the contribution of SEs and the electron scattering in the already grown deposit (Figure 2.8 b), has been conducted to understand the attainable size of the hydrocarbon contamination [112]. Rykaczewski et.al. developed a comprehensive dynamic model of electron beam induced deposition of residual hydrocarbon in 2007 [103]. The model rigorously couples surface transport of hydrocarbon molecules with electron beam processes, which results in predicting the evolution of the deposition shape. The dynamic model has been used to understand the formation of the topographically complex micro-ring-nanopillar deposition.

2.2.2 Effects of contamination on the imaging

The formation of hydrocarbon contamination on the specimen surface results in several detrimental effects. It is well known that the contamination layer can drastically modify the SE emission of the specimen, causing contrast change in the contaminated area. The build-up of contamination layers can hinder and even prevent any high-resolution imaging since nanosized features will be covered by the contamination layer. Indeed the growth of the contamination layer can be observed

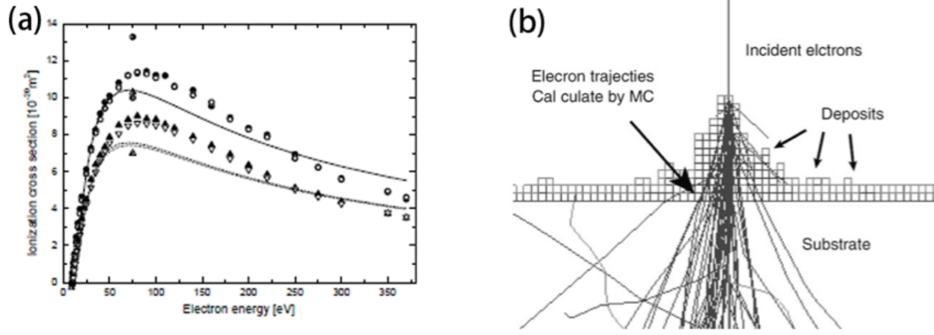

FIGURE 2.8: (a) Ionisation total cross section for electron scattering from isomers of C_3H_4 and C_4H_6 [25] (b) a schematic illustration of the dynamic profile simulation of the contamination formation [112].

from contrast variation in SE imaging. The SE yield, δ, from a contaminated area is given by

$$\delta = \delta_c + (\delta_s - \delta_c) exp\left(-\frac{t_c}{\lambda}\right) \tag{2.10}$$

where δ_c, δ_s are the SE yield from the substrate and the carbon contamination layer respectively; t_c and λ ($\cong$ 10 nm) are the thickness of the contamination layer and the mean free path of SE in the contamination layer respectively. Equation 2.10 indicates that the effective SE emission from the contaminated sample consists of the SEs from both the bulk substrate and the thin carbon contamination layer. The contribution of the substrate SEs will be attenuated due to loss when penetrating the contamination layer. On the other hand, the SE emission from the contamination layer is considered to be constant with the increase of the contamination thickness. It can be seen that as the contamination layer gets thicker the SE yield will approach the value of the carbon polymer. This will cause a change in image contrast. That is to say if the SE yield of the substrate is significantly different from that of the contamination (carbon) layer, the SE image will be altered to a great extent by the contamination.

For insulating samples, the contamination can alter the charge neutral conditions, i.e. shift the critical beam energy (E^{II}_{PE}, see Figure 2.4 a) to lower values [113]. This would deteriorate the charging effects, since the neutral state for an insulating sample under a given beam energy (where $\delta \approx 1$) can be no longer held in the contaminated region.

2.2.3 Current technology to mitigate contamination formation

Many techniques have been proposed to minimise contamination in electron microscopes [22–24, 114–118]. They are summarized as follows:

- Sample cleaning prior to the SEM session to desorb hydrocarbons from the specimen surface (the use of the treatment depends on the samples)
  - Rinse the sample with organic solvent (isopropyl alcohol and methanol) to remove organic contaminations
  - Chemical wash by using oxidising acids (for example, silicon can be treated by the mixture of 3:1 ratio of 30% hydrogen peroxide solution added to concentrated sulphuric acid) to remove residual absorbed hydrocarbons
  - Heat the specimen with an electric lamp in air (or vacuum)
  - Irradiate the specimen by an ultraviolet lamp (heat-sensitive sample)
  - Expose the specimen to energetic ions by a plasma cleaner
- Sample treatment during the SEM session
  - Flood the surrounding area with electrons to fix surface hydrocarbons and prevent them diffusing towards a focused probe
  - Heat the specimen to 300^oC in the chamber
  - Cool the specimen during observation to reduce the mobility of surface hydrocarbons
- Chamber cleaning to improve the vacuum level and cleanliness of the system
  - Use anti-contamination blade (cryo-shield) to decrease the partial pressure of molecules
  - Use dry vacuum system (magnetically levitated turbo-molecular and oil-free fore pumps)
  - Continuous bleeding in of clean dry N_2
  - Use a low-energy oxygen plasma to clean the chamber

- Contamination removal: hydrocarbon polymer has reasonable resistance to etching by chemical solutions or sputtering ion, while oxygen plasma was found to be able to remove the polymer to some extent.

As pointed by Soong et.al. [118], the major limit of these sample cleaning methods is the sample damage, especially for sensitive samples. The effectiveness of heating and vacuum heating is low, compared with plasma cleaning. However, plasma cleaning can introduce severe sample damage or redeposition of materials. Nevertheless, these cleaning techniques will help us to control the cleanliness of the sample and the chamber so that we can vary the supply of hydrocarbon sources to investigate the mechanisms of contamination formation in HIM.

2.2.4 Applications of beam-induced carbon contamination

Carbonaceous structures, formed by electron beam induced deposition of residual hydrocarbons in a SEM, have found a variety of nano science and technology applications. Examples of which are outlined as follows.

Using primary electron energies of 15 - 30keV, Rykaczewski *et. al.*, fabricated carbon pillars and compared the deposited structures to predictions they had developed from residual hydrocarbon dissociation reaction rates [104]. In doing so they enabled a quantitative method for pre-determining the physical dimensions of deposited structures, thus paving a way for the practical use of EBID simulation tools that require minimum computational input.

A detailed study by K.I. Schiffmann [36] successfully characterised the required electron beam parameters to modify standard AFM tips by growing high aspect ratio carbonaceous features (cones and conical topped cylinders) at their apex. The length of the features was controlled by deposition time with the shape of the conical feature being determined by beam energy. At higher energies the cone, or conical feature, became longer and more acute. This was due to a decrease in total electron cross-section scattering, and the mean scattering angle. Electron beam current also played a significant role. Low beam currents (3 - 30pA) provided higher growth rates as the thermal effect associated with higher currents (30 - 300pA) lead to an increase in the rate of hydrocarbon desorption. Using the appropriate paramaters the author successfully fabricated an AFM *supertip* (Lenght,

1.2 μm; Diameter, 120 nm), which was tested in both contact and non-contact modes. It was used to generate a surface topography image of a Si specimen with an etched square feature of $\sim$1 μm in depth. By doing so the floor of the feature was completely revealed with minimum scanning artificats, unlike what was revealed using a standard tip. The ultimate benifit in controlling the size and shape of the deposited *supertip* structure, is the ability precisely match it to features on the specimen to be analysed. This is of great benefit for specimens containing steep topographic structures. Although reference was made by the author on the variations observed on tip radius of curvature, ultimate lateral resolution in AFM is governed by this value. This fact was not acknowledged therefore limiting the use of such *supertip* structures to specimes containing high aspect ratio features whose surface detail is minimal or insignificant.

Carbon deposits, used to fix carbon nanofibres to AFM tips, were characterised in terms of sp^2:sp^3 bonding structure, hardness and elasitc modulus by Ding *et. al.,* [41]. The study revealed that the carbon structures deposited with higher electron voltages (20keV) had increased hardness, elastic modulus and sp^3 concentration, than those generated with lower beam energies (3 and 12keV). To test the structural integrity of the clamps, tensile testing was carried out where by a maximum force of 100μN, and an average shear stress of $\sim$30 MPa, was placed on the fiber-clamp interface. After multiple texting, when failure occurred it was always in the fibre and not the clamp. By using a paraffin precursor the authors were able to ensure a steady-state concentration of hydrocarbon molecules for the growth of identical carbon deposits, and clamps, for adequate experimental evaluation. The authors use of *Electron Energy Loss Spectroscopy* (EELS) to determine the sp^2:sp^3 concentration meant that a substrate alternative to the Si AFM tips was required, however any potential substrate related differences that could influence the bonding structure of the deposits was not discussed. Further to this Raman analysis of the carbon layers to determine sp^2 concentration was limited to one deposition energy, 3keV. The elastic modulus and hardness testing completed was characterised in terms of electron deposition energy, however the energy used to deposit the clamps was not given. As a result, the potential effects of changes in the bonding structure of the carbon clamps, arising from differences in deposition energy, on the tensile testing were not clarified.

Djenizian *et. al.* used electron beam induced carbon layers to create electrochemical deposition resistant masks, in the deposition of Au nano-structures [37]. Key

to the formation of these nano-structures was the energy and the applied dose used to deposit the carbon layers. The layers formed at a low electron beam energy (5 keV) provided uniform masking of a Si substrate, which was confined to each of the irradiated regions regardless of the applied dose. This subsequently enabled a homogeneous deposition of Au structures in the unmasked (un-irradiated) regions. The carbon layers formed with a high electron beam energy (20 keV) provided uniform masking of the substrate up to a critical dose (0.4 $C \cdot cm^{-2}$), above which the masking extended beyond the irradiated region due to the interaction of the BS signals and surface hydrocarbons. Upon subsequent Au deposition, the homogeneity of the deposited structures deteriorated in the regions where the applied electron dose exceeded the critical dose, with the extent of deterioration increasing with the increase in applied dose. The authors attribute the BS signal emitted during the formation of the higher energy masks, as the dominant factor in the rise of cross-linked carbon species outside the irradiated regions. Although differences were discussed between the influence of *Forward Scattered Electrons* (FSE) versus *Back Scattered Electrons* (BSE), the influence of the SE signal on the formation of the carbonaceous deposits, resulting from both electron scattering mechanisms, was not discussed. Also not discussed were the potential differences in deposition features arising from specimens of a higher or lower atomic number than Si. For a given electron energy, atomic number is key to the BS signal produced from a bulk specimen in SEM. It therefore has an influence on carbon formation in the regions outside that of the primary beam irradiation.

In an earlier etching study, Broers *et. al.* used the deposition of carbon lines to generate high resolution (8 nm wide) metal structures [39]. The lines were generated by irradiating a 10 nm thick AuPd foil (previously deposited onto a 10 nm thick carbon foil mounted to a Cu TEM specimen grid). The irradiation was performed with a 45 keV electron beam that delivered a specimen probe of 5 nm in diameter. Once formed, the carbon lines provided a mask for the underlying metal during a subsequent Ar^+-ion etching process. Lateral spreading of the beam during the electron irradiation was kept to $\sim$2 nm. This was due to the negligible BS effects associated with a combined specimen thickness of 20 nm. Carbon lines of less than 8 nm were also deposited, however due to variations in metal thickness the structures formed post etch were incomplete. In this work the authors commented that the major limit to resolution was the metal alloys used at the time of study (1976), not the electron beam, and that ultimate resolution

would be enabled by the use of amorphous metal alloys and electron energies above 45keV.

Carbon layers formed with 30keV primary electron energy, were characterised in terms of their optical and electrical properties by Miura *et. al.,* [119]. Raman spectroscopy revealed a mixture of sp^2 and sp^3 carbon bonds incorporated within an amorphous matrix and electrical characterisation revealed resistivity measurements of 10^{11} Ω·cm. When employed as the insulating material in *Metal-Insulator-Metal* (MIM) diodes, 150 nm^2 carbon nano-layers showed a reduced resistivity of 10^7 Ω·cm. This reduction was caused during device processing by the introduction of Ga^+ ions at the metal layer junctions and within the insulating carbon nano-layer. Regardless of the reduced resistivity, the authors determined the final barrier height (Φ_{B0} = 0.19eV) sufficient for effective device operation. Having previously determined optimum growth rates for layer formation at higher electron beam energies, the authors only used 30keV e-beam energy for generating the insulating layers in the MIM devices. Given that e-beam energy effects the carbon bonding arrangements within the deposited structures, an understanding on how this may have influenced Φ_{B0} was not established. The authors also used a *Focused Ion Beam* (FIB) method to deposit the Tungsten Carbide (WCx) contacts which in turn lead to the introduction of Ga^+ ions in the dielectric layer. An alternative method of contact deposition, e.g. formation by EBID, would have negated any influence of Ga^+ ions had on dielectric function.

Free-standing carbon-AuPd nano-electrodes, separated by gaps of < 5 nm, were fabricated by Bezryadin and Dekker and used to characterise the electrical transport properties of single Pd nano-particles [40]. Nano-structures deposited across etched features on insulating and conductively layered Si wafer substrates, in a SEM by EBID of residual hydrocarbons, were coated with a conductive AuPd layer. The minimum gap between the structures was governed by the resolution of the SEM ($\sim$ 1 nm) and the deposition growth rate (1 - 10 nm $\cdot$ s^{-1}), the latter being controlled by oxygen plasma etching (to reduce surface hydrocarbon concentration) or by cooling the specimen to 77 K (to minimise hydrocarbon mobility). The gaps produced by this method were very stable, due to the rigidity and chemical intentness of the amorphous carbon structures, the size of which remained intact during aggressive specimen cleaning. The thickness of the carbon structures influenced the resistivity of the conductive AuPd layer, the thickness of which was shown to reduce the gap size or completely bridge it. When optimised

to 4 nm in thickness, the conductive layering process maintained nano-gaps of <5 nm. By trapping Pd nano-particles within the gaps, resistance measurements before and after the trapping - combined with visualisation of the particles within the gaps by SEM - enabled their electrical characterisation. When the width of the gap matched that of a single nano-particle, optimal characterisation was performed. The authors failed to state the electron beam energy used to form the carbon nano-structures. They did however refer to those formed by Broers *et. al.,* [39] as a basis for their work, thus indicating an energy of 45keV was used. As the authors highlighted the rigidity of the carbon structures, the carbon bonding structure of high energy deposits may have lead to their noted resilience as revealed in post specimen cleaning steps.

Amorphous carbon *supertips*, grown at the end of AFM probes by EBID of residual hydrocarbon molecules, were employed as near-field optical sensors for *Photon Scanning Tunnelling Microscopy* (PTSM), by Castagne *et. al.,* [38]. Formed with a primary electron energy range of 10 - 30keV and beam currents of 100 - 1000 pA, Auger and mass spectroscopy analysis revealed the *supertips* to consist primarily of carbon and oxygen with trace amounts of nitrogen. With the ability of converting evanescent waves in the *Near Infra-Red* (NIR) range, and subsequent collection of propagating photons, they have been shown to be more effective than tapered optical fibres and standard Si AFM probes, typically used for the PTSM technique. This is due to the ability to optimise their range of effective capture (by controlling shaft length and diameter) and their collection angle (by controlling tip radius). As a result the collected signal intensity can be proportionally increased by the appropriate growth regimes. If however the *supertips* are used for simultaneous AFM imaging, lateral resolution will become limited by tip radius. Although the autors used a range of electron beam energies, and primary currents, in the generation of their supertips, the effects of these two parameters were discussed only in terms of tip shape and not in terms of their structural nature. The collection angle (a function of tip radius) is less likely to be influenced by the carbon bonding structure, however the optical transmission and coupling of the *supertips* (related to their effective capture, i.e. tip length) may have been. This factor was not considered and for those tip shape geometries that yielded the greatest increase in measured optical signals, a comparison of forming identical tips and different electron beam deposition energies may have led to further optimisation of the *supertip* optical function.

Chapter 3

Raman Spectroscopy and its application to the characterisation of carbonaceous materials

Raman spectroscopy is a highly effective material characterisation technique. It is commonly used in the study of a wide variety of nano-materials to determine their physical and chemical properties, such as, size, shape, crystallographic structure, orientation and strain [120–127]. Raman enhancement spectroscopy is based on the core principle of Raman spectroscopy however it uses an additional medium to amplify incident excitation and Raman scattered light. In terms of this thesis, Raman spectroscopy was used to characterise the bonding structure of electron beam induced amorphous carbon deposits. These deposits exhibited Raman enhancing properties, the magnitude of which was dependent upon the concentration and ratio of the carbon bonds , (i.e. the sp^2:sp^3 ratio) present within the excited carbon volume. This chapter gives an overview on Raman and Raman Enhancement spectroscopy in application towards the analysis of amorphous and crystalline carbon materials.

3.1 Raman spectroscopy

The interaction of monochromatic light with a sample generates elastic and inelastically scattered photons. The elastic, or Rayleigh, photons are representative of a zero energy loss of the incident photon to the irradiated material. The inelastic, or Raman, photons are scattered at a shifted wavelength and represent the energy losses incurred during the interaction of an incident photon and a material atom or molecule. These representative loses are unique to the conditions present within a material and can be used to finger-print specific properties that correspond to a

shifted wavelength. This inelastic scattering effect was first documented by C.V. Raman in 1928 [128], to which his name is given.

3.1.1 Raman scattering

In Raman scattering, an incident photon, of frequency ω_0, is momentarily absorbed by a material bond (atomic or molecular). This results in the simultaneous generation of a dipole moment and excitation of the vibrational state of the target to a new virtual state. Upon relaxation from this virtual state, the photon is re-emitted. The frequency of the re-emitted photon (ω_s) is determined by the energy lost or gained in the vibrational transition (ω_k), relative to the incident photon energy.

All scattering processes are bound to obey the energy conservation law, whereby the energy of the scattered system (E_k) must equal that of the scattered particle (E_s) less that of the incident particle (E_0) [129].

$$E_k = E_s - E_0 \tag{3.1}$$

As energy, E = $\hbar\omega$, equation 3.1 can be rewritten as,

$$\hbar(\omega_s - \omega_0) = \hbar\omega_k \tag{3.2}$$

$$\omega_s - \omega_0 = \omega_k \tag{3.3}$$

As E_k is an innate property of the scattering system it is independent of incident light frequency. Therefore, the scattered light frequency is independent of incident light frequency.

The energy diagram given in Figure 3.1 shows the transitions that can occur in light scattering events. When the scattered system returns to a vibrational level higher than its initial level, the energy of the emitted photon is less than that of the incident photon. This is known as Stokes Raman Scattering. If, however it returns to a lower vibrational level, the energy of the emitted photon is greater than that of the incident photon. This is known as Anti-Stokes Raman Scattering. The

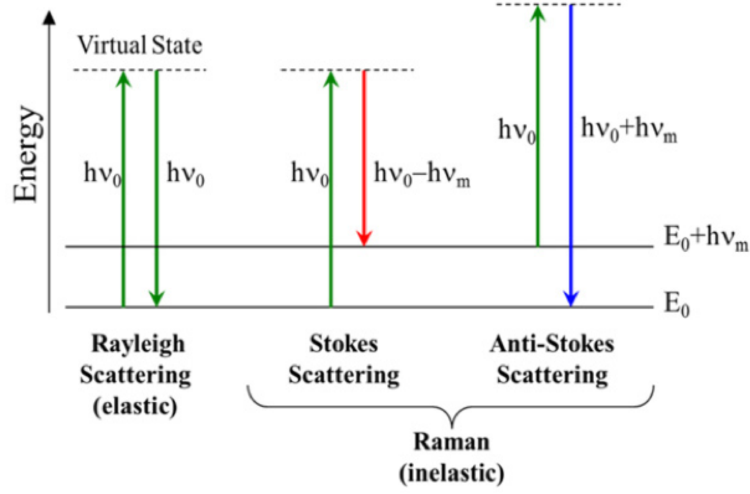

FIGURE 3.1: The vibrational energy transitions that occur during a photon-target interaction, and their resultant scattering events.

difference in photon energy is equal to the energy associated with the vibrational transition, therefore absolute values of Stokes and Anti-Stokes Raman scatter are equal. This gives an expression for first order Raman scattering as,

$$\hbar\omega_0 = \hbar\omega_s \ \pm \hbar\omega_k \tag{3.4}$$

For any given system at room temperature the highest number of excitable modes resides at the lowest vibrational level. This is given by the Boltzmann distribution which also states that the population of modes at the higher levels decreases exponentially, with increase in vibrational energy. The population of vibrational energy levels is determined using,

$$\frac{N_2}{N_1} = \frac{g_2}{g_1} exp\left[\frac{-(E_2 - E_1)}{kT}\right] \tag{3.5}$$

where N_1 and N_2 are the number of modes in the ground and first excited energy level, g is the degeneracy of the levels, T is the temperature and E is the energy of the vibrational levels. As Stokes Raman scatter is dependent upon excitations from the lowest vibrational level, it therefore has significantly higher intensity than the Anti-Stokes in most interactions.

3.1.2 Raman spectra

A Raman spectrum is a plot of Raman scattered intensity versus the photon energy shift. The enery shift termed the "*Raman shift*" is given in wavenumbers (cm^{-1}) and is described in Equation 3.6,

$$\Delta E = \frac{1}{\lambda_i} - \frac{1}{\lambda_s} \tag{3.6}$$

where λ_i is the wavelength of incident light and λ_s is the wavelength of scattered light. The Raman shift is a measure of the energy associated with a given specimen vibration, the intensity of which corresponds to the concentration of that vibration. As such, the Raman shift enables the fingerprinting of a material as each peak in a Raman spectrum corresponds to a distinct vibrational mode.

The electron fields associated with the movement of molecules or atoms in a specimen, will be mildly or significantly affected by the electro-magnetic field of the incident photons. The polarisibility of a target, i.e. its potential to produce Raman emission, is dependent upon the physical displacement of its bonds. At full bond stretch the electrons within their orbits are less influenced by their core nuclei and thus at their most polarisable potential. Known as the *k-selection* rule, for a Raman shift to occur a bond displacement greater than zero is required. The greater this displacement the greater the degree of polarisation, excitation and Raman emission.

With excitation in the visible spectrum, σ-bonds are non-polarisable however the π-bonds are easily polarised. This is due to their distributed electron fields which produce a strong Raman scatter. An increase in excitation energy, into the UV range, will help to overcome the effects of low bond polarisabilty and enable the direct probing of the σ-bonds.

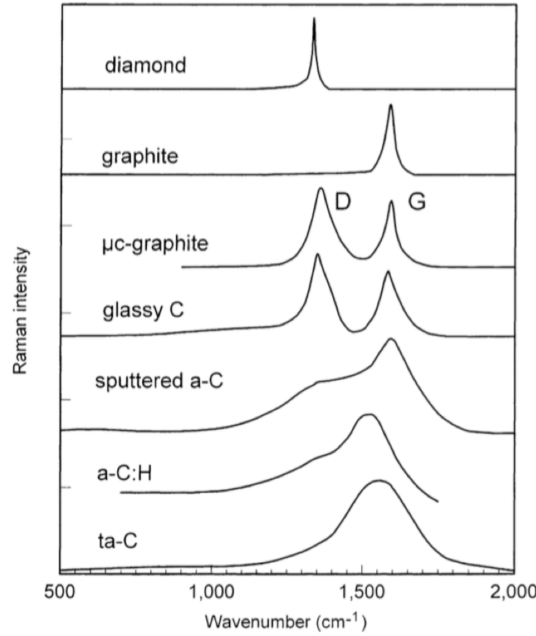

FIGURE 3.2: Typical Raman spectra of ordered and disordered carbons [130].

3.2 Raman characterisation of carbon materials

3.2.1 Raman spectroscopy of crystalline carbon

Raman spectroscopy has been extensively used to determine the physical properties of crystalline carbon materials, such as diamond [131–133], graphites, diamond like carbons (DLCs) and carbon nano-tubes (CNTs) [130]. Diamond is characterised by a single active mode, of T_{2g} symmetry, centred at 1332 cm^{-1} [130]. Single crystal graphite is also characterised by a single active mode, of E_{2g} symmetry, which is centred at 1580 cm^{-1}. Labelled 'G' for graphite, it is observed in all sp^2 carbon systems and corresponds to an in-plane tangential optical phonon, i.e. the bond stretching motion of carbon atom pairs [134]. Disordered graphite has a second mode at 1350 cm^{-1}, which is of A_{1g} symmetry. It is labelled 'D' for disorder and represents the transitions that occur as a result of a double resonant process involving a phonon and a defect in the crystal lattice [135]. It corresponds to the breathing vibrations of the rings at the k-zone boundary, which are only activated at defect sites - such as edges, vacancies or dopant sites - and not excited in an ordered crystal. A comparison of the typical Raman spectra of ordered and disordered carbons is displayed in Figure 3.2

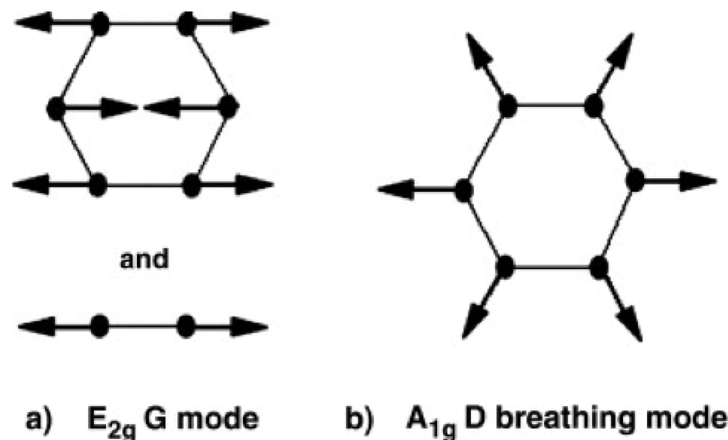

FIGURE 3.3: The vibrational motions corresponding to the *G* and *D* Raman modes of Graphetic and amorphous carbons [130, 134].

3.2.2 Raman spectroscopy of amorphous carbon

In an amorphous material there is a complete loss of periodicity which causes a breakdown of the *k* selection rule. As a result, the Raman spectra of amorphous carbons is dominated by the presence of both the *G* and the *D* modes of graphite, even without the presence of graphitic ordering [134].

The *G* band in graphite represents the stretching of any two sp^2 bonded in-plane carbon atoms. In amorphous carbon it represents the stretching of any paired sp^2 carbon bonds, from either chains or rings. The *D* band represents the breathing mode of sp^2 carbon bonds. It is not present in non-defective graphite, however it is present in amorphous carbon and originates from ring bonds only. The vibrations of the carbon atoms, in an amorphous network, assigned to the *G* and the *D* bands are depicted in Figure 3.3.

Raman spectra of amorphous carbons is dominated by scattering from sp^2 sites. This is due to the lower bonding energy of π states making them significantly more polarisable than σ states [130]. As a result they give direct representation of sp^2 configuration. They can however give an indirect indication of sp^3 fraction and this is due to the influence sp^3 sites has on the concentration of aromatic bonds, and the vibrational frequency of linear bonds.

For direct interpretation of the Raman spectra of amorphous and nano-crystalline carbons, the I_D/I_G ratio can be used to determine the average in-plane correlation length (L_a), i.e. crystallite or cluster size [134, 136]. For nano-crystalline carbons, the greater the I_D/I_G the smaller the crystallite size. This is due to the detection of an increased number of rings bonds at the edges of the crystal, relative to a decrease in the number of linear bonds associated with a reducing crystallite size. This implies an inverse relationship between L_a and I_D/I_G ratio for nano-crystalline carbons. In amorphous carbons, sp^2 clusters size is < 2 nm and with decrease in size the concentration of ring bonds falls. As a result there is a linear relationship between I_D/I_G ratio and sp^2 cluster size in amorphous carbons.

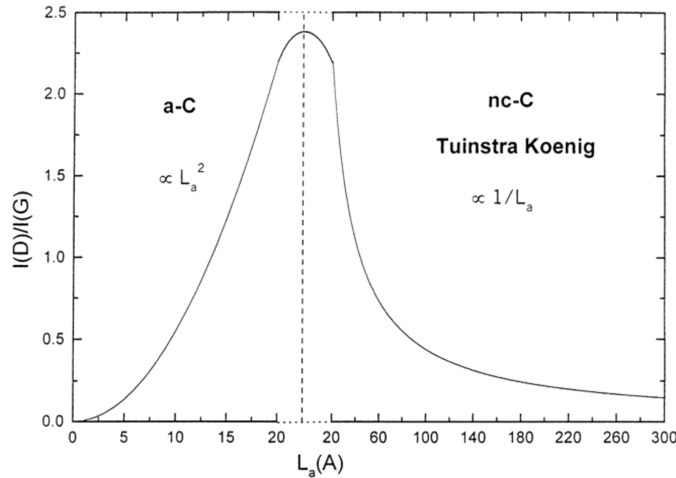

FIGURE 3.4: The relationships between sp^2 cluster size (a-C) and sp^2 crystallite size (nc-C), to I_D/I_G ratio [136].

The position and width of the Raman D and G peaks allows further direct interpretation of the bonding structure of amorphous carbons [134]. The position of the D peak can be used as a measure of aromatic disorder. Smaller aromatic clusters have higher vibrational modes which tend to vary its position. When ordered aromatic rings are replaced with non-ordered rings, D peak position decreases in line with disorder. The width of the D peak therefore correlates to the distribution of cluster size and ring order. The position of the G peak directly correlates to the sp^2 carbon bond length. Amorphous carbons with a high concentration of single bonds (C-C) reveal a reduced peak position of $\sim$1510 cm^{-1}. This is caused by a reduction in bond oscillation frequency as a result of disorder and loss of aromaticity, in comparison to graphite (1580 cm^{-1}) [130]. With the introduction

of Olefinic bonds (C=C) the G peak increases to ∼1570 cm^{-1}. This is due to the increased frequency of oscillation associated with the shorter double carbon bonds [134]. The width of the G peak correlates to bond angle order and the distribution of single to double bonded carbons. It scales with disorder and for values of G peak FWHM greater than 50 cm^{-1}, the average value for crystallite size will be less than 1 nm [131, 137, 138]. The relationships between crystallite size and the I_D/I_G ratio are graphed in Figure 3.4.

As visible Raman excitation energies are insufficient to polarise σ bonds, the concentration of sp^3 sites in an amorphous carbon matrix can not be directly determined. It can however be done indirectly by tracking the changes that occur within the *Vibrational Density of States* (VDOS) of the excited sp^2 sites. In amorphous carbon structures with a high concentration of sp^3 sites ($>$ 20%), the majority of the sp^2 bonds present exist in double-bonded short chain configurations [134, 139]. As a result, their increased vibrational frequency shifts the G peak peak position from ∼1510 cm^{-1} to ∼1570 cm^{-1}, with the extent of the shift scaling with sp^3 fraction. The formation of these olefin groups comes at the expense of aromatic ordering and results in a D peak that falls to a minimum. This results in an low I_D/I_G ratio that decreases to further with increasing with sp^3 fraction. The shape of the G peak becomes more symmetric as the sp^3 fraction reaches high values. This is due to the limited vibrational range of the double bonded sites, with its final value given by G peak position [134, 140]. A diagram predicting the changes that occur in an amorphous carbon structure, as a result of positional and intensity shifts in the carbon D and G peaks, is given in Figure 3.5. Given in Figure 3.6 is the correlation between G peak, I_D/I_G ratio and sp^3 concentration in amorphous carbons.

Prior to using the I_D/I_G and G peak position to determine the sp^3 fraction, knowledge of the processes involved in the generation the amorphous structure is required. For example, when the sp^3 fraction in tetrahedral amorphous carbons (*ta*-C) is reduced, the sp^3 sites will convert to sp^2 sites prior to sp^2 clustering or the sp^2 clustering will commence prior to the sp^3 to sp^2 conversion [134]. This hysteresis effect impacts visible Raman spectroscopy as it is most sensitive to sp^2 clustering. As a result, deriving sp^3 concentrations in amorphous carbons from an I_D/I_G ratio and a G peak position is unreliable. It is possible however to do so for *ta*-Cs with high sp^3 concentrations, whereby ultimate sp^3 concentration is given by final peak position when coupled with an I_D/I_G ratio of ∼0.

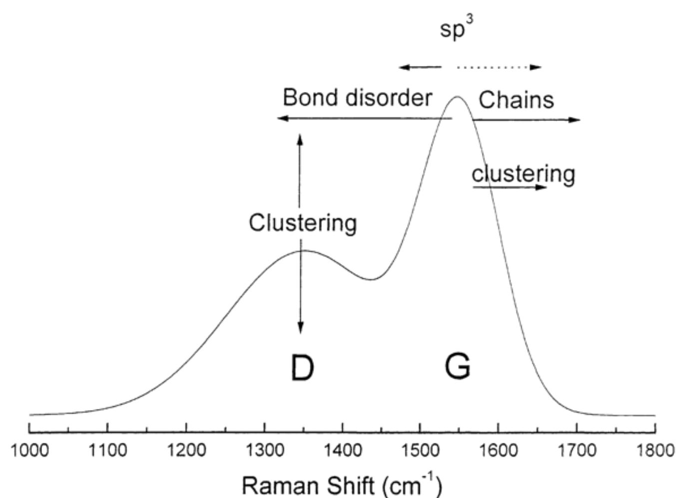

FIGURE 3.5: The changes that occur in an amorphous carbon structure as a result of positional and intensity shifts in the carbon D and G bands [134].

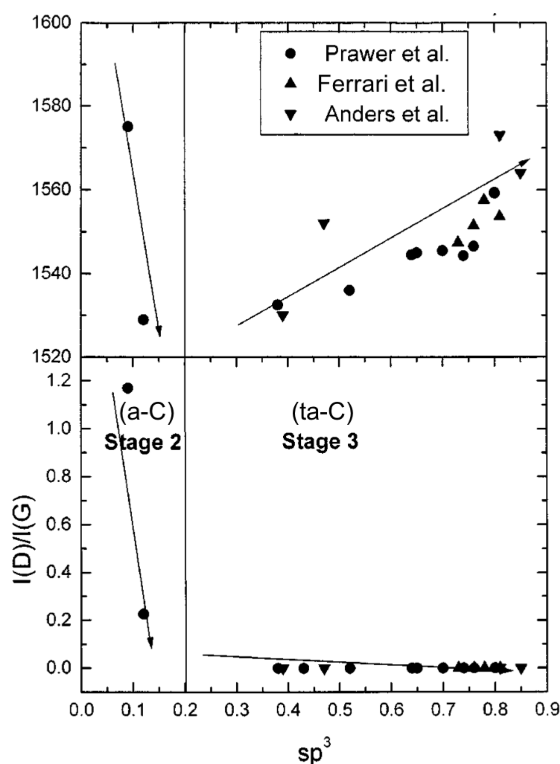

FIGURE 3.6: The shift in G peak position and I_D/I_G ratio as a result of increasing sp^3 fraction, in amorphous carbon (a-C) and tetrahedral amorphous carbon (ta-C) [134].

Visible Raman spectroscopy can be used to directly derive the sp^3 fraction of hydrogenated amorphous (*a*-C:H) materials, if there is a relationship present between optical gap (sp^2 phase) and the sp^3 phase. The main effect of hydrogen in *a*-C:H is that it modifies the C-C network when compaired to *a*-Cs of similar sp^3 content. This is achieved by the H saturation of C=C bonds as $\equiv$CH$_x$ groups rather than increasing the fraction of C-C bonds [134]. The sp^2 sites in *a*-C:H exist as both chains and rings and with the increase of H content, sp^2 cluster size is reduced and an opening of the band gap.

Bonding regimes in *a*-C:H are classified by a low, intermediate or high H content. In a low H-bonding regime, sp^2 bonding dominates and delivers a band gap of ~1 eV. In an intermediate H-bonding regime, C-C sp^3 bonding is a maximum, the deposited films have the highest density, are the most diamond-like and have a band gap of between 1 - 1.8 eV. In a high H-bonding regime, the sp^3 content is the highest, the bonding is more polymeric and delivers a band gap of $>$ 1.8 eV.

The C-H modes in amorphous hydrocarbons are neglected, due to either non-resonant enhancement (lying in the *D* peak region) or lying at Raman shifts above 3000 cm^{-1}. However when an excitation source of higher energy is used, i.e *Ultra-Violet* (UV) irradiation, these modes can be directly probed [141]. A typical feature in visible Raman spectra of *a*-C:Hs is the presence of a photoluminesence background and when the hydrogen content increases beyond 40 - 45% it overshadows the carbon Raman *D* and *G* modes [134]. This however is advantageous in the characterisation of *a*-C:Hs as the ratio of the slope of the fitted linear background (m) to *G* peak intensity (m/I$_G$) can be used to measure hydrogen content.

As the hydrogen content in *a*-C:Hs influences sp^2 cluster size, it therefore determines band gap. By examining the optical gap for *a*-C:Hs, a relationship between its Raman parameters (*G* peak position and I_D/I_G ratio) and sp^3 fraction can be attained. As reported by Ferrari & Robertson [134], and Tamor & Vassel [142], *G* peak position falls monotonically with increasing gap, due to the stretching frequencies of the C=C bonds and mixing with the sp^3 modes (Figure 3.7 (a)). Using the general relationship proposed by Robertson [143] the sp^3 content of was correlated to optical gap, which was confirmed by EELS [134] and *Nuclear Magnetic Resonance* (NMR) [142] (Figure 3.7 (b)).

Unlike the visible Raman spectral data fitted for *a*-Cs, the I_D/I_G ratio for *a*-C:Hs are area ratios and thus values of up to 3.5 are observed. Tetrahedral hydrogenated

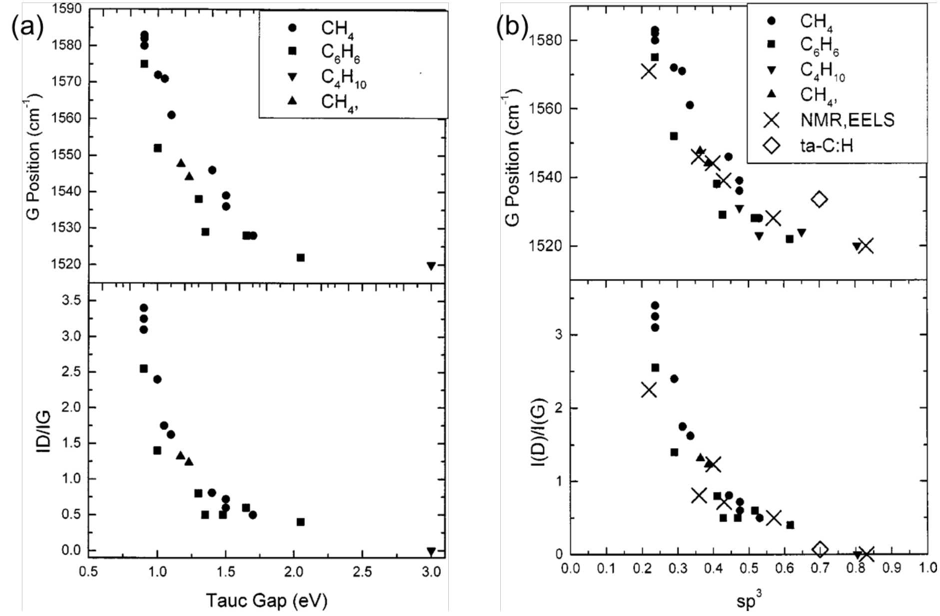

FIGURE 3.7: (a) The shift in G peak position and I_D/I_G ratio as a result of increasing optical gap, in hydrogenated amorphous carbon (a-C:H) (b) The correlation of G peak position and I_D/I_G ratio to sp^3 fraction, determined by the Robertson general relationship [143] and confirmed by NMR and EELS by [134, 142].

amorphous carbons (ta-C:H) differ from a-C:Hs with a high H-bonding, in that their high sp^3 fraction occurs at reduced hydrogen concentrations. As a result ta-C:Hs have significantly more C-C sp^3 bonding than a-C:Hs with a similar sp^3 fraction, giving a higher density and hardness. The G peak in visible Raman spectra of ta-C:H has been observed to lie above that for a-C:H with a similar sp^3 content or optical gap. This is due to the arrangement of the ta-C:H sp^2 bonds into shorter olefinic configurations [130]. D peak intensity in ta-C:H is $\sim$0 and is due to the loss of aromatic groups. The G peak position in a-C:H and ta-C:H shows dispersion with photon energy. It increases with higher photon energies and occurs from the resonant selection of wider-band gap π states from the sp^2 groups that have a higher vibrational frequency [134]. This in turn leads to a reduced sensitivity of the Raman parameters to optical gaps when higher excitation energies are used, as the optical gap is due to delocalised π-bonded structures [144]. These findings suggest that lower red extication energies (e.g. 633nm) in visible Raman spectroscopy are optimal for tracking the variations in optical gap and sp^2 order.

In a-C:H, the width of the G peak is scales with bond angle disorder of the sp^2 sites.

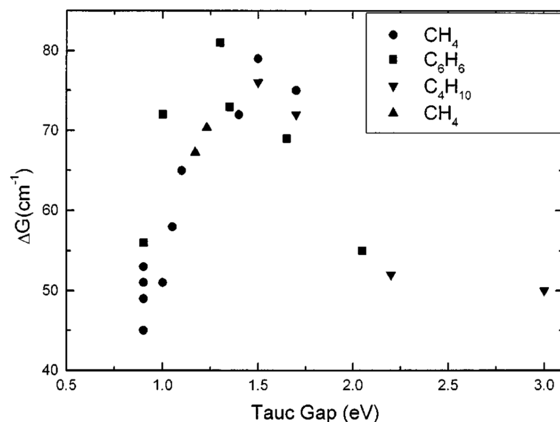

FIGURE 3.8: The relationship between G peak width (Gaussian) and optical gap for as deposited in hydrogenated amorphous carbon (a-C:H) [134, 142].

When plotted against optical gap (Figure 3.8), a maximum C-C sp^3 concentration is observed for a value of 1.5 eV [142].

3.2.3 Raman characterisation of electron beam induced carbonaceous deposits

The position, width, intensity and ratio of intensities of graphitic D and G bands in the Raman spectra can be used to determine, the sp^2-bonding configuration, the sp^2 crystallite size and the sp^2:sp^3 ratio of electron beam induced carbonaceous deposits.

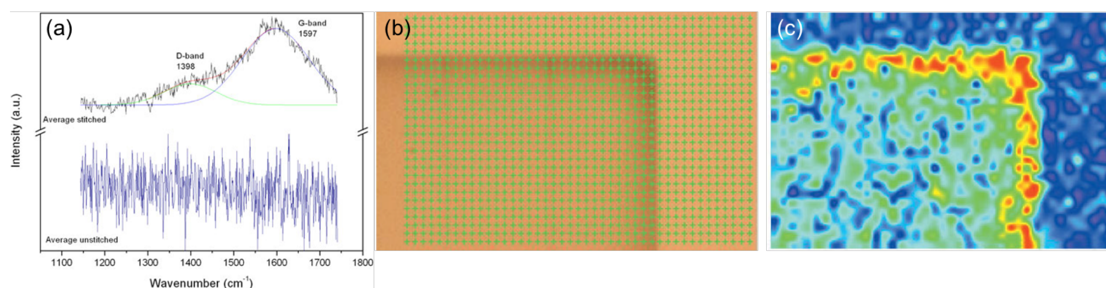

FIGURE 3.9: (a) Raman signature of the contamination layer and its uncontaminated surroundings. (b) The deposited carbon layer with an overlay of Raman excitation points. (c) Raman mapping image showing the intensity of the G peak detected across the layer [42].

Raman spectra evaluation of contamination layers, formed from residual hydrocarbons in an SEM with electron beam energy of 15keV, revealed an I_D/I_G ratio of 0.28 [42], as displayed in Figure 3.9 (a). By interpreting the calibration curve relating the I_D/I_G intensity ratio to L_a, as given by Knight and White [131], a crystallite size of 125 $\mathring{A}$ was determined. In this work the authors reported a 300% enhancement of the Raman G peak intensity - at the edges of the contamination layer in contrast to its centre - which was attributed to an discontinuity of electric permittivity at the edge.

Carbonaceous structures formed from a variety of dedicated organic precursors were classified by Raman spectroscopy as being amorphous in nature [41, 145, 146]. The Raman spectra for the deposits researched by Bret *et. al.,* yielded an average G peak position of ~1580 cm^{-1} and I_D/I_G ratios of between 2.0 - 2.8, as displayed in Figure 3.10. When referenced to the amorphorization trajectory revealed by [134], the deposits were classified as nano-crystallite graphite with an average cluster size on the order of ~2 nm and an sp^2 fraction above 90%.

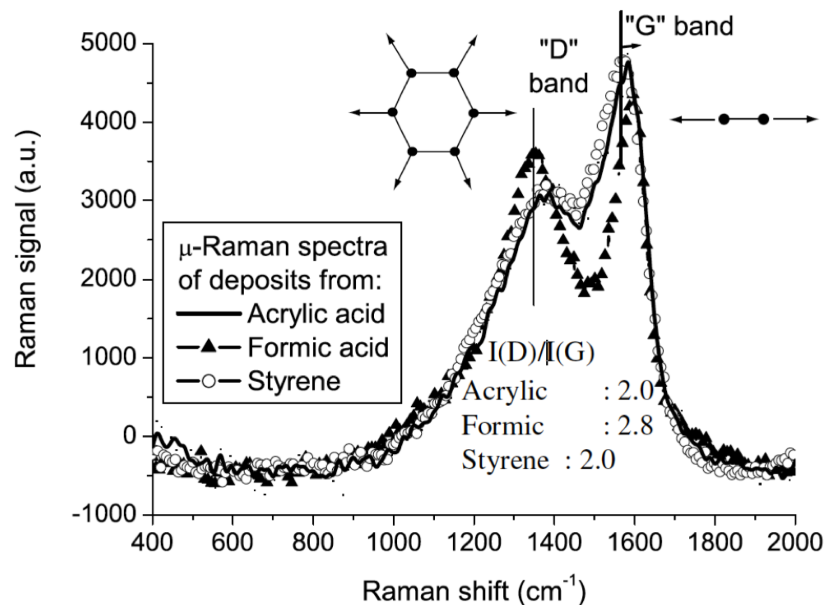

FIGURE 3.10: A comparison of the Raman spectra of three organic precursors and their associated I_D/I_G ratios [145].

When deposited over a range of primary electron energies (1 – 25keV), the deposited structures become less graphitic, showed an increase in hardness and in

elastic modulus, with the increase in beam energy [41, 146]. These changes were attributed to an observed increase in the concentration of sp^3 carbon sites in the higher energy deposits, when characterised by EELS [41].

3.3 Enhanced Raman Spectroscopy

3.3.1 The Raman enhancement effect

In enhanced Raman spectroscopy, the intensity of Raman scattered light is amplified by the presence of an enhancing medium. It is a technique used for the characterisation of specimens of low Raman efficiency. It was first reported in 1974 by Fleischmann *et al*, [147] who observed a greater than expected Raman intensity from a known concentration of pyridine molecules adsorbed onto a roughened silver electrode.

There are two types of enhancing mediums used in the application of the technique. One which physically supports the specimen analyte and the other which is brought into close proximity to it. These give rise to the two classifications of the technique termed, *Surface Enhanced Raman Scattering* (SERS) and *Tip Enhanced Raman Scattering* (TERS). SERS is the most common enhancing method and has been used extensively for understanding the mechanisms of the phenomenon. TERS is an evolution of SERS and is used to generate a spectrum from a single target molecule. When coupled with a STM, a spatial resolution of < 1 nm was revealed [148, 149].

The effectiveness of an enhanced spectroscopic technique is determined by its enhancement factor, i.e. the magnitude of an enhanced Raman shift relative to that of its corresponding non-enhanced shift. For SERS, the enhancement factor is strongly dependent upon the surface conditions of the substrate, the analyte concentration and the excitation wavelength. Quantified SERS enhancement factors in the range of 10^7 – 10^8 have enabled the detection of single molecules [150]. For TERS, a wide range of enhancement factors between 30 – 10^{13} has been reported [148, 151]. TERS enhancement factors are also dependent upon the same conditions that govern SERS, with the addition of, the instrument, the characteristics and cleanliness of the enhancing tip, and the physical gap between the tip and

specimen. This makes correct TERS enhancement factor evaluation of critical importance [152].

3.3.2 Enhancement mechanisms

There are two proposed mechanisms responsible the enhanced Raman shift. These are the *Electromagnetic Mechanism* (EM-M) and the *Chemical Mechanism* (CM). The EEM-M theory proposes an enhancement of both the incident and the scattered radiation by the generation of a resonant Plasmonic field in close proximity to the target analyte. The CM theory proposes a direct transfer of energy from the excited enhancement medium to a chemisorbed target molecule. The EM mechanism is the dominant of the two however both mechanisms have their individual contributions to the overall enhancement [153]. Separating their effects can be achieved by the wavelength and polarisation of incident radiation [154, 155]. Further specifics on both enhancement mechanisms now follow.

3.3.2.1 Electromagnetic theory

The electromagnetic field of light present at the surface of a metal can be greatly enhanced when Plasmons thereon are excited. On the occurrence of such excitations, the magnitude of both incident and scattered light can be enhanced [153, 154, 156]. When the frequency of the incident light matches natural frequency of the electron oscillations of a metal, a resonance condition is established and the dipolar field generated by the Plasmon is maximised. Depending on the geometry of the irradiated surface, Plasmons will either be propagating or confined. When the shape of the metal surface is smaller than the wavelength of the irradiating light, all of the valence electrons present within will oscillate simultaneously. Confined oscillations will form on spheres, spheroids and corrugated surfaces. These are called *Local Surface Plasmon Resonances* (LSPR) [154, 156]. *Surface Plasmons* (SP) can be induced in all systems possessing free conduction electrons, provided they are excited with irradiation of resonant frequency [153, 154]. An illustration of the LSPR generated at two metal nanoparticles is given in Figure 3.11.

The enhancement of Raman scattered light from a molecule is determined by; the strength of the field generated by the Plasmon, the position of the analyte

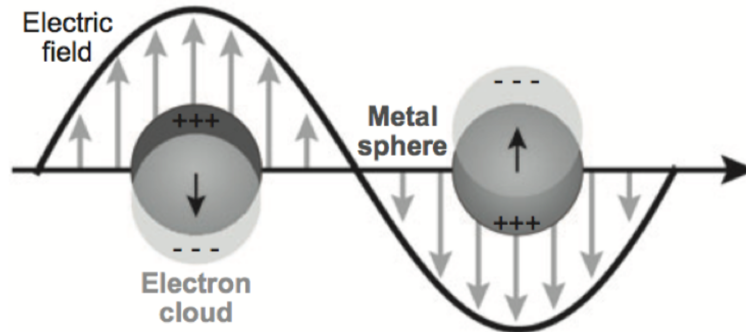

FIGURE 3.11: An illustration of the LSPR effect in nanoparticles irradiated with incident light of wavelength greater than their individual size. The electron oscillation occur across the nanoparticle-dielectric interface and account of the real part of the filed. The imaginary field component becomes the positive ionic cores within the stationary metal nanoparticles [156].

within that field and the excitation energy wavelength. For a spherical metal nanoparticle, with a radius smaller than the wavelength of the incident light, the surface Plasmon field generated has oscillation coherent with excitation energy and a uniform spatial distribution. It can be visualised a localised plane wave of light, centred on the sphere, decaying away from the surface in all directions in accordance with the dipole decay law. A representation of the filed is given in Figure 3.12

The magnitude of the field generated at the surface of the spherical particle , is calculated using equation 3.7, as given in [156],

$$E_{out}(x, y, z) = E_0\hat{z} - \alpha E_0 \left[\frac{\hat{z}}{r^3} - \frac{3z}{r^5}(x\hat{x} + y\hat{y} + z\hat{z}) \right] \tag{3.7}$$

where, x, y, and z are the Cartesian coordinates; r is the radial distance; and $\hat{x}, \hat{y}$ and $\hat{z}$ are the Cartesian vectors; E_0 is the magnitude of the incident field and α is the metal polarisability expressed as,

$$\alpha = ga^3 \tag{3.8}$$

where a is the radius of the sphere and $g$the averaged enhancement defined as,

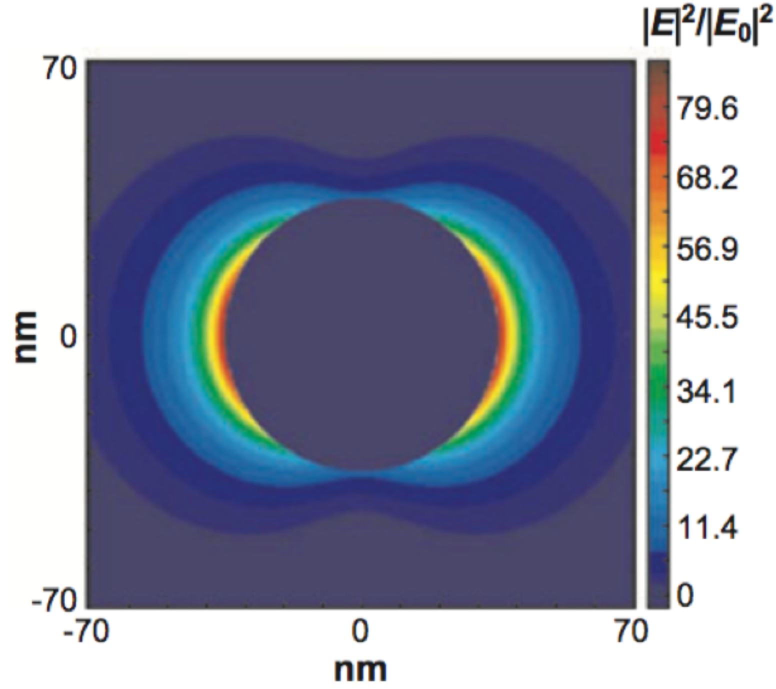

FIGURE 3.12: The extinction efficiency (ratio of the cross-section to effective area) of a spherical Ag nano-particle (r = 35nm). The $|E|^2$ contours show the strength of the real part of the enhancement field [156].

$$g = \frac{\epsilon_{in} - \epsilon_{out}}{(\epsilon_{in} + 2\epsilon_{out})} \tag{3.9}$$

ϵ_{in} is the dielectric constant of the metal nanoparticle and ϵ_{out} is the dielectric constant of the external environment [156].

The average magnitude of the field at the surface metal particle, E_s, is the product of the averaged energy of the enhanced field and the energy of the incident radiation ($E_s = gE_0$). An analyte adsorbed at the surface of the particle will be excited by E_s and its Raman scattered light E_R will be proportional to the product of the Raman tensor and the averaged field enhancement ($E_R \sim \alpha_R E_S \sim \alpha_R g E_0$). The Raman scattered light is subsequently enhanced by the magnitude of the field, by a factor g'. This secondary enhancement factor (g') is associated with the shifted wavelength and is differentiated from (g), the effect that E_s has on the enhancement of the incident radiation. The amplitude of the *Enhanced Raman* (ER) field is given by, $E_R \sim \alpha_R g g' E_0$ and the average ER intensity will be proportional to the

square modulus of E_{ER}, $I_{ER} \sim |\alpha_R|^2 |gg'|^2 I_0$, where I_{ER} and I_0 are the intensities of the enanced Raman and the incident fields respectively [156].

As optimum Plasmon excitation is achieved when the incident light is in resonance with the collective electron oscillations in the metal, optimum enhancement is achieved when the enhancement generated by the incident field g is in resonance, or as close to resonance, with the enhancement of the scattered field g'. For short wavenumber Raman scatters, when g $\sim$ g', max ER intensity is proportional to the fourth power of the excited local near-field E_L, where $|E_L|^4 = |g|^4$. For higher wave number Raman modes ER intensity becomes a function of the metal particles Plasmon resonant properties, with respect to the incident and Raman-scattered wavelengths [153].

The EM theory does not require an analyte to be in direct contact with the enhancement medium, however it is required to be within a certain distance in order to undergo polarisation and Raman shift. For a small metal sphere, the enhancing field which surrounds it decays with r^{-3} and its effect will scale with r^{-12}, when using the E^4 approximation. When analytes attach to themselves to the sphere, the surface area increases and the decay now scales with r^2. As a result, the experimental distance dependence for the enhancing field scales with r^{10} and is given as,

$$I_{ER} = \left(\frac{a+r}{a}\right)^{-10} \tag{3.10}$$

where I_{ER} is the intensity of the Raman mode, a is the size of the metal sphere, field and r is the distance from the sphere surface to the analyte [156].

In order to achieve maximum SERS intensity (I_{SERS}Max), an excitation wavelength with the ability to enhance the incident and radiated field, is required. This is achieved when the wavelength of the LSPR maximum (λ_{LSPR}) is positioned at approximately $\sim$ 50% of the energy separation between excitation wavelength (λ_{exc}) and the analyte's Raman shift wavelength (λ_R) [156].

$$I_{SERS}Max \Rightarrow \lambda_{exc} < \lambda_{LSPR} < \lambda_R \tag{3.11}$$

For SERS experiments using fixed excitation energies, a λ_{exc} matched to the extinction spectrum of the enhancing media is required prior to commencement. For those that utilise wavelength-scanned apparatus, the λ_{exc} is optimised after the analyte is adsorbed to the enhancing media.

3.3.2.2 Chemical theory

The electromagnetic theory can be applied to the enhancement of Raman scatter from all analytes, however it cannot explain the magnitude of enhancement in all cases. An enhancement mechanism should be non-selective in terms of polarisibility, however when radical differences in adsorption orientation are taken into account, they fail to explain the observed difference in enhancement of N_2 and CO ($\sim$ 2 x 10^2) under the same experimental conditions [154]. A second enhancement mechanism, termed the chemical theory, has been shown to work independently from the electromagnetic theory. For enhanced Raman experiments where both mechanisms are in operation the overall enhancement is a multiplication of both effects.

When a molecule is chemisorbed to the surface of an enhancing medium (i.e. a metal), new electronic states arise which result in a charge transfer between the molecule and the mental surface, and vice versa. Electron transitions in molecules occur between *Highest Occupied Molecular Orbital* (HOMO) and the *Lowest Unoccupied Molecular Orbital* (LUMO). The energy required for an electron transition is typically greater than excitation energies used in standard Raman experiments, but lie typically in the near UV range. For a chemisorbed molecule, these levels are adjusted to the Fermi level (E_F) of the metal and this results in a HOMO-LUMO transition being equal in magnitude to E_F. As a result excitation of the metal with energy in the visible spectrum induces a resonant Raman scatter in the absorbed molecule at approx. half of the energy required for an intrinsic excitation [154]. Figure 3.13 depicts an energy level diagram representing the charge transfer excitations between a metal surface and an adsorbed molecule.

The resultant Raman scatter from a chemisorbed molecule is greatly enhanced by a significant number of photon induced electronic transitions, which result in an equivalent number of scattered photons with an energy shift of $-\Delta E_F$. The chemical enhancement theory is selective in terms of the excited vibrational mode, the charge transition is dependent on the orientation of the molecule relative to

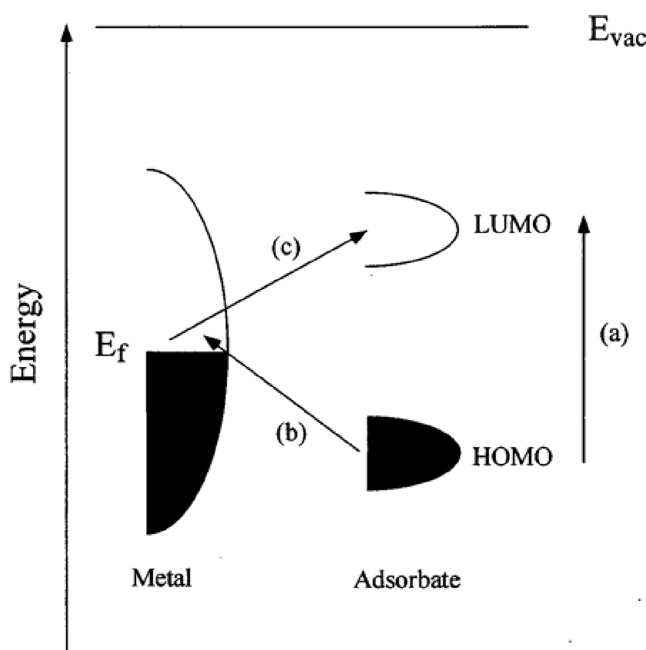

FIGURE 3.13: An energy level diagram for a molecule adsorbed on a metal surface. The occupied and unoccupied molecular orbitals are broadened into resonance when the excitation energy matches the E_F of the metal [154].

the metal and the degree of charge transfer tends to increase with increasing Fermi energy level [157].

3.3.3 Raman enhancing surfaces and materials

The purpose of a SERS/TERS experiment is to achieve quantitative chemical analysis of molecular systems that are difficult to analyse by standard Raman spectroscopy. In the first recording of an enhancement Raman shift, the aim of the study was to achieve a larger Raman cross-section by increasing the surface area of a silver electrode substrate, on to which a higher concentration of pyridine molecules could be adsorbed [147]. Its findings revealed that the observed increase in intensity was greater than what was expected for the increase in surface area and molecule concentration. A later report, which focused on exploring the mechanism behind the enhancement revealed that surfaces treated in the same manner increased in surface area by 20%, due to the creation of pit features, 300 nm in width and 100 – 200 nm in depth [158]. It concluded that increase in surface area could not account for the observed 10^5 increase in Raman intensity. A resonant

Raman effect, through the interaction of surface Plasmons, was given as a possible explanation for the enhancement, however the authors could not confirm this due to a negligible change in enhancement for an increase in excitation energy (514.5 nm to 632.6 nm). As information on the uniformity and distribution of the protruding features present on the roughened Ag surface were not explored, the generation of wavelenght dependent surface Plasmons, later found responsible for inducing an electromagnetic effect [159], may have accounted for the similar observed intensity at both excitation energies.

Plasmon resonances are localised to the features present on Au, Ag and Cu metal surfaces, provided that the surface features are smaller than the visible excitation wavelength. Under these conditions collective electron oscillations can come into resonance with the excitation wavelength inducing the Plasmonic effect [159]. The features need to maintain a minimum size, in order to remain conductive, so that the collective electron oscillations can occur [153]. Such features include, metal nano-particles, in islands and spheroids, and metal collides as well as SiO_2 conical posts, etc., [160–165]. With electron oscillations in the visible spectrum, Au and Ag are the most common metals for SERS/TERS. Al is also being explored for the SERS analysis of molecules in the UV spectra, due to its suitability for higher excitation energies [166].

Enhanced Raman spectroscopy is analyte specific, and the key to producing an enhancing medium is to ensure optimum interaction between medium and analyte upon irradiation. Sufficient uniformity and concentration of the Plasmon inducing features, as well the excitation energy being matched to the electron oscillations in the metal, are key to the EM-M theory. Matching the excitation energy to the electron oscillations enables the resonance condition to become established and the uniformity and size of the surface features determines the spatial field distribution. The enhancing mechanism in TERS is the EM-M effect and the medium by which it occurs is a Plasmon functionalised sharp tip. The CM mechanism may also play a role in TERS, if the target analyte becomes attached to the tip [167].

According to Moskovits, there are no chemical effects in SERS, as the electromagnetic effects operate regardless of analyte-surface bonding. He proposed that the chemical effects are related to the bonding, which serve to change the nature and identity of the absorbed molecules and in turn altering their Raman polarisability [153, 159]. However, a chemical mechanism has been confirmed with the use of flat single crystal surfaces that enable the separation of the electromagnetic from the

chemical enhancment effects. Studies on the bonding of *Pryomellitic dianhydride* (PMDA) to Cu surfaces resulted in a difference in the an observed enhancement between surfaces of alternate crystal orientations [154]. Upon irradiation with p (parallel) and s (perpendicular) polarised light, the s-polarised spectra were more intense than the p–polarised and stronger intensity differences were observed for Cu (111) over Cu (100). These differences revealed dissimilar bonding angles between the PMDA molecules and Cu (100) and Cu (111) surfaces, due to the dipole moments - which were oriented nearly parallel to the surfaces - being closer to the (100) surface than the (111) surface. This work [154] also studied the PMDA's HOMO-LUMO charge-transfer mechanism with the substrate. It was known that changing the Fermi energy level (E_F) of the metal, without affecting the orbital energies of the adsorbed molecule, would shift the wavelength of a charge transition. The direction of the shift would also determine the direction of transfer, i.e metal to molecule or molecule to metal. By electro-doping the Cu surface with a monolayer of Cs a resultant blue-shift in the transition energy of the adsorbed PMDA was revealed. This indicated that a photon-driven charge transfer occurred in the direction from the molecule to the metal. A further method to separate the effects of the chemical and electromagnetic enhancement mechanisms is to utilise TERS method whereby only a single Plasmonic particle on the tip is utilized to generate an enhancement effect [168]. The authors proposed a method to determine the short-range chemical effects from the long-range electromagnetic effects by determining the tip-to sample Raman enhancement over a range of a few angstroms to several nanometres.

Regardless of whether an observed enhancement derives from an electromagnetic or a chemical effect, the intensity and reproducibility of an enhanced spectrum is determined by the relationship between the molecule under analysis, the enhancing material (type and surface structure) and the excitation energy (wavelength, frequency and polarisation). As enhanced scattering is scattering by the enhancing medium and not from the absorbed molecule, qualitative and quantitative analysis rests in understanding the exact physical and chemical changes the molecule undergoes during adsorption and irradiation.

3.3.4 Applications for enhanced Raman spectroscopy techniques

Enhanced Raman spectroscopy has been used to investigate a wide variety of surface scientific questions. Surface enhanced applications differ from those of tip enhanced, due mostly to the complexity of the TERS technique. As TERS represents a refinement of the SERS, TERS applications tend to deal with definitive and quantitative questions.

SERS applications are numerous. In general, they stem from the requirement to detect analytes of low concentration or low Raman efficiency. Enhancement factors in the range of 10^6 – 10^8 have been used to successfully detect single molecules [150]. A recent optimisation of the technique has enabled the label-free detection of low abundance bio-molecules for cancer screening [169].

For the TERS, chemical mapping with sub-nm molecular imaging represents the ultimate refinement of the technique [148]. Other applications include, *ribonucleic acid* (RNA) sequencing analysis [170] and the ambient analysis of individual carbon nano-tubes with 1.7nm resolution [171].

3.3.5 Raman enhancement effect of amorphous carbon

A study on electron beam induced carbon deposition reported that an 300% increased in intensity of G band Raman scatter along the edges and corners of the deposited structures for only a 10% increase in thickness [42]. With analysis of the magnitude of the electric field across the surface of the film, a peak in field intensity was observed at its edge. This peak correlated to a discontinuity in the layer's electrical permittivity resulting in a 5.5 times enhancement of G-band intensity, in comparison to that from the centre of the film. This work however focused on characterising carbon deposits only generated at 15 keV, thus variations in the optical properties of carbon layers generated at other energies were not revealed.

3.3.6 Summary of Raman enhancement

The Enhanced Raman effect is scattering from the enhancing medium and not the adsorbed analyte. The scattering from the adsorbed analyte is however reflected

in the spectrum [153]. The extent to which the intensity of the Raman scatter is enhanced is dependent upon the analytes position within the enhancement field [156], and/or the magnitude of resonant charge transfer between the analyte and the medium. This charge transfer is a functionof the enhancing medium E_F [154]. The EM-M mechanism for SERS and TERS are near-field phenomena whereby maximum enhancement is observed in close proximity to the enhancing surface. Enhancement ultimately decays with distance from the surface, in accordance with the dipole decay law [153, 154].

Chapter 4

Experimental methods

In this chapter the experimental methodologies employed/developed for this thesis are presented. The first section will discuss the methods for contamination deposition followed by a section dedicated to the characterisation of the contamination. This is followed by the methods for SE imaging in SEM and HIM. The last section details the techniques for the Raman investigation of electron-beam induced contamination.

4.1 Contamination formation

This section describes the methods used for the formation of contamination in HIM and SEM. To enable comparative study in both microscopes, we evaluate the effects of several key factors, such as the cleanliness of specimen surface, chamber vacuum and beam parameters. A set of beam parameters for electron/He^+-ion irradiation were selected to deposit carbonaceous contamination onto silicon wafers.

4.1.1 Specimen preparation

Polished intrinsic silicon wafer specimens, with 100 orientation, are used throughout the contamination and carbon layer deposition experiments. They were supplied from the Institute of Semiconductors, Chinese Academy of Sciences, China. The wafer exhibits a surface roughness below 0.1 nm across micrometre-sized areas. Arrays of circular holes of $\sim$2.2 μm in diameter and 5 μm in depth were fabricated onto the Si wafer by photolithography patterning followed by *Inductively Coupled Plasma* (ICP) and *Reactive-Ion Etching* (RIE). The circular holes, as well as the coordinates (etched using the same method as that of the holes), serve as location marks and the spacing between them is several-hundred-micrometres wide. As a

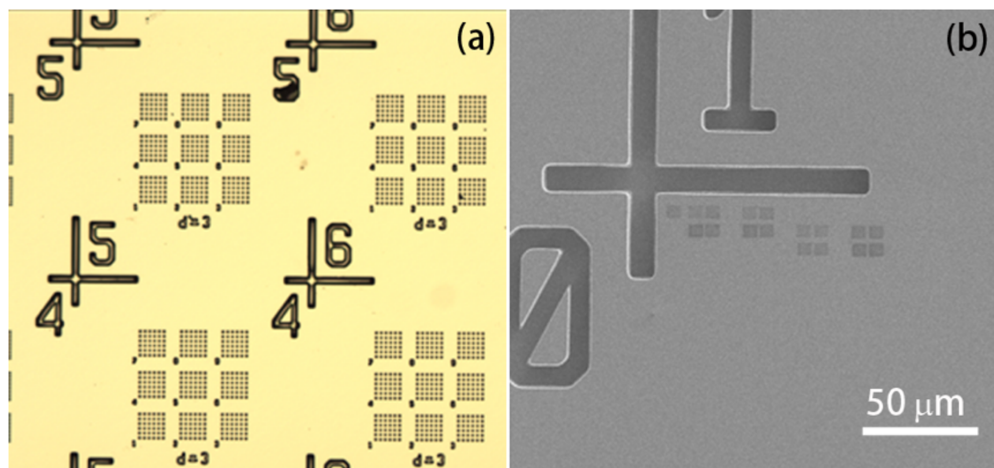

FIGURE 4.1: (a) Optical image of the Si wafer with the arrays of circular holes and reference markings. (b) SEM SE image of the substrate (the squares under the reference mark are the contaminated areas).

result they do not influence the diffusion of molecules in the formation of contamination deposits or the carbon layers. Images of a typical Si wafer specimen are displayed in Figure 4.1.

To investigate the effect of specimen cleanliness on the formation of beam-induced contamination, three batches of silicon wafers were prepared and they are termed as "*un-cleaned*", "*cleaned*" and "*pre-contaminated*". An un-cleaned (or bare) specimen was the one that had been exposed to ambient conditions for months and placed into the microscope "as is". The investigation of an un-cleaned specimen provides information on the effect sample storage conditions have on the formation mechanism. For the "cleaned" samples, a simple cleaning procedure was employed for treating Si specimens prior to the contamination study. It consisting of ultra-sonic cleaning in isopropyl alcohol (10 minutes), ultra-sonic cleaning in de-ionized water (10 minutes), direct baking at $\sim 100^o$ C on a hot plate (10 minutes) and an Argon:Oxygen plasma clean (10 minutes). The cleaning process significantly reduced the amount of adsorbed surface hydrocarbons prior to exposure to the microscope environment. The pre-contaminated specimens were generated by first wet cleaning a Si wafer specimen and wiping it with a thin film of acetone. The specimen was then left to dry in ambient before being placed into the microscope.

For the study of Raman enhancement of carbonaceous layers discussed in chapter 6, a thorough cleaning process was developed to remove other species and ensure the dominant role of beam-induced carbon in the observed Raman effects.

The cleaning process consists of a wet cleaning followed by a dry cleaning. Prior to the wet cleaning process, debris from the wafer surface was removed using an acetone soaked "lint-free" swab. The specimen was checked under an optical microscope and the process repeated until it was confirmed as visually debris free. The wet cleaning process consisted of an ultra-sonic cleaning step and a highly reactive chemical clean known as the RCA method (Called after the company who pioneered its use in semiconductor processing, the Radio Corporation of America). The ultra-sonic clean was used to agitate trapped contaminants from the etched features on the surface. These would then be removed, along with the native surface oxide, by the chemical clean. This wet cleaning was carried out as follows. Firstly, the specimen was placed in a clean glass beaker to which ~ 20 ml of Acetone was added. Then the beaker was placed into an active ultra-sonic bath for ten minutes. Post ultra-sonic clean, the specimen was removed from the acetone and placed in another clean glass beaker containing 28 ml of the chemical cleaning solution. This solution consisted of deionised water, ammonium hydroxide (NH_3) and hydrogen peroxide (H_2O_2), in a 5:1:1 ratio. The beaker was covered and placed on a hot plate that had been pre-heated to $\sim 80^o$ C. After 20 minutes the beaker was removed from the hot-plate and the specimen carefully removed from the solution. It was then placed on a lift-free wipe and immediately blown dry with compressed N_2, via a hand-held air-gun. Once dried, the specimen was checked again under an optical microscope for any signs of residual contamination. When residual contamination was detected the specimen was chemically re-cleaned using a fresh $H_2O : NH_3 : H_2O_2$ solution.

Immediately after the wet cleaning, a dry cleaning step was implemented. This was conducted in a TEM plasma cleaner (Fischione Instruments, Model 1020) with the appropriate support apparatus for scanning microscopy specimens. It was conducted as follows. The Si specimen was fixed to a standard SEM stub with conductive Ag paste. It was placed into the plasma cleaner which was connected to an Argon-Oxygen (75:25) compressed gas source and exposed to the plasma for ten minutes. The function of the plasma cleaning step was to remove any remaining contaminants, or new contaminants that may have been introduced to the specimen after the wet cleaning. It was also completed just prior to the insertion of the specimens into the microscopes.

4.1.2 Beam parameters for contamination formation

The charged-particle microscopes that are used to investigate the beam-induced contamination, and the growth of carbon layers, are a Zeiss Orion Plus HIM and a FEI Strata DB235 SEM. A comparison of the microscope specifications that are relevant to contamination formation are listed in Table 4.1. Both microscopes use oil-free pumps, which can improve the chamber cleanliness greatly. Note the highest possible beam current in HIM is about three orders-of-magnitude smaller than that available in SEM.

	Zeiss Orion Plus (HIM)	**FEI Strata DB235 (SEM)**
Pre-Vacuum	Oil Free Roughing	Oil Free Roughing
Chamber Vacuum	Turbo Molecular Pumping	Turbo Molecular Pumping
Vacuum Level	$\sim$1.0 x $10^{-6} mbar$	$\sim$1.0 x $10^{-6} mbar$
Specimen Loading	Load Port	Specimen Chamber Vent
Energy Range	30 keV $\pm$ 5 keV (Fixed)	0.5 - 30 keV
Beam Current Range	1 fA - 100 pA	1 pA - 25 nA
Probe Size	$\leq$ 0.75 nm	4 nm @ 1 keV
Detectors	Everheart Thornley (ET) Microchannell Plate (MCP)	Everheart Thornley (ET) Channel Detection Electron Multiplier (CDEM)

Table 4.1: A list of microscope specifications for HIM and SEM.

The HIM chamber is cleaned on a bi-weekly basis by using reactive O_2 plasma. The cleaning typically runs $<$ 10 hr where plasma, generated at a *Radio Frequency* (RF) energy of 10 W, floods the chamber for a period of 15 minutes per hour. During the cleaning procedure the chamber vacuum is maintained at 1.3×10^{-3} Torr. Dry nitrogen of 99.99% purity is used for the chamber and load port venting. The specimen can be plasma cleaned in the load port. The SEM chamber is also vented with 99.99% purity N_2 when loading samples. This purges the system and helps to maintain the cleanliness, however the SEM chamber does not undergo any type of plasma cleaning.

The microscope parameters which may influence the contamination growth are particle species, particle charge, beam energy, beam current, probe focus, working distance and dose. Beam dose is defined as the charged particles injected per unit area of the sample surface with a unit of C/cm^2. Since the charge injected

q is simply given by the product of the beam current i_p and the dwell time t_d (the duration that a beam scans the sample surface), i.e. $q = i_p t_d$, the dose is $q = i_p t_d / A$, where A is the area that the beam scans. It is clear that to vary the dose we can change the beam current, the dwell time, or the scanned area.

To compare the beam-induced contaminations on the silicon wafers (see chapter 5), we fixed the beam current and the scanned area but varied the dwell time by scanning the beam on the same regions of the specimen several times using the same beam current. In the SEM, the electron-beam energy was set within the range of 1 keV to 1.5 keV. This maintained a constant beam current of 80 pA during each experiment. The area of the scanned regions was fixed at 6 μm × 5 μm (30 μm^2) and the time for each scan was 2.942 seconds. A single scan over such an area delivered an irradiation dose of 7.85 pC·μm^{-2} . By repeating such a scan for 4, 8, 16, 32, 64 and 128 times, the total irradiation dose was varied from 31.4 pC·μm^{-2} to 1 nC·μm^{-2} . For this experiment, the objective aperture was fixed at 30 μm and the working distance was set to 5 mm. In the HIM, the beam energy was set to 30 keV, the beam current to 8 pA (20 μm aperture), and the working distance 8 mm. Under these parameters the time taken to irradiate a 6 μm x 5 μm region with a dose of 0.7 pC·μm^{-2} was 2.62 s . The scan area iterations were kept the same as SEM and as such the total irradiation dose varied from 2.8 pC·μm^{-2} to 89.6 pC·μm^{-2} .

For the investigation of Raman enhancement of electron-beam-induced carbonaceous layers (see chapter 6), the layer was induced by an electron beam with an energy ranging from 1 to 30 keV in the SEM. For each beam energy, an array of contamination were generated in the same manner as the contamination profiles described above (i.e. varying the dose). In order to minimise differences in hydrocarbon desorption across the electron beam energy range, the primary beam current was set to a fixed value, ($\sim$50 – 60 pA). An overview of the placement of the irradiated areas is given in Figure 4.2. A total of 18, 5 μm × 5 μm, areas of the specimen were irradiated at 1, 3, 5, 12, 20 and 30 keV, with applied doses of 1, 3 and 5 nC·μm^{-2} at each beam energy.

The steps used to irradiate the specimen to form the carbon layers is as follows. Firstly, using the 1 keV electron beam a 3.5 kX image of the specimen was acquired in standard SE mode. The resultant 100 μm × 90 μm image of the specimen was examined and found to be free from surface damage and debris. Next, the reduced raster scanning window was set to a 5 μm × 5 μm surface area and moved to the

FIGURE 4.2: Irradiation array for the carbon layer deposition experiment.

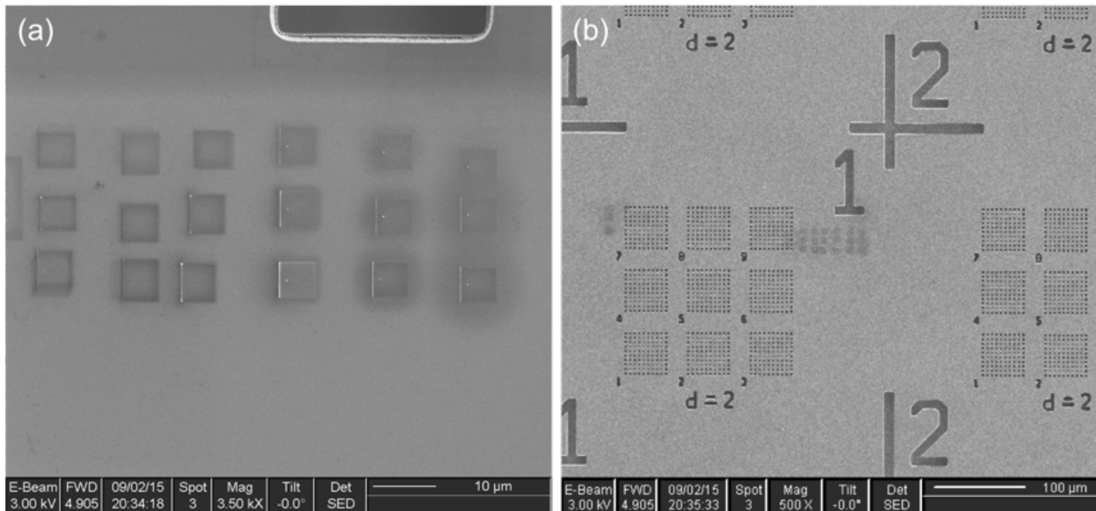

FIGURE 4.3: (a) Deposited carbon layers. (b) Deposited carbon layers with respect to the etched features on the specimen surface.

left side of the *field of view* (FOV). Once in position, the live image scanning was enabled and irradiation of the 1-1 area began. This region of the specimen was irradiated for a total of 431 seconds and once complete the raster window was moved down by ∼10 μm. The specimen was then irradiated for a further 1293 seconds. Once the second region (1-3) was irradiated, the raster window was moved down by ∼10 μm once more and the specimen was irradiated for a further 2155 seconds. On completion of the third irradiation (1-5), a quick scan image (of low dwell time) of the specimen at 3.5 kX was acquired. From this image the placement of the 1 keV irradiated regions was checked and the placement of the next irradiation set was determined.

At this point the primary electron beam energy was increased to 3 keV and allowed approx. one minute to settle before commencing irradiation. The 1 keV layer generation process was repeated at all other beam energies, at adjusted irradiation times to account for differences in primary beam current. The beam settings were not adjusted during the experiment having been optimised before hand. Upon completion of the experiment, the beam energy was set to 3 keV and a high resolution SE image of the deposited layers was acquired. Also acquired was a low magnification fast scan image of the layers along with the features etched into the Si specimen. The irradiation times for each region were determined prior to the experiment using the charge-dose calculations (given in section 4.1.2), which are given in Table 4.2. Images of the deposited carbon layers are displayed in Figure 4.3.

Beam Energy (keV)	**Beam Current** (pA)	**Irradiation Dose** (nC·μm^{-2})	**Irradiation Time** (s)
1	58	1, 3, 5	431, 1293, 2155
3	50	1, 3, 5	500, 1500, 2500
5	49	1, 3, 5	510, 1530, 2550
12	47	1, 3, 5	532, 1596, 2660
20	53	1, 3, 5	472, 1416, 2360
30	60	1, 3, 5	417, 1251, 2085

Table 4.2: Irradiation parameters for carbon layer formation.

4.2 Characterisation of carbonaceous contamination

This section describes the methods used in the analysis and characterisation of contamination deposits (HIM and SEM). The topographical information of the surface (e.g. roughness and deposition volume) was revealed by AFM.

4.2.1 Atomic force microscopy

We used an Asyulm MFP-3D AFM (Oxford Instruments) for the morphology experiments. With a lateral resolution of 0.1 nm, it was ideal for morphology characterision as the minimum height of the contamination was significantly greater

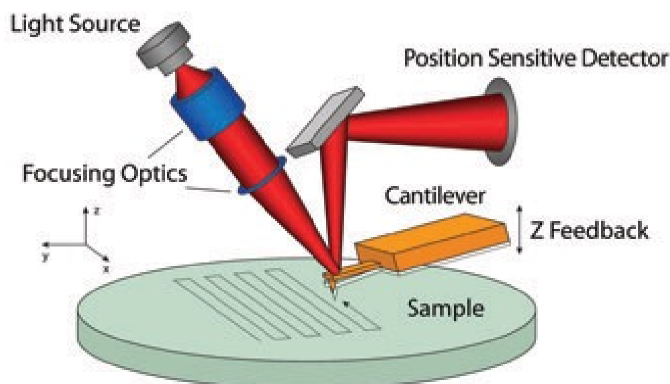

FIGURE 4.4: Schematic depicting the optical lever detection system used in AFMs. Light is reflected off of the back of a cantilever and read on a detector as the cantilever/probe is raster scanned to measure the topography of the sample. Most of the AFM instrumentation can be located above the sample, allowing for unrestricted optical access from below. (*Courtesy of Oxford Inst.*)

than this minimum detectable value. The analysis was carried out in "non-contact" mode. In this mode the region of the specimen, containing either the contamination profiles or carbon layers, is brought to a set height below the AFM probe (< 1 nm). The probe is then oscillated close to its resonant frequency and raster-scanned across the specimen surface by planar movements of the specimen stage. The change in specimen topography will alter the probe-surface gap, the variation of which influences the frequency and amplitude of the oscillating probe. A laser beam deflected off the supporting cantilever registers these changes on a sensitive photo-diode. A feedback loop between the photo-diode and the positioning of the specimen stage, ensures that the specimen is moved vertically, in "real-time", to compensate for the interaction variations experienced by the probe. As such the set height remains the same during the scan and the vertical movement of the specimen stage, required to maintain the set gap, is registered as the height of the specimen feature at a particular point in the scan. Images of the specimen are subsequently reconstructed from all the registered force interactions experienced during the scan. The lack of contact between the probe and specimen prevents any physical alteration of the contamination profiles, or carbon layers. A illustration of the optical-cantilever detection system used in this type of AFM is given in Figure 4.4.

Monolithic silicon probes, with a tip radius of curvature of < 10 nm, were used in the AFM experiments. The type of probe chosen was suited to measure features

over 200 nm in height, due to its “on-scan” angle and long cantilever configuration. The probe also had a reflective Aluminium coating which offered increased measurement sensitivity. Full specifications of the probe, (Budget Sensors, Tap 190 Al-G), are given in Table 4.3.

Probe: Tap 190 Al-G	**Typical Values**	**Range**
Resonant Frequency	190 kHz	± 60 kHz
Force Constant	48 N/m	20 - 100 N/m
Cantilever Length	225 μm	± 12 μm
Mean Width	38 μm	± 12 μm
Thickness	7 μm	± 1 μm
Tip Height	17 μm	± 2 μm
Tip Set Back	15 μm	± 5 μm
Tip Radius	< 10 nm	N/A
Coating	Aluminium Reflex	N/A
Half Cone Angle	20° - 25° along cantilever axis 25° - 30° from side 10° at apex	

Table 4.3: AFM probe specifications.

A typical AFM analysis session was carried out as follows. Firstly, the etched Si wafer specimen containing the contamination profiles, and the carbon layers, was fixed to a glass slide and mounted on the AFM stage. The AFM probe was mounted into a custom holder, which was then fitted to the scanning head of the microscope. The sensing laser was switched on and directed towards the AFM cantilever. The position of the laser on the cantilever was adjusted such that the reflected light was optimised at the photo-diode. At this point, the probe was tuned and its resonant frequency noted. Next, the region of interest of the specimen was brought underneath the AFM probe, by an X and Y adjustment of the specimen stage. The probe was then lowered by a downward adjustment of the scanning head. On lowering the probe, the instrument’s proximity detection circuitry was automatically turned on. It enabled an audible warning when the probe was near the scanning position. The final probe-surface gap was then set-up by fine adjustment of the scanning head. This was done with aid from the instruments sensing circuitry, which detected the attractive force interactions between probe and specimen. Once in position, a 50 μm × 50 μm low resolution scan of the surface was initiated. This revealed the position of the contamination profiles,

and carbon layers, and once known, a high-resolution (256 px $\times$ 256 px) mapping scan was initiated.

4.2.2 Chemical characterisation

The composition of the beam-induced contamination deposits was studied by EDX in a SEM and EELS in a TEM.

4.2.2.1 Energy dispersive X-ray spectroscopy

For the EDX analysis, we used an Oxford Inca X-Max-20 mm X-ray detector and an "EDAX Quantum" X-ray detector attached to a Carl-Zeiss 'Ultra' SEM and an "FEI Titan" TEM, respectively. In the SEM, the *working distance* (WD) was set to 8 mm, which is the optimum WD for the EDX detector to receive a sufficient number of X-ray photons. The contaminated regions of the Si substrates were irradiated at an energy greater than the activation energy for the characteristic X-rays from the expected contamination materials (for carbon K_α = 277 eV and oxygen K_α = 525 eV) and Si (K_α = 1.74 keV) from the specimen substrate. The entire 30 μm^2 contamination areas were raster scanned by the electron beam to collect the EDX spectra. A background spectrum of the Si sample was also generated for comparison to the contaminated regions.

Chemical analysis in the TEM was conducted with a 300 keV electron beam. The experiment was carried out, as follows, in less than 24 hours after the preparation of the lamellae specimens. Details of the lamella specimen preperation can be found in Appendix A. The lamella of the carbon layer was mounted in a double-tilt holder and placed into the microscope. Spot size three was chosen for illuminating the specimen and with the magnification set to 1 kX the lamella was centred in the view-screen. The magnification was then increased to 50 kX and the microscope was set to eucentric focus, i.e. the objective focus was set to the eucentric plane. The height of the specimen was adjusted with the Z-axis of the stage until it was positioned at the eucentric plane. At this point the specimen was in focus portraying minimum contrast. The Si region of the specimen was centred in the beam and the microscope was set into diffraction mode. In this mode, the Kikuchi lines in the specimen were revealed and the specimen was tilted until the

nearest low order zone axis was brought into alignment with the normal axis of the electron beam. The microscope was switched back to TEM mode, the EDX detector was inserted into position and the specimen checked to ensure it was still at the eucentric focus position. The microscope was then switched to *Scanning Transmission Electron Microscope* (STEM) mode and a high-resolution image of the Si-C interface, at 500 kx, was acquired. Using the EDX controls, a ten-point line profile, of $\sim$ 250 nm in length, was drawn over the region of interest in the specimen image. The region of interest started in the Si substrate, passed through the carbon layer and into the protective layers. An EDX spectrum was collected from each point in the line, with the dwell time of each point optimised to attain sufficient detector counts ($< 2 \times 10^4$ counts per second (cts.s^{-1}) for Si and $\sim$300 cts.s^{-1} for the carbon layer). A spectrum was saved at each point and complied in a single file for later analysis.

4.2.2.2 Electron energy loss spectroscopy

EELS spectra were recorded by an Gatan Tridiem EELS Spectrometer attached to the FEI Titan TEM. The experiment was carried out first on the pre-loaded lamella for the carbon layer, immediately after the EDX analysis. The specimen was preset to the eucentric position and the beam optimised. The microscope was switched into EELS mode and the convergence angle of the beam was noted at 10 mrad. The specimen was moved out of the beam path and the *Zero Loss Peak* (ZLP) was measured using an acquisition time of 0.01 s. This short acquisition time was selected in order to prevent damage to the detector. An energy resolution of 1.15 eV was later determined from the *full width half maximuim* (FWHM) of the ZLP. The specimen was re-centred in the beam and a ten second EELS spectrum was acquired from a single point in the carbon region. This spectrum was taken to check the presence of Si in the carbon layer. The energy loss of this Si-EELSspectrum ranged from 70 – 172.4 eV as the Si-$L_{2,3}$ edge onset was positioned at 99 eV. A second identical EELS spectrum was acquired from carbon region of the specimen. This spectrum was taken to determine if the concentration and type of carbon bonds present in the carbon layer. The energy loss of the C-EELS spectrum ranged from 240 – 342.4 eV with the C-K edge onset positioned at 284 eV. Each spectrum was collected using 2048 channel detector with a dispersion of 0.05 eV per channel.

4.2.3 Electrical characterisation

The electrical properties of the e-beam induced carbon layers were characterised by two-point probe measurements. A Si wafer specimen with a 300 nm thick SiO_2 surface layer was chosen for the experiment. The insulation was required to prevent conduction through the Si during the measurements. A series of Au-Ti contacts were deposited on top of the SiO_2, by e-beam lithography and metal evaporation processes. Between the contacts gaps of 5 – 20 μm were generated, across which the carbon layers would later be grown.

As the Au-Ti contacts present on the surface could easily be damaged by aggressive cleaning methods, an alternative method was required. This was achieved by first placing the specimen in 10 ml of acetone and ultra-sonically cleaning it for one minute. Next it was placed into 10 ml of isoproyl alcohol and ultra-sonically cleaned for a further minute. Lastly, it was placed in 10 ml of di-water for a ten minute ultra-sonic clean. Once the wet cleaning steps were complete, the specimen was removed from the di-water and immediately blown dry (with compressed N_2). It was then fixed to an SEM stub, placed into a plasma cleaner and exposed to an Argon-Oxygen (75:25) plasma for ten minutes.

Once clean, the specimen was irradiated in the SEM to form carbon layers across the contacts. This was in the same manner described in section 6.1, however the Au-Ti contacts were centred in the FOV and the irradiation delivered with full frame scanning. Carbon layers were formed at 3, 5, 12 and 30 keV, the full deposition parameters for which are outlined in Table 4.4.

Beam Energy (keV)	**Beam Current** (pA)	**Irradiation Dose** (nC$\cdot\mu$m^{-2})	**Irradiation Time** (s)
3	58	21	50400
5	50	24	59400
12	49	8.5	21600
30	47	15	7560

TABLE 4.4: Carbon layer deposition paramaters for electrical characterisation.

After deposition, the SiO_2 specimen was mounted to the electrical characterisation apparatus. This consisted of an optical microscope (Olympus BX51M) with a

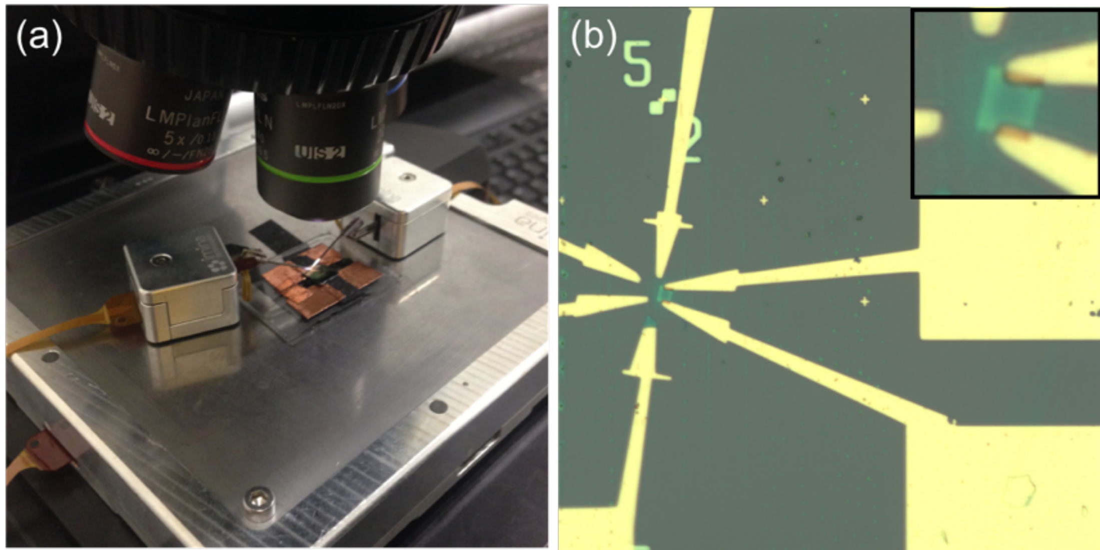

FIGURE 4.5: (a) Nano-manipulator probing set-up. (b) 30 keV carbon layer deposited across Au-Ti contacts prior to electrical characterisation.

manual X, Y and Z stage, a two probe nano-manipulator system (Imina Technologies MiBase/ MiBot) and a nano-volt micro-ohm source meter (Keysight 34420A). The probes of the manipulator system were brought in contact with the Au-Ti contact pads that were connected to one of the carbon layers. A 0 – 4 V drain-source bias sweep was initiated by the source meter. During this sweep the current measured through the layer was recorded. This procedure was then repeated for the remaining carbon layers. Images of the nano-manipulator probe set-up and an optical image of the 30 keV carbon layer and contacts, are displayed in Figure 4.5.

4.3 SE imaging of two-dimensional materials

4.3.1 Optimization of the probe size for SE imaging

To obtain an optimized SE image and minimal probe size, both astigmation and focus need to be adjusted properly. The astigmation of the obtained SE images can be evaluated from the corresponding 2D *Fast Fourier Transformation* (FFT) pattern [172], as shown in Figure 4.6. When the image is free of astigmation (Figure 4.6 (a)), the FFT pattern shows an isotropic bright circular spot in the

center (Figure 4.6 (b)). However, if the image has astigmation (Figure 4.6 (c)), the FFT pattern will become an ellipse (Figure 4.6 (d)). Therefore, by monitoring the isotropy of the FFT pattern, the astigmation in the image can easily be judged.

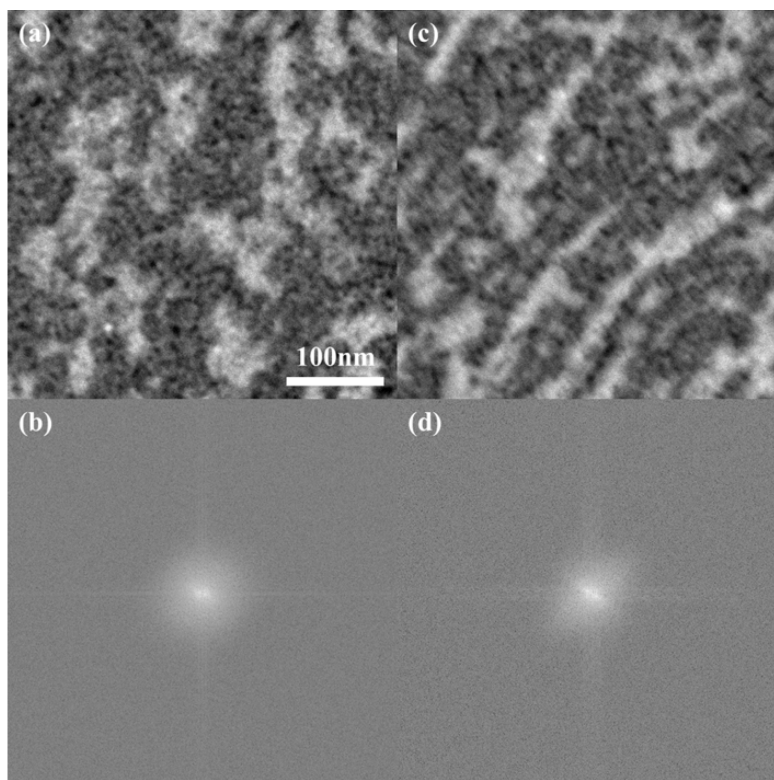

FIGURE 4.6: (a) A 0.5 keV SEM image that is free of astigmatism. (b) The corresponding FFT pattern of Figure 4.6a. An isotropic bright spot can be observed in the center. (c) A 0.5 keV SEM image that has obvious astigmatism. (d) The corresponding FFT pattern of Figure 4.6c. The spot in the center becomes an ellipse.

To evaluate the focusing state of the image, the observer first establishes an approximately in-focus state of the SE image. The image focusing is then tuned from an under-focused state to an over-focused state, going through the in-focus state. For example, HIM images (35 keV) of a graphene edge under different beam focusing conditions are shown in Figure 4.7. The first image obtained is the approximately in-focus image showing a sharp graphene edge, as presented in Figure 4.7 (e). The image field of view was set to 300 nm and pixel resolution to 2048 $\times$ 2048. This gave a pixel size of $\sim$0.15 nm. The focusing state was then changed around Figure 4.7 (e). In an over-focused state (Figure 4.7 (a)) the graphene edge was blurred. The graphene edge gradually became clear as the beam approached

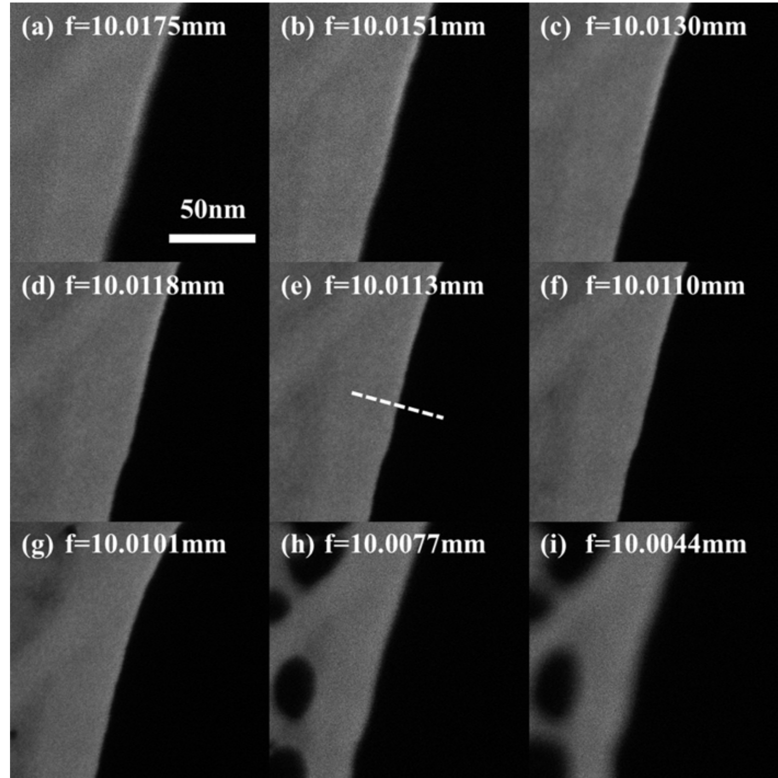

FIGURE 4.7: 35 keV HIM images of a high contrast graphene edge. (a) to (i) show that as f (the 'working distance' read from the microscope) decreases, the observed graphene edge changes from noticeably blurred to sharp, then becoming blurred again.

the in-focus state (Figure 4.7 (b) to (d)) and became blurred again when the image was in an under-focused state (Figure 4.7 (f) to (i)).

The beam probe size can be evaluated from the line intensity profile across the high contrast graphene edge. Taking Figure 4.7 (e) as an example: the white dashed line across the edge corresponds to the rapid intensity decrease shown in Figure 4.8 (a). Probe size is defined as the distance between 25% and 75% of the SE intensity near the edge, extracted using *Image J* software [8]. It gives a probe size of 0.9 ± 0.1 nm. The focusing deviation (Δf) is defined as the difference in "working distance" (read from the microscope) between the present image and the in-focus image. The relationship between beam probe size and Δf can be evaluated by plotting their correlation, as shown in Figure 4.8 (b).

The same process was performed for the SEM images for measuring the optimized probe size at different e-beam energies. The correlation between the electron

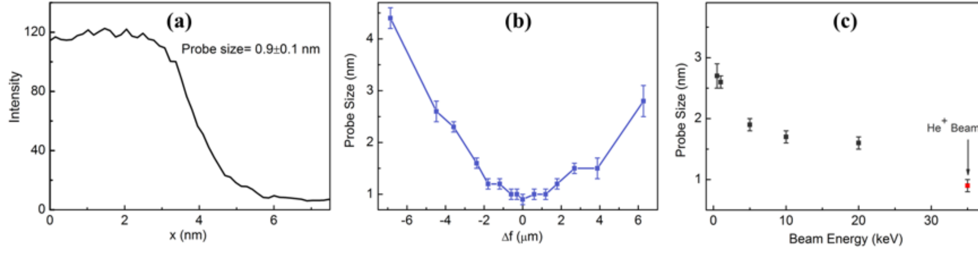

FIGURE 4.8: (a) Intensity profile of the dashed line in Figure 4.7 (e) that comes across the graphene edge. An optimized probe size of 0.9 ± 0.1 nm can be extracted from the profile. (b) The evolution of beam probe size with the change of Δf. (c) The relationship of beam probe size with the beam energy.

probe size and the beam energy is shown in Figure 4.8 (c). The electron probe size monotonously decreases from 2.7 ± 0.2 nm to 1.6 ± 0.1 nm as the e-beam energy increases, from 0.5 keV to 20 keV. The smallest e-beam probe is almost twice as large as the He^+ probe (0.9 ± 0.1 nm).

4.3.2 SE contrast analysis

Topographical contrast due to substrate roughness (< 0.1 nm) in the SE imaging can be neglected. The material contrast as well as the crystal orientation effect (channelling effect) are also negligible in these investigations, as the composition of the Si wafer is uniform and exhibits single-crystal nature.

The SE contrast as well as the effect of beam-induced contamination on SE imaging was evaluated by determining the contrast of regions of interest. The relative contrast between the contaminated regions and the substrate is defined by Equation 4.1.

$$R_C = \left(\frac{I_B}{I_C} - 1\right) \times 100\% \tag{4.1}$$

where R_C is the relative contrast, I_B is the average intensity of the background Si and I_C is the average intensity for the contaminated region.

For accurate contrast measurements, high-resolution SE images of the contamination regions were gathered under 5 keV e-beam energy and in-lens mode in a Carl-Zeiss Ultra, SEM. The images were subsequently analysed with image processing software, *Image J*. The average values for the mean pixel intensity for the I_C and I_B were thus measured and the relative contrast values were calculated.

Subsequently, values for contrast were plotted with mean contamination heights against the irradiation dose to check its effect on contamination formation by electron and He^+ion irradiation.

4.3.3 Collection of SE image and spectrum from graphene samples

SE images of few-layer graphene were obtained in SEM (Carl Zeiss Supra and FEI Strata DB235) and HIM (Carl Zeiss Orion Plus). SEM images were acquired using an electron beam energy range of 0.5 keV to 20 keV. A small aperture (10 μm) was used to minimise irradiation damage [173]. The beam current varied from 5 pA to 20 pA over the employed beam energy range. The irradiation dose of each scan varied from $\sim 3\times 10^{13}$ to $\sim 1.2\times 10^{14}$ $e^- \cdot cm^{-2}$. Graphene emitted SEs were collected by an in-lens detector. This collection method was used to minimise the influence of back-scattered electrons and chamber generated SEs, in the acquired images and spectra. All collection parameters were kept constant during the experiment (working distance: 4 mm; magnification: 2500×; resolution: 1024×768 pixel; scanning time: 26 s) and base chamber vacuum was recorded at $\sim 2\times 10^{-5}$ mBar.

In HIM the beam energy was kept constant at 30 keV for image acquisition. The working distance was fixed to 10 mm and the field of view to 80 μm. An Everhart-Thornley detector collected graphene SEs, along with a negligible amount of back-scattered ions. A 1 pA beam current was used for imaging. This delivered an irradiation dose of $\sim 5 \times 10^{11}$ ions/cm^2 per scan, thus minimising the amount of scan induced defects [8]. When imaging graphene on an SiO_2/Si substrate the instruments electron flood gun was activated. Using flood energy of 500 eV and a flood time of 10 μs, the positive charges introduced by He^+ ion irradiation were neutralised. Base chamber vacuum was recorded at $\sim 2\times 10^{-5}$ mBar.

Measurement of graphene SE energy spectra, in SEM and HIM, was carried out using a home-built energy filter. A TEM grid - with periodic holes of ~ 0.2 mm^2 in area - was placed above the graphene sample. The spacing between graphene and the top of grid was maintained at ~ 1 mm. With the graphene sample connected to ground, a negative voltage of 0 V to -10 V was placed on the grid using a voltage source meter. SEs with an energy lower than the grid potential were prevented

from reaching the detector during image acquisition and were thus filtered out. By differentiating the measured grid voltage – SE intensity curve, an SE spectrum was obtained.

4.3.4 Evaluation of graphene SE yield

A simple method was used to evaluate the SE yield of freestanding graphene. Figure 4.9 (a) shows a SEM image of monolayer graphene on an etched Si substrate (etched holes: diameter ~2 μm, depth > 10 μm). Some of the holes were covered by the freestanding graphene, i.e. the hole on the left of the image. An uncovered hole is treated as an ideal Faraday cup. Due to its large depth few SEs and BSEs can escape when irradiated, thus enabling the measurement of primary beam current. The current measured on irradiation of freestanding graphene is smaller than the primary beam current. This is due to the generation of SEs and BSEs during the beam-graphene interaction (Figure 4.9 (b)). As a result, the total electron emission yield σ_g of freestanding graphene - which contains contributions from both SE emission (δ_g) and BSE emission (η_g) - can be obtained and is given by:

$$\sigma_g = \delta_g + \eta_g = 1 - \frac{i_g}{i_p} \tag{4.2}$$

The casino simulation presented in Figure 4.9 (c) shows BSE yield for freestanding graphene irradiated with a primary electron beam energy of 0.2 to 20 keV. Electron beam energies higher than 1 keV show a low yield of < 0.5 %, which as a result can be ignored. The extracted SE yield, shown as the red squares in Figure 4.9 (d), has a high value (~120%) for a low e-beam energy of 0.2 keV. With the increase in beam energy SE yield decreases becoming < 10 % above 5 keV. At 5 keV the SE yield of SiO_2 is ~1 [174], therefore the SEs which are generated in an SiO_2 substrate diffuse into graphene and dominate the SE emission from supported specimens.

For the HIM irradiation process, the back-scattered ion coefficient can be calculated by the stopping and range of ions in matter (SRIM) simulation. This shows a much smaller value (10^{-5} at 30 keV He^+ ion beam energy) and can also be ignored. Therefore the total yield measured can be regarded as the SE yield. Shown

as the blue circles in Figure 4.9 (d), the SE yield in HIM is much higher than that generated in SEM and slightly increases with the increase of He^+ ion beam energy.

For the SE yields of the freestanding graphene and the substrate which are used in Equation 5.6 in the layer depencence of graphene SE contrast and work function extraction, Chapter 5.4.3, we simply measured their grey values in the SE images obtained under the same imaging conditions (working distance of 4 mm, brightness and contrast of in-lens detector settings were 50% and 38% respectively). Their ratio is the value of $\frac{\delta_g(E_p)}{\delta_s(E_p)}$ and is used to calculate SE contrast.

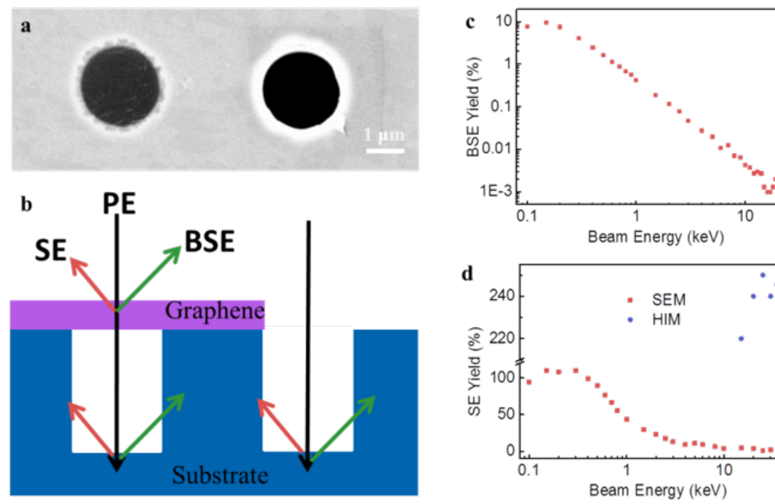

FIGURE 4.9: **a**, A 5 keV SEM image shows the existence of a hole and free-standing graphene. **b**, Diagram of graphene yield measurement. **c**, BSE yield of free-standing monolayer graphene calculated by casino simulation. **d**, SE yield of a monolayer graphene in both SEM and HIM measurements.

4.3.5 Statistics of graphene SE contrast

SE contrast of graphene was investigated in different microscopes. These included a Carl Zeiss Ultra SEM with the in-lens detector, an FEI Strata DB235 SEM with a through-the-lens (TLD) detector (similar to the in-lens detector), and a Carl Zeiss Orion Plus HIM.

The majority of the statistical contrast experiments were conduced using the Carl Zeiss Ultra SEM, operated at 5 keV primary beam energy and a4 mm WD. 158 graphene samples were measured in total. The measured samples included 60

monolayer, 62 bilayer, 22 trilayer and 14 quad-layer flakes. The distributions of the corresponding SE contrast are shown in Figure 4.10. The SE contrast of each graphene layer obeys a Gaussian distribution, indicating that each n-layer graphene will have a certain contrast value.

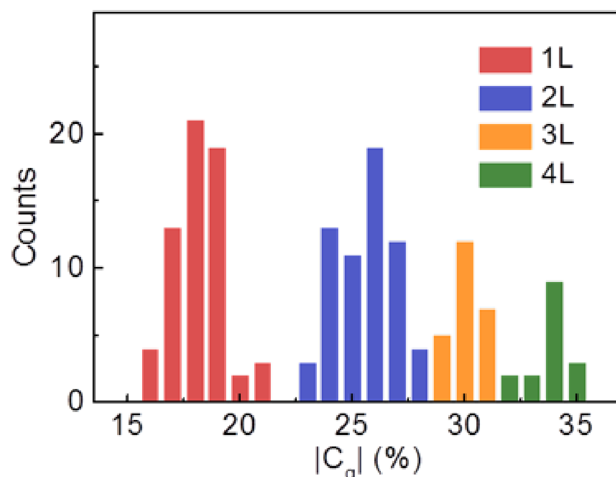

FIGURE 4.10: All the samples were imaged under the irradiation of a 5 keV electron beam. 60 monolayer, 62 bilayer, 22 trilayer and 14 quad-layer graphene samples were measured.

Also measured were eight of these samples in another SEM (FEI Strata D235). The imaging parameters, such as beam energy, working distance, etc., were kept the same. The results, shown in Table 4.5, reveal that the two different microscopes gave similar SE contrast for the same samples.

The statistical result of graphene contrast in HIM is shown in Table 4.6. 10 individual graphene samples were measured in total. These included six monolayer, two bilayer and three trilayer flakes. The imaging parameters selected were, 30 keV primary beam energy, 500 eV flood energy and 50 μs flood time (to generate a charge neutralized surface). The average contrast for the three different graphene layers are $\sim$0.17, $\sim$0.13 and $\sim$0.09 respectively. Therefore the same graphene layer thickness also reflects the same charge neutralized SE intensity in HIM.

Sample	Layer	SEM Contrast (Supra)	SEM Contrast (Strata)
1	2	0.27	0.25
2	1	0.19	0.19
3	2	0.26	0.24
4	2	0.27	0.23
5	1	0.19	0.17
6	1	0.19	0.17
7	3	0.35	0.29
8	4	0.35	0.30

Table 4.5: Contrast measurement of the same graphene flakes in two different SEMs (Carl Zeiss Ultra and FEI Strata DB 235).

Sample	Layer	HIM Contrast
1	1	0.16
2	1	0.17
3	1	0.18
4	1	0.15
5	1	0.16
6	1	0.18
7	2	0.13
8	2	0.13
9	3	0.10
10	3	0.08

Table 4.6: Contrast measurement of graphene flakes in HIM.

4.4 Raman investigation of carbonaceous contamination

4.4.1 Raman mapping

The optical properties of the carbon layers were characterised by Raman mapping spectroscopy. From this analysis, the Raman enhancing properties of the carbon layers as a function of carbon volume and carbon I_D/I_G ratio, could be determined.

The instrument used for the mapping experiments was a Witec Alpha 300R, confocal micro-Raman imaging instrument. It is based on 180° Raman scattering i.e. the excitation and the backscattered light is delivered and collected though a single lens. The scattered light is first passed through a notch filter, to remove

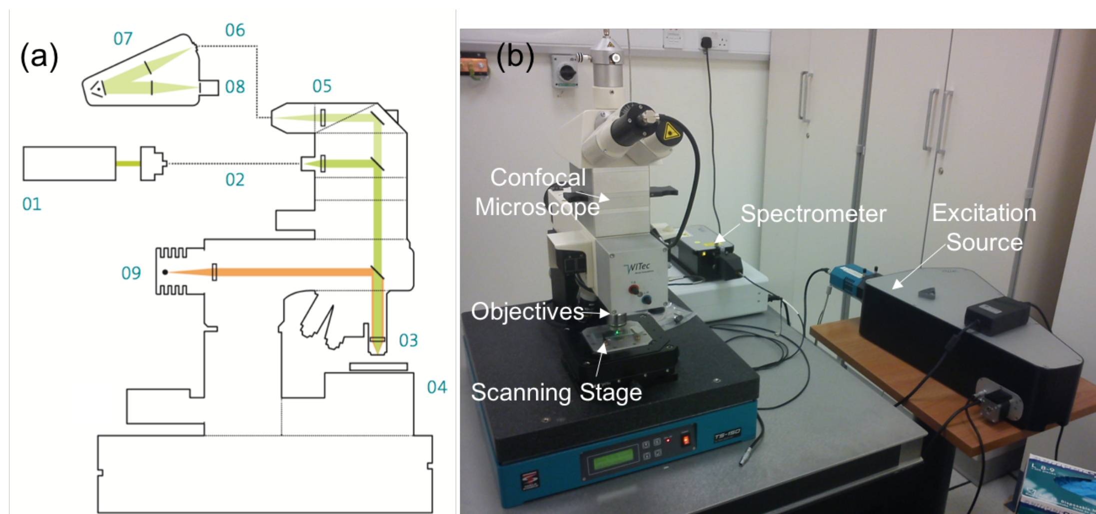

FIGURE 4.11: (a) A schematic overview of the Witec Alpha 300R Raman mapping instrument consisting of (1) excitation laser, (2) optical fibre, (3) microscope objectives, (4) scanning specimen stage, (5) notch fliter, (6) photonic fibre, (7) diffraction grating & spectrometer, (8) CCD camera, (9) white-light illumination source (*Courtesy of Witec Instruments*). (b) The Raman mapping instrument in operation at the *Architecture and Synthesis of Integrated Nanostructures* (ASIN) laboratory at Trinity College Dublin.

the Rayleigh portion. From there it enters a spectrometer and is separated into its individually scattered wavelength components, before being focused on to an ultra-fast CCD detector with integration times as low as 0.76 ms per spectrum.

For the Raman mapping analysis, Ar and HeNe lasers with excitation energies of 532.1 nm and 633.0 nm were used. The output power of each laser was ~3 mW, 10% of which was delivered to the specimen (300 μW). An 100X objective lens gave a laser probe of 300 nm and a diffraction grating of 600 lines/mm established a energy resolution of ~3 cm^{-1}. The scanning stage was piezo-driven and had a step resolution of 250 nm in the X and Y directions.

The mapping of the carbon layers was first conducted with 532 nm laser excitation, and implemented as follows. Firstly, the power of the laser delivered to the specimen was checked with a hand-held laser meter (measuring 300 μW). The Si specimen was then mounted on a standard glass slide and placed on the instrument stage. Using a low magnification objective, 20 X, the deposited region of the specimen was brought into the FOV. The microscope magnification was set to 100 X, the layers centred and brought into focus. A 35 μm x 35 μm frame was then drawn around the 1 – 5 keV layers and a sequential Raman map initiated. The

mapping frame consisted of 140 lines and in each line there were 140 points. At each point a Raman spectrum, with integration time of $\sim$ 125 ms, was acquired. On completion of the map a total of 19,600 Raman spectra were collected and compiled into a single data file. From this file, images of the specimen surface, with respect to the intensity of a particular Raman shift, were generated. From these images, point specific Raman spectra were extracted for correlative AFM-Raman analysis. This process was then repeated for the 12 - 30 keV carbon layers.

To compare the Raman enhancing properties of the carbon layers with respect to excitation energy, a second mapping experiment was carried out using 633 nm excitation. The mapping experiment was carried out in exactly the same manner as the 532 nm experiment however the integration time at each point was reduced by $\sim$ 50% ($\sim$ 74 ms). The decision to reduce the scan time was taken in order to over come suspected issues with CCD detector saturation observed during the analysis of the 532 nm results. The cause of the suspected saturation issue was later discovered and was not related to the integration time. By the time this discovery was made, these layers were destroyed in order to produce TEM lamella for EDX and EELS analysis, so the experiment could not be re-run with the same integration time as the initial 532 nm excitation.

4.4.2 Correlative Raman-AFM analysis

In order to quantify the Raman enhancing properties of the carbon layers generated at a single beam energy, a relationship between carbon volume, carbon I_D/I_G ratio, and the characteristic Si Raman peak intensity was required. Once established, the enhancing properties of carbon layers generated at multiple beam energies could be compared.

To determine the relationship between Si Raman peak intensity and the I_D/I_G ratio from layers generated at a single beam energy, the extraction of Si and carbon Raman spectral data from locations of known carbon volume was first required. Figure 4.12 shows Raman mapping images displaying variations in the intensity of the carbon Raman band (1100 - 1800 cm^{-1}), generated from the 3 keV - 5 nC$\cdot\mu$m^{-2} carbon layer. In Figure 4.12 (a), maximum image intensity has been adjusted so that distinctive points of carbon Raman intensity on the left edge of the layer are revealed, and in Figure 4.12 (b), maximum image intensity has been

adjusted to reveal distinctive points of carbon Raman intensity on the right edge of the layer. A total of 14 distinct points have been identified on each edge. At these distinctive points a Raman spectra is generated by averaging all of the Raman data present within a 2 × 2 pixel area. Each pixel in the image corresponds to a specimen surface area of 0.0625 μm^2, thus the area corresponding to each averaged spectrum is 0.25 μm^2. The deposited volume at each distinctive point on the layer edges is the spectral area times the carbon thickness. The height profiles of the left and right edge of the 3 keV - 5 nC·μm^{-2} carbon layer are displayed in Figure 4.12 (c) and (d), respectively. They were extracted from the AFM height profile of the layer, which was referenced to the clean Si surface. The carbon thickness values for the 14 distinct points identified on each edge were picked out manually from their corresponding height profiles. Examples of this manual correlation are given by the arrows labelled as 1, 7, 8 and 14 in each plot and correspond to the same points identified in each of the Raman maps. The scale in the Raman intensity images and the AFM plots assists in the manual correlation process.

Two other carbon layers were generated at 3 keV electron beam energy, at applied doses of 1 nC·μm^{-2} and 3 nC·μm^{-2} . The 1 nC·μm^{-2} layer was not thick enough to produce distinctive points of carbon Raman intensity, however the 3 nC·μm^{-2} layer produced nine distinct points from each of its edges. From these points averaged Raman spectra were extracted and were correlated to their corresponding edge heights. The carbon Raman maps of the 3 keV - 3 nC·μm^{-2} layer and its edge thickness profiles can be seen in Figure 4.13.

A total of 46 distinct correlative points were identified from the carbon layers generated at 3 keV. These ranged in thickness from 48 – 190 nm, (or a volume of 0.012 – 0.049 μm^3). The Raman spectra corresponding to each point were analysed twice. The first time was to extract the intensity of the characteristic Si peak and the second time to extract the carbon I_D/I_G ratio.

This manual AFM-Raman correlation process was repeated for carbon layers generated at 1, 5, 12, 20 and 30 keV. Due to the lack of distinct points of correlative analysis, the 1 nC·μm^{-2} layer at each beam energy was not used. The 3 nC·μm^{-2} and 5 nC·μm^{-2} layers at each energy produced an average of 40 correlative points at each beam energy.

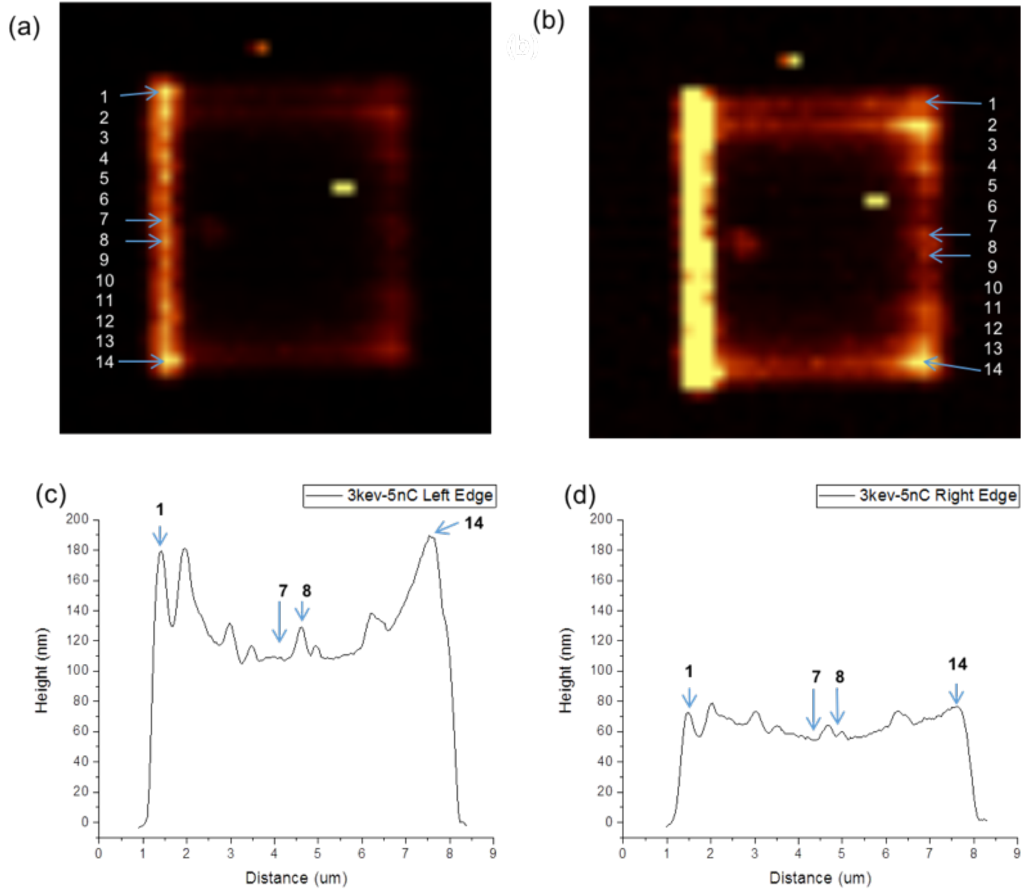

FIGURE 4.12: Raman mapping images displaying the intensity of the carbon Raman band (1100 - 1800 cm^{-1}) present in the 3 keV 5 nC$\cdot\mu$m^{-2} carbon layer. In (a), image intensity has been adjusted so distinctive points of carbon Raman intensity are revealed on the left edge of the layer, and in (b), image intensity has been adjusted so distinctive points of carbon Raman intensity are revealed on the right edge of the layer. The height profiles of the left and right edges of the layer are displayed in (c) and (d), respectively. Carbon thickness values for distinct points of Raman intensity were picked out manually from their corresponding height profiles. Examples of the Raman-AFM correlation are given by the arrows labelled as 1, 7, 8 and 14 in each plot and correspond to the same points identified in each of the Raman maps.

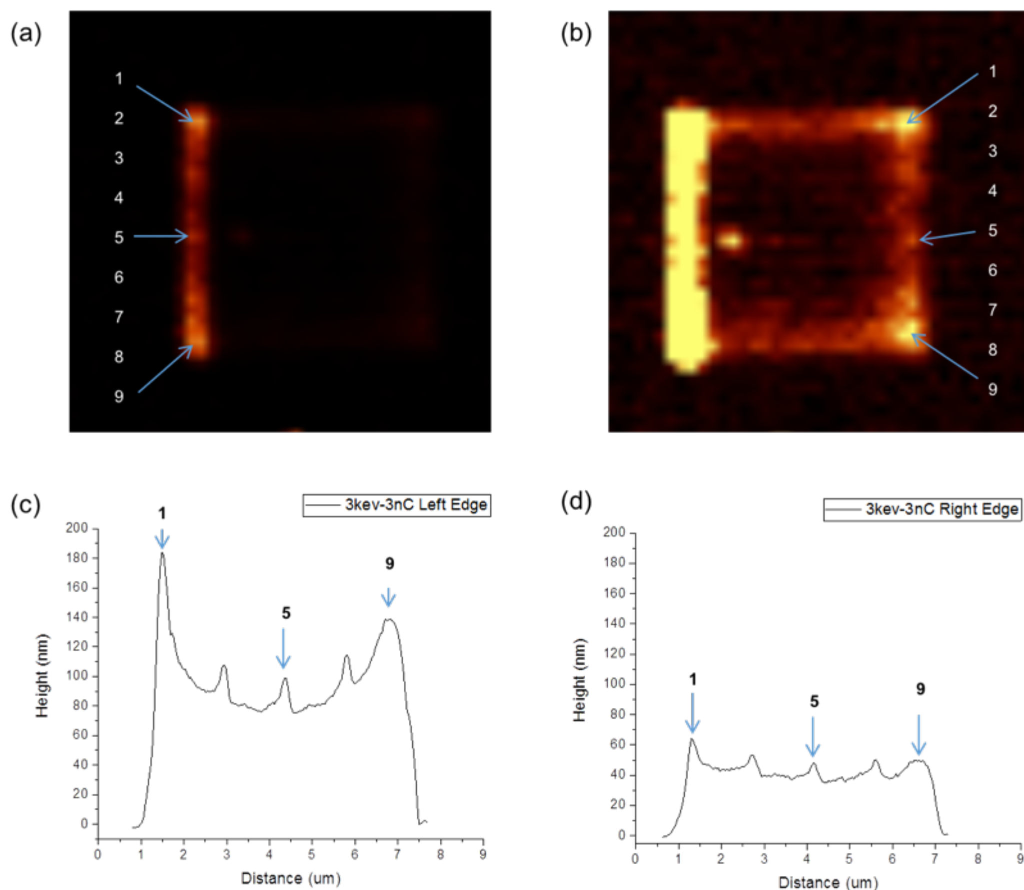

FIGURE 4.13: Raman mapping images displaying the intensity of the carbon Raman band (1100 - 1800 cm^{-1}) present in the 3 keV - 3 $nC{\cdot}\mu m^{-2}$ carbon layer. In (a), image intensity has been adjusted so distinctive points of carbon Raman intensity are revealed on the left edge of the layer, and in (b), image intensity has been adjusted so distinctive points of carbon Raman intensity are revealed on the right edge of the layer. The height profiles of the left and right edges of the layer are displayed in (c) and (d), respectively. Carbon thickness values for distinct points of Raman intensity were picked out manually from their corresponding height profiles. Examples of the Raman-AFM correlation are given by the arrows labelled as 1, 5 and 9 in each plot and correspond to the same points identified in each of the Raman maps.

Chapter 5

A comparative study: contamination formation, imaging and SE spectroscopy in SEM and HIM

Presented in this chapter are the results of a comparative study on the mechanisms of contamination formation, SE imaging and SE spectroscopy in HIM and SEM. For contamination formation, deposited structures were formed on Si specimens and characterised by AFM and EDX. Their effect on SE image contrast was evaluated. For the SE comparison study, firstly, the SE contrast of Ga^{+} implanted regions in an n-type silicon specimen was analysed. The effects of implantation dose and imaging parameters on image contrast were investigated. These revealed a similar relationship between image contrast, Ga^{+} density and imaging parameters for both the HIM *Everheart-Thornley* (ET) and SEM Inlens detectors. Dynamic charging effects were also shown to have a significant impact on the quantification of the HIM and SEM SE contrast. Secondly, we demonstrate that SE imaging can provide sub-nanometer information of a graphene surface and reveal the morphology of surface contaminants. In doing so a quantitative approach to readily obtain the physical size of the surface features was attained. Thirdly, SE imaging has been used in the development of a quantitative technique for effective extraction of graphene work function and layer identification. The measurement of few-layer graphene flakes shows the variation of work function between graphene layers with a precision of < 10 meV enabling the identification of up to ten layers from SE contrast. The final section of the chapter details the results on the implementation of an SE energy filter. Developed for use in both the SEM and HIM, it was quantified in terms SE filtering efficiency (eV) and used for the acquisition of energy filtered SE images and the generation of SE energy spectra of graphene and HOPG.

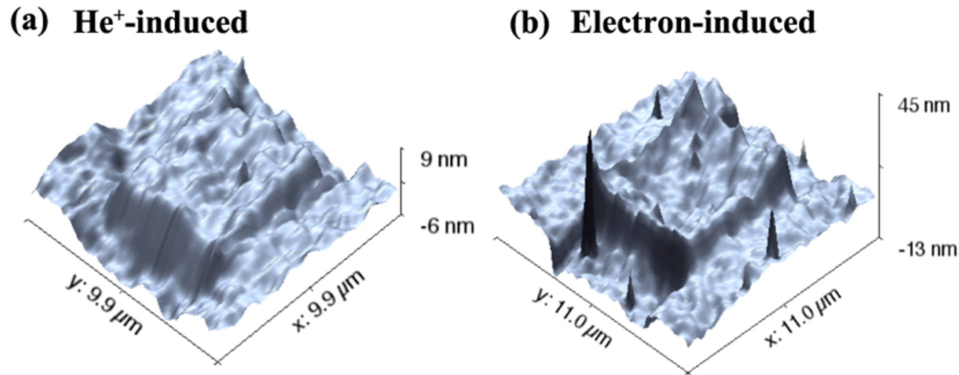

FIGURE 5.1: (a) A three-dimensional AFM height profile of the contamination layer generated by 30 keV He^+ ion irradiation, and an applied dose of 89.6 pC·μm^{-2} (8 pA beam current). Average layer height is 5 nm. (b) A three-dimensional height profile of the contamination deposit generated by 1 keV electron irradiation, and applied dose of 1004.8 pC·μm^{-2} (80 pA beam current). Average layer height is 7 nm.

5.1 Contamination formation in HIM and SEM

5.1.1 Morphology of Contamination

In order to determine the effect of He^+-induced contamination on the intensity of the SE signal, the relationship between applied dose and the resultant contamination layer thickness on an un-cleaned Si 100 substrate was first investigated. The Si substrates were first irradiated with a series of predetermined doses; the morphology of deposited contamination films was measured by AFM, followed by high resolution SEM imaging to determine changes in SE intensity. A comparative experiment for electron beam-induced contamination was run in parallel.

Figure 5.1 (a) and (b) are AFM images of the HIM and SEM contaminated regions respectively, showing their topological information. The electron dose is about 10 times as large as the helium-ion dose and the electron beam current is about 10 times as large as that of the helium ion. Average layer thickness for the SEM induced contamination layer is ∼1.5 times greater than that of the HIM induced contamination layer. The edges of the SEM contaminated region exhibit significant wall-like feature, while this is not evident in the HIM-induced region where the

contaminated region looks like a plateau. As discussed in section 2.2, this can be attributed to the large $j' = (\sigma\tau_0 j)/e$ in the SEM case.

SEM images of the contamination built in the HIM and SEM are shown in Figure 5.2 (a) and (b) respectively. The regions of electron-induced contamination are all darker than the uncontaminated silicon substrate. Most of the He^+ ion induced contaminated regions are also darker than the substrate, but two regions appear brighter, as indicated by the arrows in Figure 5.2 (a). The SEM contrast and the height of the HIM and SEM contaminated regions are plotted against the beam dose in Figure 5.2 (c) and (d) respectively. It can be seen that an electron dose of 157 pC·μm^{-2} ($\sim$ 20 scans) produced a thin layer of contamination ($\sim$ 1 nm) in the SEM, which was efficient in altering the SE emission and resulted in observable variation in the SE contrast. The contamination height is also shown to have grown almost linearly with electron dose. Also the contrast is observed to saturate at the higher doses ($>$ 500 pC·μm^{-2}) as SEs from the underlying Si wafer cannot be seen by the detector, due to the attenuation of the contamination layer with a thickness of 2 nm. Since the mean free path of typical SEs ($\leq$ 50 eV) is about 10 nm and a contrast saturation should appear at a thickness $>$ 10 nm.

In HIM, the contrast and the height do not seem to depend on the dose monotonically. The height of the He^+ induced contamination increased with dose initially, then dropped at 60 scans (42 pC·μm^{-2}) – potentially due to sputtering – and increased again at 130 scans (91 pC·μm^{-2}). The final increase may be due to the topographical modification induced by excessive He^+ ion injection and the swelling of the substrate. This might be due to the sputtering of previously formed contamination and substrate swelling of which both are induced by the heavier helium ions. It may also be due to the fact that the HIM chamber is cleaner and the supply of the hydrocarbon molecules is the limiting parameter for the formation of the contamination, i.e. the hydrocarbon molecules are depleted at the lowest dose applied. This can also explain the sputtering of the grown contamination layer surpassed the contamination formation at a dose higher than 25 pC·μm^{-2} . It indicates that the HIM imaging may self-clean the carbon contaminants due to the ion sputtering when the supply of the hydrocarbon molecules limits the contamination formation. As shown in Figure 5.2 (c), for low doses ($<$ 50 pC·μm^{-2}) the variation of the contamination height correlates to the change in its SE contrast.

To produce an equivalent SE yield, the applied He^+ dose was set to one tenth that of the electron dose. In Figure 5.2 (c) and (d) it can be seen that the average

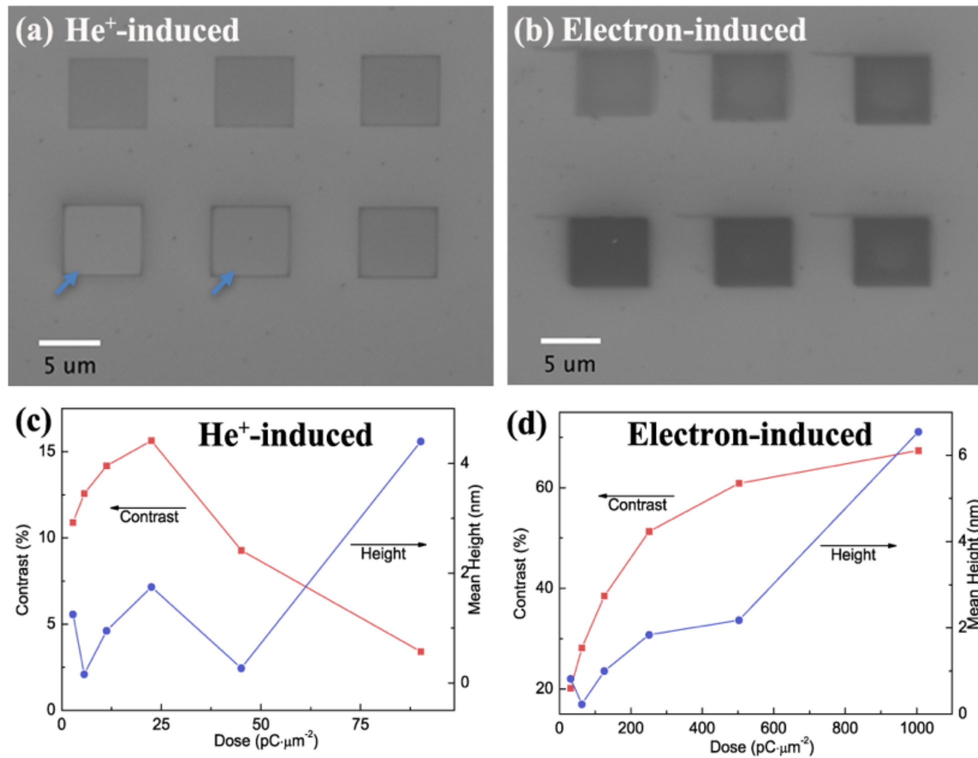

FIGURE 5.2: (a) 5 keV SEM image showing the contamination formed by He^+ ion irradiation (Beam energy 30 keV; Pixel spacing: 12nm; Dwell time: 10 μs). The squares with differing contrast show the existence of contaminants. The doses used for contamination generation increase from 2.8 pC·μm^{-2} to 89.6 pC·μm^{-2} when viewed clockwise from top left to bottom left. (b) 5 keV SEM image showing the contamination formed by electron irradiation (Beam energy 1 keV; Pixel spacing: 12nm; Dwell time: 11 μs). The irradiation doses increase from 31.4 pC·μm^{-2} to 1004.8 pC·μm^{-2} , also when viewed clockwise from top left to bottom left. (c) The contrast (red line) and average height (blue line) profiles of the six contaminated areas as function of He^+ ion dose. (d) The contrast (red line) and average height (blue line) profiles of the six contaminated areas as a function of electron dose.

height of the contamination layers grown up to doses of ~25 pC·μm^{-2} in HIM and ~250 pC·μm^{-2} in SEM, show similar values. SE yield is therefore a significant contributory factor in contamination formation process. As contamination formation in HIM is hydrocarbon limited, quantitative correlation between the beam dose, SE yield and the contamination profile needs further investigation.

5.1.2 The effect of sample treatment

The influence of specimen surface conditions on contamination formation was assessed by creating contamination profiles on the *Isopropyl Alcohol* (IPA)-treated specimens prior to the irradiation. In this experiment, we chose low doses to avoid the sputtering in HIM (< 45 pC$\cdot\mu m^{-2}$) and the saturation in SEM (< 500 pC$\cdot\mu m^{-2}$).

Figure 5.3 (a) and (b) show the SE contrast (observed in SEM) of the contamination layers as a function of the helium-ion dose and the electron dose respectively. For the helium-ion induced contamination, the SE contrast of the IPA cleaned and bare samples both positively correlates with the beam dose, indicating the increase in the contamination volume due to the increase of the dose. For a given He^+ dose, a significant reduction in the contamination contrast was observed for the IPA treated samples compared with the bare ones, which suggests a lower amount of contamination being built on the IPA sample. This indicates that the HIM chamber is quite clean and the supply of the hydrocarbon molecules is mainly due to the adsorbed molecules on the sample surface prior to the helium-ion irradiation. The IPA treatment removed some of the adsorbates and thus further reduced the hydrocarbon supply. Both samples exhibit the saturation, i.e. the contrast only weakly increases as the dose increases. The contrast saturation appears at a lower dose for the IPA sample, which matches a reduced supply of hydrocarbons and a cleaner surface.

The IPA (and other organic solvents) treatment has little effect on the contamination formation in the electron-beam irradiation. As shown in Figure 5.3 (b), for each dose, all the samples exhibit similar contrast level and hence the same contrast-dose relationship. This indicates that the SEM environment dominates the supply of the hydrocarbons and the limiting parameter for the contamination formation is the dose.

5.1.3 Composition of contamination

The composition of these contamination layers was determined by EDX. Typical EDX spectra (carbon, oxygen and silicon K_α lines) are shown in Figure 5.4 (a).

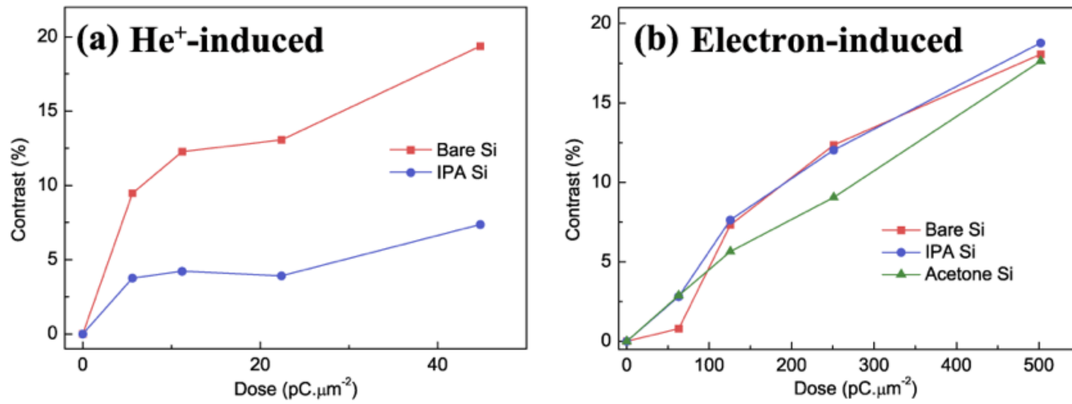

FIGURE 5.3: SEM SE contrast of samples undergone chemical cleaning treatment prior to the beam irradiation: (a) He^+-induced contamination and (b) electron-induced contamination

The variation of the intensity of the silicon peaks across these samples is negligible. This is because the contamination layer has little effect on the electron-silicon interaction volume (see the Monte Carlo simulation in Figure 5.4 (c) and (d)), which in turn generates the same amount of characteristic silicon X-ray photons. We use the silicon intensity as a reference to evaluate the change in C and O integrated intensities (I_C and I_O) which reflect the amount of corresponding elements presents within the analysed volume.

The ratios (e.g. I_C/I_{Si}) are plotted as a function of the dose in Figure 5.4 (b). It is evident that for the electron-induced contamination the carbon content increases almost linearly with the electron dose. The oxygen content of the electron-induced contamination increases slightly at low dose (< 100 pC$\cdot \mu m^{-2}$) and then saturates. This suggests the electron-induced carbon polymer contains negligible amount of oxygen. The carbon content of the He^+-induced contamination first increases with the increase of the He^+ dose and then drops at the highest dose (~ 90 pC$\cdot \mu m^{-2}$). It corroborates the AFM results that the high He^+ dose can indeed sputter away the grown carbon contamination. The oxygen content of the He^+-induced contamination keeps constant for all the He^+ doses attempted, regardless of the detectable change in the carbon content. This needs further investigation, but it may indicate that the He^+-induced contamination contains more oxygen than that of electron-beam induced contamination.

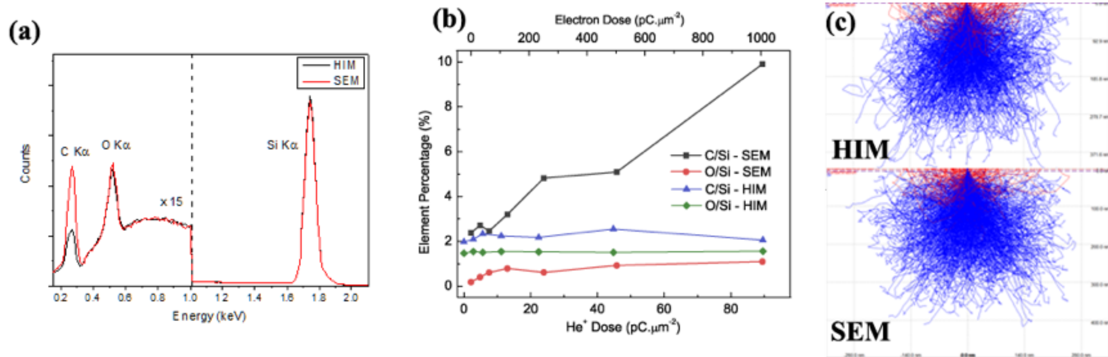

FIGURE 5.4: Typical EDX spectra collected from beam-induced regions; (b) The carbon and oxygen content in the analysed volume as a function of beam dose; (c) and (d) are Monte Carlo simulations of the electron-sample interaction for EDX detection.

5.1.4 Summary of contaminaiton formation in HIM and SEM

The formation and effect of He^+ beam-induced contamination in a HIM has been assessed in relation to specimen properties and beam parameters. The pre-exposed environments determine the level of hydrocarbons on the specimen surface. The 'cleaned' specimens showed a higher SE intensity with an approximate difference of ∼250% from the "un-cleaned" specimens. The correlation between the beam dose and the contamination profile has been investigated. When the He^+ dose increased from 0.7 to 22.4 pC·μm^{-2} , a decrease in the SE signal and an increase in the contamination height profile was observed. As the dose exceeded 22.4 pC·μm^{-2} the height of the contamination first dropped off and then increased again. The SE intensity from the most irradiated region is observed to have abnormally increased.

For SEM, beam conditions were selected as to generate an approximately equal number of SEs for inducing the contamination profiles. The observed SE intensities from electron-induced contamination profiles decreased with the increase of electron dose, accompanied by an increase in the average height of the profile. SE intensity is also saturated at higher doses. Unlike HIM, specimen cleaning did not significantly affect the contamination formation in SEM. The specimens in the HIM are also not subjected to the same level of additional hydrocarbon absorption as in the SEM, due to its design (a load port which keeps the chamber at a constant optimum vacuum). The drop and subsequent rise in measured height of

the HIM contamination profiles can be explained in terms of ion sputtering and implantation respectively. Substrate swelling in Si is known to occur at this highest dose regime and the observed increase in SE intensity confirms that it is not a contamination profile [175]. It is also worth noting that in the low dose regimes ($\leq$ 22.4 pC$\cdot\mu$m^{-2} in HIM and $\leq$ 250 pC$\cdot\mu$m^{-2} in SEM), the average height of the contamination layers formed in both microscopes show similar values. This similarity is most likely due to the generation of an equivalent number SEs in the presence of adequate hydrocarbon concentrations. A further investigation however on the correlation between the beam dose, SE yield and the contamination profile is required to clarify the characteristics of the He^+ ion irradiation.

5.2 SE imaging in SEM and HIM: Imaging modes

In this section, we compare images of Ga-implanted Si samples taken with different HIM and SEM imaging modes and investigate the effects of imaging parameters (beam energy, dwell time, etc.) on the image contrast.

5.2.1 Sample preparation and imaging modes

The samples used for imaging are Ga-implanted silicon prepared via FIB irradiation of a 110 n-doped silicon substrate. The implantation was conducted using a Zeiss-Auriga FIB at a beam energy of 30 kV and a beam current of 50 pA. Nine regions (20 $\times$ 20 μm^2) of the Si surface were irradiated by the Ga^+ beam for a set length of doping time (from 30s to 270s), corresponding to a range of implantation doses (2.34 $\times$ 10^{15} ions/cm^2 to 2.11 $\times$ 10^{16} ions/cm^2). An AFM (Asylum Research MFP-3D^{TM}) was employed to characterise the surface morphology of the implanted regions. The Ga concentration was measured using an EDX spectrometer in a Carl Zeiss-Ultra Plus SEM with a 20 keV electron beam. Raman spectroscopy was carried out at atmospheric pressure with a Renishaw spectrometer equipped with a 488 nm laser and 2400 lines/mm grating. A 100 $\times$ objective lens was used. The laser spot size was $\sim$ 1 μm. Acquisition time was fixed at 1s with 10 accumulations.

HIM images of the implanted regions were recorded using a *Micro-Channel Plate* (MCP) detector and an ET detector respectively in a Carl Zeiss Orion Plus at 30

keV. SEM images used for comparison were collected by using multiple detectors (e.g. the ET detector, the *Energy Selective Backscattered* (EsB) detector and the In-Lens detector) equipped with a Carl Zeiss-Ultra Plus SEM working at an acceleration voltage ranging from 0.5 – 5 kV. The sample was cleaned for 10 min using a O_2:Ar (1:3) plasma in a Fischione Instruments 1020 plasma cleaner at a chamber pressure of 5 mbar before insertion into the SEM or HIM chamber.

The *Stopping Range of Ions in Matter* (SRIM) software package [64] was used to simulate He^+ and Ga^+ ion interaction with the silicon substrate, to generate output plots for ion range (ion depth of penetration into target materials) and straggle (variance of the ion range within target material). The software also tracks ion implantation and material displacement during imaging with ions. CASINO V2.42 software [176] was used for the simulation of the electron interaction.

5.2.2 General morphology of the Si sample

FIB implantation results in Ga implantation as well as sample sputtering and damage [177]. Figure 5.5 (a) shows the height and *root mean square* (RMS) roughness of the implanted regions (extracted from the AFM height map) as a function of the doping time. The height of the implanted region decreases almost linearly in the doping time. For the largest dose used, the depth of the pit is 52 nm. The RMS roughness of the implanted regions is close to that of the untreated Si surface (~ 0.15 nm) at low doses ($\sim 10^{15}$ ions/cm^2) and increases to 1.7 nm for the large doses. Figure 5.1 (b) depicts the dependence of the average intensity of Ga K_α signal in the EDX mapping (the inset image) on the doping time. It is evident that the Ga content in the sample increases linearly with increase in the implantation time, which is consistent with previous reports [178]. The mean projected range of 30 kV Ga^+ ions in Si, R_p, is 27.8 nm given by the Monte Carlo simulation. Assuming all the ions are retained in the substrate, the peak atomic density of Ga at R_p is,

$$N(\phi_i) = \frac{0.4\phi_i}{\Delta R_p} \tag{5.1}$$

where $\Delta R_p = 10.3$ nm is the straggle and ϕ_i is the dose. The Ga atomic density of the 30s-implanted region is 9.09×10^{10}, corresponding to an atomic concentration

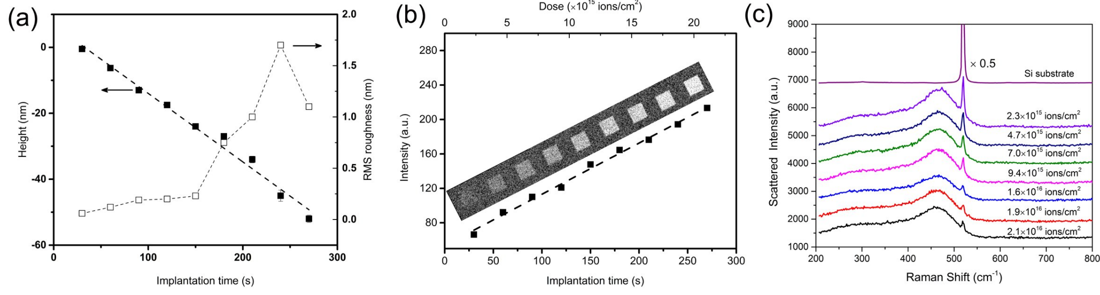

FIGURE 5.5: The effects of doping time on (a) the AFM height and RMS roughness of the FIB-implanted Si. (b) the average intensity of the EDX Ga signal (K_α) extracted from the EDX Ga mapping (inset image) (c) Raman spectra of the Ga implanted regions indicating dose dependent crystal deformation

of 2%. For the highest dose, the Ga concentration is 14%. The Raman spectra of the implanted regions (Figure 5.5 (c)) indicate that the top-layers of these regions are amorphous (the broad band at 480 cm^{-1}). Si micro-crystallites may exist in these regions, becoming amorphous as the dose increases, since the intensity of the crystalline Si scattering peak (at 521 cm^{-1}) reduces with increasing the Ga^+ dose.

5.2.3 Comparison of image contrast

For the HIM and SEM investigation, images of the Ga-implanted amorphous silicon were recorded by using several detectors. The contrast of the implanted region is extracted from the images, which is defined as,

$$C = \frac{(I_d - I_s)}{I_s} \tag{5.2}$$

where I_d is is the image intensity obtained from the implanted region, I_s is the intensity from the substrate adjacent to the implanted region. Figure 5.6 (a) shows images of the nine layers using the detectors in SEM and HIM respectively. The contrast is depicted in Figure 5.6 (b) as a function of the Ga atomic density of the implanted region. For all the implanted regions, HIM-MCP, SEM-EsB and SEM-ET images exhibit positive contrast. This means that the implanted region is brighter than the substrate adjacent to it in these images. The contrast in the SEM-EsB and SEM-ET images is linearly dependent on the Ga atomic density

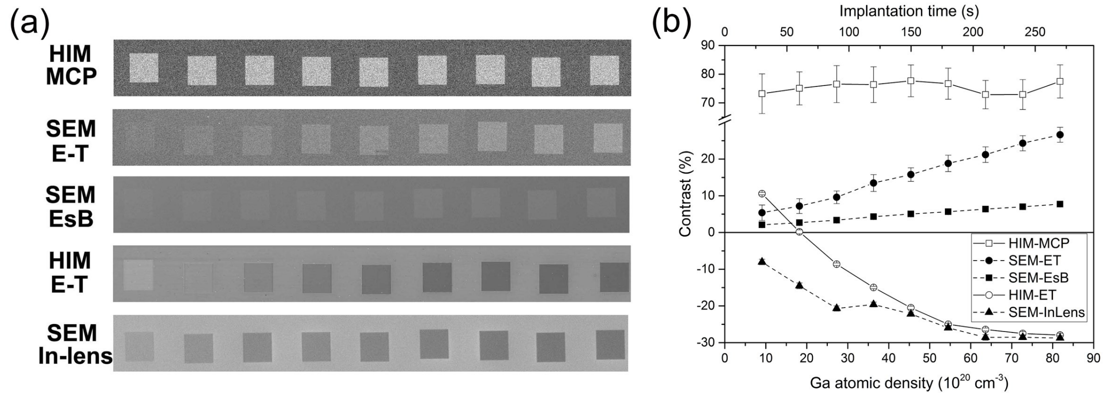

FIGURE 5.6: (a) Images of the doping contrast using different detectors (acquisition time: 4 - 5 μs) and (b) the relationship between theoretical doping concentration and image contrast. For SEM imaging, the beam energy is 5 keV, dwell time 4.32 μs, working distance 5 mm, field of view 140 $\mu m \times$ 180 μm. For HIM imaging, the beam energy is 5 keV, dwell time 1 μs, working distance 5 mm, field of view 125 $\mu m \times$ 125 μm.

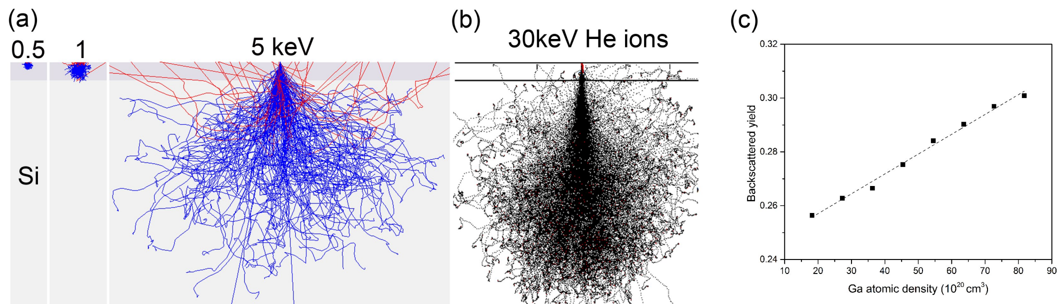

FIGURE 5.7: Monte Carlo simulation of the electron (a) and ion (b) trajectories respectively in the implanted region (the thickness of the top implanted layer is 30 nm). (c) BSE yield of a 5 keV electron beam as a function of the implanted Ga atomic density calculated by the simulation.

of the implanted region, but the HIM-MCP contrast seems to not vary within experimental uncertainty. The signals collected by the SEM-EsB and HIM-MCP detectors are mainly back scattered particles. The backscattering coefficient is proportional to Z^2 where Z is the atomic number of the target and it is expected that a heavier Ga target ($Z = 31$) produces more backscattered particles than a lighter Si target ($Z = 14$). For the BSEs, our Monte Carlo simulation (see Figure 5.7) shows that the BSE yield, η_e , increases linearly from 0.26 to 0.30 when the implantation dose increases from 2.34×10^{15} ions/cm^2 to 2.11×10^{16} ions/cm^2.

The linear dependence of the SEM-EsB contrast on the Ga density can be attributed to the increase in BSE yield, which is dominated by atomic number contrast. The SEM-ET contrast also carries the material information of the sample and linearly depends on the Ga density since a large portion of the SEM-ET signal is composed of SE2s and excited by backscattered electrons (Figure 5.7 (a)). The two linear relationships have different slopes, which might be due to the variation in the BSE angular distribution and the difference between the collection efficiency of the EsB and ET detector systems.

The HIM-MCP detects backscattered He^+ ions and the backscattered efficiency [34] is also proportional to Z^2, which varies about 10% over the implantation range. The backscattered yield of 30 keV He^+ ions in Si is about 0.012, two orders of magnitude smaller than that of a 5 keV electron beam. Thus, atomic number contrast due to the change in Ga density in the implanted regions is buried in noise due to the low overall backscattered yield. This can explain the insensitivity of the HIM-MCP contrast to the Ga density. We note that the implanted regions are much brighter than the substrate, despite the insensitivity to the Ga density. This may be attributed to the de-channeling of the ions in the top amorphous layer, which increases the backscattered yield of the implanted regions compared with the 110 crystalline Si. Note that very thin surface layers were reported to result in strong contrast due to de-channelling in HIM [179].

The SEM-InLens contrast of the implanted region has negative values and decreases monotonically with increasing the Ga atomic density (see Figure 5.6(b)). Typical Ga dopant contrast would be expected to result in positive contrast even in SEM-InLens images if the silicon crystallinity was largely preserved as Ga is a p-type dopant. The negative and hence reversed contrast observed here, points again to a strong role of the amorphous surface layer on the contrast. The HIM-ET contrast shows a similar dependence, while the sign of the HIM contrast changes from positive to negative as the Ga density increases (i.e. contrast reversal). Contrast reversal has been observed in SEM-InLens imaging of insulators by varying electron beam energies [49, 180]. The similarity between HIM-ET and SEM-InLens imaging indicates that they share the same contrast mechanism. It has been shown that the dominant SEM-InLens signal is the SE1 component which is excited directly by the primary beam [45]. In the HIM, the low He^+ backscattering efficiency results in negligible SE2 contribution to the HIM-ET imaging and the dominant signal for the HIM-ET detector is also SE1.

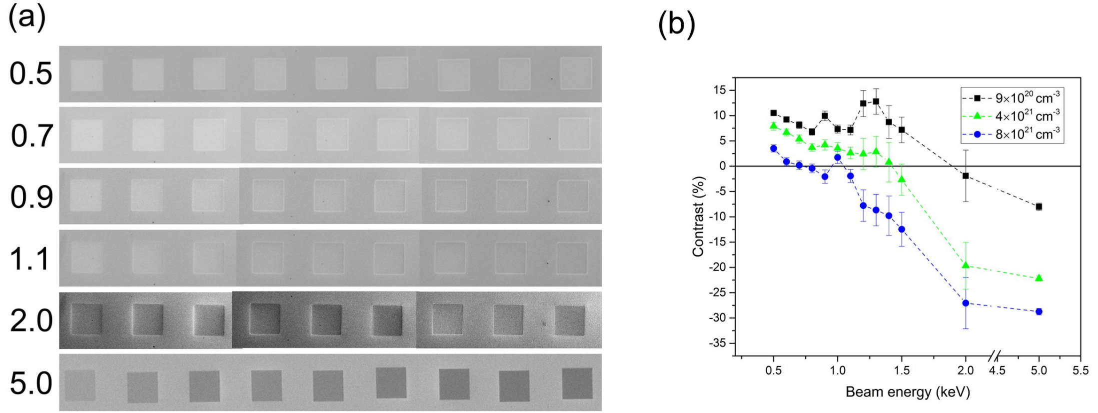

FIGURE 5.8: (a) SEM-InLens images of the implanted regions collected under different beam energies (0.5 - 5.0 keV) and a dwell time of 4.32 μs. (b) The SEM-InLens contrast as a function of the beam energy for three implanted regions.

5.2.4 Contrast reversal in SE imaging

To understand the contrast reversal, we first investigate the effects of beam energy on the SEM-InLens images. Figure 5.8 (a) shows the images collected through a range of beam energies (0.5 - 5.0 keV) and at a fixed dwell time per pixel of 4.32 μs. The contrast is depicted as a function of the beam energy in Figure 5.8 (b). The contrast decreases and reaches negative values as the beam energy E_p increases and contrast reversal occurs for all the implanted regions. However, the contrast reversal appears at a lower E_p for the implanted regions with a higher Ga density. The difference between the contrast of the implanted regions appears to be more significant as the beam energy increases. The contrast also varies with the dwell time. Figure 5.9 (a) is composed of the images collected with a fixed beam energy of 0.5 keV and a dwell time in the range of 0.54 - 4.32 μs, and the corresponding contrast is shown in Figure 5.9 (b) as a function of the dwell time. It is evident that the contrast increases with increasing dwell time. For the most heavily implanted regions (Ga density $> 2.7 \times 10^{21} cm^{-3}$), contrast reversal occurs because of changing the dwell time. As shown in Figure 5.9 (c) and (d), the dwell time has similar effects on the HIM-ET imaging. The HIM-ET contrast also increases with increasing dwell time and contrast reversal is observed for the implanted regions with a Ga density $> 9 \times 10^{20} cm^{-3}$.

It is known that SEM contrast changes with imaging conditions and sample charging has been proposed for the mechanism of contrast reversal [181, 182]. To understand the SEM-InLens contrast observed in our experiment, we sketch the dependence of SE yield on the beam energy, i.e. $\delta(E_p)$ in Figure 5.10 (a). The amorphous region has a smaller work function than that of the crystalline silicon [183] and hence a larger peak SE yield compared with the Si substrate. The mean free path of SEs also varies with the Ga density, and the SE escape depth varies accordingly. In terms of i.e. $\delta(E_p)$, we speculate the amorphous region behaves more like an insulator [26], which means i.e. $\delta(E_p)$ has a narrower peak and shifted towards lower beam energy as the Ga density increases. When the implanted region has the same SE yield as the substrate, the contrast of the region is 0. We assume the SE yield is i.e. δ_{Si}, δ_h and δ_l for the substrate and the regions with a high and low Ga density respectively, and the beam energy is E_h when $\delta_{Si} = \delta_h$. We define E_l in a similar way, e.g. E_l is defined as the primary beam energy at which $\delta_{Si} = \delta_l$. When the beam energy, E_p is lower than E_h, the contrast of the implanted region is positive since $\delta_h > \delta_{Si}$. When $E_h < E_p < E_l$, the contrast of the high-Ga region becomes negative and contrast reversal happens. When the beam energy increases to a value larger than E_l (at which $\delta_l = \delta_{Si}$), all the implanted regions exhibit negative contrast. Figure 5.10 (a) also explains the decrease of the contrast in the beam energy observed in Figure 5.8 (b) since the ratio of $\delta_{h,l}/\delta_{Si}$ decreases as the beam energy increases.

The charging effects may play the key role in the dwell-time effects shown in Figure 5.9 (a) and (b). The amorphous Ga-implanted regions have limited electrical conductivity and thus charge accumulation occurs when irradiated by a charged-particle beam. For a 0.5 keV electron beam, the electron range is smaller than the thickness of the amorphous layer (see Figure 5.7 (a)). Therefore, the charging behaviour of the Ga implanted region is solely determined by the properties of the top amorphous layer, irrelevant to the underneath Si substrate. As shown in Figure 5.10 (b), if the beam energy E_p is in the range of $E_h < E_p < E_l$, $\delta_h < \delta_{Si} < \delta_l < 1$ and the high-Ga and low-Ga regions have a negative and positive contrast respectively. For the high-Ga region, the landing energy of the primary beam reduces as negative charges build up in the region ($\delta_h < 1$). For a coarse approximation, we treat the region as an ideal insulator and the charging stops when the SE yield becomes unity (the red arrow in Figure 5.10 (b)). A larger dwell time results in more negative charges accumulated in the surface layer, lowering the landing energy of the electron beam. Consequently, a beam of lower

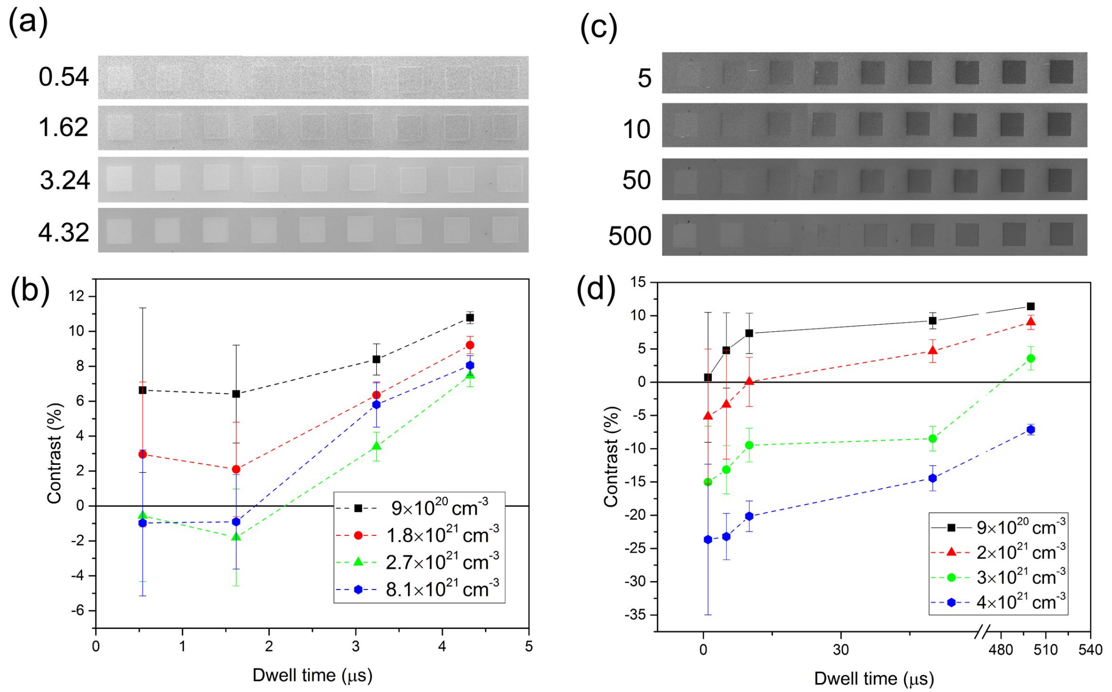

FIGURE 5.9: (a) SEM-InLens images taken with different dwell times (in s) and a fixed beam energy of 0.5 keV. (b) The SEM-InLens contrast as a function of the dwell time. (c) HIM-ET images taken with different dwell times (in μs) and a fixed beam energy of 35 keV. (d) The HIM-ET contrast as a function of the dwell time.

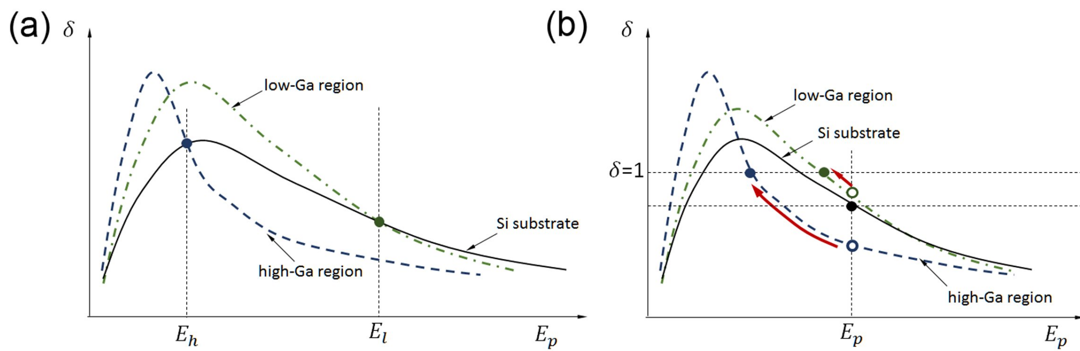

FIGURE 5.10: The SE yield as a function of the primary electron beam: E_h and E_l are the two beam energies where $\delta_h = \delta_{Si}$ and $\delta_l = \delta_{Si}$ respectively. (b) The charging effects in the implanted regions: The landing energy of the electron beam decreases as the dwell time increases when $\delta < 1$ for an insulator sample.

landing energy produces a larger δ_h. The contrast reversal occurs when $\delta_h > \delta_{Si}$. For the low-Ga region, δ_l increases but $\delta_l > \delta_{Si}$ during the charge process and the contrast of the low-Ga region is positive which increases with increasing dwell time. We note that the presence of a native oxide layer of varying thickness usually covers silicon surface. This may cause non-uniform charging of the substrate and the grey levels are hence not constant across the substrate. The typical thickness of the native oxide is < 1 nm [184], which is much smaller than the 0.5 keV beam range. Therefore, the variation in δ_{Si} due to charging may not be as significant as the implanted regions.

However, the $\delta(E_p)$-related charging effects cannot directly be applied to the HIM-ET contrast reversal shown in Figure 5.9 (c) and (d) where the contrast increases with increasing dwell time. This is because the SE yield in HIM is much larger than unity [185] and the charging effects would cause a continuous decrease in contrast when the dwell time increases and the SE yield of the implanted regions decreases towards unity. As shown in Figure 5.7 (b), most of the He^+ ions penetrate the top insulating implanted layer and the charging of the top layer is mainly due to the emission of SEs. The positive charges built in the layer reduces the SE emission and are responsible for the observed negative contrast. As the dwell time increases, the amount of the positive charges will reduce due to diffusion to the underneath Si substrate and thus the contrast increases, i.e. the implanted region appears less dark and the magnitude of the contrast decreases. The charge diffusion is more significant for the low-Ga region because it has a lower degree of damage induced by the Ga implantation. This may be responsible for the positive HIM contrast of the lowest-Ga region and the contrast reversal for the region next to it in Figure 5.9 (c). Hence the HIM-ET contrast reversal is a good indicator of limited charge mobility due to implantation damage. To avoid distortions of the implantation profile due to charging long dwell times are recommended.

5.2.5 Summary of the effects of imaging parameters on image contrast

Amorphous Ga-implanted Si regions were prepared on a Si substrate by using Ga^+ FIB irradiation. The Ga atomic density in each 30-nm-thick implanted region varies from 9.1×10^{20} cm^{-3} to 8.1×10^{21} cm^{-3}. Images of the regions were collected by using the InLens, ET, EsB detectors in a SEM as well as MCP and ET

detectors in a HIM. The SEM-EsB and ET images show materials contrast which linearly depends on the Ga density and is attributed to the Z-dependence of the backscattered electron yield. The HIM-MCP images do not show material contrast due to the low yield of backscattered ions but the visibility of the implanted regions in the images may be due to the de-channeling effects of the top amorphous layer. HIM-ET and SEM-InLens images bear the most similarity and the dominant signal of the two types of imaging is SE1. In both cases, the contrast decreases linearly with increasing the Ga density and for each implanted region the contrast increases with dwell time. The modification of the SE yield due to the Ga implantation as well as the dynamic charging effect are responsible for the dependence of the SEM-InLens contrast on the imaging parameters, while charge diffusion may be the key factor that causes the observed contrast reversal in the HIM ET images.

5.3 High throughput secondary electron imaging of organic residues on a graphene surface

In this section, we used both HIM and SEM to image freestanding graphene fabricated on a Si substrate. The *polymethyl methacrylate* (PMMA) residues can be observed by SE imaging in both microscope. The observed contrast and morphology varied with the beam condition (i.e. beam type and beam energy). We have proposed a model based on the stacking of PMMA nanoparticles to explain the contrast. The contrast variation has been discussed based on the beam-sample interaction and SE formation. The results establish a quantitative method to evaluate the fidelity of SE imaging and provide a highly efficient method to reveal PMMA residues on a graphene surface.

5.3.1 Graphene sample and characterisation methods

The continuous monolayer graphene was grown on the 25 μm thick Cu foils (Alfa Aesar, 99.8% purity) by the chemical vapour deposition process reported previously [186]. A thin PMMA layer (Molecular weight = 950k a.m.u.) was spin-coated on the graphene/Cu foil, followed by the etching of Cu foil in an aqueous iron(III) chloride solution. The remaining PMMA/graphene film was rinsed in deionized water three times and then transferred onto the target Si substrate. As described

in Chapter 4, the substrate contained arrays of circular holes of ~2.2 μm in diameter and 5 μm in depth. The PMMA layer was dissolved in 55 ^{o}C hot acetone for 15 minutes first, then transferred to 55 ^{o}C hot IPA for 15 minutes, slowly taken out of the solvent and then dried in ambient conditions.

The imaging of the fabricated graphene sample was carried out in both a HIM and SEM. The SEs in HIM (Zeiss Orion Plus) were excited by a focused He^+ beam of 35 keV beam energy and 0.6 pA beam current (10 μm aperture), and collected by an Everhart-Thornley detector. While the SEs in SEM (Zeiss Supra) were excited by the beam energy from 0.5 keV to 20 keV and collected by an in-lens detector. The beam current increased from 10 pA to 35 pA. To minimize the influence of possible beam induced contamination, the selected region was only scanned once. All the captured SE images were transformed so that the intensity histogram was extended to the whole grayscale of 255 channels. The morphology of graphene was also characterized by optical microscopy (Olympus BX51, 50 × objective lens) and atomic force microscopy (Asylum MFP-3D, tapping mode with tip diameter <20 nm).

5.3.2 Comparison between SE imaging, optical microscopy and AFM: general features

Figure 5.11 shows low-magnification images of different regions of the graphene sample observed using HIM, SEM, AFM and an optical microscope. The optical image in Figure 5.11 (a) reveals the 2.2 μm holes in the Si substrate but neither the graphene nor its surface contamination are visible in the optical image. The graphene could be clearly seen when imaging using SEM and HIM (e.g. Figure 5.11 (b) and (c) respectively). The freestanding graphene across the substrate holes (marked 'G' in Figure 5.11) exhibits a distinct contrast with respect to the bare holes (marked 'H' in Figure 5.11). The contrast is evident from ruptured graphene that covers a fraction of a hole. The boundary of the ruptured graphene is still visible in the supported area if we track the boundary from the hole to the substrate region. This contrast (i.e. graphene vs. substrate) is most distinguishable in the HIM image Figure 5.11. As a comparison, an AFM phase image is shown in Figure 5.11 (d), which also demonstrates the empty substrate holes, ruptured graphene across the holes, and rugged graphene surface. However, surface chemical residues, if present, are not resolvable at this magnification by using any of

the microscopy techniques attempted.

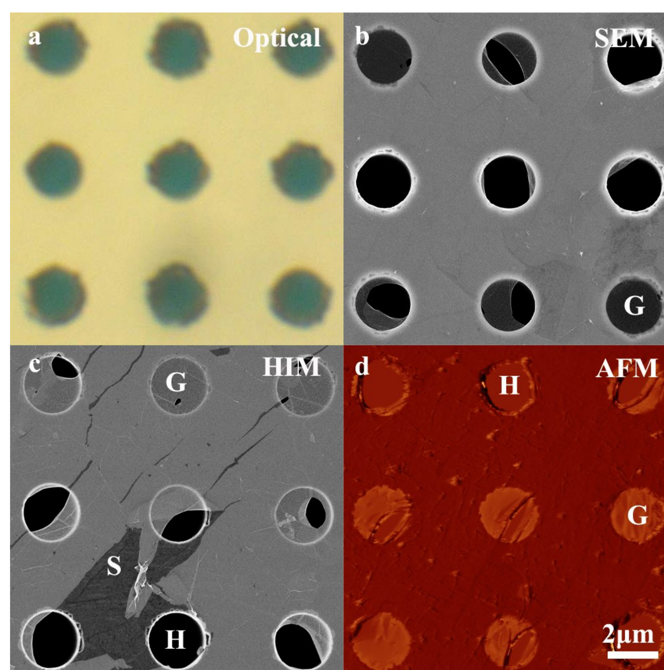

FIGURE 5.11: (a) An optical image of the graphene sample. Only the 3×3 hole arrays are shown on the Si substrate and no graphene contrast can be observed. (b) A 5 keV SEM image of the graphene sample. The existence of graphene (marked as 'G' in the image) can be identified from the substrate ('S') and the bare holes ('H'). (c) A 35 keV HIM image of the graphene sample. The image also shows the existence of graphene, substrate and bare holes. The graphene has a better contrast in HIM in comparison with SEM. (d) An AFM phase image of the graphene sample. Holes and freestanding graphene can be identified. The covering of graphene on the substrate is difficult to identify in the image at the selected magnification. All the images have the same field of view (2 μm scale bar shown in Figure 5.11a).

Figure 5.12 shows the SEM, HIM and optical images of edges between the monolayer and bilayer graphene (this sample is prepared by mechanical exfoliation). The red arrows show the edges between monolayer to bilayer graphene which are used to obtain the line intensity profile in Figure 5.13 (d). It is evident that SE images provide much better spatial resolution.

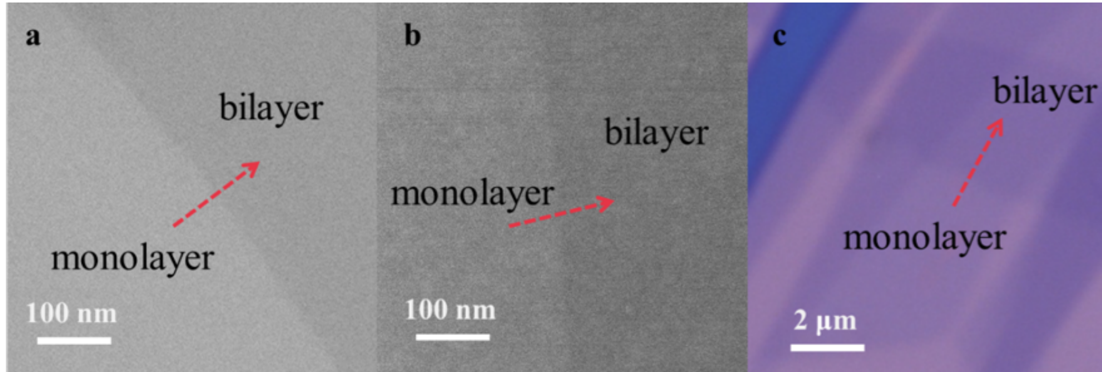

FIGURE 5.12: a, a SEM image. b, a HIM image. c, an optical image.

5.3.3 Visibility of graphene in the SE imaging

We evaluate the visibility of graphene in the SE imaging and compare it with optical imaging. The images shown in Figure 5.13 (a) were taken from a few-layer graphene flake (on a Au substrate) using an *Optical Microscope* (OM), a SEM and a HIM, respectively. The flake is almost invisible in the optical image, while it is evident in the SE images captured by both SEM and HIM. We have found that few-layer graphene on other metal substrates (e.g., Cu and Ni) shows similar optical and SE visibilities. To be able to see few-layer graphene through an OM, the reflective amplitude of the illumination light at the air/graphene/substrate interface must be significantly different from that at the air/substrate interface, which depends on both the wavelength of the light and the optical behaviour (i.e. the reflective coefficient) of the substrates [187, 188]. This means the graphene is visible for a restricted combination of substrates and light. Monoatomic metallic substrates cannot produce such differences in the amplitude of the reflected light, which results in the low optical contrast for the whole visible light range. However, graphene flakes are discernible in SE images regardless of the type of primary beam (electrons or He^+ ions) or the substrates.

The contrast of a graphene flake in a SE image must be larger than c.a. 2% to be visible. The contrast (C_g) is defined as the intensity difference between graphene (I_g) and its substrate (I_s): $C_g = (I_g/I_s) \times 100$. The contrast varies with imaging conditions. For example, Figure 5.13 (b) shows SEM images of few-layer graphene on a highly p-doped Si substrate covered with 285 nm SiO2 (SiO_2/Si). They were acquired with electron beam energies ranging from 0.5 keV to 20 keV. The graphene appears "brighter" than the substrate at a low energy of 0.5 keV with a

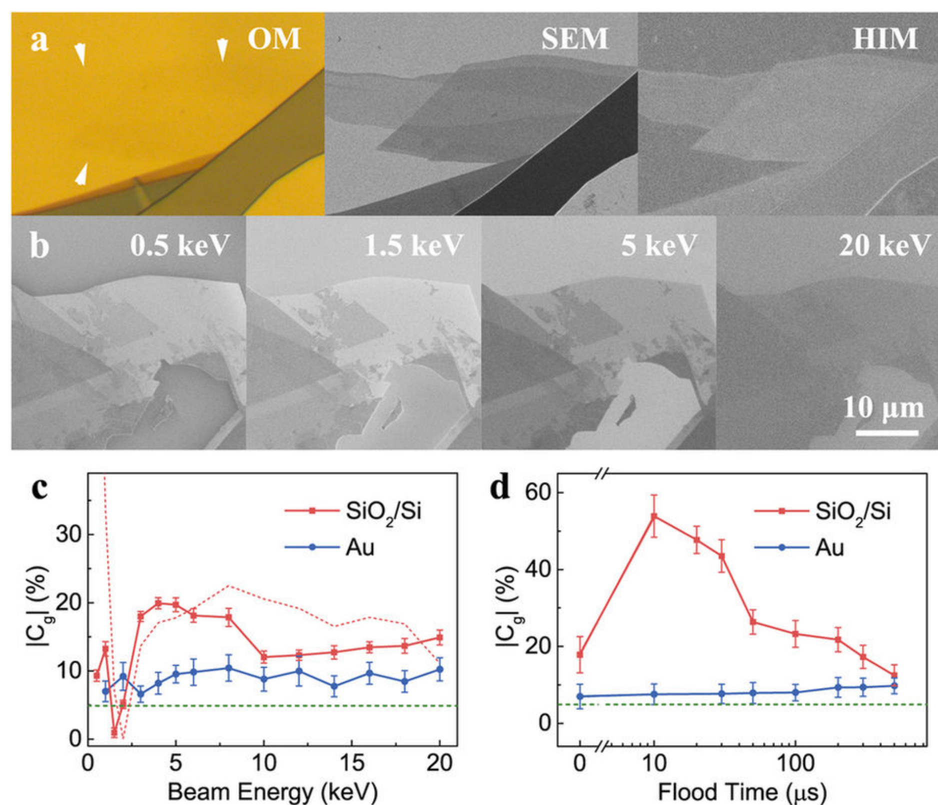

FIGURE 5.13: **a**, Images of a few-layer graphene flake on a Au substrate from an OM, a SEM and a HIM respectively. The graphene is almost invisible in the optical images, its position is marked by the white arrows. However, the same graphene flake can be clearly observed in SEM and HIM images. **b**, A series of SE images of graphene on a highly p-doped Si substrate covered with 285 nm SiO_2 (SiO_2/Si) irradiated with different electron beam energies of 0.5 keV, 1.5 keV, 5 keV and 20 keV. The monolayer graphene is almost invisible with a 1.5 keV electron beam but is visible at all the other beam energies. **c**, The SE contrast of monolayer graphene on SiO_2/Si (red squares) and Au (blue circles) substrates under different electron beam energies. The red dashed line shows the calculated SE contrast of monolayer graphene on SiO_2/Si substrate using Equation 5.3. **d**, The SE contrast of monolayer graphene on SiO_2/Si (red squares) and Au (blue circles) substrates with a different charge neutralization parameter (flood time) in HIM. The value of optical contrast (~ 5 %) is drawn as a green dashed line in both figures for comparison. The error bars in Figure 5.13 c and d were calculated using the errors of corresponding measured image grey value intensities.

contrast ratio of 9 %. At 1.5 keV the monolayer graphene exhibits a similar SE intensity to the substrate, i.e. the SE contrast ratio is 1 %. The graphene is still discernible since its edge exhibits a visible contrast (7 %). At higher energies (> 2 keV), the graphene appears "darker" than the substrate ($\sim$ -10%). In Figure 5.13 (c), the magnitude of SE contrast ($|C_g|$) for the monolayer graphene on different substrates (SiO_2/Si and Au) is sketched as a function of electron beam energy. For the SiO_2/Si substrate, a contrast maximum ($\sim$ 20 %) appears around a beam energy of 5 keV and a minimal contrast (< 5 %) at c.a. 1.5 keV. On the contrary, the SE contrast of graphene on Au (Figure 5.13 (c)) is independent of the beam energy, retaining its value ($\sim$ 10 %). Both the maximum contrast in SEM and HIM can be larger than that in OM ($\sim$ 5 %), making the graphene more identifiable by SE contrast. The key to understanding the contrast variation is the illumination of the supported graphene. Both the primary beam and the backscattered electrons from the substrate can cause SE emission from the graphene. The SE contrast of monolayer graphene, as a function of primary beam energy is given by:

$$C_g(E_p) = \frac{\delta_g(E_p)}{\delta_s(E_p)} \cdot [1 + \beta\eta_s(E_p)] + const \quad (5.3)$$

where δ and η are the SE and BSE yields and the subscripts s and g indicate the substrate and the graphene respectively. β accounts for the lower energy of the substrate BSEs (compared with the primary beam). The SE and BSE yields vary with the beam energy, which can be measured independently (see Chapter 4.3.4, evaluation of the graphene SE yield). The calculated result is consistent with the experiments as shown in Figure 5.13 (c). The deviation at low beam energy (< 1 keV) is due to the charging of the substrate which is not considered in the calculation and suppresses the SE yield. For the monoatomic metallic substrates, as the beam energy varies the variation in the BSE yield is negligible, which results in the constant graphene contrast.

In the HIM, an insulating substrate will always be charged positively. This positive charging suppresses SE emission by attracting them back into the sample and reducing the landing energy of the primary beam. Without additional compensation mechanisms, the positive charging increases continuously and SE emission will eventually be prohibited when the sample potential is higher than that of the detector. The charged sample appears dark. The charging effect can be compensated by using an electron flood gun which injects electrons into the sample and

neutralises the excess positive charges. However, as the flood gun electrons have an energy of 500 eV they may excite SEs with a yield greater than unity. This means that either inadequate or excessive flooding results in a positively charged surface and reduces the SE emission. Therefore, a properly compensated neutral surface exhibits a maximum brightness and SE contrast, which can be acquired by varying the compensation strength (e.g. electron flood time shown in Figure 5.13 (d)). A maximum contrast of ~ 54 % for a single layer of graphene on a SiO_2/Si substrate was observed at a flood time of 10 μs. We note that the charge compensation does not vary the contrast observed on the non-charging Au substrate since the sample is always electrically grounded. For the insulating substrate, the contrast maximum consistently appears under a set of well-defined imaging parameters (see Section 5.4.2 optimisation of the SE imaging conditions in SEM). The results presented hereafter are taken with these parameters.

5.3.4 Typical features in SE images of graphene with polymer residues

Figure 5.14 shows the SE image of substrate-supported graphene in HIM and SEM. In all the SEM and HIM images, a non-uniform contrast can be observed on the graphene surface, which verifies the existence of PMMA residues. The featured structures we have observed on the freestanding graphene, such as bright spots, clusters and dark dots are also revealed in the SE images of supported graphene Figure 5.14 (a). The spots and dots have a similar size distribution to those on the freestanding graphene. However, the contrast of clusters becomes less obvious on the Si substrate. They are even hard to identify in the high energy e-beam images Figure 5.14 (d). Since both the freestanding and supported graphene are prepared in the same process, the PMMA residues should have the same morphology across the sample surface. The contrast difference between freestanding and supported graphene images could be attributed to SE signal from the Si substrate which contributes to the SE contrast.

As shown in Figure 5.15 (a), a white dashed line is drawn across the dark dot shown in the inset figure. The SE intensity across the line is shown in Figure 5.15 (b). An intensity valley is observed across the dot. The average maximum and minimum intensity for the profile is $\sim$75 and $\sim$30 (red dashed lines). Therefore the half maximum value is $\sim$52.5 and corresponds to a distance of $\sim$2.4 nm in the

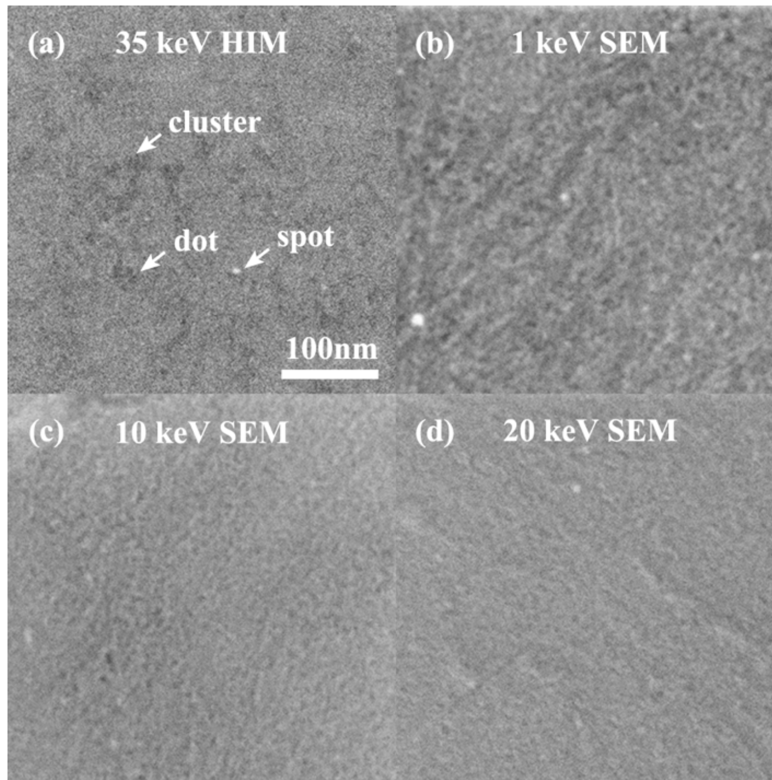

FIGURE 5.14: (a) A 35 keV HIM image of the substrate-supported graphene. (b) A 1 keV SEM image of the substrate-supported graphene. (c) A 5 keV SEM image of the substrate-supported graphene. (d) A 20 keV SEM image of the substrate-supported graphene. The featured structures such as spots, clusters and dots can also be observed in all these images.

image (8 pixels). We then define this FWHM value as the diameter of the dark dot. The size of the spots and clusters can be measured by the same method.

Besides the residues on the graphene surface, the SE imaging reveals abundant surface information, for example, the multilayer folds, ridges and the surface ruggedness (Figure 5.16), while the detailed contrast of these features, i.e. their apparent morphology in the images, depends on the imaging conditions as well. For example, as shown in Figure 5.16 (a), in the HIM image the folds of graphene are portrayed as regions of uniform brightness - in contrast to the darker graphene background - with clearly defined straight edges. The folds observed in the 0.5 keV SEM image are similar to those in the HIM; however in the 20 keV SEM image their contrast significantly decreases due to the increase of sample translucency. Figure 5.16 (b) and (c) are topographical features of the graphene (ridges and

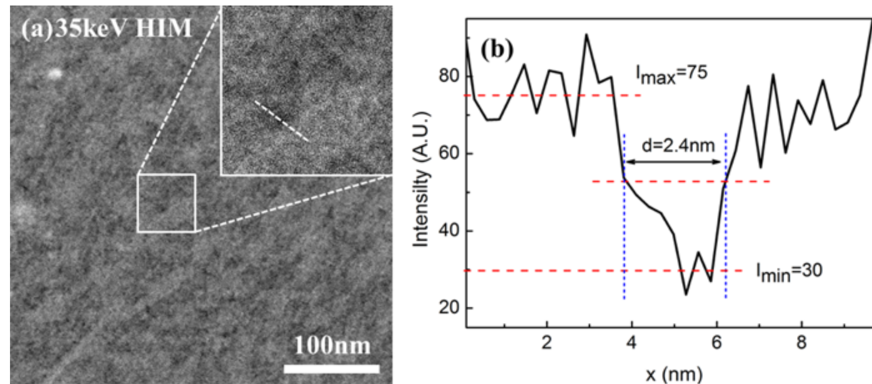

FIGURE 5.15: (a) A HIM image of the same freestanding graphene as shown in Figure 5.17a . An additional white dashed line is drawn - across the dark dot in the inset - of which a line profile was obtained. (b) Line profile of the intensity across the dots in the inset of Figure 5.15 (a). The FWHM of the intensity valley gives the dot size as ∼2.4 nm.

corrugation), which demonstrate the high surface sensitivity of HIM imaging.

5.3.5 SE imaging of polymer residues in HIM and SEM

Figure 5.17 (a) is a HIM image of freestanding graphene, with a 0.3 nm pixel size and a 400 nm FOV. A non-uniform contrast is evident in the image; as marked in Figure 5.17 (a), the typical contrast features include bright spots (∼10 nm in diameter), less-bright clusters (several hundred nanometers) and relatively dark areas surrounding these clusters. The contrast inside the dark area is not uniform, and the darkest regions appear as dot-like features, as shown in the inset of Figure 5.17 (a). We measured the diameters of 20 such dark dots (the diameter is defined as the FWHM, of the SE intensity peak in the line-scan profile across the dot centre, see Figure 5.15). The average size of these dots, measured from the HIM image (Figure 5.17 (a)), is 2.7 ± 0.4 nm. To evaluate the fidelity of the HIM imaging, we then investigate the SE imaging of the same graphene sample in the SEM.

High-magnification SEM images (Figure 5.17 (b) to (d) were taken under e-beam energies of 0.5 keV, 10 keV and 20 keV, respectively. To facilitate the comparison, all the images in Figure 5.17, including the HIM image (Figure 5.17(a)), have a similar pixel size and same FOV, i.e. the same magnification. They show similar

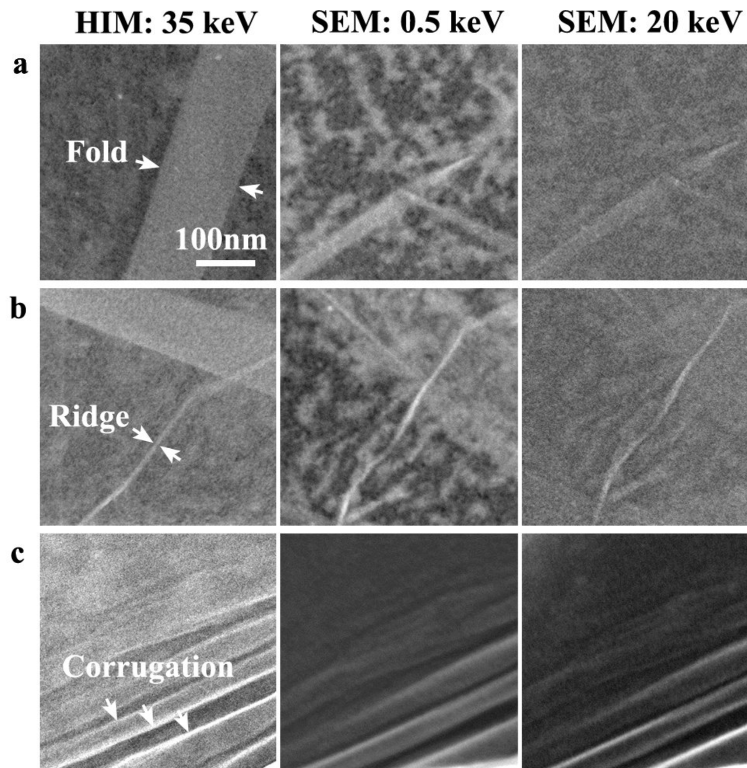

FIGURE 5.16: (a) The observation of the graphene folds in different microscopes. Graphene folds show different contrast in the 35 keV HIM, 0.5 keV SEM and 20 keV SEM images. (b) The observation of the graphene ridges in different microscopes. (c) The observation of graphene corrugations in different microscopes.

contrast features, and we can identify the bright spots, clusters and dark dots in the SEM images as well (see the inset of Figure 5.17 (b) to (d)). We mention in passing that these contrast features can also be observed on the substrate-supported graphene in both SEM and HIM images (see section 5.3.4). However, there are significant differences between these images (Figure 5.17). The lower the e-beam energy becomes, the higher the contrast exhibited in the corresponding image. That is to say, the typical features in the images (i.e. bright spots, clusters, and dark dots) have a larger difference in SE intensity at lower e-beam energies (see Figure 5.17(b)). To highlight the contrast variation, we plotted the histograms of the images as in Figure 5.17 (e). The most probable intensity for the 35 keV HIM image, i.e. the peak position in the histogram, is lower than the 20 keV SEM image, indicating that less SEs are escaping from the thick clusters in HIM. However, both the 35 keV HIM and the 20 keV SEM images demonstrate similarly

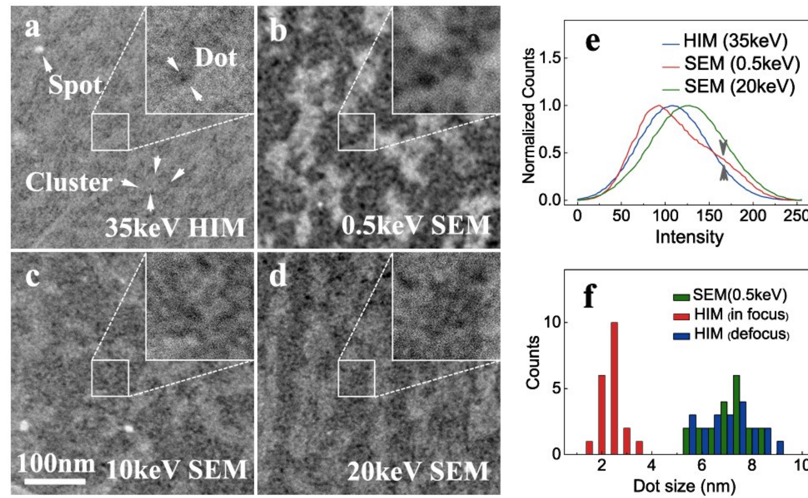

FIGURE 5.17: **a**, A 35 keV HIM image of the freestanding graphene. The featured structures such as bright spots, clusters and dark dots are marked by the arrows to show their existence. The dark dots can be observed more clearly from a selected and magnified area as shown in the white square frame. **b**, A 0.5 keV SEM image of the freestanding graphene. **c**, A 10 keV SEM image of the freestanding graphene. **d**, A 20 keV SEM image of the freestanding graphene. The featured structures can also be observed in all these SEM images. All the SE images have the same FOV of 400 nm. **e**, The intensity distributions for 35 keV HIM, 0.5 keV SEM and 20 keV SEM images. The 35 keV HIM and 20 keV SEM images exhibit similar and symmetric peaks. The peak of the 0.5 keV SEM image is asymmetric and has an additional peak at the high intensity value, as marked by the grey arrow. **f**, The size distribution of the dark dots observed in the different imaging conditions. The dots observed in a finely focused 35 keV HIM image Figure 5.17 (a) have small size values. The dots observed in a 0.5 keV SEM image Figure 5.17 (b) and an over-focused 35 keV HIM image (Figure 5.18 **c**) have similar size values due to their close probe size values.

symmetrical peaks in their image histograms. On the contrary, the histogram of the 0.5 keV SEM image exhibits an asymmetric peak, which is due to the existence of another peak at a high intensity value (indicated by the grey arrow).

Another significant difference among these images is the dimension of the dark dots. Although these dots are most discernable under the 0.5 keV e-beam imaging due to its high contrast, they have the largest apparent size of 7.2 ± 0.9 nm. As the electron beam energy increases, the size of the dark dots reduces. At the highest e-beam energy that we used (20 keV), the average size of the dots decreases to 4.9 $\pm$ 0.7 nm, which is twice as large as that in the HIM images. As an example, the size distributions of the observed dark dots measured in the 0.5 keV SEM and 35 keV HIM are delineated in Figure 5.17 (f). It is evident that HIM gives a much

narrower distribution and much smaller values for the measured sizes of the dark dots.

5.3.6 The effect of probe size on resolution of SE graphene imaging

Since the images taken at different beam conditions (beam species, beam energies, etc.) show distinct features, a valid question is which one of them exhibits the best fidelity to the graphene surface. To investigate the formation mechanisms of the SE contrast is thus of great importance to the interpretation of the images. It is well understood that the size of the beam probe is crucial to the resolution of the image [8]. The minimal probe size for a set of beam conditions is achieved when the probe is in focus and free of astigmatism (see section 4.3.1 for the optimization procedure to minimize the probe size). The images in Figure 5.17 were acquired with optimized probes, but the size of the smallest probe varied with the beam conditions. The electron probe size monotonously decreases from 2.7 $\pm$ 0.2 nm to 1.6 $\pm$ 0.1 nm as the e-beam energy increases from 0.5 keV to 20 keV, while in HIM the superlative probe size obtainable was 0.9 $\pm$ 0.1 nm (Figure 4.8 (a) in section 4.3.1). The decrease of the beam probe size corresponds to improvement of spatial resolution. Therefore, the morphology difference observed in Figure 5.17 can be attributed to the variation of the probe size. As shown in Figure 5.18 (a), the size of the dark dots measured from a SEM image linearly depends on the size of the electron beam probe that was used to acquire the image. The linear relationship is valid for the e-beam energies that we tested (from 0.5 keV to 20 keV). A striking feature is that the He^+ probe fits the linear relationship as well. This can be demonstrated by tuning the He^+ beam into defocusing states and thus varying its probe size (see Figure 4.8 (b) in section 4.3.1). Figure 5.18 (b) and (c) show the same area imaged by a focused He^+ beam (probe size $\sim$0.9 nm) first and then an over-focused beam (probe size $\sim$2.7 nm) respectively. The featured structures such as bright spots, clusters and dots are still visible in the over-focused image. However, the average size of the dark dots in the over-focused image increases to 7.4 $\pm$ 1.2 nm, which is larger than the value (2.7 $\pm$ 0.4 nm) measured from the well-focused HIM image, but also quite close to the size (7.2 $\pm$ 0.9 nm) obtained from the 0.5 keV SEM image in Figure 5.18 (d). The distributions of the dark dot sizes in the over-focused HIM and 0.5 keV SEM images match well (see Figure 5.17

(f)). The similarity of the two images can be inspected in Figure 5.18 (c) and (d), which is due to the fact that the size of the over-focused He^+ probe (∼2.6 nm) is almost the same as that of the 0.5 keV SEM probe (∼2.7 nm). Therefore the correlation indicates that the measured size of the dark dots depends on the probe size and is independent of the beam type. The smaller the probe size becomes, the finer the dot which will be observed.

We note that for all the imaging conditions, the probe size is smaller than the size of the dots in the corresponding image. It should be noted that the measured dot size is a convolution of, the probe size and the actual physical size of the features on the specimen corresponding to the dot. The correlation of probe size and dot size indicates that the finite size of the probe may introduce errors to the measurement of feature dimension, even when the probe is smaller than the apparent size of the feature in the image. When the probe size decreases to zero, the apparent size of the feature will converge at the true feature size. As shown in Figure 5.18 (a), the y-intercept (0.7 ± 0.3 nm) corresponds to a zero-sized probe, and it might be the physical size of the dark dots, which is beyond the resolution limits of SEM and HIM. Nevertheless, compared with SEM, HIM imaging reveals the surface morphology with higher fidelity due to its finer probe.

5.3.7 A contrast model of SE graphene imaging in HIM and SEM

To understand the contrast mechanism of the SE imaging, we require knowledge of the graphene surface which should be acquired from other independent characterisation methods. Ishigami et.al. have exploited AFM and proved that a graphene surface —which has undergone a similar PMMA spin-coating process to our samples— will be covered by a continuous PMMA residue film [71]. Figure 5.19 (a) is the high magnification AFM three-dimensional height image of our graphene film on the Si substrate. The featured structures observed in the SE imaging (Figure 5.17) appear in the AFM image, which can be directly interpreted as the surface roughness caused by the PMMA residues. Figure 5.19 (b) shows the height variation across the bright spots in Figure 5.19 (a) (A and B marked by the arrows). The height of the spots is about 4 nm. Since PMMA long chain molecules can form nanoparticles on the material surface with sizes of several nanometers

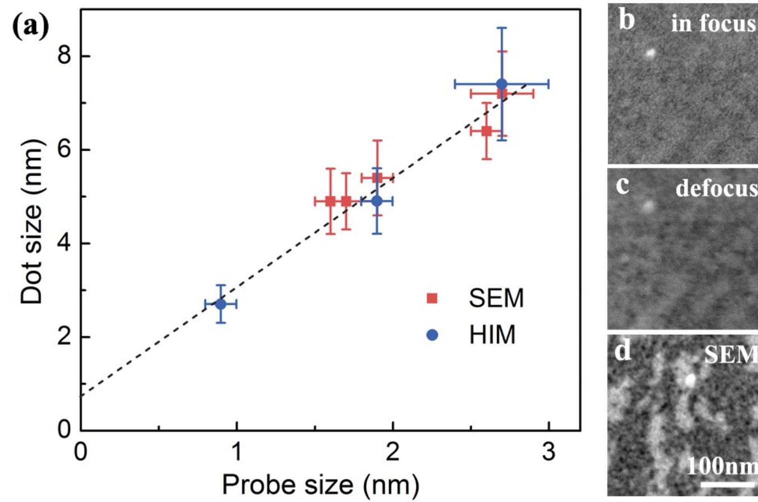

FIGURE 5.18: **a**, The relationship between the beam probe size and the dark dot size. A linear relationship (black dashed line) can be fitted for both the conditions of e-beam (red squares) and He^+ beam (blue circles). **b**, A finely focused 35 keV HIM image of the freestanding graphene. The image shows a small dot size similar to Figure 5.17 a. **c**, A de-focused HIM image of Figure 5.18 b. The observed dot size becomes larger than that of Figure 5.18 b. **d**, A finely focused 0.5 keV SEM image. The dot size is quite close to that of Figure 5.18 c because of the close beam probe sizes for these two images.

[189, 190], we postulate a model for the morphology of the graphene surface which is consistent with our AFM observation.

Figure 5.19 (c) is a simulation carried out using Casino (v2.48), showing the distribution of 500 simulated electrons in the substrate material which was defined as PMMA (composition $C_5O_2H_8$). Two beam energies of 0.5 keV and 20 keV were selected, and 20000 electrons were used to simulate the energy distribution. As sketched in Figure 5.19 (c), the PMMA nanoparticles are assembled on the graphene surface to form a continuous but non-uniform film [190]. The in-plane close packing of the nanoparticles will form a uniform monolayer of residues. Regions of multi-layered PMMA residues are also present. The thickness of the monolayer PMMA is ∼4 nm, the same as the size of the nanoparticles. The AFM height profile shows that the multi-layered regions are normally thinner than ∼12 nm, i.e. less than three layers. The SE contrast (i.e. spots, clusters and dots) can be attributed to the non-uniform coverage of the residue layer. The formation of a SE image involves the propagation of the primary beam in the sample, the interaction between the primary particles and the sample atoms and the excitation and escape of the SEs.

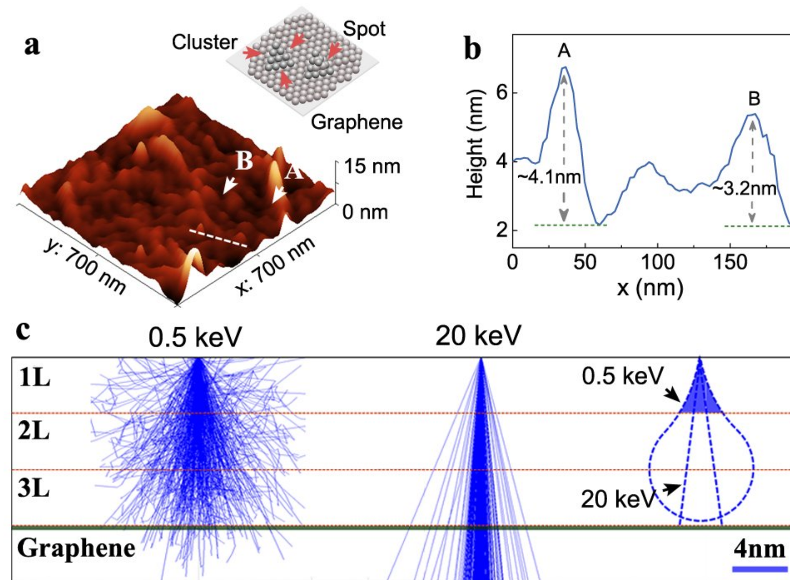

FIGURE 5.19: **a**, The three-dimensional AFM height image of the substrate-supported graphene with a FOV of 700 nm. A white dashed line is drawn across two peaks (marked as A and B by the arrows) to show its height variation. **b**, The height profile of the dashed line in Figure 5.19 a. Spots A and B are shown as two peaks that have large height intensities. **c**, A demonstration of the stacking model for the PMMA nanoparticles. PMMA nanoparticles can be stacked as monolayer or multilayers (clusters and dots) on the graphene surface. The simulated interaction volume of the electrons in the top three layers of PMMA on a graphene surface. The interaction volume of the 0.5 keV electrons in the region exhibits a pear-like shape, while the interaction volume of the 20 keV electrons is a narrow conical shape (see the dashed shapes in the figure). The volume ratio of the top PMMA layer to the total PMMA layers is smaller for the interaction with the 0.5 keV electrons than the 20 keV electrons.

As shown in Figure 5.19 (d), the interaction range of the 0.5 keV e-beam in PMMA is ∼10 nm and a pear-like interaction volume extends across the top three PMMA layers. For the 20 keV e-beam, the interaction volume in the top three PMMA layers is a narrow cone (Figure 5.19 (d)). To understand the significance of the geometry variation of the interaction volume, consider the interaction volume of the e-beam in the three layers of PMMA on the graphene surface at low energy (0.5 keV) (V_L) and for the high energy (20 keV) (V_H). Now we label the interaction volumes for just the top layer as (V_H^T) and (V_L^T) for the high and low energies respectively. Since the interaction volume of the high-energy beam approximates to a conical shape, the ratio of V_H^T/V_H is close to 0.03. As shown in Figure 5.19 (d), it is clear that the ratio of V_L^T/V_L is smaller than V_H^T/V_H due to the fact

that the majority of the pear-like interaction volume situates in the second layer. We see that for a low energy beam a lower portion is lost in the top layer than the portion lost for a high energy beam. For the low energy beam, this results in a larger intensity difference across regions with different thicknesses. This is responsible for the increased contrast and contributes to the larger probe size found at the lower beam energy. On the other hand, the higher the electron beam energy is, the lower the scattering cross section between the energetic electrons and the material electrons. This effect results in the translucent appearance of the sample at higher beam energies. This translucency is not apparent in the HIM imaging. This is due to the stopping power of the 35 keV He^+ beam and the electron beam's different interaction behaviour with carbon. As the He^+ beam propagates through the sample, it continues losing energy. The lower the beam energy, the lower the stopping power, and thus the lower excitation of secondary electrons. This means that the majority of the SEs collected in the HIM is from the top layer, resulting in the high surface sensitivity of the HIM imaging. The stopping power of the electron beam behaves in an opposite way, which enhances the SE emission from the underlying layers and thus increasing the translucency of the sample. To summarize, the nanoparticles identified in the AFM height profile (Figure 5.19 (a)) correspond to the brightest spots in the SE images (Figure 5.17 (a)). The darkest dots in the SE images indicate areas of the sample surface that might not be covered by the residue PMMA, i.e. the interstice of the PMMA nanoparticles. The close stacking of spherical nanoparticles with a diameter of $\sim$4 nm will result in an interstice of $\sim$0.6 nm, which coincides with the size of the dark dots extrapolated for a zero-sized probe (Figure 5.19 (c)).

5.3.8 Summary of imaging organic residues on a graphene surface

In summary, we have demonstrated the visibility of nanoscale PMMA residues on a graphene surface in secondary electron imaging. Artefacts have been attributed to the finite probe size and the varying nature of the beam-sample interaction at different beam conditions. In terms of imaging fidelity, HIM is superior to SEM, since HIM provides a sub-nanometer probe and increases surface sensitivity. The low-energy SEM images however demonstrate higher contrast. Other features such as folds, ridges and ruggedness could also be observed in the SE imaging. The

results establish a quantitative method to evaluate the fidelity of SE imaging and provide a high efficiency method to reveal the PMMA residues on a graphene surface.

5.4 Quantitative SE imaging for work function extraction and layer identification of graphene

In this section, we present a method to extract quantitative information from the SE contrast of graphene. We have established imaging parameters to acquire reproducible SE contrast from graphene samples. Atomic level identification of graphene thickness up to 10 layers is demonstrated. A model based on illumination by both the primary beam and backscattered particles was established to explain the observed layer-dependent SE contrast. Furthermore, by subtracting the contribution from SE attenuation, this model allows the quantitative determination of work function variations. The validity of the model is further supported by the obtained graphene SE energy spectra. Our work shows a high throughput, high resolution way to effectively determine the work function of graphene, and extends the application fields of SE contrast to quantitative analysis.

5.4.1 Graphene preparation

Graphene on a highly p-doped SiO_2/Si substrate was prepared using the micromechanical exfoliation method with flake location and layer number determined by optical reflection contrast via an optical microscope (Olympus BX51 with a 50 $\times$ objective lens) [191]. A SiO_2 layer thickness of 285 nm provided the best optical contrast for imaging. Graphene on metal substrates was prepared by transferring exfoliated flakes onto target substrates with the assistance of a PMMA film [192]. These substrates were prepared by depositing 50 nm metal films (Au, Cu and Ni) on Si substrates. The freestanding graphene was also prepared by transferring exfoliated flakes onto a target Si substrate. This Si substrate was patterned with circular holes 2 μm in diameter and > 10 μm deep. The PMMA film was then removed in hot acetone (50° C) prior to the sample being transferred into hot IPA (50° C) then left to dry in air.

5.4.2 Optimisation of the SE imaging conditions in SEM

Parameters that might have potential influence on SE imaging of graphene in SEM include WD, scan speed, beam current and beam energy. The effects of beam energy are detailed in next section however the effects of other parameters are discussed below. All experiments were done in the Carl Zeiss *Supra* SEM.

We first varied the WD while keeping beam energy constant (5 keV). The variation in SE intensity of the substrate and the different graphene layers is shown in Figure 5.20 (a). As the working distance increased from 3 mm to 7 mm the SE intensities of both substrate and graphene layers first increase and then decrease. Maximum intensity occurs between 4 and 5 mm WD. The variation in SE intensities can be explained as the change in the collection efficiency of in-lens detector with highest efficiency occuring at 4 - 5 mm. The different graphene layers behave with individual SE intensity/WD dependencies. For the thicker layers, maximum intensity shifts slightly to lower working distances. This observation can be attributed to the angular distribution of SEs and the work function variations between the different layer thicknesses. The kinetic energies of SEs in graphene and vacuum have a relationship with material work function (Φ), given by $E_s = E_k + \Phi$. Graphene surface work function is known to increase with layer thickness, therefore SEs with same kinetic energy in graphene (E_s) have a decreased energy in vacuum (E_k). According to the SE angular distribution at the surface [99], as the emission angle for escaped SEs becomes larger less are collected by the in-lens detector. For layer thickness's greater than four the work function remains constant and thus the emission angle does not change.

Figure 5.20 (b) shows graphene SE contrast as a function of working distance. At the optimized working distance (4 - 5 mm) the graphene contrast is almost constant. Therefore, graphene work function extraction based on the contrast model presented is not sensitive to working distance, i.e. the SE collection efficiency. However, all graphene flakes were imaged at the optimal condition for efficient SE collection.

Also investigated were the influence of other imaging parameters on graphene SE contrast. Figure 5.21 shows SE images of a graphene flake taken at scan (frame) speeds of 122 ms, 220 ms, 731 ms and 10.2 s, in **a** to **d** respectively. Image quality (i.e signal to noise) is observed to increase with the increase in scan time. SE

contrast however remains constant for short scanning times (< 1 s) but decreases for longer times, as shown in Figure 5.22 (a). The decrease in graphene contrast at the longer scanning time is due to substrate charging. The variation in SE contrast with beam current is shown in Figure 5.22 (b). Beam current is controlled by the SEMs objective aperture, which is varied between 7 μm and 30 μm. Only a slight decrease in SE contrast was observed as the beam current increased. Variations in scan speed and beam current will therefore not greatly influence graphene SE contrast.

In conclusion, working distance can significantly affects the SE contrast while scan speed and beam current induce only slightly changes. In the SE contrast experiments, a working distance of 4 mm is selected to obtain best contrast.

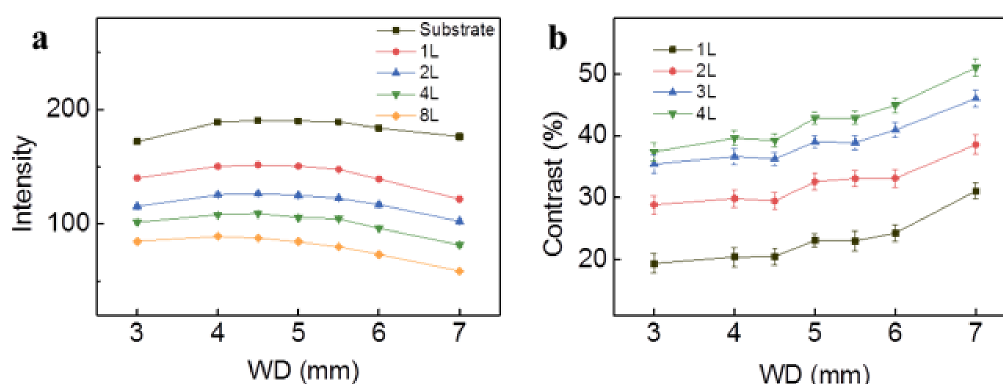

FIGURE 5.20: The variation of SE intensity **a** and SE contrast **b** with the change of working distance.

5.4.3 Layer dependence of graphene SE contrast and work function extraction

The layer dependence of graphene SE contrast in different situations was investigated. Few-layer graphene flakes on an SiO_2/Si substrate and imaged under various electron beam energies, placed on different metal substrates and imaged in SEM, and imaged in HIM and under different flood times are displayed in Figure 5.23 **a**, **b** and **c**, respectively. The observed layer dependence of SE contrast is similar to that presented in Figure 5.26, i.e. a rapid contrast decrease for the few layers (1 - 3) followed by an almost linear decrease in contrast for thicker layers.

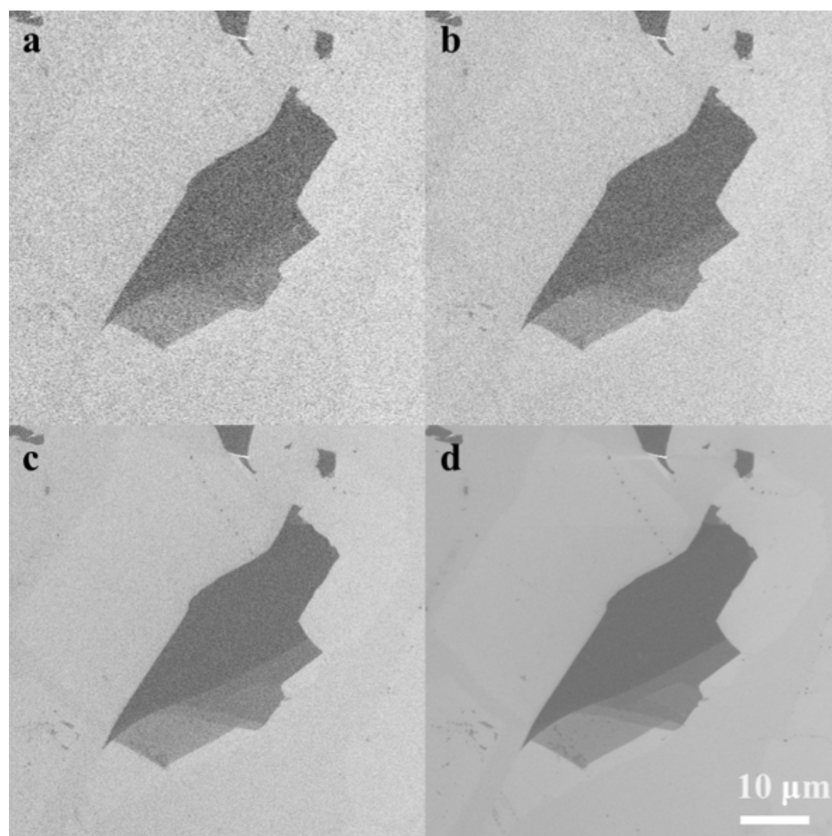

FIGURE 5.21: (**a** - **d**) SE images of a graphene flake acquired with scan (frame) times of 122 ms, 220 ms, 731 ms and 10.2 s, respectively

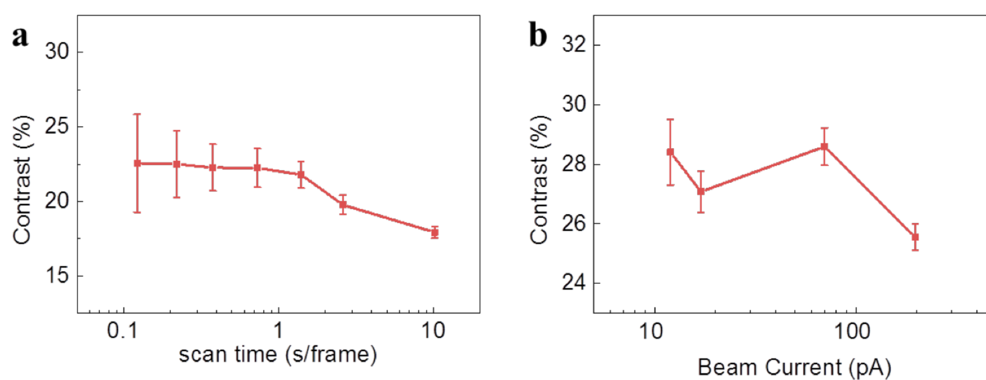

FIGURE 5.22: Observed variation in graphene SE contrast as a function scan speed (**a**) and beam current (**b**).

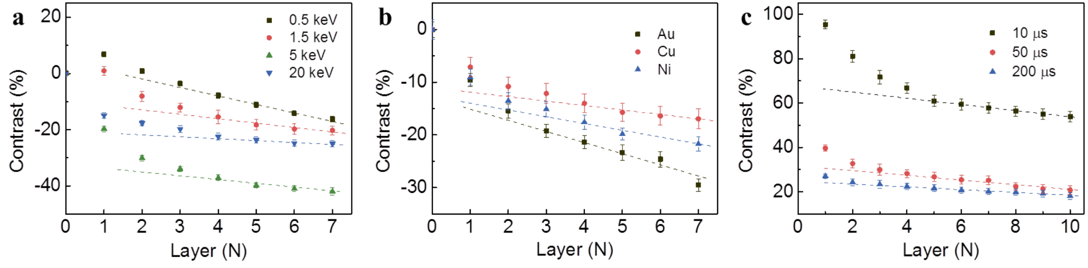

FIGURE 5.23: **a**, SEM SE contrast of graphene on a SiO_2/Si substrate, imaged in under primary beam energies of 0.5 keV, 1.5 keV, 5 keV and 20 keV. **b**, Graphene on different metal substrates (Au, Cu and Ni) imaged by SEM (5 keV). **c**, Graphene on a SiO_2/Si substrate and imaged by HIM (30 keV)with different flood times of 10 μs, 50 μs and 200 μs.

Figure 5.24 (a) and (b) show the layer dependence of graphene SE contrast in SEM (5 keV) and HIM (30 keV), respectively. Graphene work function is extracted using Equation 5.8. For the layer dependence of SE contrast in Figure 5.24 (a), the SE contrast values obtained for 1 - 4 layers were, -0.181 ± 0.011, -0.256 ± 0.013, -0.302 ± 0.013, -0.338 ± 0.012. The linear fitting to the 4 - 8 layers gave a slope of -0.0238 ± 0.0004, and the extended linear fitted values for 1 - 4 layers were -0.266 ± 0.002, -0.290 ± 0.002, -0.314 ± 0.002, -0.337 ± 0.002. The contrast for bulk graphene is measured from a thick graphite flake. Exhibiting a golden colour under an optical microscope, its layer thickness can be estimated as > 100 layers with a saturated value of contrast of -0.606 ± 0.013. According to Equation 5.8, the work function for 1 - 4 layer graphene is calculated as, 4.25 ± 0.06 eV, 4.45 ± 0.07 eV, 4.54 ± 0.012 eV, 4.60 ± 0.07 eV, respectively. From the slope of the 4 - 8 layer linear fitting we can estimate the IMFP (Equation 5.5) by a linear approximation for layer thickness a, as derived from the Seah and Dench model (Equation 5.4) [193].

$$\lambda(E) = a\frac{538}{(E-E_F)^2} + 0.41a(E-E_F)^{1/2} \tag{5.4}$$

$$C_g(N) \cong -\alpha\frac{d}{\lambda} \times N + [\alpha + \frac{\delta_g(N)}{\delta_s}(1+\beta\eta_s) - 1] \tag{5.5}$$

For the measurements in HIM, the SE contrast of bulk graphite is measured to be 0.435 ± 0.025. The slope of linear fitting is -0.0143 ± 0.0005. Using Equation 5.8

with n=5.3 the obtained work function values for 1 - 4 layer graphene were, 4.31 ± 0.02 eV, 4.43 ± 0.03 eV, 4.49 ± 0.03 eV 4.55 ± 0.03 eV, respectively.

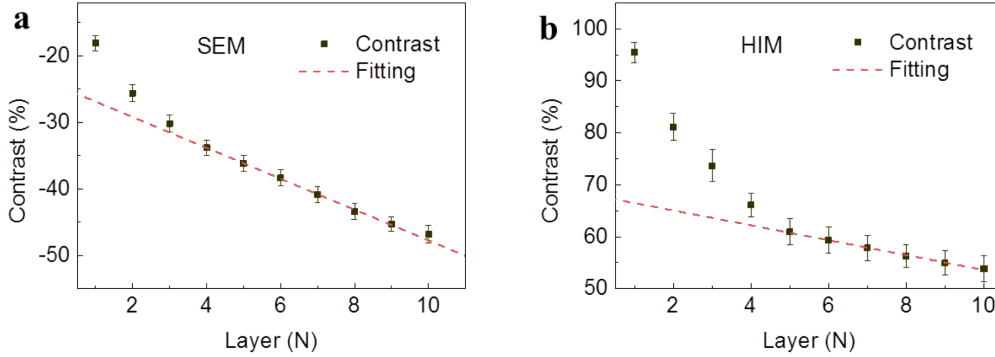

FIGURE 5.24: Layer dependence of graphene SE contrast with linear fitting for thicker layers in 5 keV SEM (**a**) and 30 keV HIM (**b**).

Figure 5.25 (a) and (b) show SE images of few-layer graphene with varying thickness captured in SEM and HIM respectively. The thickness of the graphene was determined by its optical contrast and Raman spectrum prior to the SEM imaging [191, 194]. These images show domains of uniform contrast, which correspond to regions of the same thickness. In Figure 5.25 (c), line-scan profiles of the SE contrast are sketched as a function of lateral locations. The intensity decreases monotonically as the thickness increases and it changes abruptly across the boundary of adjacent domains. The physical boundary of adjacent domains with one-layer thickness difference is atomically sharp, i.e. its lateral extension is at the atomic scale. The boundary revealed in SE images extends ca. 10 nm (see Figure 5.25 (d) and section 4.3.1, high resolution SE images of the graphene edges). Although the value is larger than the physical dimension, it is much smaller than the diffraction-limited value of ∼680 nm in an OM. Therefore, the SE contrast provides a much higher lateral spatial resolution than the optical contrast typically used in high-throughput measurement of graphene flake dimensions. This enables us to investigate the properties of graphene that correlate with SE emission at the nanometre scale.

To identify graphene thickness by using SE imaging, the question is whether we can assign a contrast value to a specific thickness, for example, a SE contrast value of ∼ -20 % in SEM indicating a single layer. To validate this, we need to demonstrate the reliability of the imaging conditions and the reproducibility of the

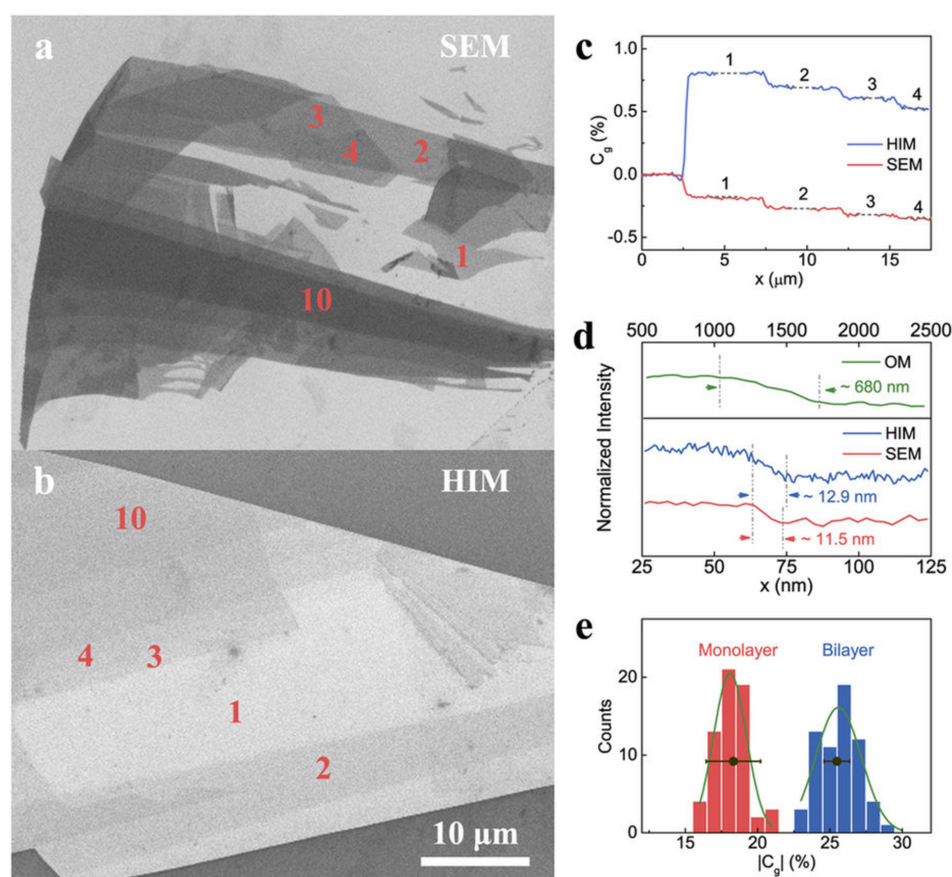

FIGURE 5.25: **a**, A SE image of few-layer graphene under 5 keV electron beam irradiation **b**, A SE image of few-layer graphene under 30 keV He^+ irradiation. The location of thin (monolayer to quad-layer) and thick (10-layer) graphene layers are marked by the numbers in the two images. **c**, Line profiles of SE contrast for the 1 - 4 layer graphene measured from Figure 5.25 a and b. Different graphene layer thickness corresponds to the distinct intensities that can be identified. **d**, High resolution line intensity profiles across the monolayer (right side) and bilayer (left side) graphene edge in three different microscopes: OM, SEM and HIM. The intensities are normalized by the left (brighter) side of bilayer graphene. The measured graphene edge width in OM is ~680 nm, much larger than that in SEM and HIM. **e**, Normalized intensity statistics of the monolayer and bilayer graphene under 5 keV electron beam irradiation. Both graphene layers obey the Gaussian distribution (green curves) with two peaks separated from each other. The two black circles with error bars show the contrast values of monolayer and bilayer graphene measured in a different SEM. Close values were obtained for the same layer thickness.

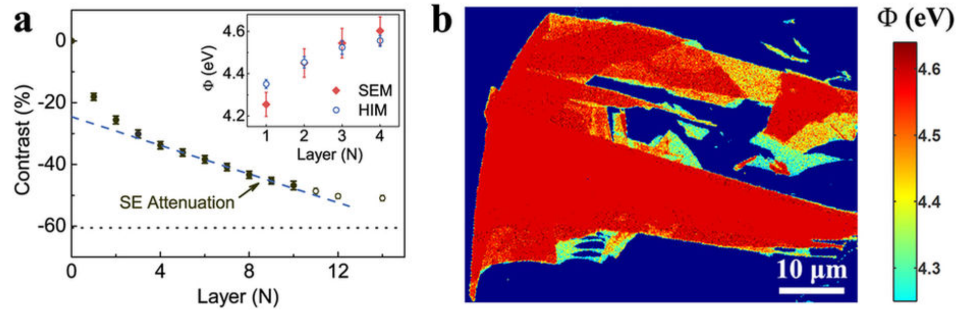

FIGURE 5.26: **a**, SE contrast for the 1 - 14 layer graphene under 5 keV electron beam irradiation. The relative SE intensities for 11 - 14 layer graphene were obtained from individual samples and marked as open black circles. The blue dashed line is the linear fitting to the layer graphene, which represents the attenuation effect of SEs from thick graphene $N \geq 4$ surface. The deviation from the linear fitting for the 1 - 3 layer graphene layers corresponds to the work function variation from the saturated value of $\Phi(4) = 4.60eV$. The work function for monolayer graphene is extracted to be $\Phi(1) = 4.26eV \pm 0.05eV$. The error bars were obtained from the deviations of measured intensity values. The dot line shows the saturated contrast (~ -60 %) value for very thick graphite. The inset figure shows the dependence of graphene work function Φ extracted from 5 keV electron beam imaging (red squares) and 30 keV He^+ beam imaging (blue open circles). The error bars were obtained from both the SE intensity errors and the linear fitting errors in Figure 5.26 a. **b**, A work function map of a graphene flake, which was transformed from the SE image of Figure 5.25 a. The cyan coloured area has a lowest work function around 4.3 eV while the red coloured area has a highest work function around 4.6 eV.

contrast under these conditions. Over 100 individual graphene flakes with different thicknesses varying from 1 - 10 layers on the SiO_2/Si substrate were imaged using the same imaging parameters. Figure 5.25 (e) shows the distributions of the SE contrast (absolute values) have a Gaussian profile with most probable values of (10 ± 1%) and (26 ± 2%) for monolayer and bilayer graphene respectively. The two distributions do not overlap. The absolute values of the maximized contrasts as well as the separation of the two distributions are instrument independent. For example, the two black circle data points in Figure 5.25 (e) are the SE contrast of monolayer and bilayer graphene that were obtained in another SEM instrument and they fall in the same intensity range (see section 4.3.5, statistics to graphene SE contrast). Figure 5.26 summarizes the thickness dependence of the graphene contrast in SEM. As the thickness increases, the contrast decreases. A linear dependence is observed for the thickness range of four to twelve layers, while the contrast decreases more rapidly than the linear relationship for thinner graphene.

The rate of contrast reduction becomes slower for thicker layers and the contrast appears to be saturated at about 14 layers.

Based on the consistent SE contrast of graphene, we now demonstrate quantitative extraction of the work function of graphene from SE imaging. The SE intensity I_g collected from the supported graphene is contributed from two sources: the SEs emitted from the graphene and the contribution of the substrate. As mentioned in Equation 5.3, the SE emission of the graphene was excited by the primary beam I_p and the backscattered electrons from the substrate $\eta_s I_p$. The SEs of the substrate that diffuse through the graphene also contribute to the graphene intensity. The attenuation of the substrate SEs by the graphene depends on graphene thickness and the total reflection at the graphene-vacuum interface. The attenuated substrate contribution exhibits an exponential decrease as layer thickness d increases, i.e. $\alpha I_s exp(-N \cdot \frac{d}{\lambda})$ where α is due to the total reflection, I_s is the SE intensity of the substrate given by $I_s = \delta_s I_p$, N is the graphene layer number, $d = 0.335$ nm is the thickness for one layer of graphene and λ is the IMFP of SEs in graphene. Therefore, the SE contrast for the N-layer graphene is given by:

$$C_g(N) = \frac{\delta_g(N)}{\delta_s} \cdot (1 + \beta \cdot \eta_s) + \alpha \cdot e^{\frac{N \cdot d}{\lambda}} - 1 \qquad (5.6)$$

Equation 5.6 quantitatively describes the experimental results presented in Figure 5.26 (a). The linear contrast decrease for the 4-12 layer graphene indicates $\delta_g(N)$ can be regarded as a constant for $N \geq 4$ and $N \cdot \frac{d}{\lambda} \ll 1$. We used the 4-8 layer graphene (blue dashed line in Figure 5.26 (a)) to fit the linear contrast decrease and obtained an IMFP value of $\lambda \approx 5.7 \pm 0.1$ nm, which is quite close to the value estimated by the Seah and Dench model [193]. The value of IMFP also explains the slower rate of contrast reduction and the contrast saturation for thicker layers. For the thick graphite ($N > 100$) a saturated contrast of $\sim -0.60 \pm 0.001$ is observed. It corresponds to a situation in Equation 5.6 where the IMFP is much shorter than the thickness ($N > 10$), and the substrate attenuation effect can be ignored ($e^{-\frac{N \cdot d}{\lambda}} \approx 0$). The SE contrast becomes: $C_g^s = [\frac{\delta_g}{\delta_s} \cdot (1 + \beta\eta_s) - 1]$, which gives a similar value of $\sim$ -0.6.

Most importantly, the deviation from linearity for graphene thinner than four layers (see Figure 5.26 (a)) indicates δ_g depends on the thickness. The differential

of δ_g to the SE energy E_K, i.e. the SE energy spectrum can be well described by Chung and Everhart's model [62]:

$$\frac{\partial \delta}{\partial E_K} \propto \frac{E_K}{(E_K + \Phi)^n} \tag{5.7}$$

where Φ is the work function of graphene. The index number n can be determined as $n = 4.6$ for graphene (see the discussion below). Therefore is determined by the work function, and we can extract the work function directly from the observed contrast, which is given by:

$$\phi(N) = \phi(4) \left[1 + \frac{C_g(N) - C_g^i(N)}{C_g(\infty) + 1} \right]^{1/(2-n)} \tag{5.8}$$

where $C_g(N), C_g^i(N), C_g(\infty)$ are the measured graphene contrast, the extrapolated value of the linear relationship and the graphite contrast respectively. $\phi(4)$ is the work function of four-layer thick graphene and n is given by the SE energy spectrum.

The evolution of work function for few-layer graphene is presented as red squares in the inset of Figure 5.26 (a). The work function of monolayer graphene is determined to be 4.26 $\pm$ 0.05 eV. The value increases to 4.60 $\pm$ 0.07 eV for quad-layer graphene. Similarly, the graphene work function can also be extracted from the He^+ irradiated SE images (see section 5.4.3). The work function varies from 4.35 $\pm$ 0.02 eV for monolayer to 4.56 $\pm$ 0.03 eV for quad-layer graphene. The two different excitation sources give a similar work function value for each layer, which is consistent with previous reports [88, 195, 196]. This supports the quantification developed in our contrast model. The work function map can be calculated from the corresponding SE image, as shown in Figure 5.26 (b). A significant difference in work function can be clearly observed between the thin graphene layers while the difference becomes less distinguishable for thicker layers.

To further verify our model, we measured the SE energy distribution of the sample. Figure 5.27 (a) shows the measured SE energy spectrum for the freestanding monolayer graphene in SEM with a maximum around 1.5 eV. SE spectra of several few-layer freestanding graphene (monolayer through quad-layer and thicker) were measured and then fitted using the reported work function values (from 4.3 eV for

monolayer to 4.6 eV for thicker than quad-layer) and Equation 5.7. The optimal index number was determined to be from the fitting results (see section 5.5.3.6). The fitting of the freestanding monolayer graphene spectrum by 5.7, with $n = 4.6$, gives a work function value of 4.33 eV. A similar energy spectrum measurement was also carried out in HIM and the fitting index number was determined to be $n = 5.3$ for graphene. Since the measured graphene SE spectrum and its SE contrast were both formed by the partially collected SEs, our work function extraction using Chung and Everhart's SE distribution equation in Figure 5.26 is reliable. The error is less than 0.05 eV.

The measured spectra of the substrate supported graphene also support the validity of our SE contrast model. Figure 5.27 (b) shows the SE spectrum of monolayer graphene on a SiO_2/Si substrate, in comparison with the spectra of freestanding monolayer graphene and a SiO_2 surface. According to our SE contrast model, the SE emission from graphene on a substrate contains the SEs generated within graphene and those which diffuse from the substrate. These two contributions should also be revealed in the SE spectrum of graphene on a substrate. We calculated this SE spectrum using the measured spectra of freestanding monolayer graphene and the SiO_2 surface, the result is shown as a green dashed line in Figure 5.26(b). The peak properties (height, position and decay) in the calculated spectrum are similar to that of the peak in the measured spectrum. This similarity supports our contrast model.

The work function variation with number of graphene layers observed in SE imaging is related intimately with the electronic structure of graphene. Figure 5.26 (c) shows the band structures of the monolayer and quad-layer graphene on a SiO_2/Si substrate. The band structure of monolayer graphene consists of a simple linear energy dispersion, while thicker graphene has a different band structure. For example, the band structure of bilayer graphene has a parabolic shape, while the band structure of quad-layer graphene becomes more complex and similar to bulk graphite [66]. These band structure differences cause variations in the energy difference between the Fermi level E_F and the potential energy E_0 at infinite distance from the system, i.e. a work function difference. For thicker graphene layers, the higher surface work function will result in a larger energy loss for SEs while approaching the surface. Therefore less SEs can escape from the thicker graphene surface. This is in accordance with the energy spectra measurements in

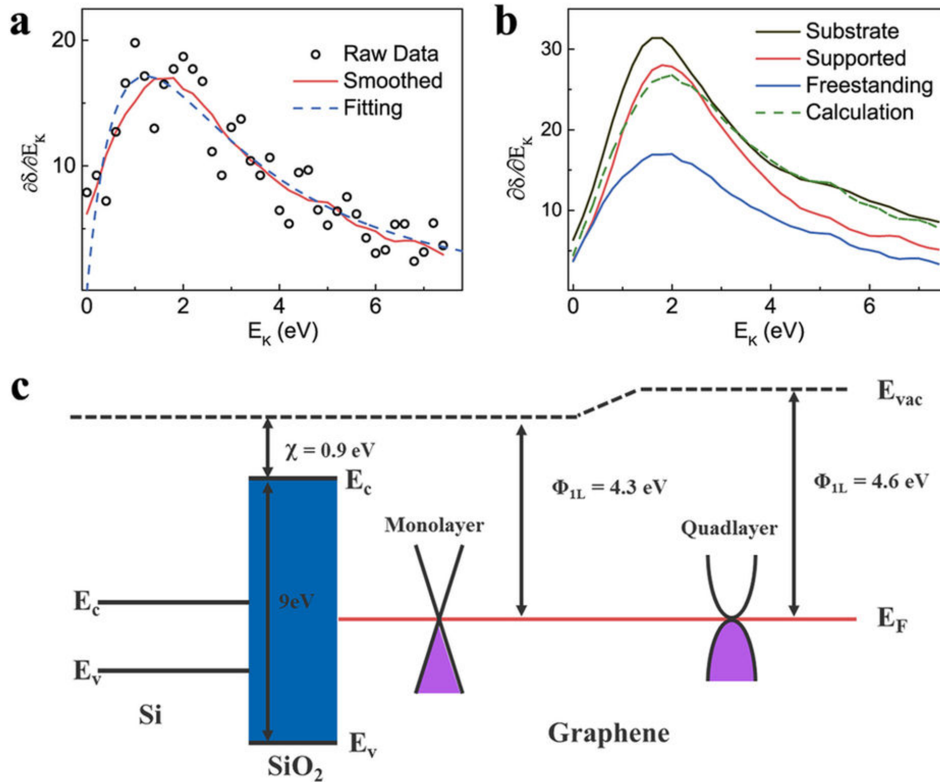

FIGURE 5.27: **a**, SE energy spectrum for freestanding monolayer graphene. The result contains raw data (black open circles), smoothed spectrum (red line) and spectrum fitted by Chung and Everhart model (blue dashed line). The spectrum exhibits a maximum peak around a SE energy of 1.5 eV and can be well fitted by Equation 5.7 with $n = 4.5$. The fitting value of work function for the freestanding monolayer graphene is 4.33 eV. **b**, SE spectrum of the substrate supported monolayer graphene (red line), in comparison with the spectra of freestanding monolayer graphene (blue line) and the substrate (black line). The green dashed line shows the spectrum calculated by our SE contrast model. **c**, Band structure diagram of graphene on a SiO_2/Si substrate. The band structures of the Si substrate, SiO_2 layer, monolayer and quad-layer graphene are shown in the diagram from left to right.

Figure 5.26 (a), in which the spectrum for quad-layer graphene has a lower peak height than that of monolayer graphene, indicating a decrease in SE intensity.

5.4.4 Summary of quantitative SE imaging for work function extraction and layer identification of graphene.

In this work a method to quantitatively analyse SE images of graphene on SiO_2/Si substrates has been established. It has been demonstrated that the SE contrast exhibits a universal visibility of few-layer graphene. Graphene with layer numbers of less than ten can be determined from the SE contrast. Besides the quantification of graphene layer thickness, the work function of few-layer graphene can also be quantified by extracting the SE attenuation contributions from the layer-dependent SE contrast. This method provides a high-throughput measurement of graphene's work function and extends the application fields of SE contrast to quantitative analysis.

5.5 Fabrication and application of a SE energy filter in HIM and SEM

5.5.1 SE energy filter design and fabrication

A simple *High-Pass* filter design was chosen, which works on the principle of limiting the kinetic energy of the SEs prior to their arrival at a detector (e.g. ET). As shown in Figure 5.28 (a), limiting SE energy can be achieved by applying a negative bias to a retarding grid, placed directly over, and in close proximity to, the irradiated specimen. The negative bias generates a retarding field, relative to the specimen bias, which prevents SEs of a lower potential from reaching the detector. By setting the filter bias prior to the acquisition of a specimen image, then changing the bias prior to the acquisition of a second image, the differences observed in image intensity can be directly related to SE emission characteristics of the specimen. To ensure the success of this technique, the irradiation and detection parameters must remain unchanged between image acquisitions. When performed over a large number of image acquisitions - on specimens of known work function and by applying small changes to energy filter bias ($\sim$0.1 V) - the filtering efficiency of the energy filter can be determined. Once calibrated, the energy filter can be used to generate SE energy spectra and energy filtered SE images.

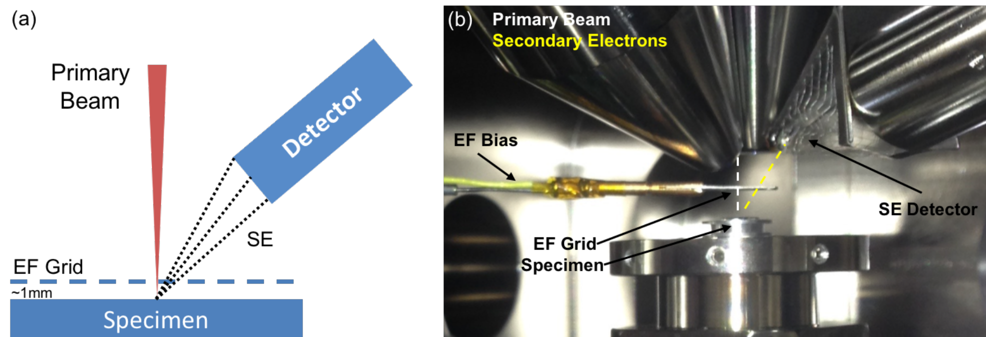

FIGURE 5.28: (a) A graphic depicting the placement of the EF retarding grid relative to the specimen and SE detector. (b) The fabricated EF device in-situ in the HIM.

The following practical requirements were considered when designing the energy filter. To produce a homogeneous filtering effect, a planar grid composed of symmetrical mesh-patterns and made from a uniformly conductive material was required. The physical dimensions of grid had to provide adequate filtering without obscuring the specimen during image acquisition. To minimise the impact of SE emission-angle on spectral resolution, in-situ optimisation of grid height above the specimen was required. To accommodate specimens of different heights, and to centre the grid over a specific region of interest, an adjustable filter mounting with sub-μm precision movements (horizontal and vertical) was required. Safe retraction of the energy filter during specimen transfer, without venting the microscope chamber, was also required. Finally, the electrical biasing of the filter would be supplied from a source external to the microscope chamber. An overview of the energy filter design is outlined in Figure 5.28 (b).

A 50-mesh hexagonal Cu TEM grid was chosen for the energy filter retarding grid. This is displayed in Figure 5.29 (a). It had an external diameter of 3.05 mm and a thickness of $\sim$10 μm. The Cu lines within the mesh were $\sim$60 μm wide. The edges of the hexagonal shapes which formed the grid were $\sim$275 μm in length. This gave each hexagon an area of $\sim$0.2 mm^2. The grid was mounted to a flat and rigid Al support, measuring 20 mm $\times$ 5 mm and a thickness of $\sim$200 μm. The grid was secured to the Al support with conductive Ag paste. The mounting of the grid to the Al support is displayed in Figure 5.29 (b). The opposite end of the Al support was inserted into a brass connector, attached to which was a vacuum compatible conductor. The brass connector was mounted to, but insulated from, a mild-steel rod. This supporting rod, a reformed paper clip, was then inserted into

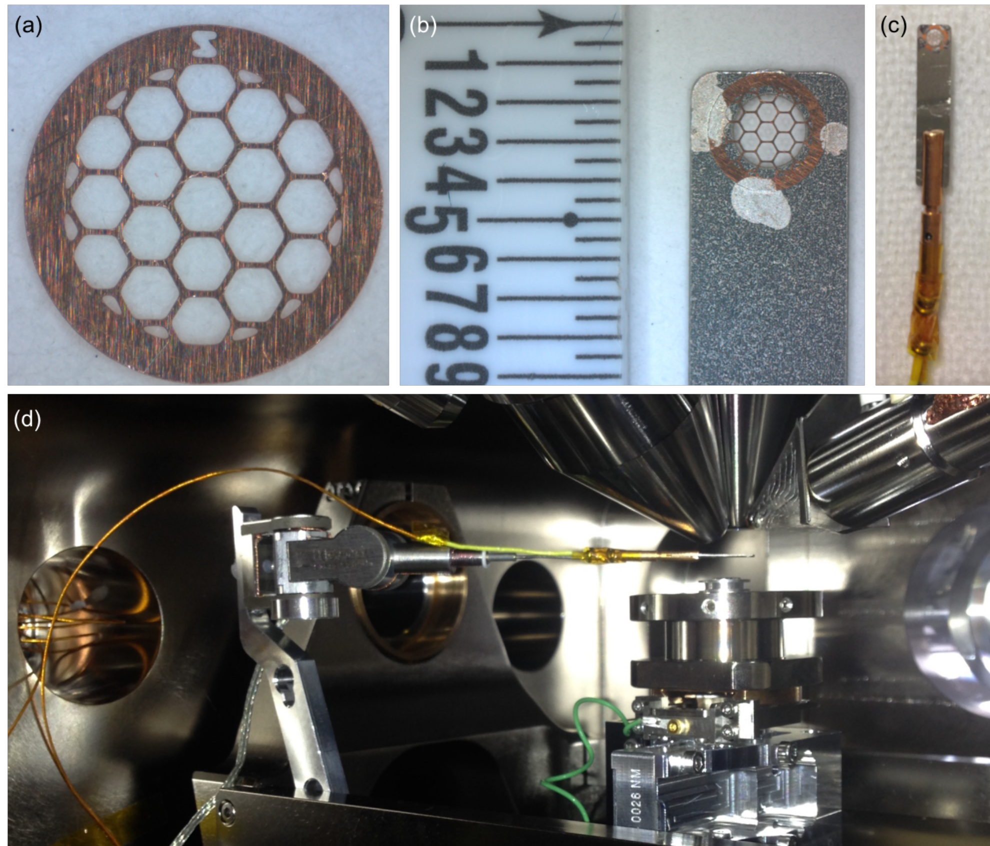

FIGURE 5.29: (a) The EF retarding grid, a circular 3.0 mm hexagonal Cu mesh, (b) mounted to the Al support, (c) both mounted to the micro-manipulator biasing connector and (d) full energy filter assembly as mounted in the HIM

a specific mounting attachment for a Kliendeik MM3A micro-manipulator. This is displayed in Figure 5.29 (c). The energy filter assembly was then attached to the micro-manipulator and both were fixed to the microscope stage assembly by a support bracket. The completed SE energy filter device can be seen in Figure 5.29 (d).

The external biasing of the filter was delivered through an electrical vacuum feed-through flange. On the outside of the flange a *Bayonet Neil-Concelman* (BNC) coupling enabled an electrical connection to a source meter (Keithley 2400) and on the inside of the flange an *Ultra High Vacuum* (UHV) Kapton wire (AWG 35) made the electrical connection to the retarding grid. Once the construction of the energy filter was complete, a series of test biases, of ± 1, 5 and 10 V, were placed between the external electrical connection and the microscope ground. Then, using a *digital volt-meter* (DVM), the electrical potential between the retarding grid and

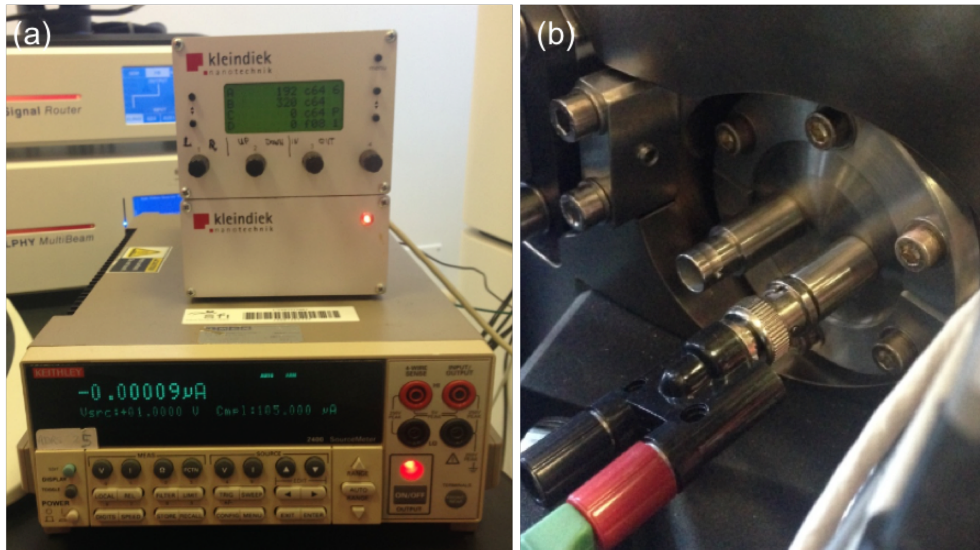

FIGURE 5.30: (a) Micro-manipulator control unit for in-situ positioning of the EF grid and source meter for glsEF bias control. (b) Electrical vacuum feed-through connection with BNC biasing connection to source meter.

the microscope ground was checked and compared to the test bias. A difference of $< 3\%$ was observed between the supplied and measured bias. Images of the EF external control and biasing can be seen in Figure 5.30 (a).

Prior to the assembly of the energy filter, all components were thoroughly cleaned as follows. The hexagonal TEM grid and the Al support were ultra-sonically cleaned for 10 minutes in IPA and blown dry with compressed N_2. The TEM grid was reactive ion cleaned in an Argon-Oxygen (75:25) plasma for a further ten minutes. The remaining components were wiped down with 100% IPA using lint-free cloth. The Al support, the brass connector, the insulated conductor and the micro-manipulator support bracket were re-purposed components of an SEM SE detector.

5.5.2 SE energy filter calibration

5.5.2.1 Initial evaluation

A Ta (110) specimen was used to test the SE energy filter. Mounted to a standard SEM specimen stub and treated to a ten-minute plasma clean immediately prior to insertion into the HIM. Once loaded, the microscope imaging was enabled and

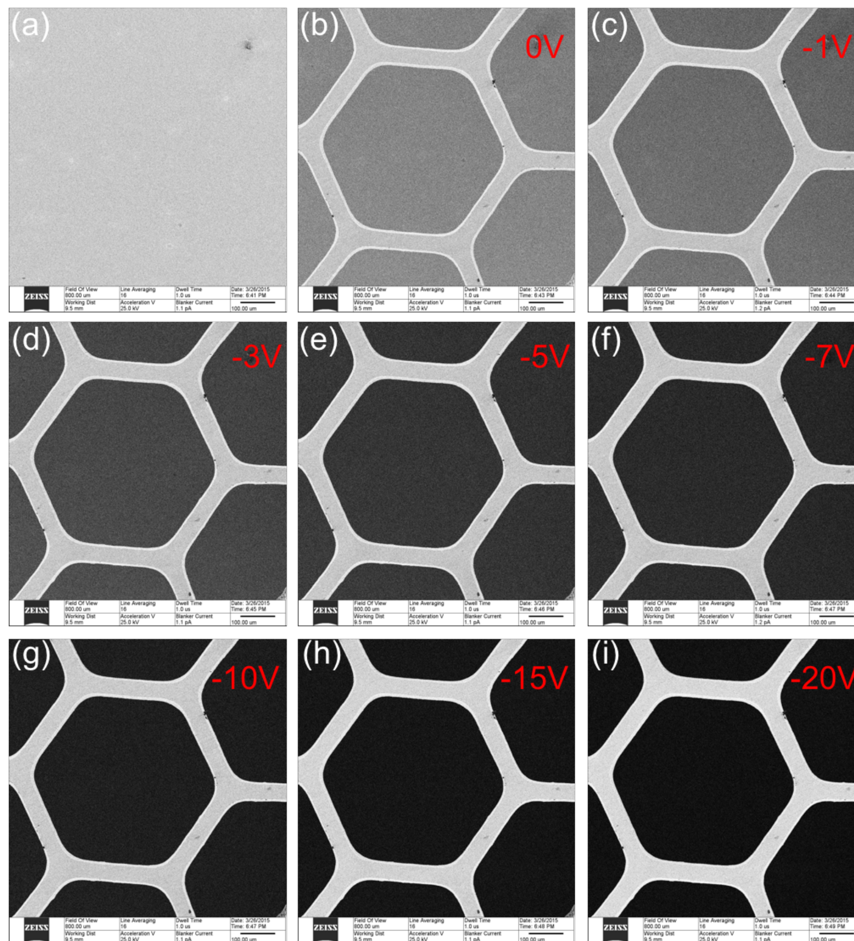

FIGURE 5.31: HIM energy filter test images from an un-biased Ta (110) specimen. (a) Prior to the insertion of the EF. (b) post insertion of the EF at an initial 0 V bias and, (c) - (i) with it biased at -1, -3, -5, -7, -10, -15 and -20 V, respectively.

specimen was centred in the FOV. The operating parameters of the microscope were adjusted to deliver a ∼1pA beam at an acceleration voltage of 25 keV. The specimen stage was adjusted to give a 20 mm WD and the micro-manipulator controls were used to position the energy filter above the specimen and in the centre FOV. Once in place the top surface of the filter was focused upon and the focal distance was noted. The objective focus of the microscope was then set to 9 mm and the vertical position of the grid was adjusted so that its top surface was brought to the focus plane. With the filter at the correct position the specimen height was adjusted to enable a 10 mm WD. This set a ∼1 mm gap between the filter and the specimen. In this short gap the retarding field could effectively suppress SE emission from the specimen.

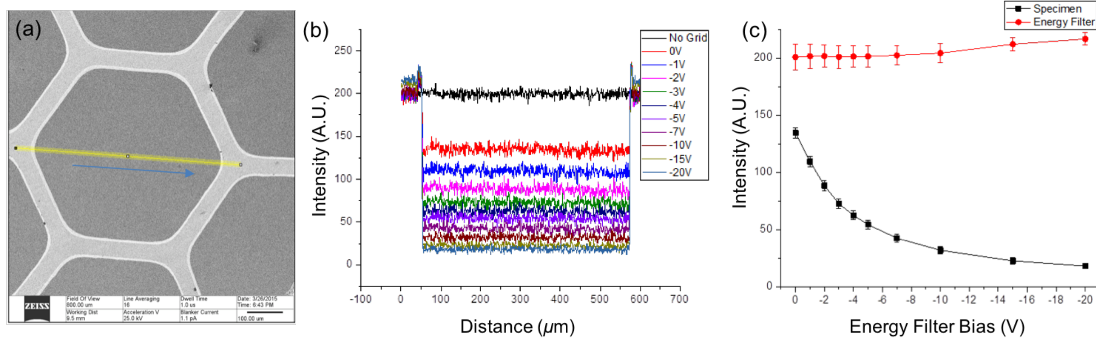

FIGURE 5.32: (a) HIM image of the EF suspended over the Ta (110) test specimen. Both specimen and EF are un-biased (0 V). The region of the specimen from where the SE intensity profile was acquired is indicated by the yellow line. (b) The intensity profiles were acquired from the energy filtered imaging sequence over a EF biasing range of 0 to -20 V. (c) The relationship between the averaged line intensity and the applied energy filter bias.

Before testing the energy filter the FOV was set to 800 μm, a clean surface region was centred in the image and the specimen surface was brought into focus. At this large FOV, the effect of the biasing field on SE emission from the specimen and grid, i.e. their SE intensity level, could be tested simultaneously. Prior to biasing the filter the image contrast and brightness were set to 50 and 60, respectively. With imaging dwell time set to 1 μs and line averaging to 16, an image of the grid and specimen was acquired. The grid was then biased to -1 V and without changing any microscope parameters, a further image was acquired. The energy filter was biased a further 8 times, at -2, -3, -4, -5, -7, -10, -15, -20 V and after each biasing step an image was acquired. Finally, the energy filter was moved horizontally out of the FOV and an image of the specimen without the grid was acquired. The acquired images of the energy filter test are displayed in Figure 5.31.

The test images were uploaded to "Image-J" and using its image stacking and line profile functions, variations in image intensity observed across the hexagonal filter area was evaluated for all bias settings. The results of this evaluation are displayed in Figure 5.32 (b) and are explained as follows. With the grid removed, the specimen surface intensity is measured at 200 $\pm$ 10 (A.U.). With the grid inserted, and at 0 V bias, the specimen surface intensity is reduced to 135 $\pm$ 10 (A.U.). Upon application of the energy filter bias, average surface intensity decreases with increasing negative bias. The line profiles at each energy filter bias

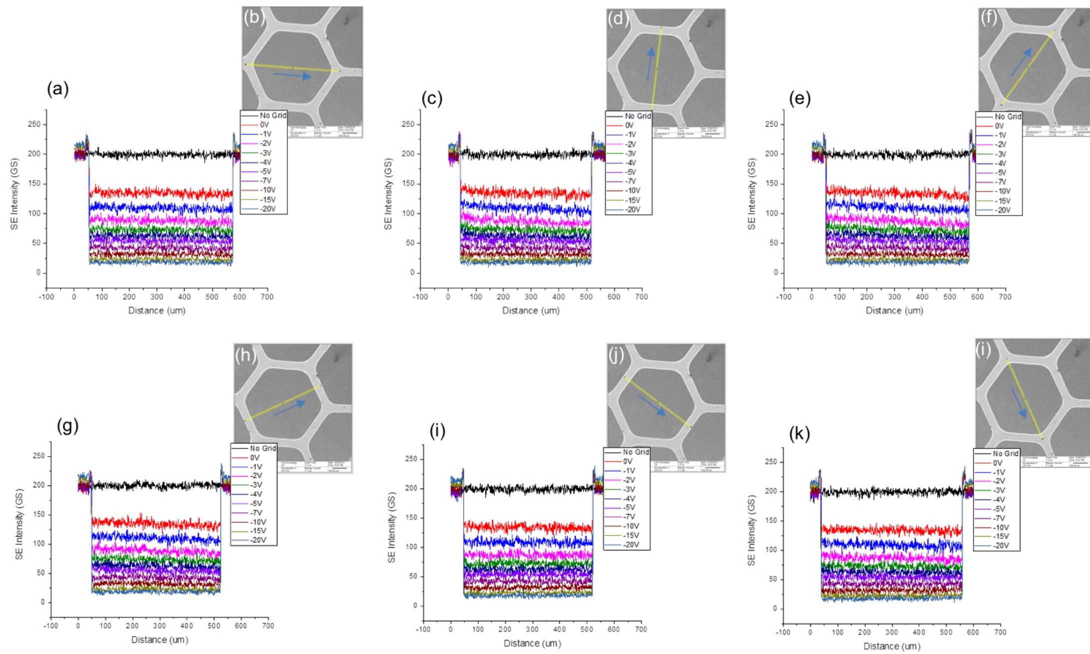

FIGURE 5.33: The homogeneous filtering effect of the retarding grid on SEs emitted from the specimen from within the hexagonal area.

remain uniform regardless of the distance from the Cu grid lines. This indicates a homogeneous filtering effect along the central axis of hexagonal area.

Figure 5.32 (c) shows the average image intensity values for the specimen and the grid over the applied bias range of 0 to -20 V. Specimen intensity is observed to decrease with the increase in grid bias. The intensity of the energy filter grid is constant between 0 and -10 V, however between -10 to -20 V grid intensity increases by ∼7%. This increase suggests a uniform spatial electric field distribution below -10 V and a non-uniform distribution above -10 V, however this deviation is still within an acceptable range.

To verify the homogeneity over an entire hexagonal energy filtering area, a series of line intensity profiles were analysed along five other axes. The results of which are presented in Figure 5.33. These results show a homogeneous energy filtering effect on SEs emitted from the specimen within the hexagonal grid area.

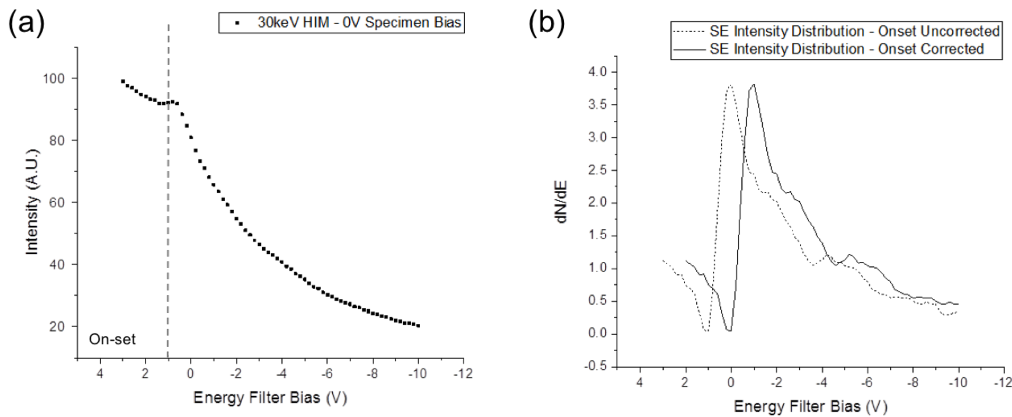

FIGURE 5.34: (a) He^+ ion induced SE intensity profile from an unbiased Ta (110) test specimen, upon the application of an increasing negative EF bias. (b) The corresponding SE energy distribution, referenced to the EF bias, corrected and uncorrected to the SE onset

5.5.2.2 SE energy calibration

Figure 5.34 (a) shows the change in He^+ ion induced SE image intensity from an unbiased Ta (110) test specimen upon the application of an increasing negative energy filter bias. The images were captured in a HIM in the same manner described in the initial testing of the energy filter, section 5.5.2.1, however the microscope and acquisition parameters were changed as follows. The ion acceleration voltage was increased to 30keV, the FOV was reduced to 55 μm, line averaging was set to 8 and pixel dwell time was set to 0.2 μs. Due to variations in reference bias, the placement of the un-biased energy filter over the un-biased specimen resulted in an immediate reduction in image intensity. As a result, the SE on-set, the point at which the kinetic energy of specimen SEs are filtered, was reduced below 0 V. To overcome this an initial +3 V bias was placed on the retarding grid. This was then reduced to -10 V, in 0.2 V steps.

As SE image intensity is directly proportional to SE emission, intensity differential (dN/dE) can be used to generate a SEED from an irradiated specimen. A SEED for the Ta test specimen intensity profile, referenced to the applied energy filter bias, is displayed in Figure 5.34 (b). When the intensity data was shifted so that the SE onset (1.0 V) was aligned to the 0 V position, the corrected SEED gives peak SE energy at 1.0 eV. The variation in SE intensity over the remainder of the filtered energy range is indicative of interactions occurring within the SE escape

depth of the specimen. To correlate specimen interactions to the features in the SEED, the ratio of retarding grid bias (ΔV_{GRID}) to the kinetic energy of the SEs (ΔE_K) was required.

The shape of the SEED obtained under He^+ ion extraction given by [59] has been defined in Equation 2.5, as $\frac{dN}{dE} \sim \frac{E_{se}}{(E_{se}+\phi)^n}$ where, E_{se} is the kinetic energy of the emitted SEs, ϕ is the material work function and n is the exponent. In the case of the Ta (110) test specimen, its ϕ is known and therefore its SEED can be fitted and checked for accuracy. Before this is done the grid bias (V) is directly converted to SE energy (eV), in order to complete the plot fittings. The value of n is derived from the slope of the logarithmic transform of the SEED shape, Equation 5.9, and displayed in Figure 5.35. Taking $n = 4.584$ and a text book value for the ϕ of Ta (110) as 4.8, a non-linear curve was fitted to the SEED of the test specimen. This is displayed in Figure 5.36. The fitting is a close match to the general shape of the SEED plot, suggesting a $\Delta V_{GRID} : \Delta E_K = 1{:}1$.

$$\ln\left(\frac{\frac{dN}{dE}}{E_{se}}\right) \sim n\ln(E_{se}+\phi) \tag{5.9}$$

To confirm this relationship, the ϕ for Ta (110) was determined from the uncorrected SEED data presented in Figure 5.34 (b) using the HIM *F(Ese)* dependence given in Equation 2.7. By plotting the dependence *F(Ese)* as a function of the SE energy (eV), a value for ϕ was acquired by extrapolating the plot fitting to its zero value. This is displayed in Figure 5.37 and gives an intersection of -4.8 eV and thus a ϕ value of 4.8 eV.

The uncorrected SEED data was used for the *F(Ese)* function to account for true bias applied on the emitted specimen SEs, by the retarding field established between the specimen and energy filter grid. The correspondence between text book and measured value for ϕ, confirms a 1:1 relationship between applied EF bias (V) to SE energy (eV), in this experimental set-up.

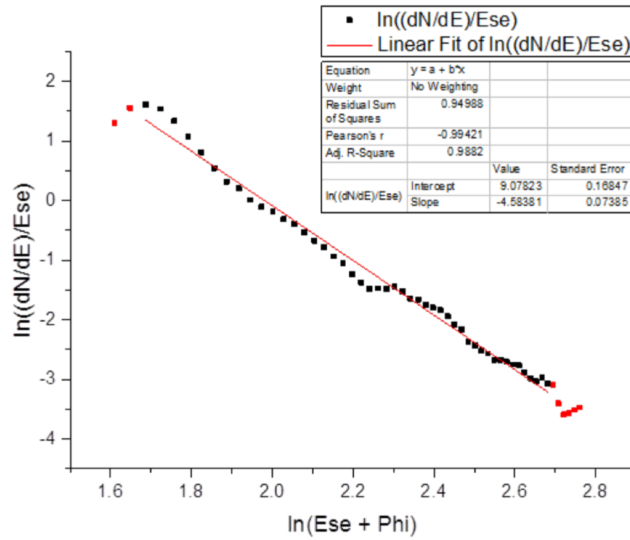

FIGURE 5.35: The logarithmic transform of the SEED shape collected from the Ta(110) test specimen, using a textbook value of 4.8 eV for ϕ. The fitting gave a slope of -4.584.

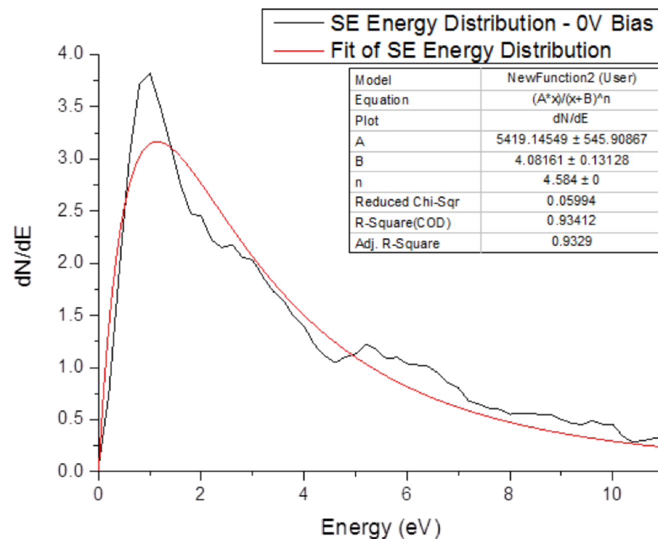

FIGURE 5.36: The SEED from the Ta (110) test specimen fitted to a non-linear curve using Equation 2.5 with n = 4.584.

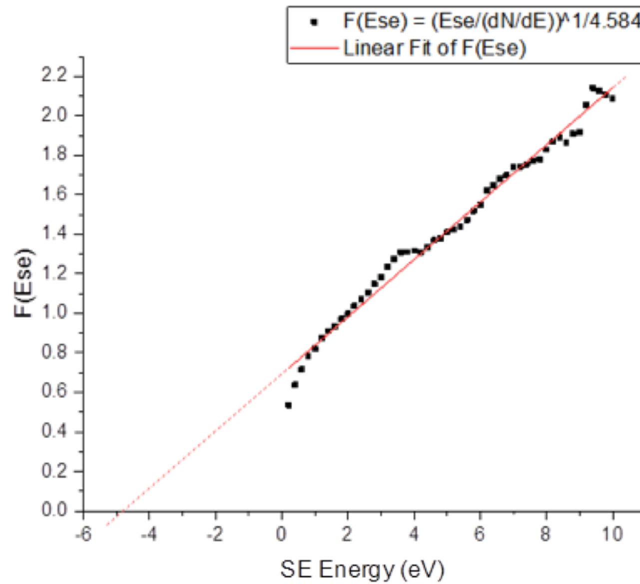

FIGURE 5.37: The dependence *F(Ese)*, as given in Equation 2.7, is plotted as a function of SE energy (eV) and delivered a value for $\phi = 4.8$ (eV).

5.5.2.3 Spatial electric field characterisation

The effect of specimen bias.

The effect of specimen bias was evaluated to determine its influence on the spatial electric field distribution of the retarding grid, i.e. its filtering efficiency. This was achieved by completing three further image sets, using the same energy filter retarding grid and microscope set-up used in section 5.5.2.2. Each image set was acquired on a clean, un-irradiated region, with the specimen bias set to -1, -3 and -5 V. For each image set, the positive 3 V EF starting bias was referenced to the specimen bias, i.e. for -1 V specimen bias EF biasing commenced at 2 V, for -3 V specimen bias EF biasing commenced at 0 V, and for -5 V EF biasing commenced at -2 V. The resultant image intensity profiles are displayed in Figure 5.38 (a) along with the intensity profile for the 0 V specimen bias. The shape of the intensity profiles changes with the increase in specimen bias, even though the same relative EF biasing range is applied in each case.

A SEED for each intensity profile presented in Figure 5.38 (a) was generated by referencing each profile to the applied energy filter bias. These are presented in Figure 5.38 (b) and reveal four distinct energy distributions. The onset of SE

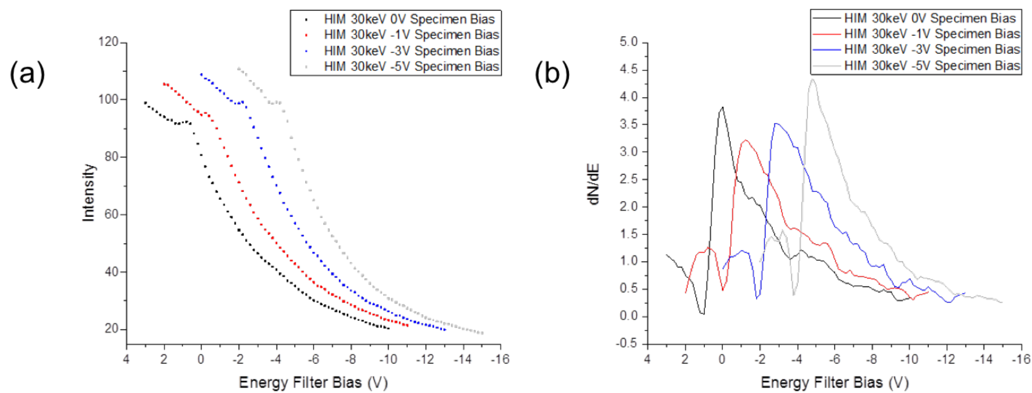

FIGURE 5.38: (a) He^{+} ion induced SE intensity profiles from a Ta (110) test specimen, biased at 0, -1, -3 and -5 V, upon the application of an increasing negative EF bias. (b) The corresponding, SE energy distributions, referenced to the EF bias.

energy filtering for each specimen bias corresponds to their distribution minima. These were determined at 0.0, -1.8, and -3.8 V for -1, -3 and -5 V specimen bias settings, respectively. Peak heights and FWHM vary with specimen bias. The 0 V SEED is almost a mirror image of the -5 V SEED, however peak height and FWHM for are greater for the latter. The SEEDs for -1 V and -3 V also display the same mirror-like attributes. Relative to the 0 V and -5 V distributions, a reduced peak height and greater FWHM are observed for the -1 V and -3 V SEEDs. In comparison to 0 V SEED, the features present above peak height in all other distributions, exhibit distinct variations.

Presented in Figure 5.39, Figure 5.40 and Figure 5.41 are the evaluation results for the SEEDs associated with the stage bias settings of -1, -3 and -5 V. They were evaluated for, accuracy of fit to HIM SEED shape and extraction of specimen work function. All of the SEED shapes show a good match to their fitted curves. The ϕ values for -1 and -5 V specimen bias vary slightly from the Ta (110) text book value, at 5.1 and 4.7 eV, respectively. The -3 V specimen bias however, reveals exact correlation to the correct ϕ value, 4.8 eV.

The SEEDs for all stage bias settings were corrected so that their onsets coincided with 0 eV position. These are presented in Figure 5.42 and show the effect specimen bias has on the retarding field of the energy filter. Altering specimen bias does not change the general shape of the SEED or peak SE energy position, however it has been show to effect fine features in the energy distributions. Such features are

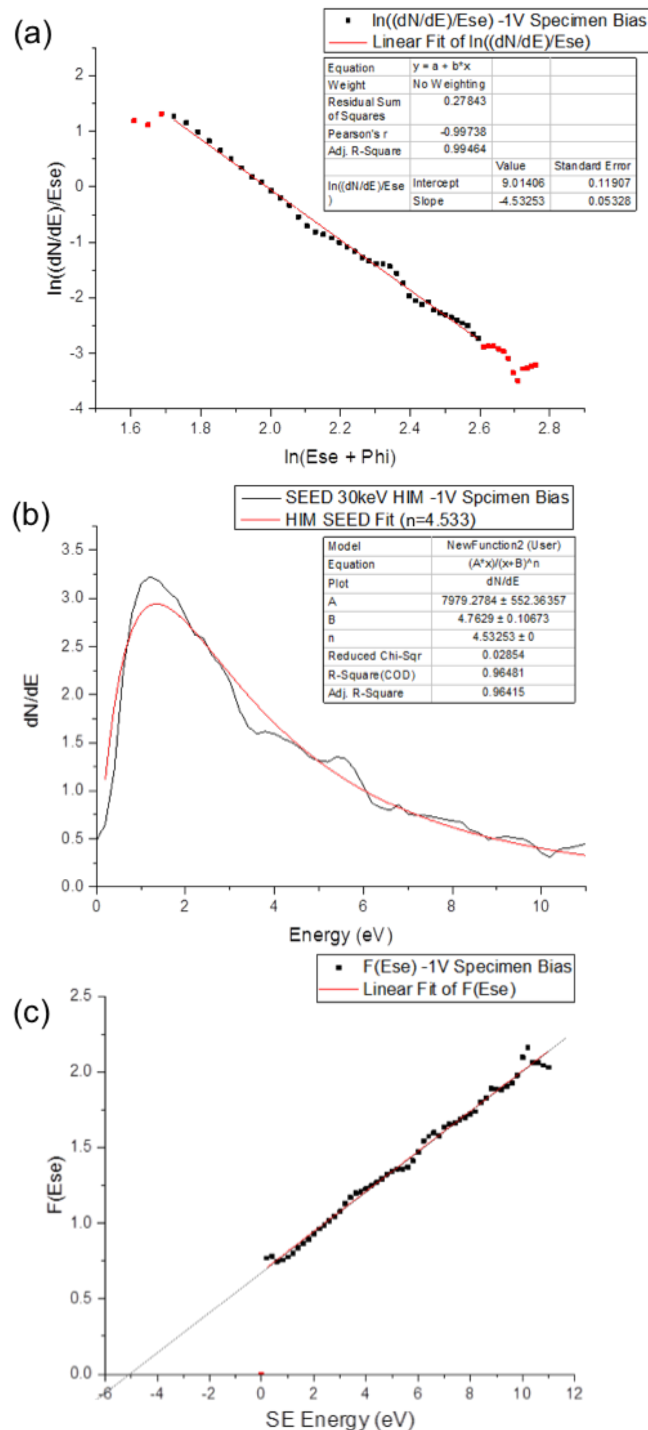

FIGURE 5.39: (a) Logarithmic transform of the SEED shape collected from the Ta(110) test specimen, biased at -1 V. (b) The SEED fitted to a non-linear curve using $n = 4.533$, given by the slope of the fitting in (a). (c) The dependence *F(Ese)*, plotted as a function of SE energy which gives a value for $\phi = 5.1$ (eV).

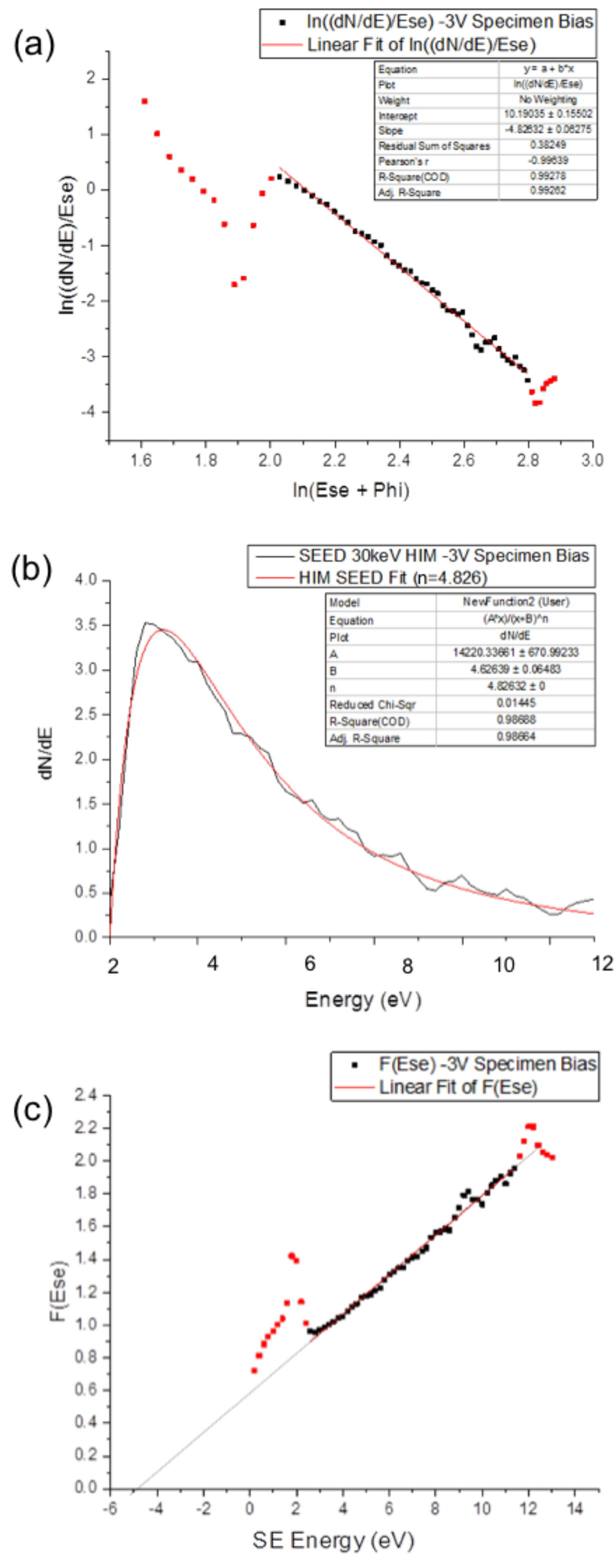

FIGURE 5.40: (a) Logarithmic transform of the SEED shape collected from the Ta(110) test specimen, biased at -3 V. (b) The SEED fitted to a non-linear curve using $n = 4.826$, given by the slope of the fitting in (a). (c) The dependence *F(Ese)*, plotted as a function of SE energy which gives a value for $\phi = 4.8$ (eV).

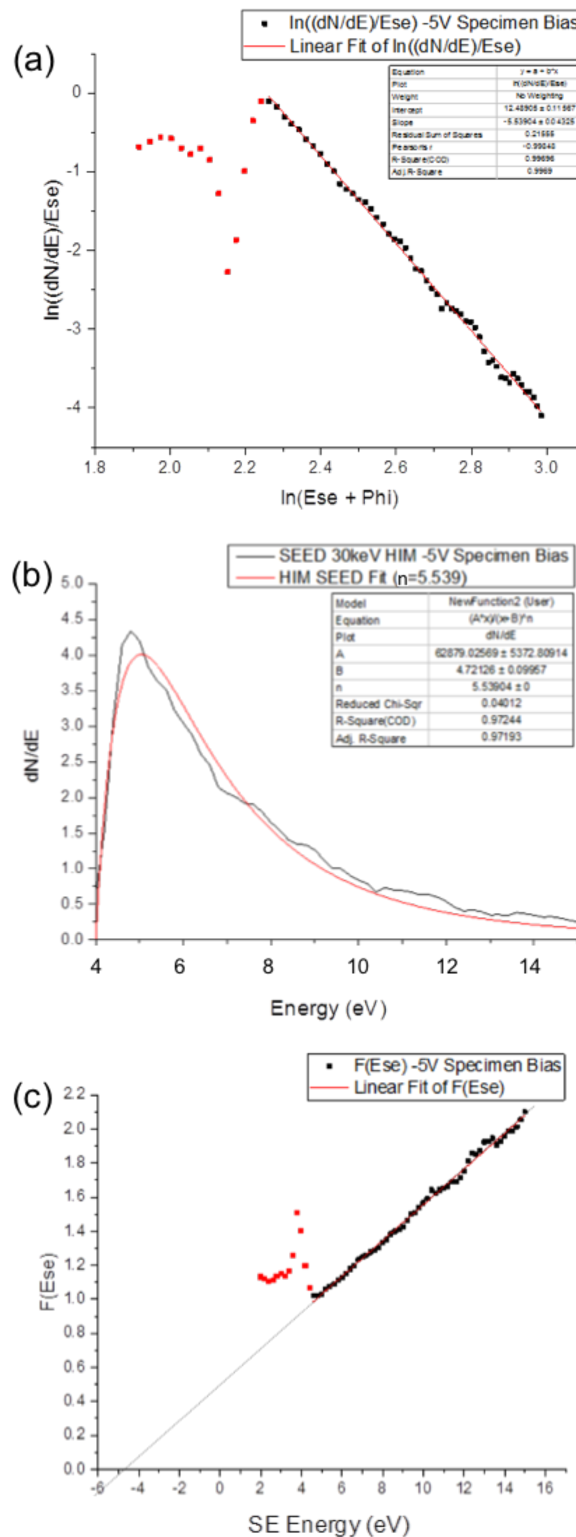

FIGURE 5.41: (a) Logarithmic transform of the SEED shape collected from the Ta(110) test specimen, biased at -5 V. (b) The SEED fitted to a non-linear curve using $n = 5.539$, given by the slope of the fitting in (a). (c) The dependence *F(Ese)*, plotted as a function of SE energy which gives a value for $\phi = 4.7$ (eV)

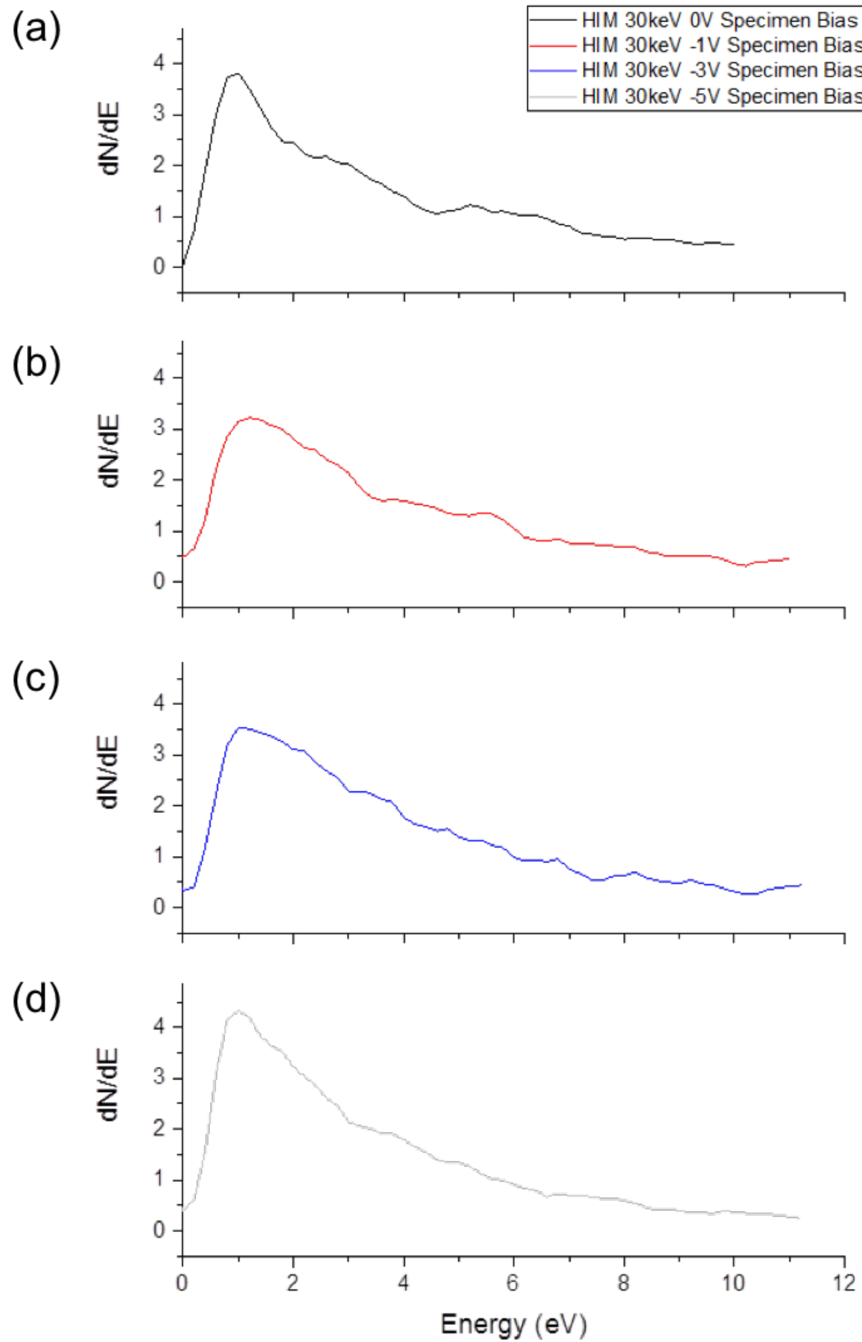

Figure 5.42: The SEEDs for all stage bias settings are displayed in (a) - (d), each corrected so that SE onset coincides with 0 eV. The fine structure in each energy distribution is observed to vary, however the general shape and peak SE energy remains constant.

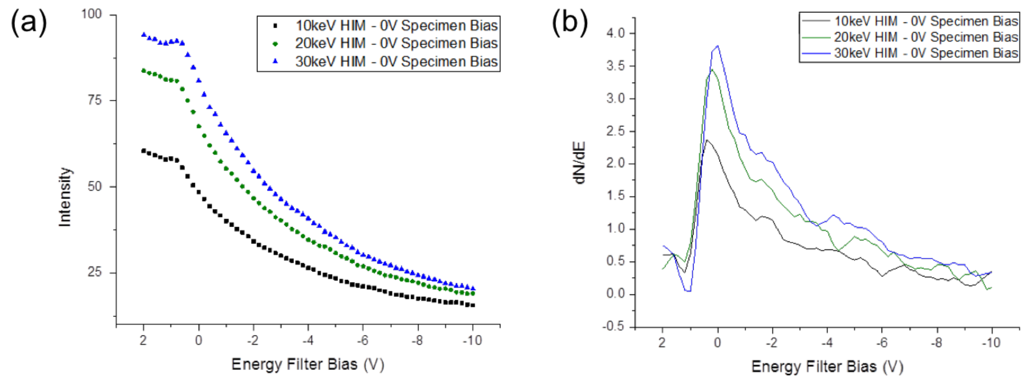

FIGURE 5.43: (a) SE image intensity profiles generated from Ta (110) test specimen irradiated with primary He^+ ion beam energies of 10, 20 and 30 keV. (b) SE energy distributions generated from each of the image intensity profiles.

of particular interest when extracting specimen information thus, careful consideration on specimen biasing is required during the acquisition of SE energy filtered imaging and spectra.

The effect of primary He^+ ion energy

To determine the influence primary He^+ ion energy had on the filtering efficiency of the retarding grid, a series of SE energy filtered images of the Ta (110) specimen were generated at 10, 20 and 30 keV. The experimental conditions employed in section 5.5.2.2 were repeated for this image series, with the exception of the primary beam current at 10 keV. It was approximately doubled in comparison to beam currents used at 20 and 30 keV. The SE image intensity profiles generated from the primary He^+ ion beam energy analysis are displayed in Figure 5.43 (a). The SE onset from each profile occurred at an energy filter bias setting of 1.2 V. SE energy distributions for each image intensity profils were then generated. These are presented in Figure 5.43 (b). The features in each SEED beyond the peak position occur at similar positions (eV). Prior to comparing the experimental results however, the efficiency of the EF at each primary He^+ ion beam energy required investigation.

Presented in Figure 5.44, Figure 5.45 and Figure 5.46 are the evaluation results for the 10, 20 and 30 keV SEEDs. The SEED shape for each beam energy shows good correlation to their fitted curves. For a given material, ion induced SE yield

is proportional to velocity of the impinging ions, i.e. their kenitic energy [97], however as the incident beam current for 10 keV, 1.8 pA, was twice that of the other beam energies, greater image intensity was observed at each energy filter bias setting. In order to compare the results between the beam energies, the intensity value of each image in the 10 keV image series was halved. The ϕ values determined from the 20 and 30 keV SEED data are aligned with the expected text book value of 4.8 eV ± 1eV, however for 10 keV the SEED data gave $\phi = 4.5$ eV. The variation in SE yield at 10 keV in comparison to the other beam energies, may have influenced its SEED and as a result the extracted value for ϕ. A further comparative investigation at lower beam energies would be required to confirm this assumption.

Presented in Figure 5.47 are the onset corrected SEED spectra for each beam energy. Peak energy occurs at ∼1 eV in all three spectra, with secondary peaks observed at ∼3 and ∼5.5 eV. Above 5.5 eV the features present in the spectra are not comparable. These differences could be accounted for by slight variations in surface potential present at each imaging site. Such differences would impact the number of SEs generated at these relatively higher energies. With the Ta (110) specimen it was not possible to alter the surface condition to try to promote uniform ϕ at, and between, each imaging site, however in section 5.5.3.4 this was attempted by using a HOPG specimen.

From analysis of the SEED spectra generated with He^+ ion energies of 10, 20 and 30 keV, the performance of the energy filter is not influenced beam energy. The results indicate a $\Delta V_{GRID} : \Delta E_K$ = 1:1, for 20 and 30 keV ion energy. The exact energy filtering ratio for 10 keV could not be determined from this data set.

5.5.2.4 Comparative evaluation in SEM

For an operational comparison the energy filter was installed in a SEM (Carl Zeiss, Ultra Plus) and was used to acquire electron induced SEEDs from the Ta (110) test specimen. The experimental set-up mirrored that implemented in the HIM, with a few instrument specific exceptions. The working distance in the SEM was set to 5 mm, and the gap between the specimen and the energy filter grid was maintained at 1 mm. Having the highest sensitivity to SE1 signals, the InLens detector was chosen to collect the specimen images. For image acquisition its collector bias was fixed to 300 V. All images were captured at a FOV of 54 μm, with a 1024 × 768

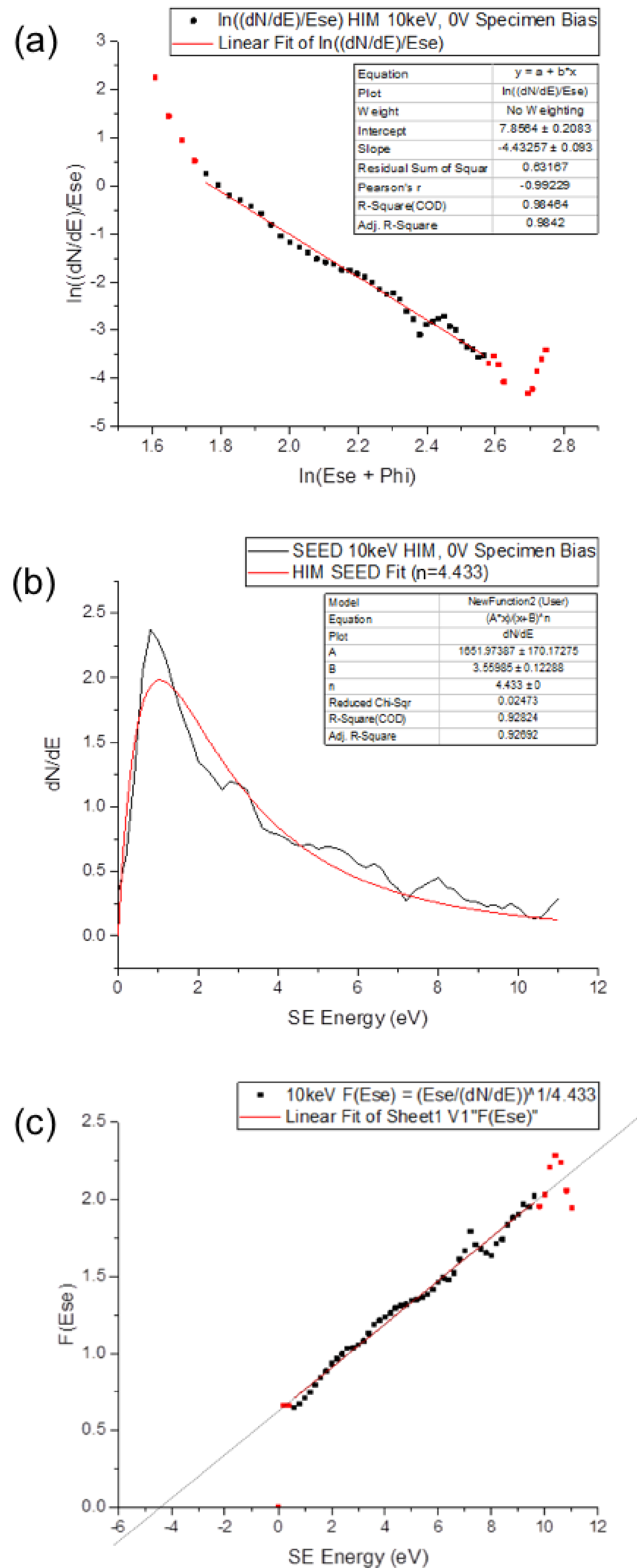

FIGURE 5.44: (a) Logarithmic transform of the SEED generated by irradiating the Ta (110) test specimen with a He^+ ion energy of 10 keV. (b) The SEED fitted to a non-linear curve using $n = 4.433$, given by the slope of the fitting in (a). (c) The dependence *F(Ese)*, plotted as a function of SE energy which gives a value for $\phi = 4.5$ (eV)

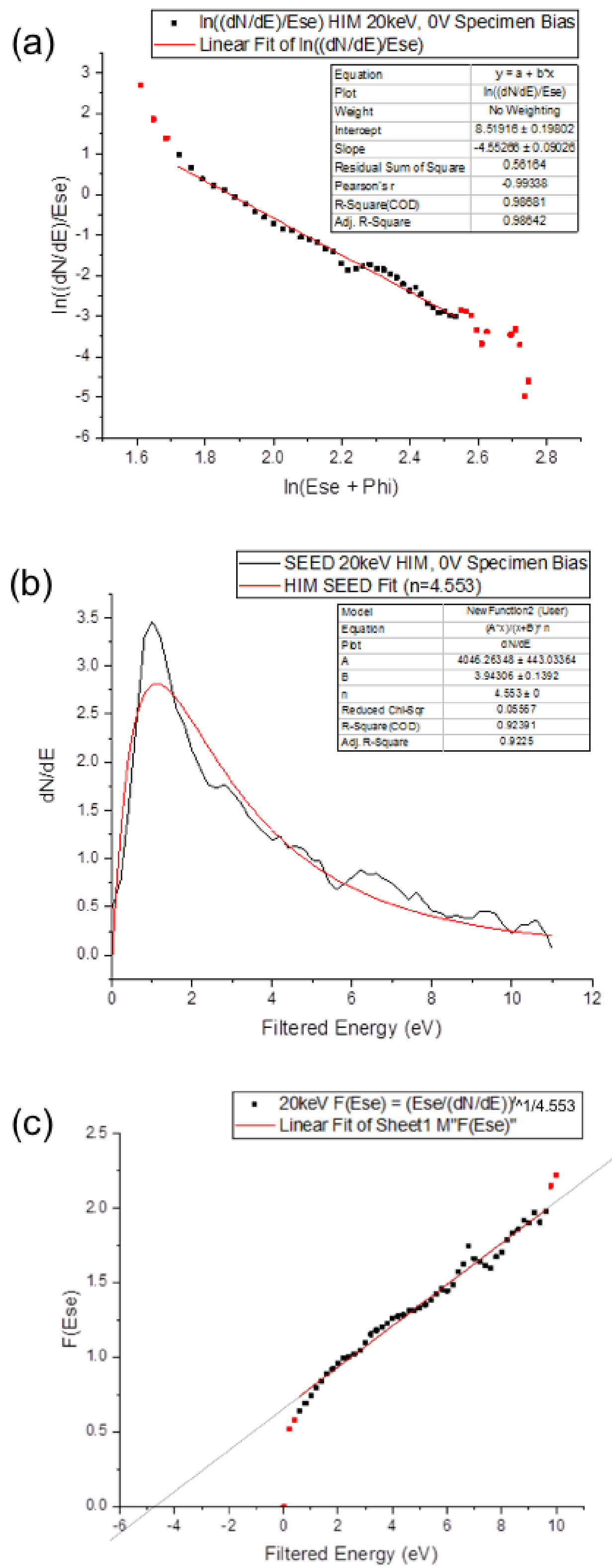

FIGURE 5.45: (a) Logarithmic transform of the SEED generated by irradiating the Ta (110) test specimen with a He^{+} ion energy of 20 keV. (b) The SEED fitted to a non-linear curve using $n = 4.553$, given by the slope of the fitting in (a). (c) The dependence $F(Ese)$, plotted as a function of SE energy which gives a value for $\phi = 4.8$ (eV)

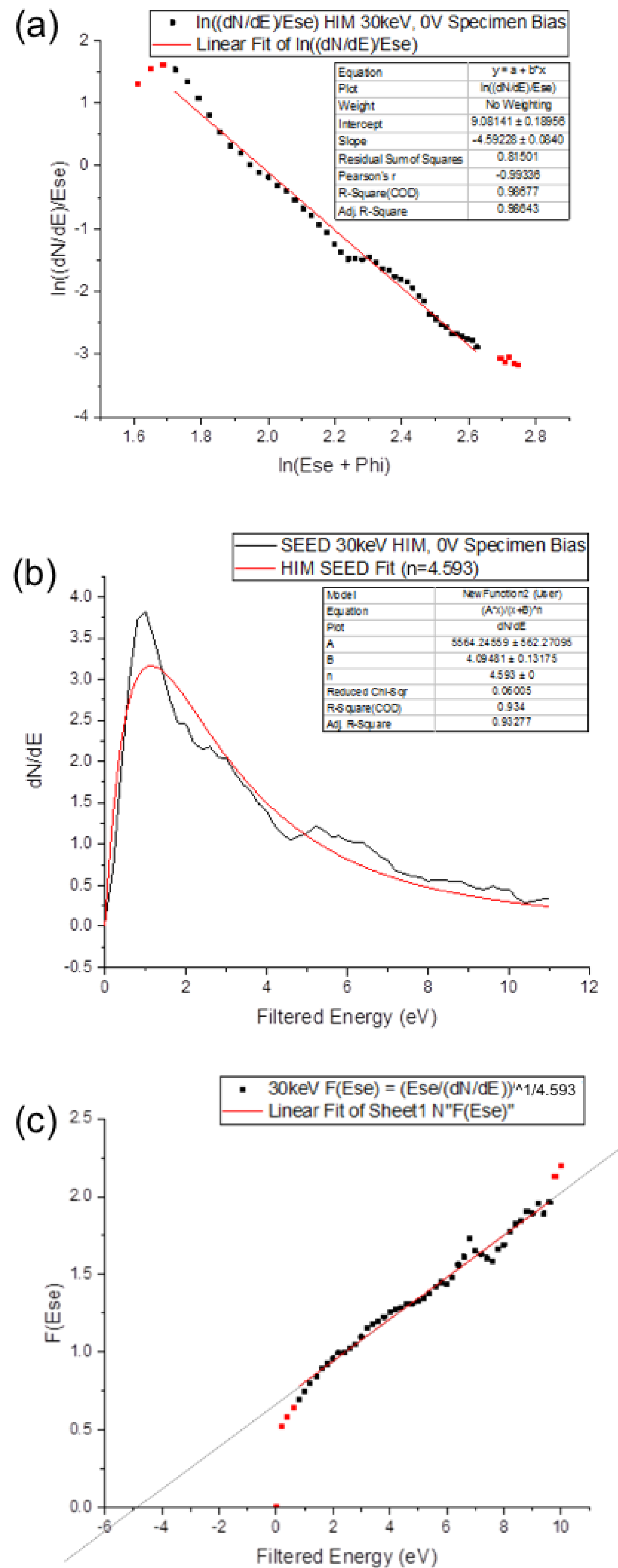

FIGURE 5.46: (a) Logarithmic transform of the SEED generated by irradiating the Ta (110) test specimen with a He^+ ion energy of 30 keV. (b) The SEED fitted to a non-linear curve using $n = 4.593$, given by the slope of the fitting in (a). (c) The dependence *F(Ese)*, plotted as a function of SE energy which gives a value for $\phi = 4.8$ (eV)

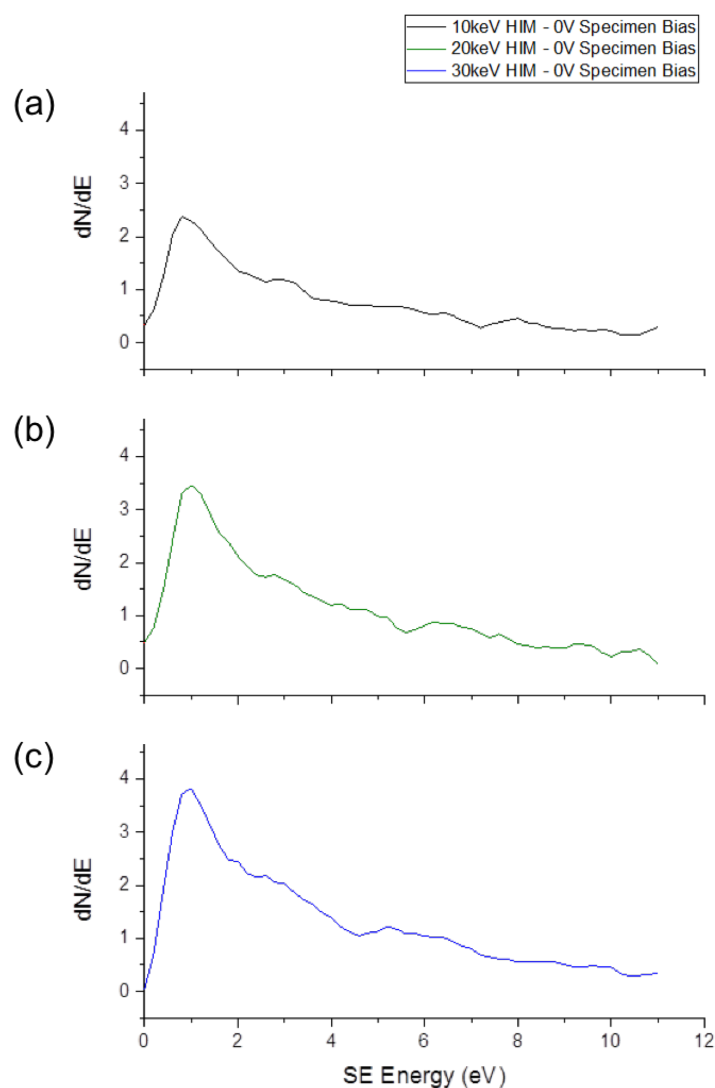

FIGURE 5.47: The SEEDs for He^+ ion primary energies of 10, 20 an 30 keV are displayed in (a) - (c), respectively. Each has been corrected so that SE onset occurs at 0 eV. The general shape of the distributions and peak SE energy does not change with primary He^+ ion energy. The features present in the spectra below 5.5 eV are comparable however those above are not.

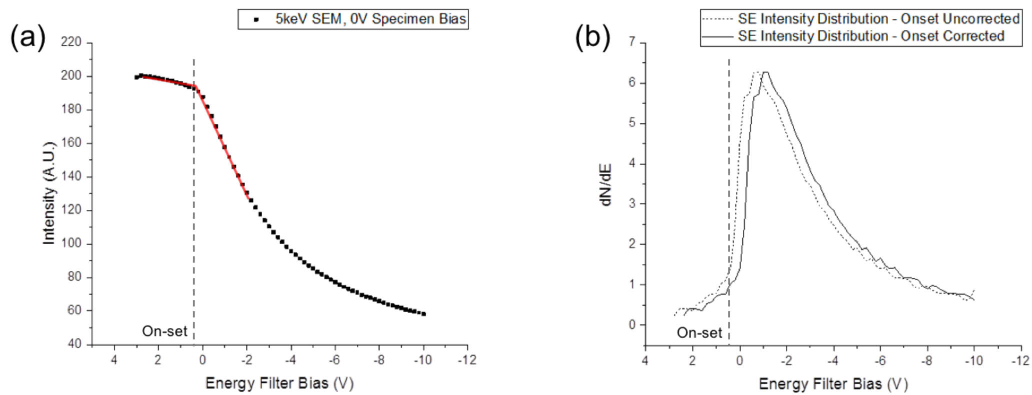

FIGURE 5.48: (a) An electron beam induced SE image intensity profile from an unbiased Ta (110) test specimen, upon the application of an increasing negative energy filter bias. The SE onset was determined from the intersection of the slopes of the first and second phases of the profile, as indicated by the overlapping red lines. (b) The corresponding SE energy distribution referenced to the EF bias. The SE onset in (a) correlates with the commencement of peak SE energy in (b).

pixel resolution and a dwell time of 0.1 μs. Also, detector contrast and brightness were set to 35% to 50%, respectively.

Figure 5.48 (a) shows the electron induced SE image intensity profile, from the unbiased Ta (110) test specimen, upon the application of an increasing negative energy filter bias. A primary electron beam energy of 5 keV was used to excite the specimen. As observed with the placement of the energy filter over the specimen in the HIM, the presence of the energy filter over the specimen in the SEM reduced the SE on-set below 0 V. As a result, the biasing range commenced at +3 V, prior to being reduced to -10 V, in 0.2 V steps. At each step, an image of the specimen was acquired and from the entire image series the intensity profile was compiled. Unlike the onset in the HIM experiments, the onset in the SEM is not associated with an SE energy minima. It was however determined from the intersection of the plotted slopes of the first and second phases of the reducing intensity profile, as indicated by the overlapping red lines.

Figure 5.48 (b) shows an energy distribution of the Ta test specimen, which was generated from its intensity profile in reference to the energy filter bias. The onset ($\sim$0.4 V) correlates with the commencement of peak SE energy. When the intensity data was shifted so that the onset was aligned to the 0 V position, the corrected SEED gives peak SE energy at $\sim$1.2 eV. The width of the SE peak is

$\sim$50% of the energy range and its over-all shape is smooth with minimum features present above peak maximum.

To compare the electron induced SEED of the Ta specimen to that of the He^+ ion induced SEED, the efficiency of the EF in SEM was determined. Firstly, the shape of the curve was fitted to the SEED function, Equation 5.10, as given in [59]. This is displayed in Figure 5.49 (a) and shows a good fit between the SEED shape and function.

$$\frac{dN}{dE} \sim \frac{E_{se}}{(E_{se} + \phi)^4} \tag{5.10}$$

The SEM SEED data was then used to check specimen work function by applying the *F(Ese)* dependence (Equation 2.6), given by [59], as a function of energy filter bias (eV).

This plotting is displayed in Figure 5.49 (b) and upon extrapolation to its zero value, an intersection of -3.4eV was revealed. For correct correspondence with the ϕ for Ta (110), an intersection of -4.8eV would have been the result. Peak SE energy, as presented in Figure 5.49 (a), is therefore incorrect, as $\Delta V_{GRID} : \Delta E_K \neq 1:1$. To confirm that this is the case, the SEED data was adjusted by a factor of 1.41 (-4.8/-3.4). The corrected SEED data was plotted and is presented in Figure 5.50 (a). It shows the fitting curve perfectly aligned to the plot. The *F(Ese)* dependence was replotted for the corrected SEED, as presented in Figure 5.50 (b), and reveals the expected intersection at -4.8eV.

In the work presented by Petrov *et. al.* [59], peak SE energy in the HIM was observed to increase with specimen ϕ, and for a given material (Mo), peak SE energy in the SEM was $\sim$1.5 times that observed in the HIM. To confirm the method proposed in section 5.5.2.2 - which correctly extracted specimen ϕ from the SEED data using the *F(Ese)* dependence - the HIM data presented in [59] (Figure 5.51(a)) was re-plotted and fitted using Equation 2.7. This is displayed in Figure 5.51 (b) and shows an intersection of -4.2 eV. The plotting confirms the value of specimen ϕ (4.2eV) as previously determined from the SEM data of the Mo specimen. It also confirms the method outlined above for calibrating the SE energy filter in both the SEM and HIM.

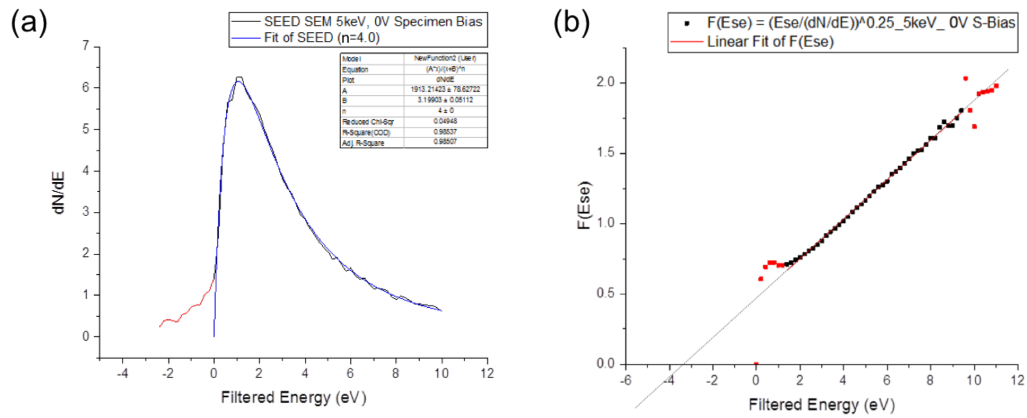

FIGURE 5.49: (a) The onset corrected electron beam induced SEED of the Ta (110) specimen, fitted to Equation 5.10. A good fit between the SEED shape and the fitted function is observed. (b) The *F(Ese)* dependence of the Ta (110) SEED is plotted and reveals an intersection of -3.4eV upon extrapolation to its zero value.

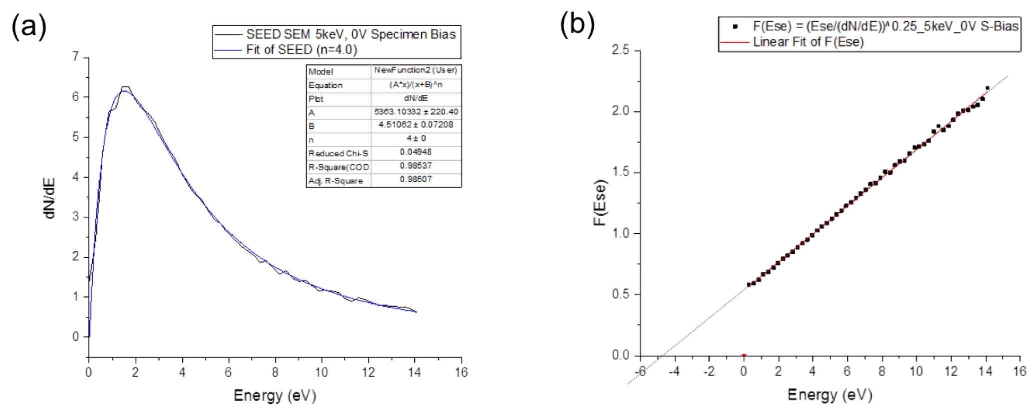

FIGURE 5.50: (a) The SEED data of the Ta (110) specimen, presented in Figure 5.49 (a) is adjusted by an energy correction factor of 1.41. The fitted curve is perfectly aligned to the corrected distribution. (b) The *F(Ese)* dependence was replotted for the corrected data revealing an expected intersection of -4.8eV.

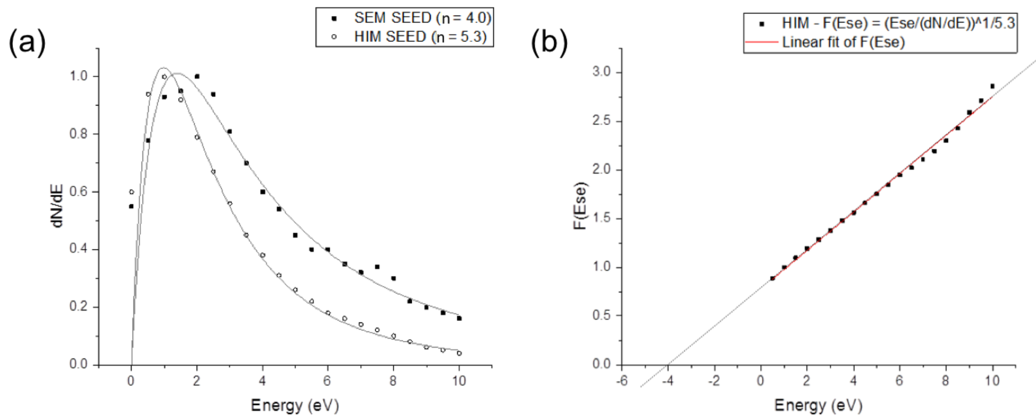

FIGURE 5.51: (a) The HIM and SEM SEED data of the Mo specimen, extracted from [59] were fitted to Equation 2.5, using their appropriate exponents. (b) The plotting of *F(Ese)* of the HIM SEED data reveals an intersection of -4.2 eV confirming specimen ϕ (4.2eV), as determined from the SEM SEED data.

A comparison of electron and He^+ ion induced SEED spectra is presented in Figure 5.52, with each spectrum normalised to their peak SE energy values. These occur at 1eV in HIM and 1.7eV in SEM. Beyond peak energy there are a variety of features present in both spectra, some of which occur at comparative energies. Due to the nature of this specimen however, an evaluation of the finer details of both SEEDs is beyond the scope of this SE energy filter calibration work.

The effect of specimen bias in the SEM was also evaluated and completed in the same way described for the HIM evaluation, section 5.5.2.3. The image intensity profiles acquired for stage bias settings of -1, -2, and -3 V are displayed in Figure 5.53 (a), along with the intensity profile for the 0 V specimen bias. As expected, the position of each profile shifts with the applied EF biasing range. Their shape also changes with the increase in stage bias although not as pronounced as the changes observed for the HIM profiles (as displayed in Figure 5.38). SEEDs for each of the SEM intensity profiles were generated, each of which were referenced to the applied energy filter bias (eV). These are displayed in Figure 5.53 (b) and reveal four distinct energy distributions. The onset of SE energy filtering for each specimen bias corresponds to the commencement of peak SE energy in each spectrum, occurring at -0.6, -1.6 and -2.6 V for the -1, -2 and -3 V specimen bias settings, respectively. Unlike in the HIM, peak heights and FWHM do not vary significantly with specimen bias, however like the HIM, some SEEDs are "mirror-like" images of others, i.e. the 0 V SEED is comparable to that produced for -2 V

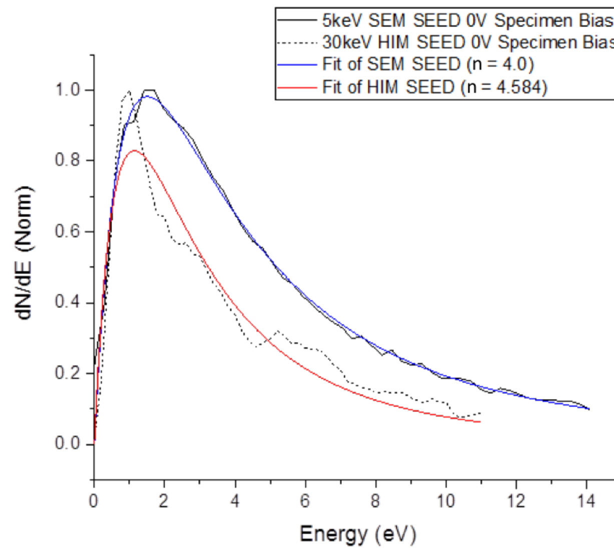

FIGURE 5.52: A comparison of electron and He^+ ion induced SEEDs, of the Ta (110) specimen, both fitted to their respective exponents. Each spectrum is normalised to peak SE energy which occur at 1eV for HIM and 1.7eV for SEM.

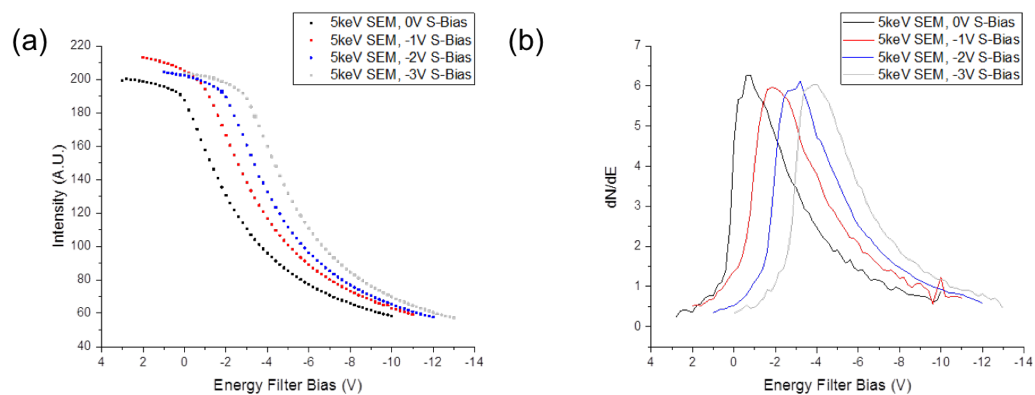

FIGURE 5.53: (a) SEM SE image intensity profiles for stage bias settings of 0, -1, -2, and -3 V. The position and each profile shifts with the applied EF biasing range. (b) SEEDs for each of the SEM intensity profiles referenced to the applied energy filter bias (eV).

and the -1 V SEEDs is comparable to that produced for -3 V. Peak height however and FWHM for are greater for the 0 and -2V SEEDs. With the exception of the -2 V SEED, there are features present at all energies above peak maximum.

5.5.2.5 Summary of SE energy filter calibration

The SE energy filter device was first evaluated in the HIM in terms of the homogeneity of its applied biasing field and its SE filtering efficiency. Energy filtered SE images of a Ta (110) test specimen were acquired upon biasing the retarding grid between +3 to -15 V. The homogeneity of the energy filter was assessed by acquiring image intensity profiles from six intersecting axes within a central hexagonal grid area. Analysed in terms of uniformity across their individual lengths, the results showed a homogeneous filtering effect of the applied retarding field. The efficiency of the energy filter, i.e. the ratio of the retarding grid bias to the kinetic energy of the filtered SEs ($\Delta V_{GRID} : \Delta E_K$) was then determined. This was achieved by firstly generating an SE intensity profile of the test specimen from which an SE energy distribution (SEED) was generated. From this SEED the modified *F(Ese)* dependence was plotted, which revealed a ϕ value equal to the text book value of Ta (110) (4.8 eV) and confirmed a 1:1 relationship between applied EF bias (V) and filtered SE energy (eV).

Secondly, the influence of specimen bias and primary He^+ ion beam energy on SE filtering efficiency was determined. The influence of specimen bias was assessed by generating SEEDs at a specimen bias settings of -1, -3 and -5 V, plotting their modified *F(Ese)* dependences, and checking each plot for correspondence to specimen ϕ. The -1 and - 5V plots varied slightly ($\leq$ 5%) however the -3V plot revealed exact correlation to Ta (110) ϕ. Correcting the SEEDs so that their onsets coincided with the 0 eV position showed that altering the specimen bias did not change their general shape or peak position, however it was observed to effect the fine features present in the distributions. The influence of primary He^+ ion beam energy was determined in the same way, however when comparing SEEDs, generated at 10, 20 and 30 keV, the specimen bias was kept at 0 V. With the exception of 10 keV, the modified *F(Ese)* dependences for the 20 and 30 keV SEEDs revealed exact correlation to Ta (110) ϕ and therefore confirmed an SE filtering efficiency 1:1. The 10 keV data was off by $\sim$5% however the exact filtering ratio could not be determined from this data set. This result however would not

impact He^+ induced SE spectroscopy studies, due to the majority of HIM imaging being conducted between 20 - 35 keV.

Next, the operation of the SE energy filter device in the SEM was tested. Using a primary electron beam energy of 5 keV, a specimen bias of 0 V, and retarding biasing range of 3 V to -10 V, a SEED of the Ta (110) test specimen was generated. Its *F(Ese)* dependence was plotted however it did not reveal a value corresponding with specimen ϕ. The filtering efficiency of the EF device in SEM was therefore not 1:1, which gave incorrect peak SE energy. On application of the appropriate correction factor, the SEED and *F(Ese)* dependence were replotted both of which revealed correct peak SE energy and specimen ϕ.

To confirm the method of qualifying the energy filter, the HIM SEED data presented in [59] for an Mo test specimen was extracted and its modified and *F(Ese)* dependence was plotted using Equation 2.7. This revealed a specimen ϕ of 4.2 eV exactly the same as the SEM data presented by the authors, thus confirming the methods for calibrating the SE energy filter in SEM and HIM.

In SEM, the effect of specimen bias on the efficiency of the SE energy filter device was also evaluated. Similar to the results presented for HIM, altering specimen bias primarily influences the detail in the energy distributions, however the general shape and peak SE energy is not effected. This effect requires careful consideration when extracting SE spectra from electron and He^+ irradiated specimens.

The observations presented on the evaluation of the energy filter in a SEM, demonstrates its ability to generate a SEED from a specimen comparable to that generated from the same specimen in a HIM. This in turn enables the use of the energy filter in both instruments for correlative SE energy-filtering and spectroscopy techniques for material characterisation.

5.5.3 Application of the SE energy filter device: SE Image spectroscopy in HIM

The interaction of a charged particle with a material atom can give rise to the generation of a SE. If sufficient energy transfer occurs during the interaction the SE can escape from the surface of the material into vacuum. The minimum kinetic energy required for SE emission is known as the material's work-function (ϕ).

Within the scope of an electron, or an ion, microscope, certain physical, chemical or crystallographic properties of a material can be revealed by analysing its SE energy profile [50, 60, 197]. By controlling the energy range of the SEs delivered to the detector, regions of distinct work function difference can be highlighted or removed from a specimen image. Selective SE energy detection can therefore enhance the characterisation and imaging functions of a charged-particle microscope.

5.5.3.1 HOPG Specimen preparation

A HOPG specimen was used for the generation and evaluation of SE spectra in the HIM. Affixed to a standard Al SEM stub using silver paint, as shown in Figure 5.54. In order to generate a true SE spectra from the specimen, surface contaminants and fractured layers first needed to be removed. This was done by a mechanical cleaving method using an adhesive cellophane tape and performed as follows.

Firstly, along one edge of the HOPG specimen the Al supporting stub was marked and placed into a stub holder. This mark would indicate the direction of exfoliation once the cleaving procedure was complete. A straight edge was cut across a piece of tape attached perpendicularly to a pen. The tape was extended out from its holder by the pen and a strip, of approx. 7cm, was cut free. The free end of the tape was stuck to the side of the stub holder with the mark. With the tape held firm to the holder with one hand it was kept taut with the other and brought over the HOPG specimen. Keeping it taut, the tape made a homogenous contact with the HOPG surface. Slight pressure was then applied to the top surface of the tape ensuring full contact with the specimen surface, required for optimal cleaving. The end of the tape attached to the pen was then moved back over the HOPG surface, by a gentle rolling action of the pen. While doing so, care was taken to ensure that no kinks or creasing occurred in the tape and a firm hold was kept on the specimen stub holder.

Once complete, the HOPG surface was ready for analysis, however as it contaminates quickly the cleaving process was done just prior (< 3 minutes) to insertion into the microscope.

FIGURE 5.54: The HOPG test specimen affixed to an Al SEM stub. The marking on the stub, indicated by the blue arrow, was used to indicate the direction of ex-foliation after surface cleaving.

5.5.3.2 Image acquisition and SEED generation parameters

The method by which energy filtered images were captured in the HIM from the HOPG specimen, was the same as that described in the SE energy calibration section (Section 5.5.2.2), but refined to suit the HOPG specimen as follows. The ion acceleration voltage was increased to 30 keV. The FOV was reduced to 10 μm. Line averaging was changed to frame averaging and set to 4. Image contrast was set to 66% and brightness to 33%. Image resolution was set to 512 $\times$ 512 and pixel dwell time to 1 μs. The biasing range of the EF grid was set between +1 to -6 V and images were acquired at every 0.1 V interval.

5.5.3.3 Assessment of the HOPG surface condition

Upon insertion into the HIM the HOPG surface was evaluated for the generation SE energy spectra. The various surface features observed during this examination and are displayed in Figure 5.55. Such features included, remnants of partially pulled off flakes, HOPG grain boundaries, micron-sized features with well-defined straight edges and small (< 1 μm) dark non-crystalline features. The small dark

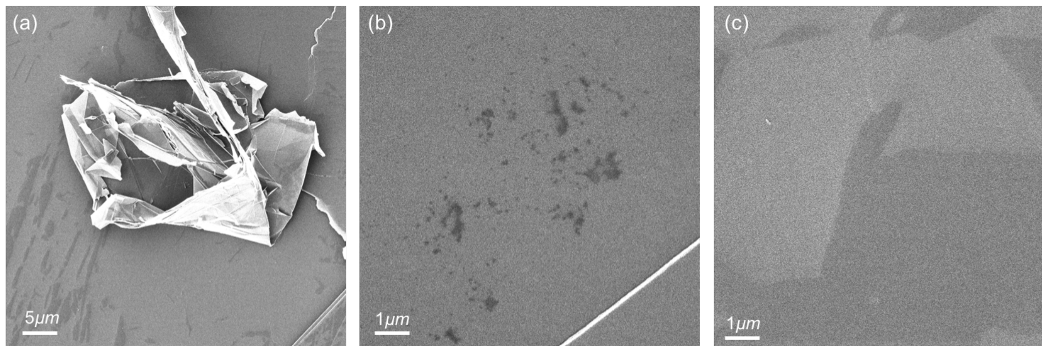

FIGURE 5.55: The features observed in the HIM on the surface freshly cleaved HOPG specimen included, (a) remnants of partially pulled off flakes, HOPG grain boundaries and micronized features with well-defined straight edges. (b) Dark non-crystalline features, presumed to be surface contamination. (c) Sharp-edged features which became more clearly visible at higher magnifications.

features are presumed to be surface contamination, while the features with well-defined edges appeared to be weakly bound flakes, aligned along a particular direction. The sharp edges are more clearly visible in the higher magnification image in Figure 5.55 (c). Such features are the result of mechanical stresses as a consequence of the cleaving and are consistent with the features observed in HOPG conductivity maps [198].

5.5.3.4 HOPG SEED generation

Although the specific features observed were common to all areas of the specimen surface, three particular regions were identified for spectra collection. These were classified in terms of their concentration of loosely bound HOPG flakes and were denoted as types A, B and C. Type-A and Type-B were areas were observed as being free from flakes but varied in SE intensity when imaged side by side. Type-C was an area containing no more than 50% of prominent small flakes, $\leq 10\mu$m in width.

Type-A HOPG surface region.

Figure 5.56 shows the results of a four SEED progression generated from a Type-A region of the specimen. Figure 5.56 (a) shows the SEED generated after the central region in Figure 5.56 (b) was imaged 81 times (whereby a total irradiation

dose of ∼1 pC·μm^{-2} was delivered). Figure 5.56 (c, e & g) show the SEEDs generated from the same central region of the specimen, after the second, third and fourth energy filtered imaging sequences. The changes induced in the HOPG surface after each imaging sequence are shown in Figure 5.56 (d, f & h). Due to the sensitive nature of the HOPG specimen, high resolution surface scans of the surface were not captured prior to the commencement of the imaging sequences, however the area surrounding the concentrated irradiation is representative of the Type-A surface region.

The dashed lines that overlap all of the SEEDs in Figure 5.56 indicate the expected SE energy peaks from the HOPG substrate. These were reported at 1 and 3 eV for He^+ ion induced SE emission, and 4.3 and 5.4 eV for electron induced SE emission [60, 197]. Prominent in Figure 5.56 (a) are the 1 and 3 eV peaks. The 4.3 and 5.4 eV peaks are clearly seen, however the 4.3 eV peak is shifted to a slightly higher energy of ∼4.5 eV. Also present are three further peaks at 0.3, 1.8 and 2.5 eV. In comparison to the initial SEED presented in (a), all of the other energy distributions are similar in shape but exhibit peaks at different energies.

Taking the text book value for HOPG ϕ at 4.6 eV, the initial SEED generated from the first imaging sequence, presented in Figure 5.56 (a), was fitted to the HIM SEED expression, Equation 2.5 and is displayed in Figure 5.57 (a). Prior to fitting, the exponent n for the fit was determined using Equation 5.9. The fit is a good match to the SEED however a noticeable difference in the height and width of the peak, below its maximum, are observed. To check the relationship between EF bias (V) and filtered SE energy (eV) for the HOPG experiment, the HIM *F(Ese)* dependence, given in Equation 2.7, was plotted for the initial SEED data. As displayed in Figure 5.57 (c), this check resulted in an Y-axis intersection of -4.6 V confirming a filtering efficiency of $\Delta V_{GRID} : \Delta E_K$ = 1:1.

The SEED presented in Figure 5.56 (a) is representative of the SE emission from the Type-A region, however during SEED generation the surface is altered by the He^+ ion irradiation and is therefore not a true representation of a pristine surface. The SEEDs presented in Figure 5.56 (c), (e) and (g) are representative the surface conditions present during and after the second and third and fourth imaging sequences, respectively. It is clear that the continuing the He^+ ion irradiation is changing the surface features in the area under bombardment and these changes are altering peak positions and intensity.

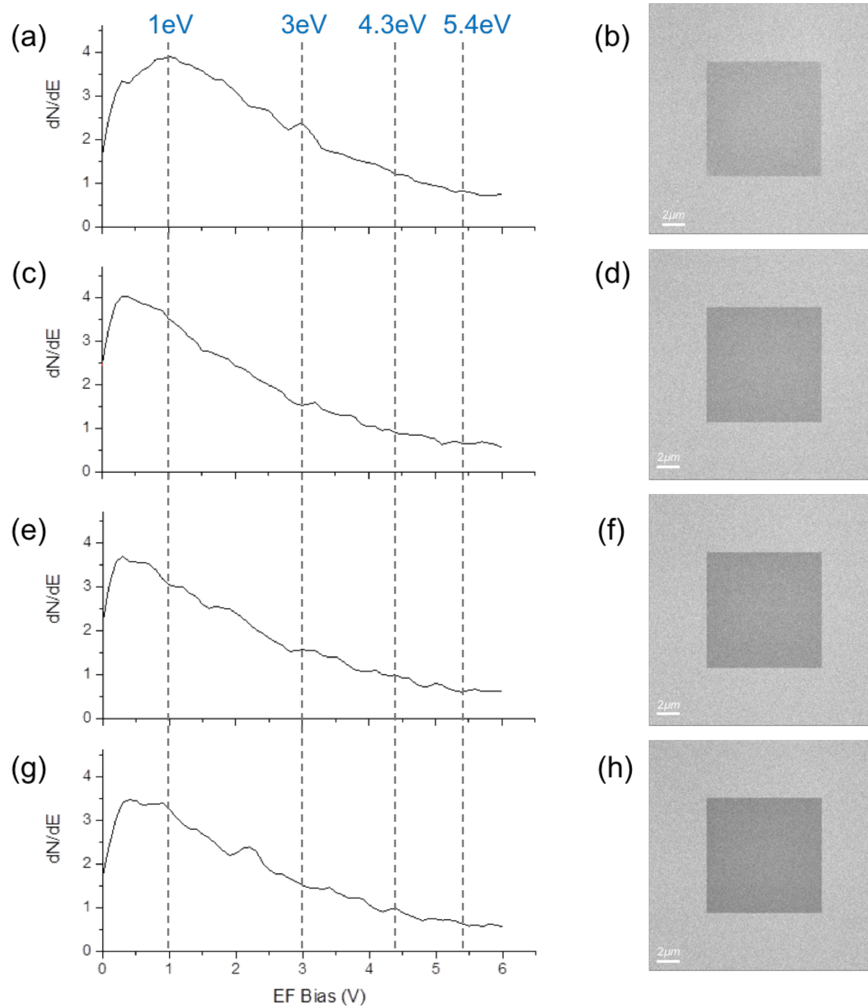

Figure 5.56: (a, c, e & g) A SEED progression generated by four energy filtered imaging sequences from the same irradiated region of a Type-A HOPG surface area, using irradiation parameters of, 30 keV beam energy, resolution 512 × 512 pixels, 19.5 nm pixel spacing and a 1 μs dwell time. The overlapping dashed lines indicate the expected HOPG SE energy peaks induced by He^{+} ion irradiation, at 1 and 3 eV, and for electron induced SE emission at 4.3 and 5.4 eV [60, 197]. An image of the specimen surface after each imaging sequence is displayed in (b, d, f &h) whereby total irradiation doses of ~1, ~2, ~3 and ~4 pC$\cdot\mu$m^{-2} were delivered, respectively.

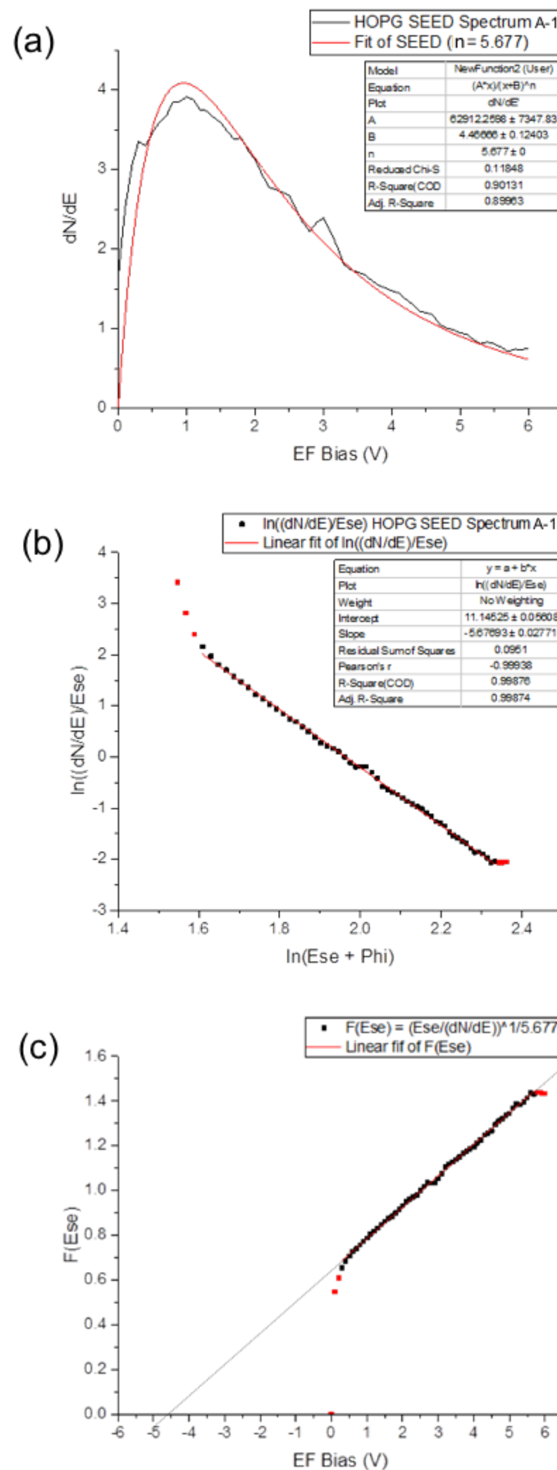

FIGURE 5.57: (a) The SEED generated from the first imaging sequence of the Type-A surface area was fitted to Equation 2.5, taking HOPG ϕ as 4.6 eV. (b) Prior to fitting the SEED the exponent n was determined using Equation 5.9. (c) The *F(Ese)* dependence was plotted for the SEED data and resultes in an intersection of -4.6 V, confirming a filtering efficiency of $\Delta V_{GRID} : \Delta E_K = 1{:}1$.

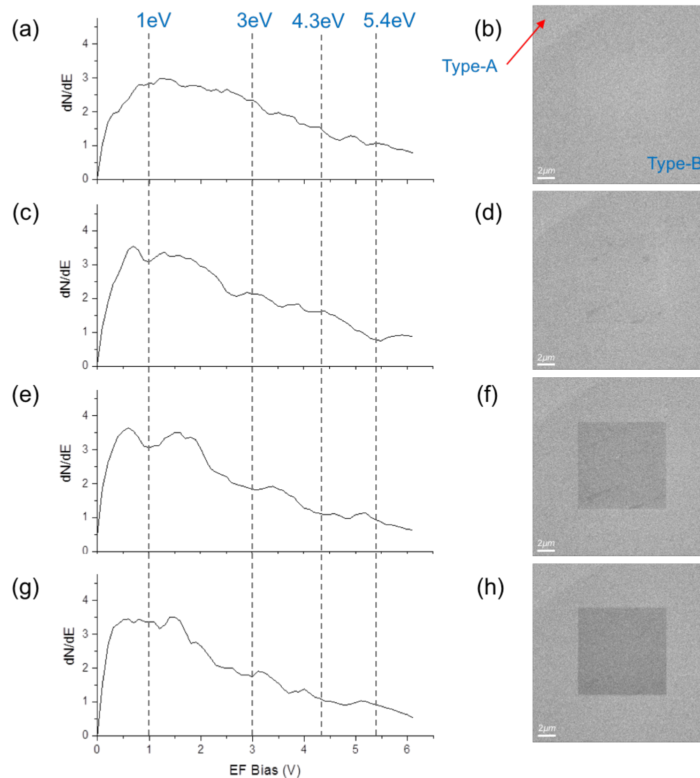

FIGURE 5.58: (a, c, e & g) A SEED progression, generated by the first set of four energy filtered imaging sequences, from an irradiated region of a Type-B HOPG surface area, using irradiation parameters of, 30 keV beam energy, resolution 512 × 512 pixels, 19.5 nm pixel spacing and a 1 μs dwell time. The overlapping dashed lines indicate the expected HOPG SE energy peaks induced by He^+ ion and electron irradiation. An image of the specimen surface after each imaging sequence is displayed in (b, d, f &h) whereby total irradiation doses of ∼1, ∼2, ∼3 and ∼4 pC·μm^{-2} were delivered, respectively.

Type-B HOPG surface region.

Presented in Figure 5.58 and Figure 5.59 are the results of an eight part SEED progression generated from a Type-B HOPG surface region. The spectra and associated images were generated in the same manner as those generated from the Type-A region. Figure 5.58 (a) shows the initial SEED. It is similar to the initial Type-A SEED, having clearly visible peaks at all of the expected SE energy levels. New spectral features (peaks) are also observed at 0.3, 1.2, 1.8, 2.5 eV and 5eV.

The SEEDs generated with the progressing imaging series from the Type-B region hold the same general shape, however the features observed in the initial SEED are either missing or shifted. Similar to the Type-A SEEDs, the generation of SEEDs

from the Type-B region results in a change in the condition of the specimen's surface. These changes are clearly seen in the first part of the spectral progression presented in Figure 5.58. The SEEDs presented in Figure 5.59 are the second part of the spectral progression. These were generated from the same region irradiated in the first part of the progression and after each SEED the contrast of the irradiated region continues to darken. This indicates further surface changes which is confirmed by the changes to the features observed in their progressing SEEDs. In contrast to the the initial SEED, the SEEDs presented in Figure 5.59 (e & g) have lost a significant portion of the spectral details. This indicates that the greatest specimen changes occur at the highest irradiation doses, which is also confirmed by the appearance of cracks in the at the corners of the irradiated region.

Type-C HOPG surface region.

A typical Type-C area is displayed in Figure 5.60 (a). It shows the loosely bound, several micron sized, HOPG flakes exhibiting a darker SE intensity than that of the supporting plane. Prior to completing a SEED imaging sequence, the surface was irradiated with a total of eight *cleaning* scans. These scans had the same properties as the energy filtered imaging scans with the exception of dwell time, which was adjusted to 5 μs. Each cleaning scan produced an SE image and these are shown in Figure 5.60 (b - e) for the 2nd, 4th, 6th and 8th scan. The final scan reveals uniform SE intensity.

Three imaging sequences were performed over the cleaned Type-C region, the SEEDs from which are displayed in Figure 5.61 (a), (c) and (e). The specimen images generated at the end of each SEED sequence are displayed in Figure 5.61 (b), (d) and (f). None the features present in the initial SEED (Figure 5.61 (a)) align with the characteristic HOPG SE energy peaks, as indicated by the overlapping dashed lines. In comparison to the inital Type-A and Type-B SEEDs, its general shape is significantly altered. The second SEED (Figure 5.61 (c)) more closely resembles the initial Type-A and Type-B SEEDs. With the exception of its 1 eV peak, none of its features align with the characteristic SE energy peaks. The SE energy peaks in the final SEED for the Type-C region, as displayed in Figure 5.61 (c), are also not aligned with the characteristic HOPG SE energy peaks. With the exception of the peak at 1.5 eV this energy distribution does not share any of the peaks observed in the first and second SEEDs.

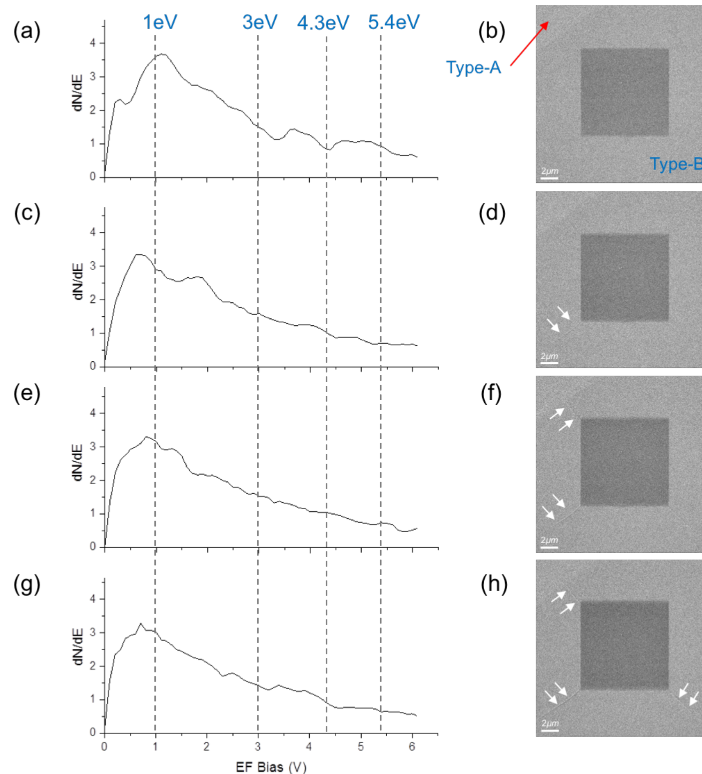

FIGURE 5.59: (a, c, e & g) The continuation of the SEED progression, presented in Figure 5.58, generated by the second set of four energy filtered imaging sequences from the same irradiated region of a Type-B HOPG surface area, using irradiation parameters of, 30 keV beam energy, resolution 512 × 51 pixels, 19.5 nm pixel spacing and a 1 μs dwell time. The overlapping dashed lines indicate the expected HOPG SE energy peaks induced by He^+ ion and electron irradiation. An image of the specimen surface after each sequence in displayed in (b, d, f &h) whereby total irradiation doses of ~5, ~6, ~7 and ~8 pC·μm^{-2} were delivered, respectively. At an applied dose of ~6 pC·μm^{-2} the top surface layer begins to crack at the corners of the irradiated region. These cracks are indicated in images (d, f &h) by the white arrows.

It is clear that the SEEDs produced from the Type-C surface region differ significantly from those produced from Type-A and Type-B. Even though a cleaning sequence was initiated prior to the commencement of the first energy filtered imaging sequence, the information present in the SEEDs show that the surface conditions prior to producing the initial SEED were significantly different than those present in the Type-A and Type-B regions. The true surface conditions prior to SEED generation are unknown, however it is unlikely that the cleaning steps removed the loose HOPG flakes as intended.

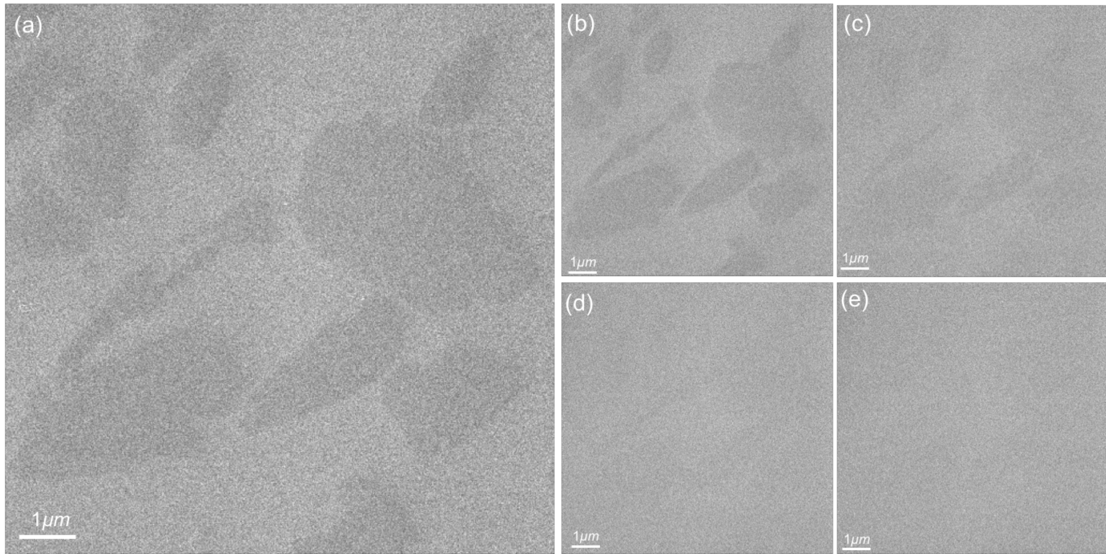

FIGURE 5.60: (a) A typical Type-C area showing loosely bound, HOPG flakes exhibiting darker SE contrast than the underlying plane. This region of the specimen was irradiated by a total of eight cleaning scans. Each cleaning scan delivered a total irradiation dose of ∼5 pC·μm^{-2} using irradiation parameters of, 30 keV beam energy, resolution 512 × 512 pixels, 19.5 nm pixel spacing and a 5 μs dwell time. The SE images produced after the 2nd, 4th, 6th and 8th scans are displayed in (b - e). The final scan reveals uniform SE intensity, indicating the removal of the loosely bound HOPG flakes.

5.5.3.5 Discussion and analysis of HOPG SEED generation

When AFM was used to measure the step height of loose HOPG flakes it was found to be slightly larger than the atomic spacing expected along the c-axis [198]. The increased gap size was linked to a reduced conductivity between the top graphene layer and the bulk HOPG material. This was supported by their darker appearance (SE contrast) having an increased ϕ relative to that of the underlying plane. The implication for SE spectra from the Type-C area is that the loose HOPG flakes would not be suitable for SE spectra collection as conductivity differences could translate into local potential differences. This is a well-known effect which has been exploited for mapping small potential differences in semiconductor dopant studies [17] and work function mapping of graphene [9]. If SEs were collected from several flakes simultaneously, each flake would have a slightly different potential and therefore a slightly different SE onset. When averaged over numerous flakes, this would lead to SE onset and peak broadening as any local potential variation would result in shifts within the energy distribution. It is clear from the SEEDs

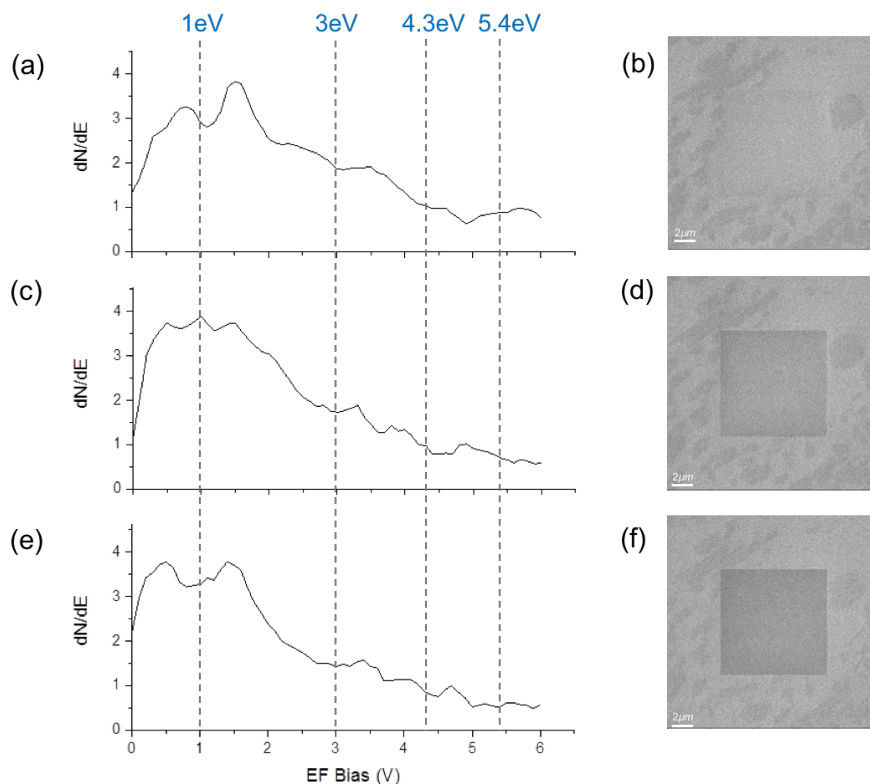

FIGURE 5.61: (a, c & e) A SEED progression, generated three energy filtered imaging sequences, from an irradiated region of the pre-cleaned Type-C HOPG surface area, using irradiation parameters of, 30 keV beam energy, resolution 512 × 512 pixels, 19.5 nm pixel spacing and a 1 μs dwell time. The overlapping dashed lines indicate the expected HOPG SE energy peaks induced by He^+ ion and electron irradiation. An image of the specimen surface after each imaging sequence is displayed in (b, d & f), whereby total irradiation doses of ~1, ~2 and ~3 pC·μm^{-2} were delivered, respectively.

presented for the Type-C region that the prominent peaks are shifted from the expected SE energy levels implying a variation in the local surface potential.

To date, clear evidence has not been given to show that HOPG cleaved in air remains free of hydrocarbon absorption. Reported data for peaks in He^+ ion induced SE emission spectra were carried out on air cleaved HOPG, however spectra collection took place under UHV conditions and after the specimen was annealed at 1100 K for several minutes [60]. Regardless of the lack of a specimen heating facility, or the availability of UHV in the HIM, no attempt was made to remove surface hydrocarbons following the unsuccessful cleaning of the Type-C region.

The features present in the initial SEEDs produced from the Type-A and Type-B regions show good alignment with the characteristic HOPG He^+ ion and electron induced SE peaks. This indicates that the surface conditions in these regions prior to irradiation were most likely free from features with the potential to alter surface work function. It is clear from the SEED progressions of the Type-A and Type-B regions that the specimen changed with each imaging sequence. Whether or not these changes were due cross-linked hydrocarbon formation or the sputtering of specimen atoms is unclear. It is clear however that repeated irradiation changes specimen surface work function. In the Type-B region, the overall shape of the spectrum remains the same after damaging inducing He^+ ion doses. The damage, as revealed by the appearance of cracks in the corners of the irradiated regions in Figure 5.59 (d, f, and h), is coupled with the removal of the majority of the fine spectral structure in Figure 5.59 (c, e, and g). These energy distributions now fit the description of glassy carbon given in [199], thus the change in shape of the HIM SE spectrum is likely to indicate the conversion of HOPG to glassy carbon.

5.5.3.6 Measurements of graphene SE spectra in SEM and HIM

Displayed in Figure 5.62 (a) is a SEM image of a freestanding monolayer of graphene. The data directly obtained from the SE energy filtering measurement on the monolayer graphene was a retarding grid bias (V) vs SE intensity curve. It is displayed in Figure 5.62 (b). From the curve the intensity is observed to decrease rapidly at an onset point of $V_{onset} \approx$ -1.6 V. This onset indicates the commencement of SE energy filtering. The relationship between filtered SE energy (E_k) and retarding grid voltage (V_{Bias}) is, $E_k = -e(V_{Bias} - V_{onset})$. By converting the x-axis in Figure 5.62 (b) to SE energy and differentiating the filtered SE intensity (using Savitzky-Golay Smooth in Origin 9.0, Polynomial Order = 2, Points of Window = 8), an SE spectrum of the freestanding graphene was obtained. This is displayed in Figure 5.62 (c). To determine the work function from SE spectrum, we convert Equation 5.7 to,

$$n\sqrt{\frac{E_K}{\left(\frac{\partial \delta}{\partial E_K}\right)}} \propto (E_K + \Phi) \tag{5.11}$$

Using Equation 5.11 the spectrum displayed in Figure 5.62 (c) was fit by varying n between 3.5 to 5.0. The work function value associated for each fit was obtained from the intercept. This changed from 2.51 eV to 4.98 eV, as displayed in Figure 5.63 (a). We compared the extracted work function values at different values for n with reported values ($\sim$ 4.3 eV), and found that $n = 4.6$ gave the closest value. Using $n = 4.6$, the fitting gave a work function value of 4.32 eV.

A total of five freestanding graphene specimens were measured. These were monolayer, bilayer, trilayer, quadlayer and relatively thick ($>$ 10 layers). Their SE energy spectra are shown in Figure 5.63 (c). Using Equation 5.11 and a given index number n, we compared the extracted work function values to the reported values for monolayer (4.3 eV), bilayer (4.4 eV), trilayer (4.5 eV) and quad/thicker layers (4.6 eV). The average deviations for all the measured samples were then calculated, the results of which are shown in Figure 5.63 (d). For all of the measured samples, with layer thickness from 1 - >10, $n = 4.6$ gave the closest calculated to reported work function values.

Equation 5.12 was used for calculating the SE spectrum of graphene supported on SiO_2/Si substrate, as displayed in Figure 5.27 (b).

$$\left(\frac{\partial \delta}{\partial E_K}\right)_{cal} = \left(\frac{\partial \delta}{\partial E_K}\right)_s \cdot \alpha'(E_K) + \left(\frac{\partial \delta}{\partial E_K}\right)_g \cdot (1+\eta) \tag{5.12}$$

Where the subscripts *cal*, s and g indicate the calculated, substrate and graphene spectra respectively. $\alpha' = \frac{\theta_m}{\pi/2}$ describes the proportion of SEs with an energy E_k that can escape the surface and η represents the BS coefficient.

The SE spectra of graphene was also measured in HIM. Figure 5.64 (a) shows the He^+ ion induced SE spectra of a freestanding monolayer of graphene. Figure 5.64 (b) shows the deviation of extracted work function values from the reported value (4.3 eV), where an $n = 5.3$ gave the closest result.

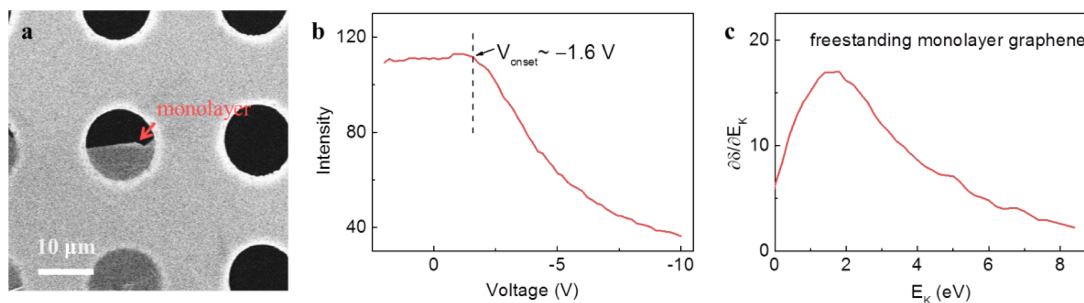

FIGURE 5.62: **a**, SEM image of the measured freestanding graphene monolayer, as marked by the red arrow. **b**, Grid voltage vs SE intensity curve from the monolayer. **c**, SE spectrum of the measured monolayer generated by differentiating the SE intensity curve in **b**.

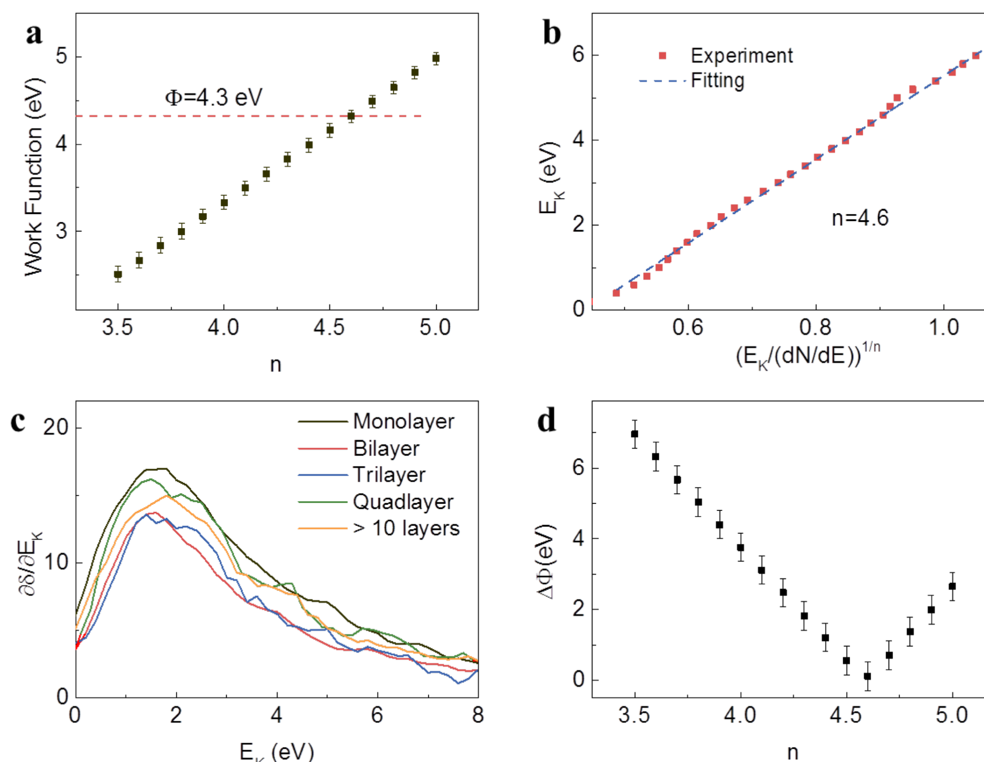

FIGURE 5.63: **a**, Extracted work function value for monolayer graphene at different n, where $n = 4.6$ gives the closet extracted value to reported value. **b**, Linear fitting of monolayer SE intensity data using Equation 5.11 with $n = 4.6$. **c**, SE energy spectra of the monolayer, bilayer, trilayer, quadlayer, and thick (> 10 layer) freestanding graphene. **d**, The deviation of extracted work function values from the reported values, at different values for n. The smallest difference between two values is given by $n = 4.6$.

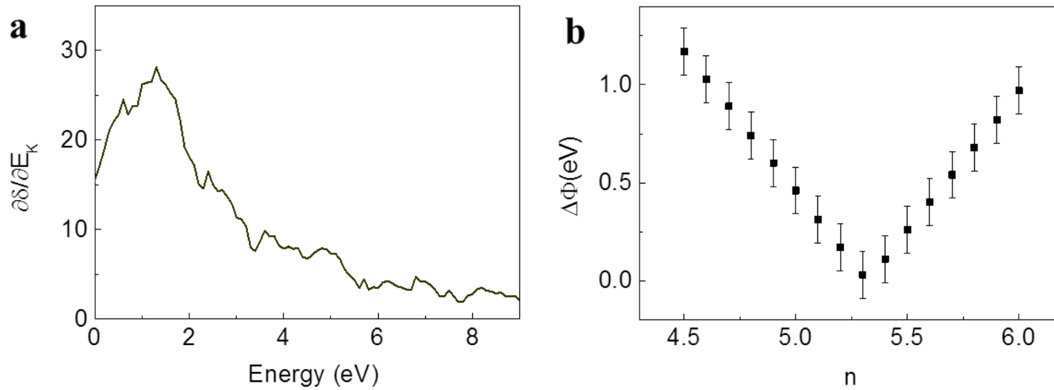

FIGURE 5.64: **a**, SE energy spectrum of the freestanding graphene monolayer in generated in HIM. **b**, Deviation of extracted work function values from reported values at different n, where n=5.3 gives the smallest difference between two values.

5.5.4 Summary of fabrication and application of a SE energy filter in HIM and SEM

A *High-Pass* energy filter device was designed and fabricated for use in HIM and SEM. When placed directly over a specimen region of interest, a retarding field was generated between the device and specimen, on the application of a negative bias to the device. The retarding field limited the kenitic energy (eV) of the SEs delivered to the detector enabling the generation of SE energy distributions (spectra) and energy filtered SE images.

The EF device was initially evaluated in the HIM. The retarding field was assessed as being homogeneous with unity SE filtering efficiency, (i.e. $\Delta V_{GRID} : \Delta E_K$ = 1:1). The influence of specimen bias and He^+ ion beam energy on the operation of the device were evaluated. Specimen bias did not influence filtering efficiency, however the fine details in the spectral were impacted. Changes to He^+ ion beam energy did not influnce filtering efficiency or spectral information. The EF device was evaluated in SEM and its SE filtering efficiency was not 1:1. However on application of the appropriate correction factor, reliable SEM SEED data was generated.

The EF device was used to generate SE energy spectra from HOPG and graphene specimens. The HOPG specimen was analysed in HIM with SEEDs generated

from three types of surface regions. The spectral data in the initial SEEDs from two surface regions show good alignment with the expected SE energy peaks. The third revealed a distinctively different initial SEED, suggesting that the surface conditions prior to He^+ ion irradiation in this region were significantly different. Continued irradiation on all regions resulted in changes to the SEED profiles, with damage inducing doses (≥ 6 pC$\cdot\mu$m^{-2}) changing the visible appearance of the specimen. The spectra associated with the damaged regions were comparable to the SE energy profile of glassy carbon, indicating the occurrence of material conversion by the high dose He^+ ion irradiation. SE spectra of graphene were generated in SEM and HIM. These were used to determine the work function monolayer and multi-layer (2 - >10) graphene specimens. The accuracy of fit of the extracted SE spectral data, to the expected work function values, was the method used to confirm correlation between SE energy spectral profile and layer thickness.

5.6 Summary of the comparative study on contamination formation, imaging and SE spectroscopy in SEM and HIM

The results of a comparative study on the mechanisms of contamination formation, SE imaging and SE spectroscopy in HIM and SEM, presented in this chapter, are summarised as follows.

In the contamination study, outlined in section 5.1, deposited structures formed on Si specimens were characterised by AFM and EDX, and their effect on SE image contrast was evaluated. He^+ ion beam-induced contamination was assessed in relation to specimen properties and beam parameters. These results were compared to contamination formed in SEM. Contamination formed in HIM was hydrocarbon limited and it attenuated the SE signal from the underlying specimen in proportion to its thickness. Due to an increased availability of hydrocarbons, the contamination formed in SEM was not hydrocarbon limited. In both microscopes the beam conditions were set in order to generate an approximately equal number of SEs. The average height of the contamination layers, formed below the apparent sputtering doses in HIM, revealed similar values to those formed with

comparative doses in SEM. This observation confirms the significance of the SE signal in the contamination process, implying that SE yield must be considered when attempting to promote or minimise its formation.

For the first part of the SE imaging study, given in section 5.2, the effects of the imaging parameters and sample charging on image contrast were explored in SEM and HIM. The imaging modes associated with the SE1 signal in both microscopes showed the greatest similarity. Analysis of SE images of Ga-implanted n-type Si samples showed the contrast of the implanted regions decreased linearly with increasing Ga density, and increased for each region with the increase in dwell time. In SEM, the contrast changes were due to the modification of the Si SE yield in the implanted regions and to a dynamic charging effect which occurred at increased dwell times. In HIM, the contrast changes in the implanted regions were due to positive charging and subsequent charge diffusion to the surrounding Si. Arising as a result of the Ga implantation, the charge diffusion increased with the increase in Ga density. As a result, contrast decreased inversely with the charge diffusion. SE yield was the critical factor determining image contrast in this comparative study. It is influenced by the primary particle (type and energy) and the imaged specimen (work function and electronic structure).

For the second part of the SE imaging study, given in section 5.3, graphene surfaces were analysed in HIM and SEM. The analysis revealed the presence of nanoscale PMMA residues associated with graphene device fabrication. For both imaging techniques, feature size directly correlated to probe size. The varying nature of the beam-sample interactions, at the different beam conditions, determined the SE contrast. In SEM, images produced at a low beam energy revealed high contrast. This was due to the majority of the interaction occurring within the top ~12 nm of the specimen. The images produced at high beam energy portrayed a reduced overall contrast and a higher degree of translucency. This was due to a lower primary electron scattering cross-section within the available depth of the specimen. In HIM, image contrast was determined by the SE emission associated with the increased stopping power of the He^+ ions in the specimen, and image sensitivity by the localisation of the beam-specimen interaction. SE emission and the finite size of the probe ultimately determined the spatial resolution and fidelity of the graphene specimens analysed in this study. The methodology used provides a quantitative approach to readily obtain the physical size of the features on a

graphene surface. HIM was assessed as being a superior SE imaging technique to SEM, due to its sub-nanometer probe and increased surface sensitivity.

In the third part of the SE imaging study, given in section 5.4, graphene specimens supported by SiO_2/Si substrates were analysed in SEM and HIM. In both techniques, the visibility of few-layer (< 10) graphene was revealed. Quantatitive SE contrast for each graphene layer was determined by accounting for all of the individual contributions to the total SE signal. These included, the SEs emitted from the graphene - those excited by the primary beam and those excited by the BSEs exiting the supporting substrate - and the SEs which were emitted from the substrate and diffused through the graphene. The quantification of graphene layer thickness enabled the determination of few-layer (1 - 4) graphene work function. This was achieved by extracting the SE attenuation contributions from the layer-dependent SE contrast, the results of which revealed a $< 1\%$ difference in the work function values determined for both excitation sources.

The final section of the chapter (section 5.5) details the results on the implementation of an SE energy filter device. Designed and fabricated for use in HIM and SEM, its function was to limit the kinetic energy of the SEs received at the detector so that specimen images of known energy (eV) could be collected. From these images SE energy distributions of the analysed specimens were derived. Quantified in terms SE filtering efficiency, the device produced SEED data that revealed spectral detail true to the material under analysis. The EF device was used to generate SE energy spectra of HOPG and graphene specimens. For pristine HOPG surface regions the spectra generated showed good alignment with the expected SE energy peaks. For damaged surface regions the spectra changed to fit the description of glassy carbon. For graphene, the SE spectra generated were used to determine the work function of monolayer and few-layer specimens. The main advantage of the EF device is its ability to elicit information from a specimen pertaining to the SE emission process, i.e. specimen work function. Also the SEED data generated can be used to finger print and characterise changes in a particular material.

Chapter 6

Raman enhancement of electron-beam induced carbon layers

In this chapter, we investigate the optical properties of electron-beam induced carbon layers deposited on an intrinsic silicon 100 substrate. These layers were characterised by AFM, SEM, TEM, EDX, EELS and Raman spectroscopy. They have been observed to enhance the intensity of the characteristic Si Raman peak (520 cm^{-1}) from the underlying substrate, the extent of which varies with the thickness of the carbon layer and electron beam deposition energy. The morphology of the carbon layers are first discussed, followed by a systematic investigation on the Raman enhancement.

6.1 Characterisation of the carbon layers

Carbonaceous layers were formed on a Si wafer specimen, by rastering the focused electron beam over a series of 5 μm $\times$5 μm areas with doses of 1, 3 and 5 nC$\cdot\mu m^{-2}$ for primary electron beam energies of 1, 3, 5, 12, 20 and 30 keV. The Si specimen was cleaned by the wet and dry cleaning methods outlined in section 4.1.1, immediately prior to insertion into the microscope. In order to minimise differences in hydrocarbon disassociation and desorption, a constant beam current (i_p) of 55 $\pm$ 5 pA was maintained for each beam energy. A layout of the resultant carbon layers is given in Figure 6.1(a). In this section, we will first present the general morphology of the layers followed by their chemical information and electrical properties.

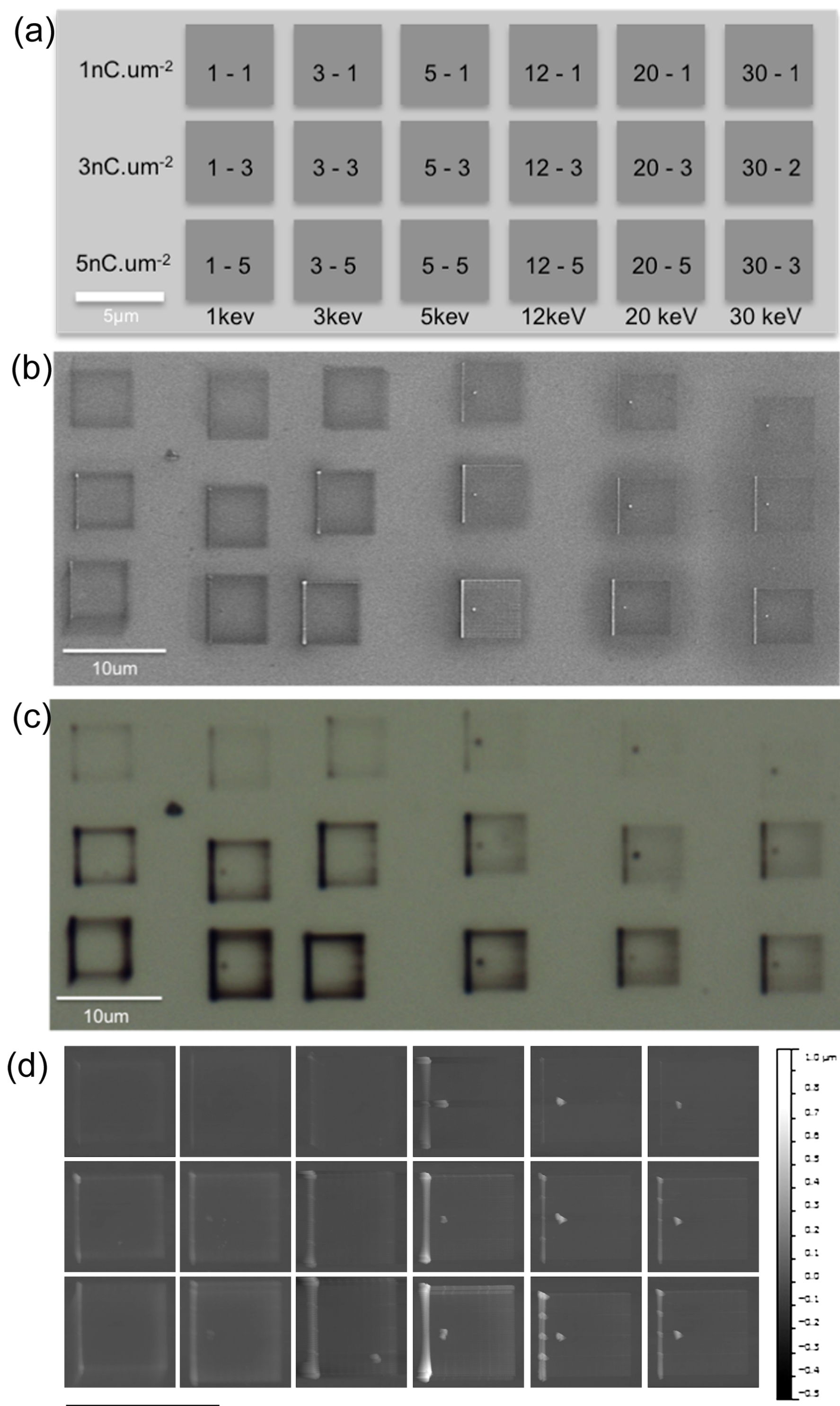

FIGURE 6.1: (a) A schematic of the carbon layer array with deposition parameters. (b) SE image acquired with a 3 keV beam. (c) An optical image of the carbon layers. (d) AFM height mapping of the layers.

6.1.1 General morphology

Immediately post deposition, a SE image of the carbonaceous layers was captured in the SEM using a primary beam energy of 3 keV, a beam current of 50 pA, a dwell time of 6 μs and a pixel resolution of 1024 $\times$ 924. This is shown in Figure 6.1(b). All of the layers display a reduced intensity relative to that of the Si specimen. Each layer displays distinctive edge and centre features, which change in appearance with the dose and energy of the depositing electron beam. Surrounding some of the layers is a region of reduced intensity. This region extends beyond the edges of the carbon layer, the distance of which increases with the increase in electron beam energy. A blurring of the edges is also present in some of the layers produced at 1 and 3 keV. A distinctive high intensity dot feature is present in all layers induced with an electron beam energy of 12 – 30 keV. A bright X and Y line pattern is present in the layers generated at 12 keV and is most prominent for the 5 nC$\cdot\mu$m^{-2} layer.

An optical image of the carbonaceous layers is displayed in Figure 6.1(c). This image reveals similar layer features to those observed in the SE image. The intensity of the carbon layers is reduced relative to the Si specimen with each layer also displaying distinctive edge and centre features. At each beam energy the average intensity of each carbon layer decreases with increase in dose, however at each dose the average intensity increases with increase in beam energy. The distinctive dot features revealed in the SE image are also observed optically for the 12 - 30 keV layers and the 3 and 5 nC$\cdot\mu$m^{-2} layers induced at 3 keV.

The morphology of each individual carbon layer was revealed by AFM profiling in non-contact (tapping) mode. This enabled the generation of thickness, volume and surface roughness data for each layer. A collage of these height profile images is displayed in Figure 6.1 (d). For each carbon layer, the edge is higher than the centre region, with the left edge being significantly higher than the remaining part of the layer. The distinctive dot features present in the SE and optical images were revealed to have an increased height relative to their immediate surroundings. The profile images also reveal stripe and zig-zag patterns in the morphology of each of the layers, being most prominent in the layers generated with an applied electron dose of 5 nC$\cdot\mu$m^{-2}.

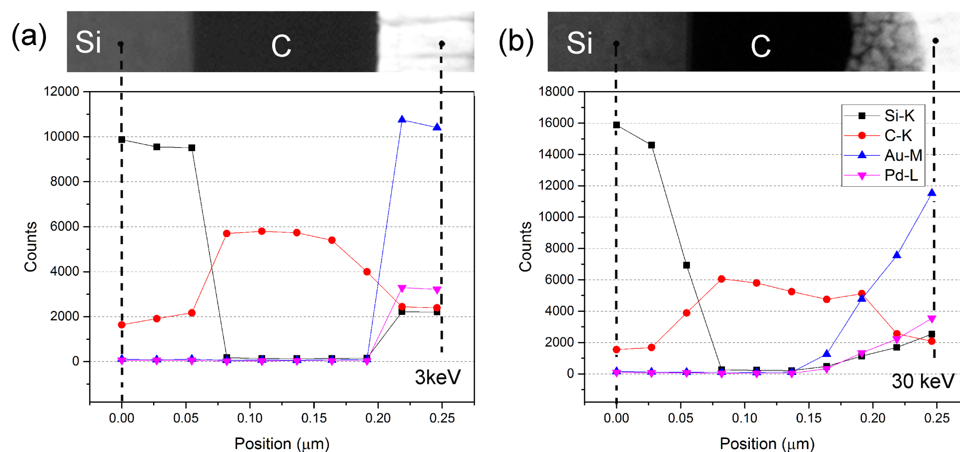

FIGURE 6.2: EDX line scan for (a) the 3 keV layer and (b) the 30 keV layer with its corresponding STEM cross-sectional images. The additional Au-Pd and Pt layering was required to protect the underlying carbon layers during the TEM lamella preparation stages.

6.1.2 Chemical Analysis of the carbon layers

Chemical analysis of the carbon layers by EDX was conducted in a Titan TEM operating at 300 keV. Cross-sectional TEM lamellas (~60 nm in thickness) of the layers produced at 3 keV and 30 keV electron beam energy were analysed to investigate the presence of Si in the amorphous carbon structure. Figure 6.2 shows the results of the EDX line-scan analysis in which a STEM image of each deposit is displayed with a corresponding plot of Si($K\alpha$), C($K\alpha$), Au($M\alpha$) and Pd($L\alpha$) X-ray intensity. From the EDX results it is clear that neither carbon layer shows a detectable level of Si.

EELS was conducted on the carbon layers to determine relative the sp^2/sp^3 ratio. This analysis was performed in a TEM operating at 300 keV. To reveal the relative differences in the sp^2/sp^3 ratios of the carbon layers, it was vital was conduct the EELS analysis of both specimens with exactly the same beam-specimen interaction conditions. To achieve, this lamellas of equivalent thickness (~60 nm) were produced and the incident beam was directed parallel to the same crystallographic orientation of the Si substrates. Figure 6.3 shows the EELS spectra for the carbon (1s) K absorption edges of the two layers as well as their STEM images. The normal range for π^* excitations is 285 - 290 eV and for σ^* excitations is 290 - 305 eV [200]. Immediately prior to acquiring the energy loss spectra, the ZLP was

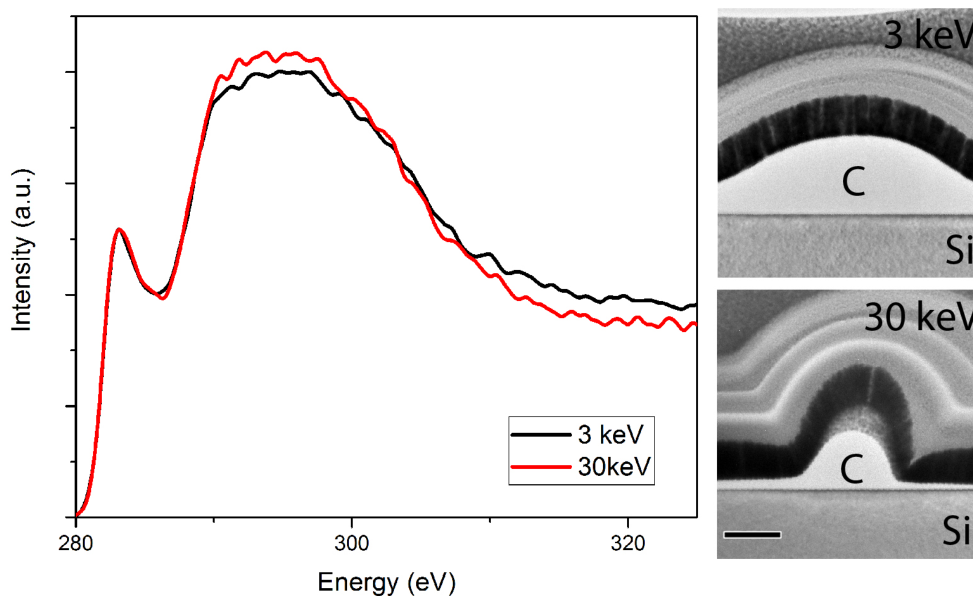

FIGURE 6.3: EELS data showing C (1s) K absorption edges of the carbon layers generated at 3 keV and 30 keV and the corresponding TEM images.

recorded. This was used to ensure the energy scale was correct for the core loss peaks. The spectra were normalised for comparison. The minimum between the π^* pre-peak and the σ^* peak was used as the edge of two integrating windows. The π^* window had a width of 5 eV and was to the left of the minimum. The σ^* window was 15 eV wide and to the right of the minimum. According to Cuomo et al., to a good approximation the ratio of the integrated areas under the π^* and σ^* energy windows is proportional to the relative number of π^* and σ^* orbitals [200]. For 100% sp^2 carbons this ratio is 1/3 and for 100% sp^3 carbons it is 0. The concentration of bonds relative to the overall concentration of π and σ bonds is used to calculate the relative differences in the sp^2 concentration present within the two carbon layers. For the 3 keV carbon layer the ratio 0.4925, and for the 30 keV carbon it is 0.5073. This indicates a 3% increase in the relative concentration of sp^2 carbon bonds present in the layer generated at 30 keV in comparison to the layer generated at 3 keV electron beam energy. The data provided by the EELS spectra can be used as a comparative measurement of the differences in the sp^2 or sp^3 bond concentration present in the layers and not for determining their exact concentrations.

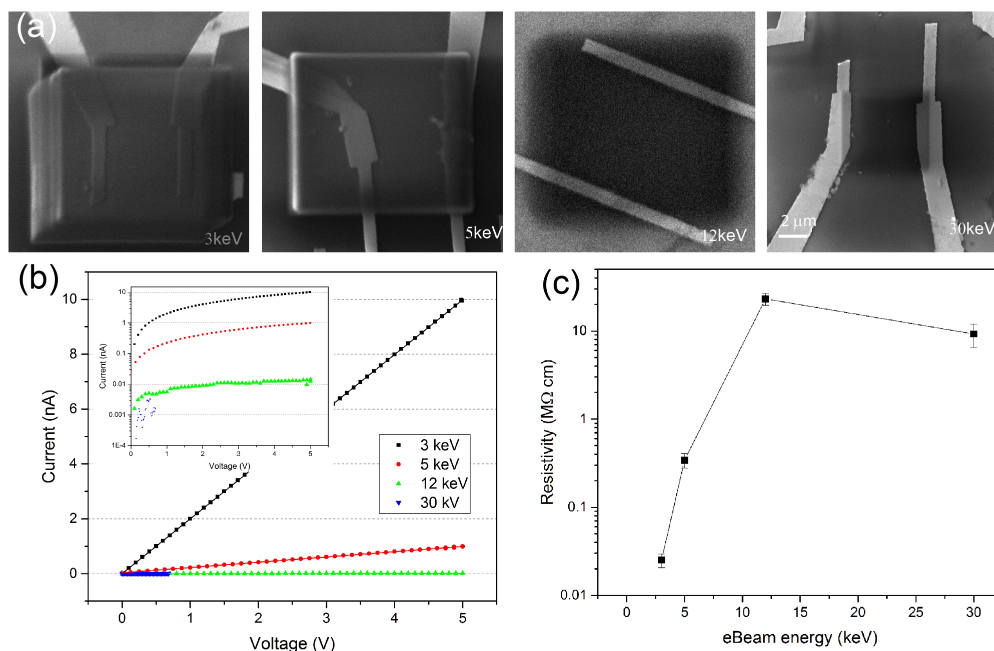

FIGURE 6.4: (a) Images of the carbon layers (3, 5, 12 & 30 keV) deposited across the Au electrodes. (b) The current measured across the carbon layers for an applied biasing range of 0 - 4 V. (c) The resistivity of the carbon layers as a function of electron beam deposition energy.

6.1.3 Electrial property of the carbon layers

Figure 6.4 shows the results of the electrical characterisation of the carbon layers by two-point probe measurements. Prior to the carbon deposition, Au contacts had been deposited on the substrate surface through photolithography. The carbon layers were then deposited with a fixed dose of 5 nC·μm^{-2} for a given e-beam energy (e.g. 3, 5, 12 and 30 keV). As displayed in Figure 6.4 (a), the carbon layer can be seen in contact with two electrodes. Immediately after the deposition the specimen was removed from the SEM and placed on an electrical characterisation apparatus. A voltage of 0 - 4.0 V was then applied across the Au contacts via nano-manipulator probes.

The resistivity of individual carbon layers was determined by using the standard formula for resistivity (i.e. $R = \rho L/A$). As all layers were deposited with the same dose and beam current, they have similar thickness ($\sim$ 300 nm). With the same lateral dimension they had similar cross-sectional area (A), however due to slight variations in the spacing between the sets of Au contacts the length (L) of each deposit varied. Figure 6.4 (c) shows the resistivity of the carbon layers as a

function of electron beam energy. With the increase in beam energy, from 3 keV to 30 keV, an increase in the resistivity of the layers of 0.025 – ∼10 MΩ cm is observed.

6.2 Raman mapping and correlative study

Raman spectral maps of the carbon layers, displaying the characteristic Si Raman peak (520 cm^{-1}) and the carbon Raman band (1000 - 1800 cm^{-1}), are shown in Figure 6.5 (a) and (b), respectively. In Figure 6.5 (b), all of the carbon layers can be identified from their Si Raman signature, however those generated with a dose of 1 nC·μm^{-2} have a minimum contrast relative to the un-deposited regions of the Si specimen. The intensity of the Si Raman peak varies from layer to layer and within each layer. Edge and center features can be seen for each carbon layer, as well as some of the distinctive dots and line patterns previously observed. In Figure 6.2 (c), only carbon layers generated with an applied dose of 3 and 5 nC·μm^{-2} are identified from their carbon Raman band signature. Layers generated at 1 – 5 keV clearly reveal edge and center features however these features are not clear for the layers generated at 12 – 30 keV. The distinctive dots are also observed and can now be seen in the region of the image where the 1 nC·μm^{-2} layers are located.

Figure 6.6 (a) shows the AFM generated height profile image of the carbon layer deposited by a 3 keV electron beam with a dose of 5 nC·μm^{-2} . The X and Y coordinates in the image represent the area of the Si specimen over which the AFM probe was scanned. The surface height variations encountered during the AFM scan are represented by the grey scale intensity (range). The carbon layer, centred in the image, varyies in height between ∼50 – 250 nm relative to the Si surface. The edges of layer are higher than its interior region with the left edge being the highest. The elongated feature observed along its left edge in the SEM image is confirmed as being raised above the Si surface with a height range of 150 – 250 nm. The layer morphology also reveals a vertical stripe-like pattern and a double-line effect at the top edge. The brighter segments of these features are higher than the darker segments. As the dwell time of the electron beam significantly influences the rate of contamination growth, the areas revealed as being greater in thickness received a higher dose than the thinner regions. The X, Y and Z data in the AFM scan was used to generate a *Three-Dimensional* (3D) representation of

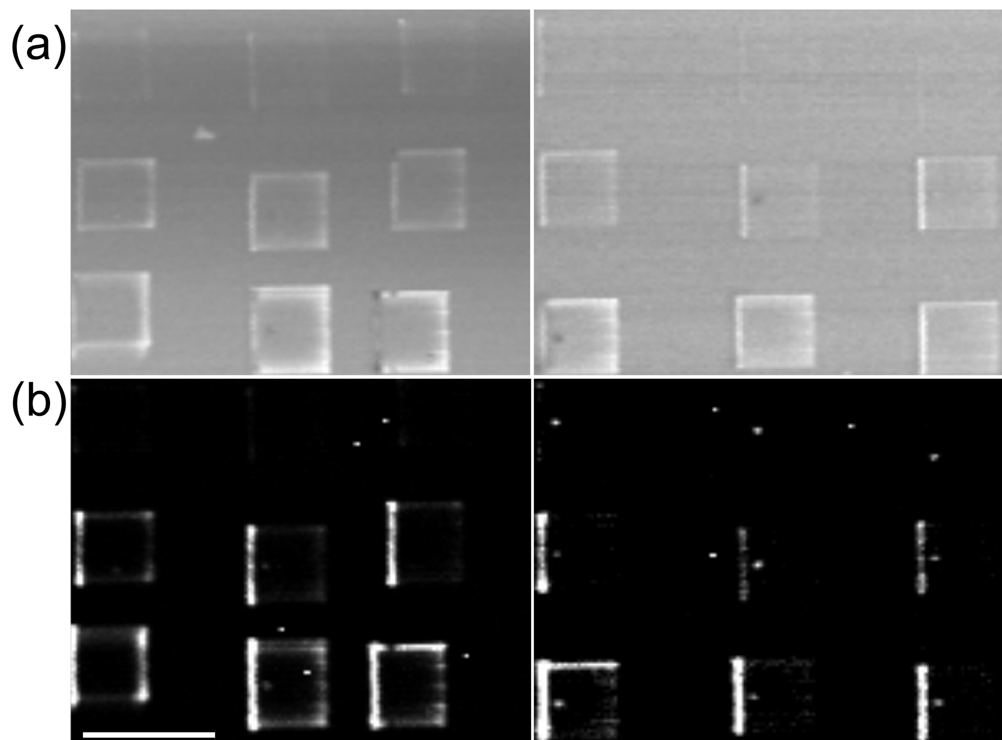

FIGURE 6.5: Raman intensity maps, generated with an excitation energy of 532 nm, showing the square electron beam induced deposits. (a) intensity map of the characteristic silicon Raman peak (520 cm^{-1}) and (b) intensity map of the carbon Raman band (between 1050 - 1800 cm^{-1}). The scale bar indicates 10 μm.

the contamination layer volume and this is displayed on the far left of the figure. The grey level of each pixel (0 - 255) in the AFM height profile is correlated to carbon layer height (0 - 250 nm). The pixel intensity distribution is plotted in the histogram, from which a mean grey level value of 86 was determined. This corresponds to a layer height 84 nm. The black and white *binary* image represents the relative location of the pixels in the AFM image above (white) and below (black) the mean height.

Figure 6.6(b) shows an SE image of the carbon layer. The resultant contamination is revealed as being darker than the un-irradiated region. The SE intensity of the layer varies, with its edges being darker than its centre. On the left edge an elongated narrow feature can be seen. It is measured at ~0.5 μm in width and is the darkest feature in the image. The carbon layer serves to attenuate the SE emission from the underlying Si specimen with the degree of attenuation being dependent upon layer thickness. The grey level of each pixel (0 - 255) in the image

is correlated to SE intensity (arb.). The pixel intensity distribution is plotted in the histogram, from which a mean grey level value of 108 pixels was determined. The black and white *binary* image represents the relative location of the pixels in the SE image above (white) and below (black) the mean SE intensity.

In Figure 6.6 (c) a Raman intensity map of the carbon band (1050 – 1800 cm^{-1}) collected from the Si specimen is presented. The intensity of each is pixel corresponds to the concentration of the carbon bonds excited during the acquisition of each spectrum, with a minimum to maximum intensity range of 2 – 200 detector counts. The carbon layer is centred in the map with its edges displaying an increased intensity relative to its centre and the clean Si surface. The intensity of the carbon band is observed to increase with the increase in layer thickness. This can be clearly seen in the left edge of the contaminated region, where maximum carbon Raman intensity coincides with maximum layer thickness. A 3D representation of the intensity of the Si Raman peak as it varies across the contamination layer is also displayed. The grey level of each pixel (0 - 255) in the carbon Raman image is correlated to carbon band intensity (2 - 200 counts). The pixel intensity distribution is plotted in the histogram, from which a mean grey level value of 105 was determined. This corresponds to a carbon Raman intensity of 83 counts. The black and white *binary* image represents the relative location of the pixels in the carbon Raman map above (white) and below (black) the mean carbon Raman intensity value.

In Figure 6.6(d) a Raman intensity map of the characteristic Si peak (520 cm^{-1}) from the Si specimen is presented. Each pixel in the map represents a single Raman spectra collection point. Each point in the Si map coincides with each point in the C map, having an equal area and an equal pixel per point ratio. The area on the surface of the specimen where each spectra was collected equalled 0.065 μm^2 (140 $\times$ 140 pixels, over a 35 μm $\times$ 35 μm FOV). The grey level of each pixel represents the intensity of the characteristic Si Raman peak collected at each point, with a minimum to maximum intensity range of 200 – 800 detector counts. The intensity of the Si signal emitted from the contamination is observed to vary across the layer. The centre of the layer exhibits a similar Si intensity to that of the non-contaminated regions of the specimen. The top, bottom and right edges of the deposit exhibit an increased intensity, however the left edge shows regions of increased and decreased intensity. When the Raman map is overlaid on the AFM height profile image, the relationship between Si peak intensity and

layer thickness was attained. This revealed an initial increases the Si peak intensity with the increase in layer thickness, followed by a decrease in intensity as thickness continued to increase. A 3D representation of the intensity of the Si Raman peak as it varies across the contamination layer is displayed as well. The grey level of each pixel (0 - 255) in the Si Raman image is correlated to Si peak intensity (200 - 800 counts). The pixel intensity distribution is plotted in the histogram, from which a median grey level value of 91 was determined. This corresponds to a carbon Raman intensity of 91 counts. The black and white *binary* image represents the relative location of the pixels in the Si Raman map above (white) and below (black) the mean intensity value.

By contrasting the white to black pixels of the binary images (presented in Figure 6.6), intensity ratios of the pixel data presented in the AFM, the SEM, and Raman intensity profiles were correlated to each other relative to their statistical means. The results of this correlation are presented in Table 6.1. Ratios between 0.5 - 1 indicate a strong correlation. A strong correlation is observed between the carbon layer (AFM) and the attenuation in the SE image (0.7381). This correlation is spatially represented by the position of the white pixels in the AFM *binary* image relative to the black pixels in SEM *binary* image. A strong correlation is also observed between AFM and Si-Raman peak (0.7355) and is spatially represented by the position of the white pixels in AFM *binary* image relative to white pixels in Si-Raman *binary* image. The carbon layer shows weak correlation with the C-Raman intensity, however a strong correlation exists between SEM and C-Raman (0.5965). The correlation between SEM and C-Raman can be used to spatially correlate the C-Raman signal to the corresponding pixels in the AFM height profile. SEM also shows a strong correlation to Si-Raman.

	AFM	SEM	C-Raman	Si-Raman
AFM	1(0)	0.1011(0.7381)	-0.0162(0.2042)	0.7355(0.1674)
SEM	0.1011(0.7381)	1(0)	-0.2048(0.5965)	0.0192(0.7511)
C-Raman	-0.0162(0.2042)	-0.2048(0.5965)	1(0)	0.0045(0.3005)
Si-Raman	0.7355(0.1674)	0.0192(0.7511)	0.0045(0.3005)	1(0)

Table 6.1: Results of the statistical correlation study. 0-0.09 non-relevant, 0.5 - 1 strongly relevant.

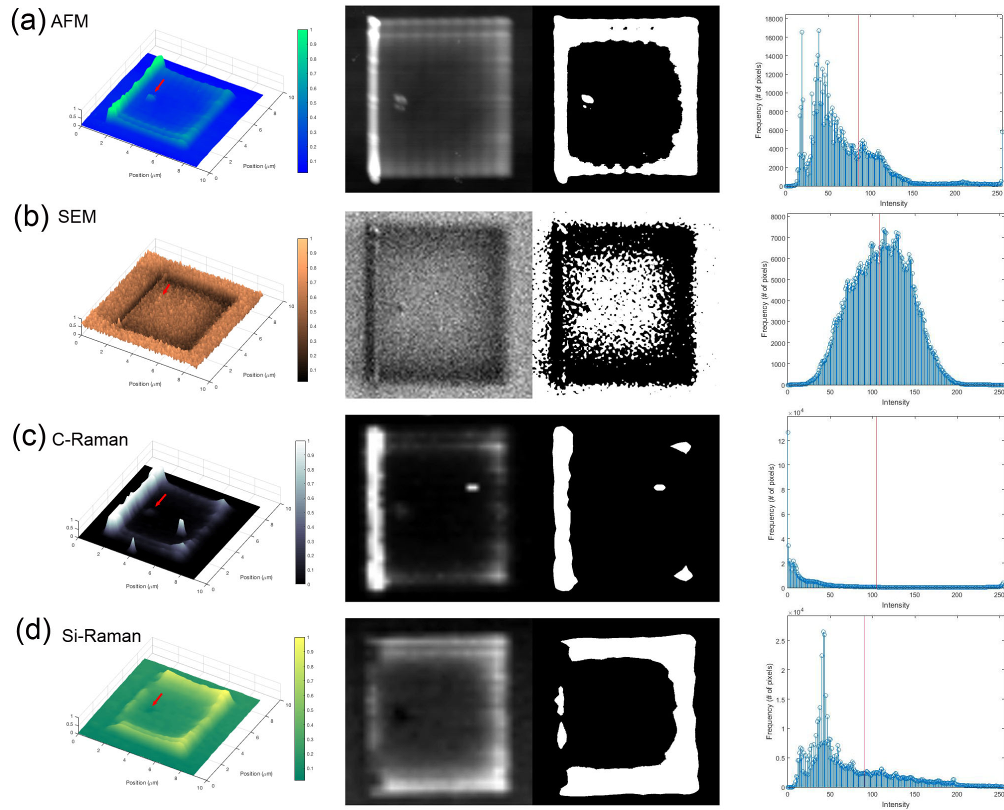

FIGURE 6.6: Images and statistical data from the Carbon-Raman correlation study on a carbon layer deposited by 3 keV electron beam with a dose of 5 nC$\cdot\mu$m^{-2} showing, (a) 3D AFM height projection, 2D AFM height profile, binary image representing pixels with heights above (white) and below (black) mean layer height and the pixel intensity distribution corresponding to the 2D AFM profile. (b) 3D SE intensity projection, SEM SE image, binary image representing pixels with attenuation values below (white) and above (black) mean SE attenuation and the pixel intensity distribution corresponding to the SE image. (c) 3D Raman intensity projection and Raman intensity map of the carbon Raman band (1050 – 1800 cm^{-1}) present within the layer, binary image representing pixels with intensity values above (white) and below (black) mean C-Raman intensity, and the pixel intensity distribution corresponding to the C-Raman map. (d) 3D Raman intensity projection and Raman intensity map of the Si Raman peak (520 cm^{-1}) present within the layer, a binary image representing pixels with intensity values above (white) and below (black) mean Si-Raman intensity, and the pixel intensity distribution corresponding to the Si-Raman map.

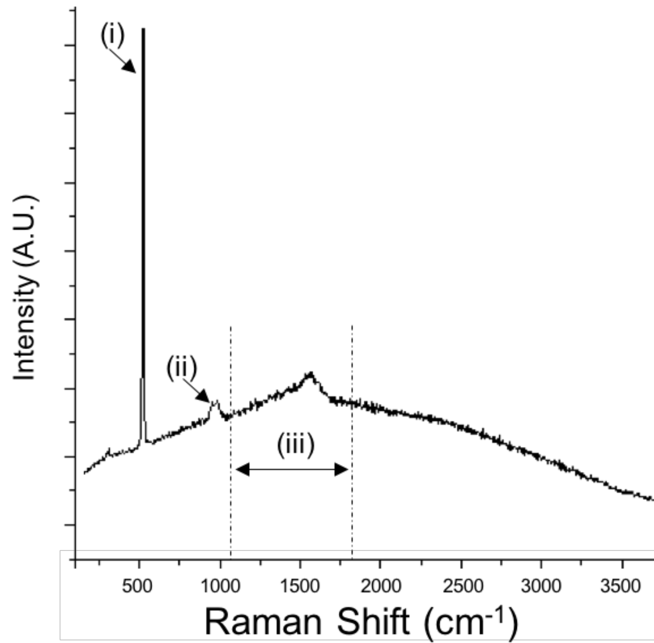

FIGURE 6.7: Averaged Raman intensity spectra from the carbon layer deposited at an electron beam energy of 3 keV and an applied dose of 5 nC·μm^{-2}, showing the first (i) and second (ii) order Si peaks and the asymmetric carbon band (iii). The spectra was collected upon 532 nm laser excitation.

6.3 Raman spectral analysis of the carbon layers

6.3.1 Collective spectra

The bonding structure of the electron beam induced amorphous carbon deposits, i.e. the sp^2 phase, average crystallite size and sp^2/sp^3 ratio, is characterised by the position, spread, intensity and intensity ratios of the characteristic D and G carbon Raman bands.

As the amorphous carbon layers were induced on the Si wafer specimen, the dominant Raman peaks observed in the spectra are those for Si and Carbon. A typical averaged spectrum from a carbon structure deposited with 1 keV electron beam energy is displayed in Figure 6.7. For Si, the characteristic peak at 520 cm^{-1} and the second order peak at 970 cm^{-1} can be seen. For carbon, an overlapping asymmetric band from 1050 – 1800 cm^{-1} is observed. It contains the D and G peaks

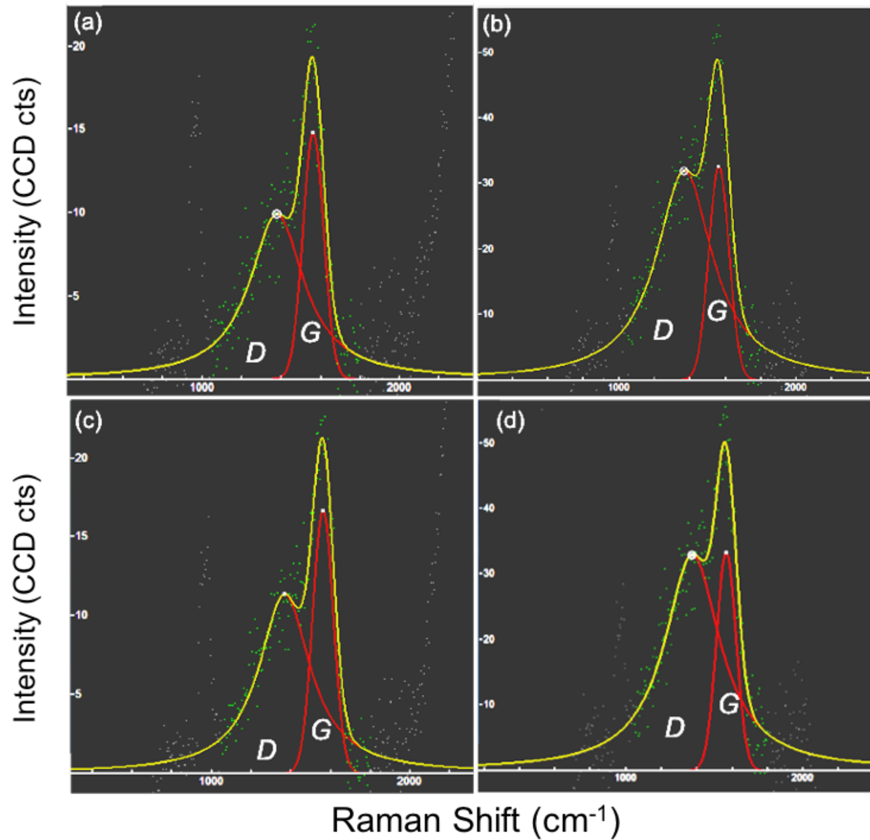

Figure 6.8: Fitted carbon D and G peaks from averaged spectral data collected across carbon deposits generated at 3 keV (a, b) and 5 keV (c, d) with applied electron doses of 3 nC$\cdot\mu$m^{-2} and 5 nC$\cdot\mu$m^{-2} for each energy. The D and G peaks across all spectra were centred at ∼1370 cm^{-1}and ∼1560 cm^{-1} on fitting. All Raman data was fitted with *Fit-YK* spectral software.

which are centred at ∼1350 and ∼1580 cm^{-1}, respectively. The D peak is associated with the breathing mode of the aromatic bonds and the G peak with the stretching mode of aromatic and linear bonds [134]. For the purposes of spectral analysis, the first order Si and the D and G peaks are of interest.

6.3.1.1 Peak position and intensity

Figure 6.8 shows the fitted carbon D and G peaks from averaged spectral data collected across carbon deposits generated at 3 keV and 5 keV electron beam energies. The peaks for all other spectra were then fitted using the same approach. The fitted peak data for comparison of their intensity ratios and positions is given

in Table 6.2.

Profile	I_D	I_G	I_D/I_G	D - Peak (cm^{-1})	G - Peak (cm^{-1})
(a) 3keV - 3nC·μm^{-2}	10 ± 2	15 ± 5	0.7 ± 0.3	1378	1561
(b) 3keV - 5nC·μm^{-2}	32 ± 4	33 ± 8	1.0 ± 0.3	1364	1563
(c) 5keV - 3nC·μm^{-2}	11 ± 3	17 ± 5	0.7 ± 0.3	1367	1560
(d) 5keV - 5nC·μm^{-2}	33 ± 4	33 ± 8	1.0 ± 0.3	1374	1565

Table 6.2: A comparison of the carbon D and G intensities (CCD counts), intensity ratios, and peak positions from the fitted Raman profiles displayed in Figure 6.8

6.3.2 Individual spectra

From the image displayed in Figure 6.5 (a) the intensity of the Si Raman signal is observed to vary significantly within each of the deposited carbon layers. To understand the correlation between Si Raman intensity and deposition thickness (or volume), a detailed analysis of the carbon bonding structure as a function of electron beam energy was conducted.

6.3.2.1 5 keV Carbon Layer

Figure 6.9 shows the Raman spectra collected from a 0.25μm^2 areas of the specimen, i.e. clean and contaminated regions of the Si (100) substrate. The height and volume of the carbon were extracted from the specimen's AFM profile. The characteristic Si Raman shift (centred at 520 cm^{-1}) collected from an uncontaminated region of the Si specimen is displayed in Figure 6.9 (a). Raman spectra of the clean Si surface did not reveal discernible carbon peaks. The Si and carbon Raman shifts from the contaminated regions with different heights are presented in Figure 6.9 (b – d). In each spectrum, the Si shift is centred at 521 cm^{-1} and the carbon band ranges from ~1000 – 1800 cm^{-1}. Within the carbon band, the characteristic D and G peaks were fitted.

The intensity of the characteristic Si Raman shift (I_{Si}) and the I_D/I_G ratio vary with the thickness of the carbon layer. In Figure 6.9 (b), the I_{Si} for 0.011 μm^3 of the carbon layer is 85% greater than that of the clean surface (Figure 6.9 (a)). In Figure 6.9 (c), the I_{Si} for 0.012 μm^3 of the carbon layer is 106% greater than that

of the clean surface. In Figure 6.9 (d), the I_{Si} for 0.02 μm^3 of the carbon layer is 25% less than that of the clean surface. As the carbon layer volume increases from 0.011, to 0.012, to 0.02 μm^3, the I_D/I_G changes from 1.17, to 1.25, to 0.80, respectively.

Figure 6.10 shows the effects of the carbon layer on the intensity of the characteristic Si Raman shift (I_{Si}). In Figure 6.10 (a) the I_D/I_G ratio and the sum of the carbon peak intensities ($I_D + I_G$) are sketched as functions of the carbon volume. As the volume increases the I_D/I_G ratio decreases. On reaching ~0.019 μm^3 the I_D/I_G ratio falls below 1.0 and saturates at ~0.8 with further increase in volume. As the D peak represents the breathing mode of aromatic carbon bonds, a decrease in I_D/I_G ratio indicates a decrease in their concentration. The $I_D + I_G$ first increases in the carbon volume, when the volume is less than 0.03 μm^3, and tends to saturate for thicker carbon layers. The $I_D + I_G$ gives an indication of the total concentration of carbon bonds present within a given carbon layer and the saturation may be due to the information depth of the Raman collection.

Figure 6.10 (b) shows the variation in I_{Si} with the increase in carbon layer thickness. Between ~35 – 60 nm the I_{Si} is greater than that of the clean surface and peaks at a thickness of 47 nm. At ~75 nm the I_{Si} drops to a level below that of the clean surface and decreases gradually with the increase in carbon layer thickness.

Once a layer thickness of ~40 nm is reached, I_{Si} becomes greater than that of the clean surface. In this phase, I_{Si} is more sensitive to fluctuations in the I_D/I_G ratio than the concentration of the carbon bonds given by $I_D + I_G$. In phase ii., the $I_D + I_G$ continues to increase however and I_D/I_G drops below 1.0 when a thickness of ~75 nm is reached. I_{Si} is now less than that of the clean surface and changes little with increase in thickness, up to ~120 nm. In this phase I_{Si} is influenced by the stable I_D/I_G ratio and not the increasing $I_D + I_G$. With further increase in the thickness of the carbon layer (phase iii.), the rate of increase in $I_D + I_G$ is reduced and the I_D/I_G ratio remains unchanged having saturated at ~0.80. I_{Si} begins to decrease and decreases further with the increase in layer thickness.

From the results displayed in Figure 6.10, the carbon layer has an enhancing effect on the Si Raman shift when its I_D/I_G ratio is above 1.0. A maximum enhancement occurs for a volume of ~0.012 μm^3 (or a thickness of 47 nm) when an I_D/I_G ratio of 1.25 generates a 106% increase in I_{Si}, relative to that of the clean surface. When the I_D/I_G ratio is less than 1.0 the carbon has an attenuating effect on I_{Si}. This

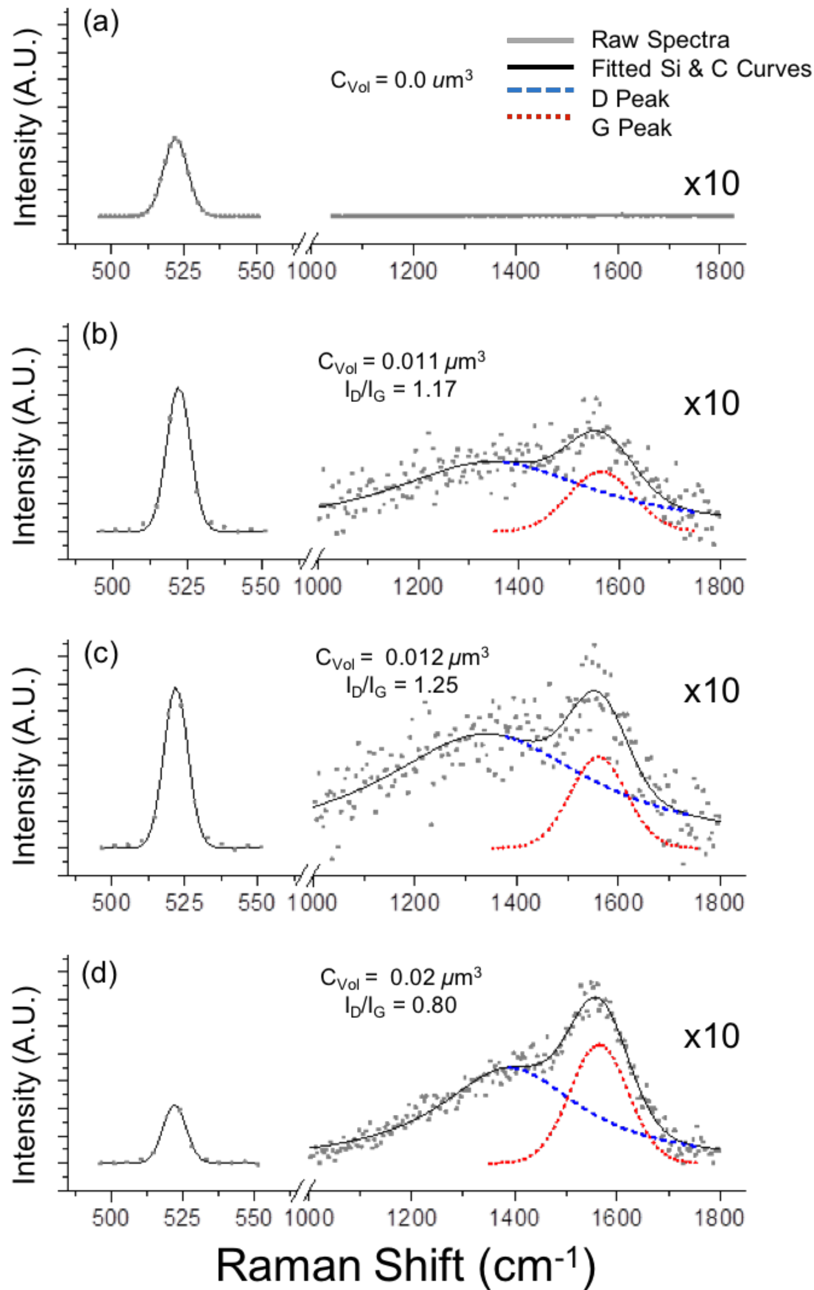

FIGURE 6.9: Raman spectra of Si specimen which had previously been contaminated in a scanning electron microscope by a 5 keV. The Raman spectra presented above shows the Si and carbon Raman shift present in an uncontaminated region of the specimen (a), and contaminated regions of the specimen with increasing volume in (b – d). In each spectrum the Si peak is centred at 520 cm^{-1} and the carbon shift is observed between ∼1000 – 1800 cm^{-1}. The carbon band has a significantly reduced intensity to that of the Si peak and in each spectrum a ×10 multiplication factor is applied. The carbon band is comprised of the *D* and *G* peaks. These are presented in each spectra by the blue and red fitted curves, centred at 1350 cm^{-1} and 1580 cm^{-1} respectively.

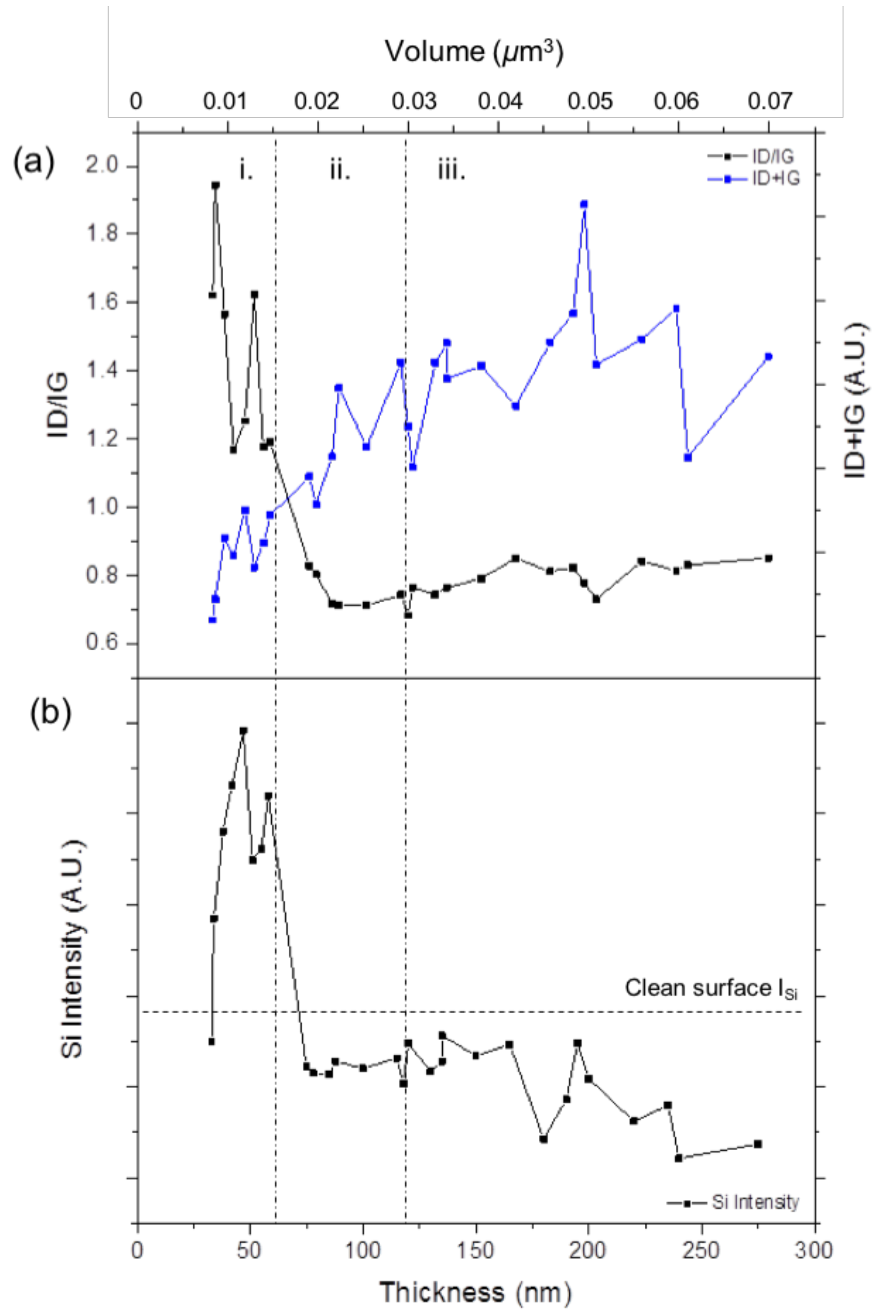

FIGURE 6.10: Carbon layers formed with 5 keV electron beam energy. (a) The relationship between carbon peak intensity ratio (I_D/I_G) and the sum of the carbon peaks ($I_D + I_G$) as a function of increasing carbon volume. (b) The variation in Si Raman shift (I_{Si}) observed for the increase in layer thickness. Fluctuation of the measured scattered light accounts for a ± 10% maximum variation in the carbon and Si Raman intensity values.

occurs for contamination volumes of ~0.019 μm^3 (or a thickness of ~75nm) and above. The attenuation results in a 25 – 50% decrease in I_{Si} with the degree of attenuation dependent on the carbon thickness and the saturated level of the I_D/I_G ratio.

Carbon layers formed at other electron beam energies were analysed exactly the same as the 5 keV layer. These results are displayed in Figure 6.11 to Figure 6.20.

6.3.2.2 1 keV Carbon Layer

The Raman spectra for carbon species formed with 1 keV, is displayed Figure 6.11. In Figure 6.11 (b), the I_{Si} for 0.011 μm^3 of the carbon layer is 25% less than that of the clean surface (Figure 6.11(a)). In Figure 6.11 (c), the I_{Si} for 0.015 μm^3 of the carbon layer is 4% greater than that of the clean surface. In Figure 6.11 (d), the I_{Si} for 0.018 μm^3 of the carbon layer is 50% greater than that of the clean surface. As the carbon layer volume increases from 0.011, to 0.015, to 0.018 μm^3, the I_D/I_G changes from 0.78, to 0.74, to 0.69, respectively.

Figure 6.12 shows the effects of the 1 keV carbon layer on the intensity of the characteristic Si Raman shift (I_{Si}). In Figure 6.12 (a) as the volume increases the I_D/I_G ratio first increases but quickly decreases. On reaching ~0.011 μm^3 the I_D/I_G ratio peaks at ~0.8. Between 0.011 – 0.018 μm^3 the I_D/I_G ratio declines and saturates at ~0.7 with further increase in volume. A decrease in I_D/I_G ratio indicates a decrease in the concentration aromatic carbon bonds. The $I_D + I_G$ initially increases with increase in carbon volume, peaking at 0.035 μm^3, prior to saturation. Figure 6.12 (b) shows the variation in I_{Si} with the increase in carbon layer thickness. Between ~60 – 125 nm, I_{Si} is greater than that of the clean surface and reaches a maximum for a layer thickness of ~80 nm. At ~125 nm, I_{Si} drops to a level below that of the clean surface and decreases further with the increase in carbon layer thickness.

In phase (i) as the layer thickness increases the I_D/I_G ratio increases however both $I_D + I_G$ and I_{Si} remain relatively unchanged and at a low value. In this phase there is an insufficient presence of carbon bonds within the layer to enhance the characteristic Si Raman scatter from the underlying Si specimen. In phase (ii) as I_D/I_G decreases, $I_D + I_G$ and I_{Si} begin to increase. I_{Si} peaks for a layer thickness of 75 nm at which point the I_D/I_G ratio has reached a minimum value of ~0.65.

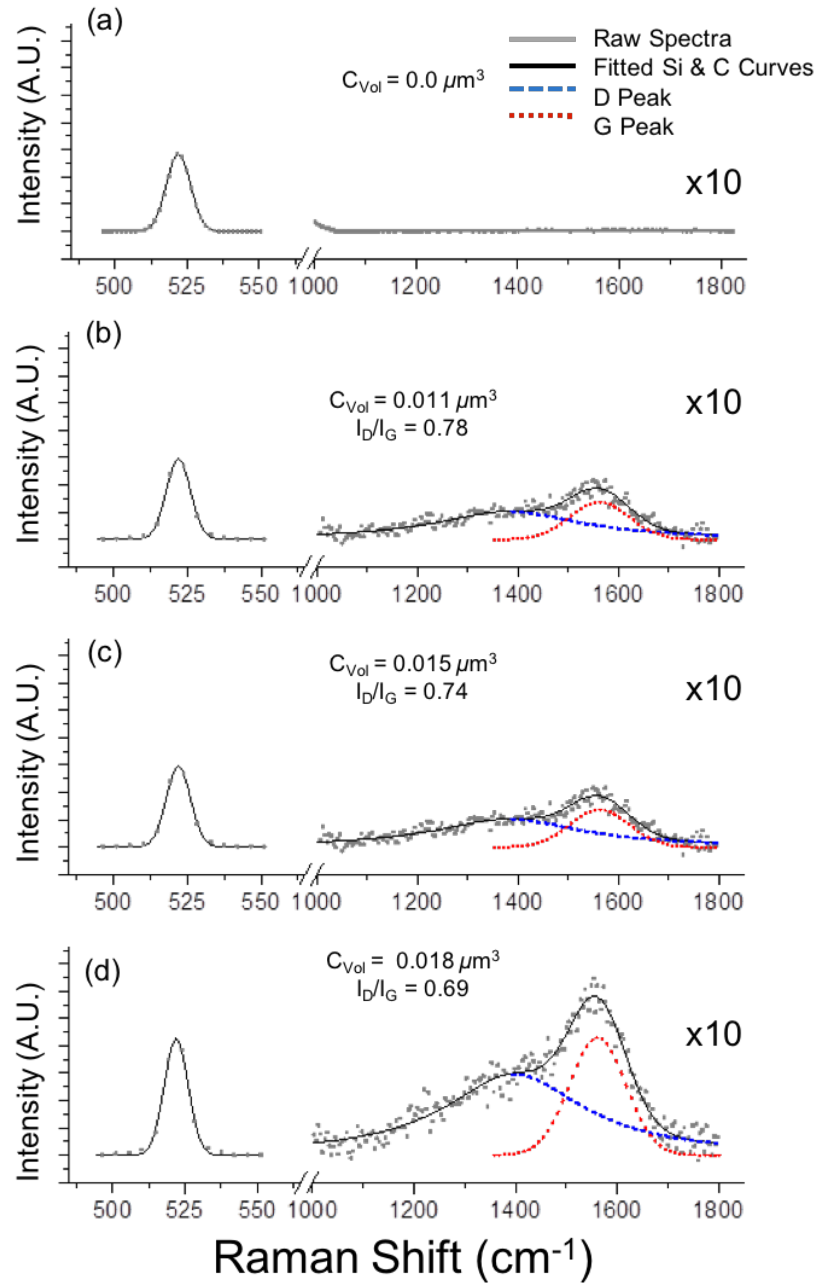

FIGURE 6.11: Raman spectra of the Si specimen which had previously been contaminated in a scanning electron microscope by a 1 keV electron beam. The Raman spectra shows the Si and carbon Raman shift present in an uncontaminated region of the specimen in (a), and contaminated regions of the specimen with increasing volume in (b – d).

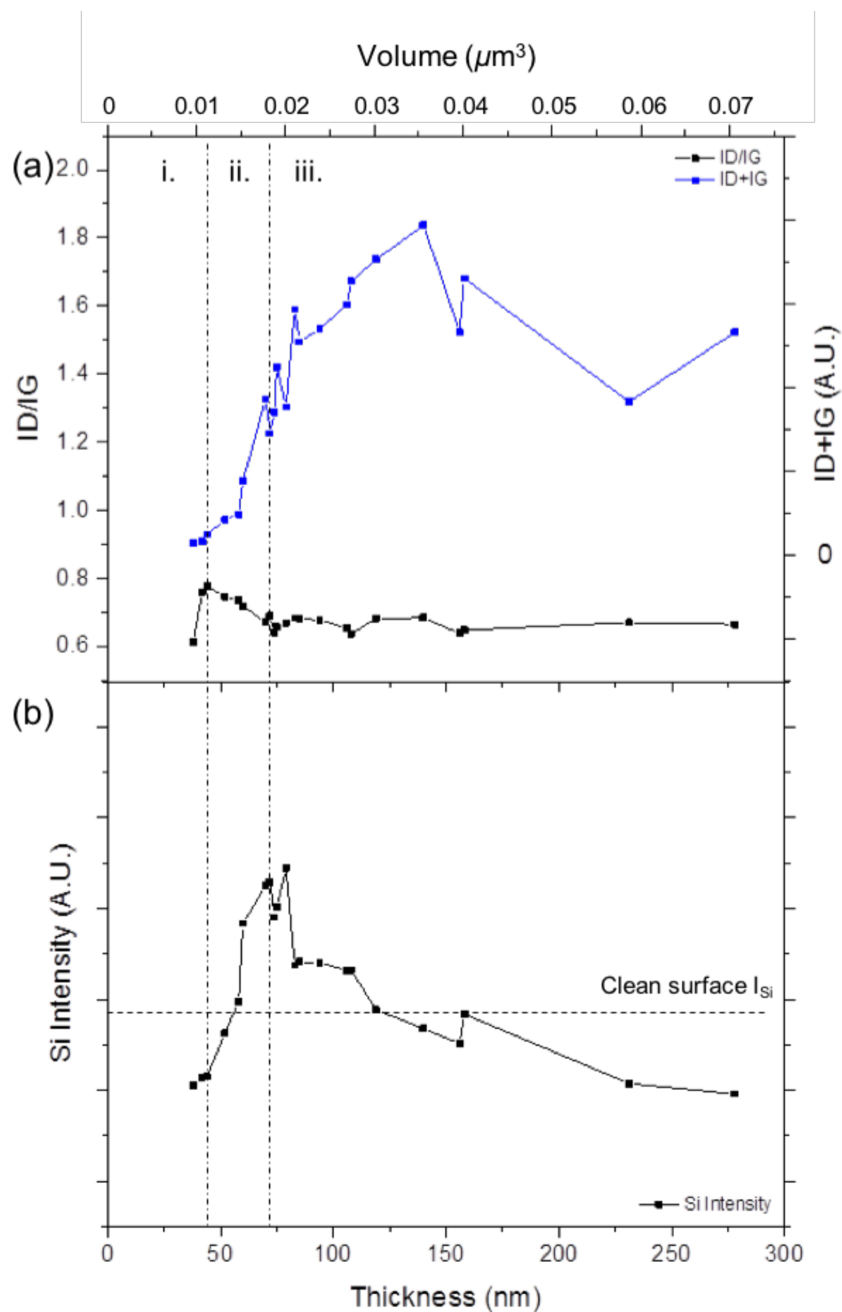

FIGURE 6.12: Analysis of the carbon layers formed with 1 keV electron beam energy. (a) The relationship between carbon peak intensity ratio (I_D/I_G) and the sum of the carbon peaks ($I_D + I_G$), as a function of increasing carbon volume. (b) The variation in Si Raman shift (I_{Si}) observed for the increase in layer thickness. Fluctuation of the measured scattered light accounts for a ± 10% maximum variation in the carbon and Si Raman intensity values.

In this phase I_{Si} is sensitive to the I_D/I_G ratio, which increases with the decrease in the I_D/I_G ratio. In phase (iii) $I_D + I_G$ continues to increase before saturating at ~150 nm, while the I_D/I_G ratio remains saturated at ~0.7. I_{Si} begins to decrease and becomes less than that of the bare Si specimen once a thickness of 125 nm is reached. In this phase I_{Si} is influenced by layer thickness whereby it is initially attenuated from the point of maximum enhancement and is eventually lost within the carbon layer.

From the results displayed in Figure 6.12, the carbon layer generated with 1 keV electron beam energy has an enhancing effect on the Si Raman shift from the underlying specimen for a thickness range of 60 – 125 nm (or a volume of 0.015 – 0.03 μm^3). A maximum enhancement of 55% occurs at a layer thickness of 80 nm (or a volume of 0.02 μm^3), when the I_D/I_G ratio has reached a minimum value of ~0.65. Once the carbon layer reaches a thickness of ~125 nm, the Si Raman shift from the underling specimen is attenuated. A maximum attenuation of ~30% is observed between ~125 – 275 nm.

6.3.2.3 3 keV Carbon Layer

The Raman spectra for carbon species formed with 3 keV, is displayed Figure 6.13. In Figure 6.13 (b), the I_{Si} for 0.014 μm^3 of the carbon layer is 38% greater than that of the clean surface (Figure 6.13 (a)). In Figure 6.13 (c), the I_{Si} for 0.016 μm^3 of the carbon layer is 64% greater than that of the clean surface. In Figure 6.13 (d), the I_{Si} for 0.02 μm^3 of the carbon layer is 9% greater than that of the clean surface. As the carbon layer volume increases from 0.014, to 0.016, to 0.02 μm^3, the I_D/I_G changes from 1.19, to 1.20, to 0.88, respectively.

Figure 6.14 shows the effects of the 3 keV carbon layer on the intensity of the characteristic Si Raman shift (I_{Si}). In Figure 6.14 (a) as the volume increases the I_D/I_G ratio immediately increases and peaks at ~1.7. As the volume continues to increase the I_D/I_G ratio begins to decrease. On reaching ~0.024 μm^3 the I_D/I_G ratio falls below 1.0 and saturates between 0.7 – 0.8 with further increase in volume. The $I_D + I_G$ initially increases with increase in carbon volume and saturates on reaching a volume of ~0.03 μm^3. Figure 6.14 (b) shows the variation in I_{Si} with the increase in carbon layer thickness. Between 50 – 90 nm the I_{Si} is greater than that of the clean surface, reaching a maximum for a thickness of

∼80 nm. Above 90 nm the I_{Si} drops to a level close to that of the clean surface, eventually dropping below it above 150 nm.

In phase (i) as the layer thickness increases peak I_D/I_G ratio of ∼1.7 is initially established at ∼50 nm. With further increase in layer thickness the I_D/I_G ratio begins to decrease and falls below 1.0 at ∼90 nm. The $I_D + I_G$ and the I_{Si} both increase with the increase in layer thickness. I_{Si} peaks for a layer thickness of 80 nm and an I_D/I_G ratio of ∼1.3. A decrease in I_D/I_G ratio indicates a decrease in the concentration aromatic carbon bonds. In this phase I_{Si} increases with the decrease in the I_D/I_G ratio, however the value of I_{Si} is more sensitive to fluctuations in the I_D/I_G ratio rather than the concentration on the carbon bonds given by $I_D + I_G$. In phase (ii) with further increase in layer thickness, the I_D/I_G ratio remains below 1.0 however the $I_D + I_G$ continues to increase. I_{Si} remains at a saturated level just above the clean surface intensity up to 150 nm, at which point it drops below it. In this phase I_{Si} is influenced by the stable I_D/I_G ratio and not the increasing $I_D + I_G$, until a saturation thickness is reached whereby it is attenuated by the thickest regions of the carbon layer.

From the results displayed in Figure 6.14, the carbon layer generated with 3 keV electron beam energy has an enhancing effect on the Si Raman shift from the underlying specimen for a thickness range of 50 – 90 nm (0.014 – 0.024 μm^3). A maximum enhancement of 104% occurs at a layer thickness of 80 nm (0.018 μm^3). The Si Raman shift from the underling specimen is attenuated for a carbon layer thickness of ∼150 nm (0.038 μm^3) and above, with a maximum attenuation of ∼25% being observed between ∼150 and ∼200 nm (0.038 – 0.048 μm^3). Within the thickness range of 90 – 150 nm (0.024 – 0.038 μm^3), the carbon layer is neither enhancing nor attenuating as the collected Si Raman shift is equal in magnitude to that of the clean Si surface.

6.3.2.4 12 keV Carbon Layer

The Raman spectra for carbon species formed with 12 keV e-beam energy is displayed Figure 6.15. In Figure 6.15 (b), the I_{Si} for 0.045 μm^3 of the carbon layer is 56% greater than that of the clean surface (Figure 6.15 (a)). In Figure 6.15 (c), the I_{Si} for 0.05 μm^3 of the carbon layer is 10% greater than that of the clean surface. In Figure 6.15 (d), the I_{Si} for 0.063 μm^3 of the carbon layer is 12% greater

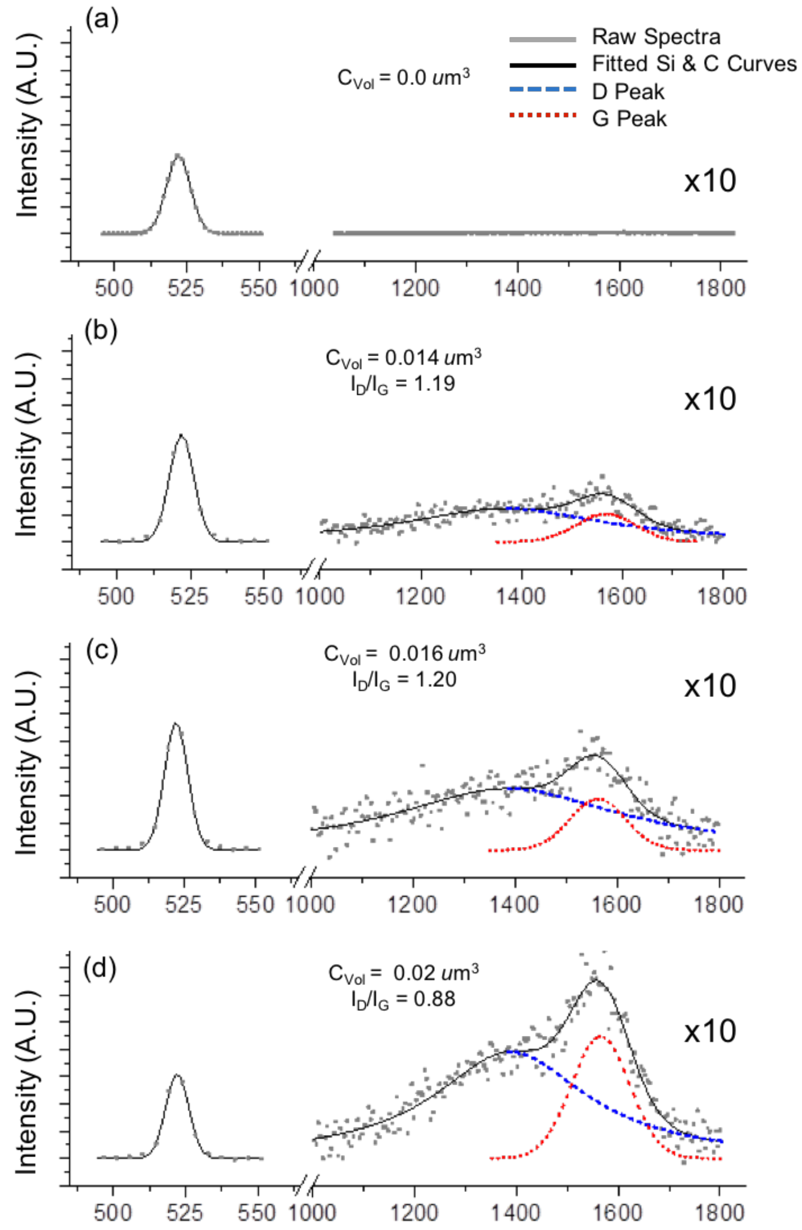

Figure 6.13: Raman spectra of Si specimen which had previously been contaminated in a scanning electron microscope by a 3 keV electron beam. Raman spectra shows the Si and carbon Raman shift present in an uncontaminated region of the specimen (a), and contaminated regions of the specimen with increasing volume in (b – d).

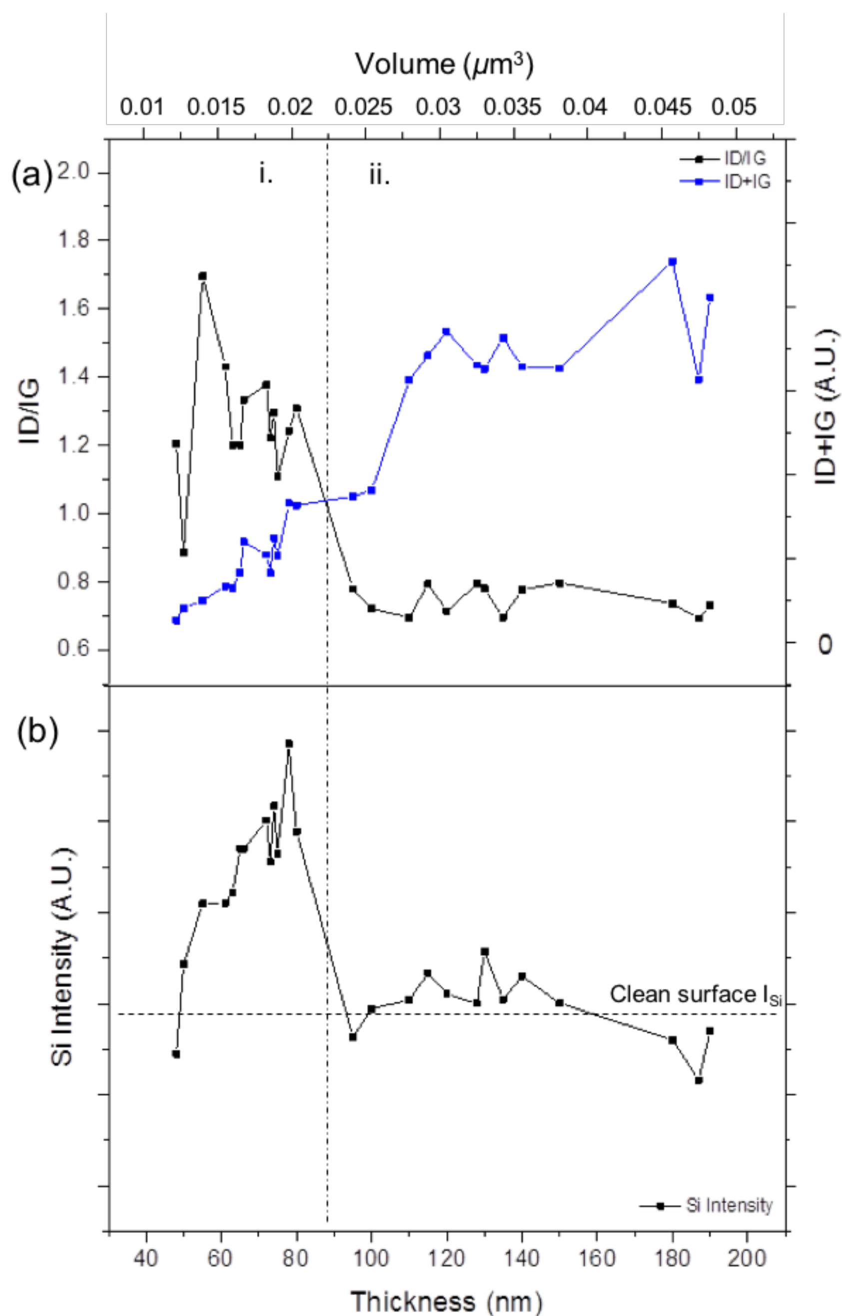

FIGURE 6.14: Carbon layers formed with 3 keV electron beam energy. (a) The relationship between carbon peak intensity ratio (I_D/I_G) and the sum of the carbon peaks ($I_D + I_G$) as a function of increasing carbon volume. (b) The variation in Si Raman shift (I_{Si}) observed for the increase in layer thickness. Fluctuation of the measured scattered light accounts for a ± 10% maximum variation in the carbon and Si Raman intensity values.

than that of the clean surface. As the carbon layer volume increases from 0.045, to 0.05, to 0.063μm^3, the I_D/I_G changes from 2.11, to 1.17, to 1.14, respectively.

Figure 6.16 shows the effects of the 12 keV carbon layer on the intensity of the characteristic Si Raman shift (I_{Si}). In Figure 6.16 (a) as the volume increases the I_D/I_G ratio increases and peaks at ∼2.4. As the volume continues to increase the I_D/I_G ratio quickly decreases and on reaching ∼0.05 μm^3 the I_D/I_G ratio falls to a min value of ∼1.0. With further increase in volume, the I_D/I_G ratio fluctuates between 1.0 – 1.5. The $I_D + I_G$ initially fluctuates up to a volume of ∼0.05 μm^3, but then gradually increases with further increase in volume. Figure 6.16 (b) shows the variation in I_{Si} with the increase in carbon layer thickness. Between ∼150 – 180 nm the I_{Si} is significantly greater than that of the clean surface, peaking at a thickness of ∼175 nm. Above 180 nm the I_{Si} drops to a level close to that of the clean surface and eventually drops below it upon reaching a thickness of 550 nm.

In phase (i) as the carbon volume is increased, the I_D/I_G ratio initially drops from 2.2 to 1.8 and then increases to a peak of 2.4 on reaching ∼0.046 μm^3. The $I_D + I_G$ fluctuates as it increases in magnitude. I_{Si} from the carbon is observed to be significantly greater than that of the clean surface. It increases with the increase in layer thickness and peaks for a layer thickness of ∼185 nm. In this phase I_{Si} is sensitive to the changes in the I_D/I_G ratio however its peak coincides with the peaks in both I_D/I_G and $I_D + I_G$. In phase (ii) as the contamination volume increases the I_D/I_G ratio initially drops to ∼1.2 and remains between 1.1 – 1.6 for the remainder of the sampled volume range. I_{Si} initially decreases and remains at a saturated level above the intensity of the characteristic Si Raman peak from the clean surface, up to a thickness of 550 nm. Above this point I_{Si} drops below that of the clean surface. In this phase I_{Si} influenced by the saturated I_D/I_G ratio and not the increasing value $I_D + I_G$. As the saturated I_D/I_G ratio is greater than 1.0, the carbon layer remains enhancing up to a significantly increased thickness, at which point the layer begins to attenuate the Si Raman shift from the underling Si specimen.

From the results displayed in Figure 6.16, the carbon layer generated with 12 keV electron beam energy has an enhancing effect on the Si Raman shift from the underlying specimen, for a thickness range of 150 – 550 nm (0.038 – 0.13 μm^3). A maximum enhancement of 52% occurs at a layer thickness of 185 nm (0.046 μm^3). The Si Raman shift from the underling specimen is attenuated for the carbon layer

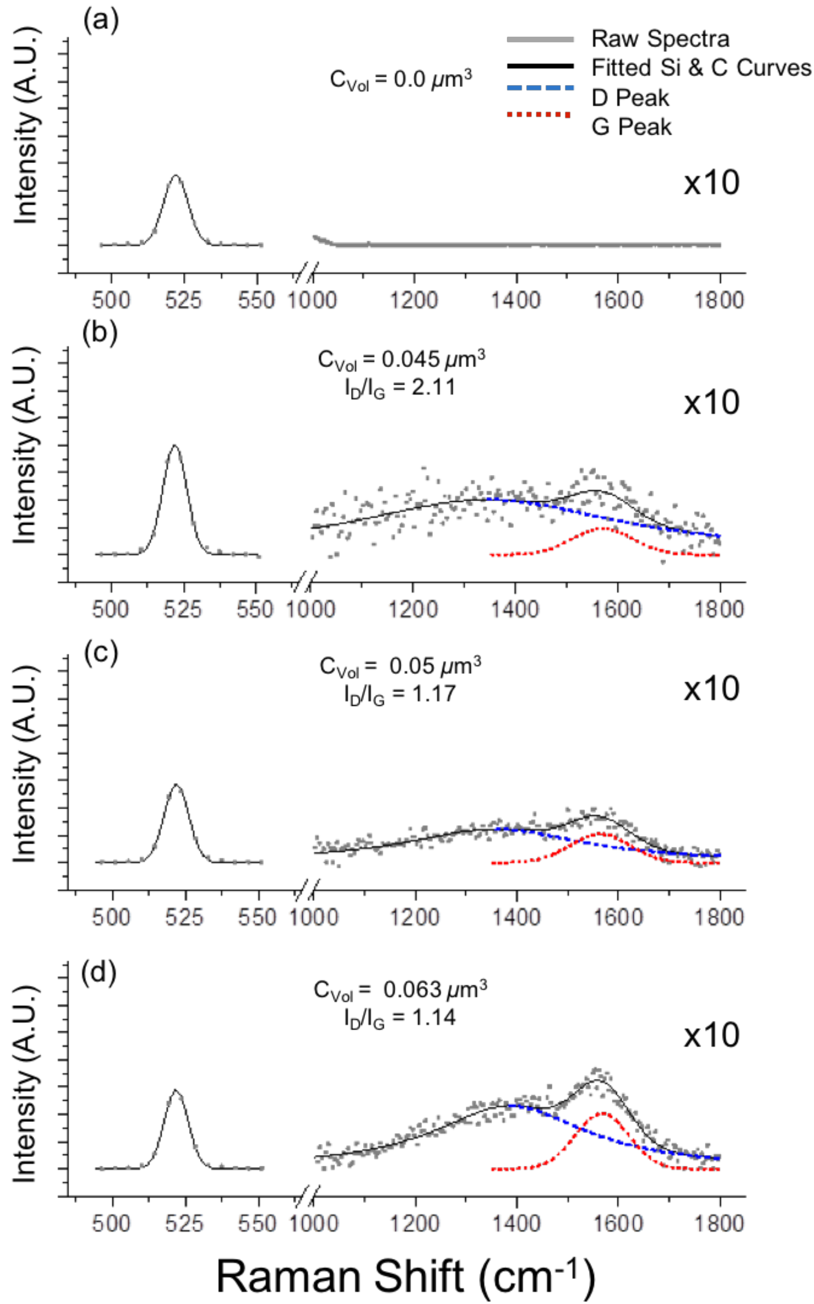

FIGURE 6.15: Raman spectra of Si specimen which had previously been contaminated in a scanning electron microscope by a 12 keV electron beam. Raman spectra shows the Si and carbon Raman shift present in an uncontaminated region of the specimen (a), and contaminated regions of the specimen with increasing volume in (b – d).

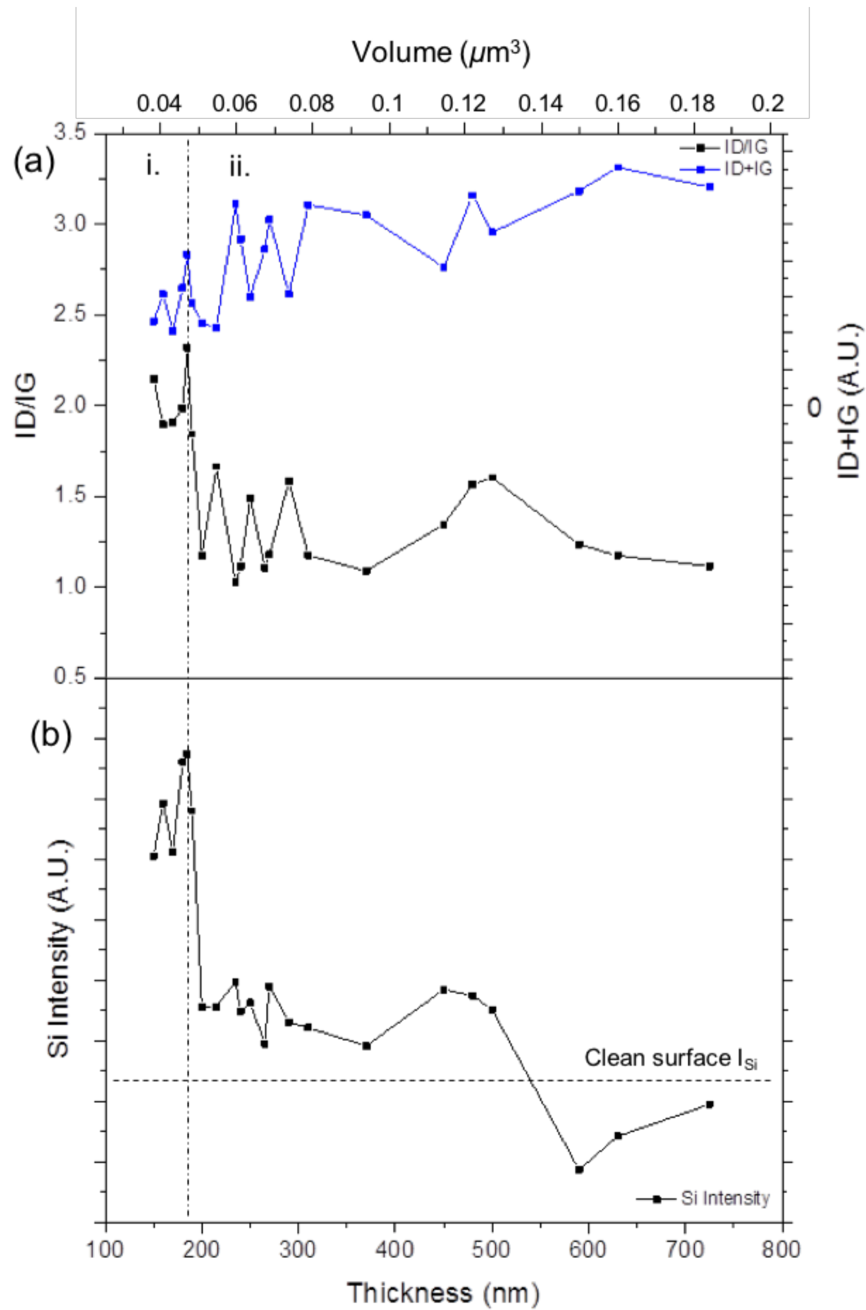

FIGURE 6.16: Carbon layers formed with 12 keV electron beam energy. (a) The relationship between carbon peak intensity ratio (I_D/I_G) and the sum of the carbon peaks ($I_D + I_G$) as a function of increasing carbon volume. (b) The variation in Si Raman shift (I_{Si}) observed for the increase in layer thickness. Fluctuation of the measured scattered light accounts for a ± 10% maximum variation in the carbon and Si Raman intensity values.

thicknesses of ~550 nm and above, with a maximum attenuation of ~15% being observed between ~550 and ~750 nm (0.125 – 0.185 μm^3).

6.3.2.5 20 keV Carbon Layer

The Raman spectra for carbon species formed with 20 keV, is displayed Figure 6.17. In Figure 6.17 (b), the I_{Si} for 0.053 μm^3 of the carbon layer is 34% greater than that of the clean surface (Figure 6.17 (a)). In Figure 6.17 (c), the I_{Si} for 0.064 μm^3 of the carbon layer is 27% greater than that of the clean surface. In Figure 6.17 (d), the I_{Si} for 0.081 μm^3 of the carbon layer is 37% greater than that of the clean surface.As the carbon layer volume increases from 0.053, to 0.064, to 0.081 μm^3, the I_D/I_G changes from 1.29, to 1.52, to 1.19, respectively.

Figure 6.18 shows the effect of the 20 keV carbon layer on the intensity of the characteristic Si Raman shift (I_{Si}). In Figure 6.18 (a), as volume increases the I_D/I_G ratio increases rapidly from 1.4, peaks at 2.5 before immediately returning to its initial level. As the volume continues to increase the I_D/I_G ratio remains between 1.3 – 1.5, up to a maximum volume of 0.125 μm^3. The $I_D + I_G$ also increases with increase in carbon volume. It peaks for a carbon volume of ~0.075 μm^3 and saturates for the remainder of the volume range. Figure 6.18 (b) shows the variation in I_{Si} with the increase in carbon layer thickness. Over the entire thickness range I_{Si} is greater than that from the clean surface. It increases initially and peaks at a layer thickness of ~215 nm. Between 200 – 350 nm I_{Si} remains within 10 – 15% of the peak value prior to falling back to levels observed at the initial rise in layer thickness.

In phase (i) as the carbon volume is increased, the I_D/I_G ratio increases significantly and peaks at 2.4 on reaching ~0.038 μm^3. The I_D+I_G and I_{Si} also increase with the increase in carbon volume but at a reduced rate. I_{Si} is observed to be significantly greater than that of the clean surface. It increases with the increase in layer thickness and peaks for a layer thickness of ~150 nm. In this phase I_{Si} increases with the increase in I_D/I_G ratio and $I_D + I_G$ however the value of I_{Si} is less sensitive to the fluctuations in the I_D/I_G ratio and responds to changes in the concentration on the carbon bonds given by $I_D + I_G$. In phase (ii) as the contamination volume increases the I_D/I_G ratio drops from its peak to a value of ~1.3 and remains between 1.2 – 1.5 for the remainder of the sampled volume range. I_{Si} increases and peaks for a thickness of ~215 nm. Between 200 – 350

nm I_{Si} remains within 10 – 15% of this peak value prior to falling back to levels observed at the initial rise in phase (i). In phase (ii), I_{Si} is influenced by the saturated I_D/I_G ratio and the increasing and saturated level of $I_D + I_G$. As the saturated I_D/I_G ratio is greater than 1.0, the carbon layer remains enhancing over the observed thickness range.

From the results displayed in Figure 6.18, the carbon layer generated with 20 keV electron beam energy has an enhancing effect on the Si Raman shift from the underlying specimen across its entire thickness range of 100 – 500 nm (0.025 – 0.124 μm^3). A maximum enhancement of 35% occurs at a layer thickness of 210 nm (0.053 μm^3). Beyond this thickness the carbon layer has a further enhancing effect of between to 25 – 35% up to a maximum thickness of 350 nm (0.09 μm^3), prior to the onset of attenuation.

6.3.2.6 30 keV Carbon Layer

The Raman spectra for the carbon formed with 30 keV electron beam energy, is displayed Figure 6.19. In Figure 6.19 (b), the I_{Si} for 0.036 μm^3 of the carbon layer is 50% greater than that of the clean surface (Figure 6.19 (a)). In Figure 6.19 (c), the I_{Si} for 0.06 μm^3 of the carbon layer is 46% greater than that of the clean surface. In Figure 6.19 (d), the I_{Si} for 0.078 μm^3 of the carbon layer is 34% greater than that of the clean surface. As the carbon layer volume increases from 0.036, to 0.06, to 0.078 μm^3, the I_D/I_G changes from 1.82, to 1.87, to 1.19, respectively.

Figure 6.20 shows the effects of the 30 keV carbon layer on the intensity of the characteristic Si Raman shift (I_{Si}). In Figure 6.20 (a) as the volume increases the I_D/I_G ratio drops initially from ∼1.8 to ∼1.4 before immediately increasing and peaking at 2.2, for a volume of ∼0.042 μm^3. As the volume continues to increase the I_D/I_G ratio begins a gradual decline and reaches a value of 1.4 for a volume of 0.094 μm^3. The $I_D + I_G$ initially increases with increase in carbon volume and reaches a distinctive peak at ∼0.042 μm^3. After this point its magnitude plateaus at its initial magnitude prior to peaking again at ∼0.08 μm^3. After this second peak $I_D + I_G$ returns once again to the initial level. Figure 6.20 (b) shows the variation in I_{Si} with the increase in carbon layer thickness. Over the entire thickness range I_{Si} is greater than that from the clean surface. From an initial high starting value, at a thickness of 140 nm, I_{Si} decreases gradually until reaching a layer thickness of ∼225 nm, at which point it begins to increase. It peaks again

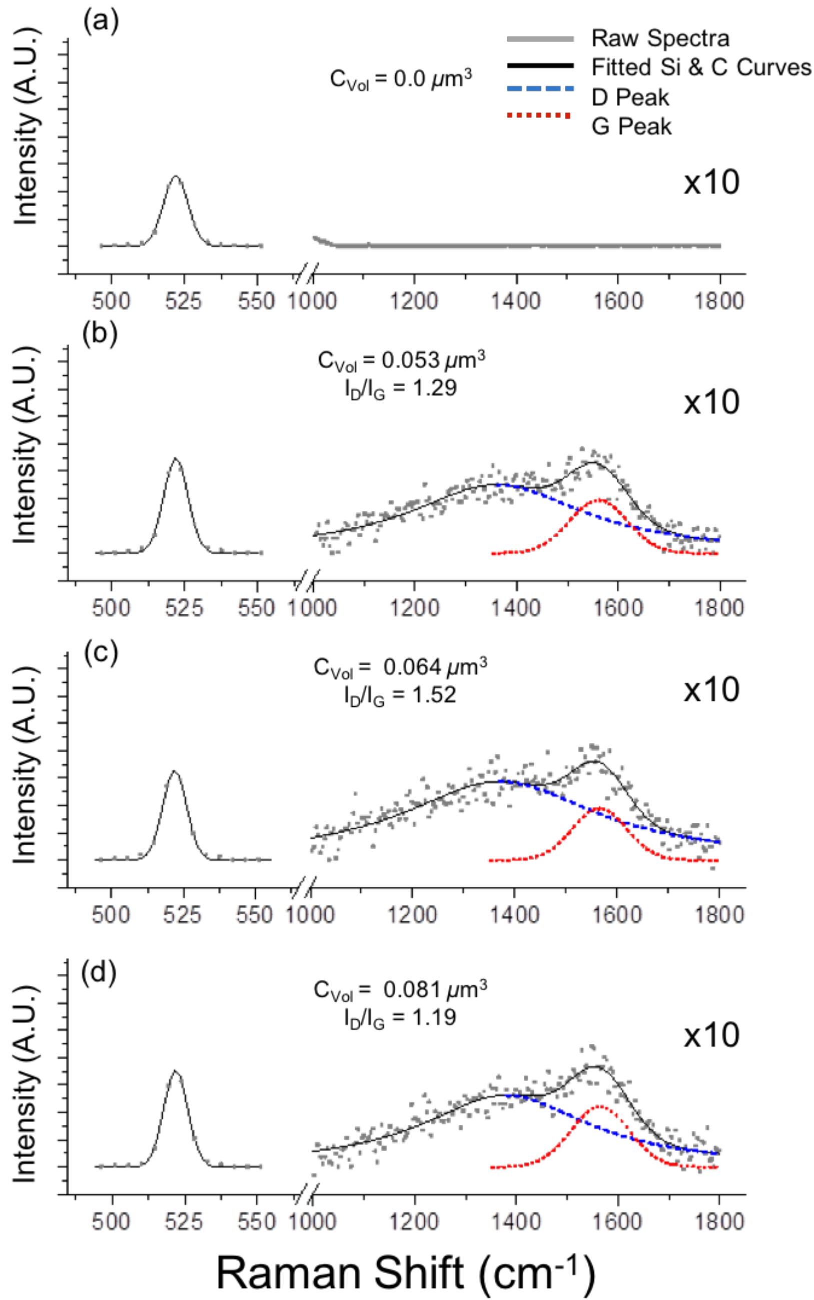

FIGURE 6.17: Raman spectra of Si specimen which had previously been contaminated in a scanning electron microscope by a 20 keV electron beam. Raman spectra shows the Si and carbon Raman shift present in an uncontaminated region of the specimen (a), and contaminated regions of the specimen with increasing volume in (b – d).

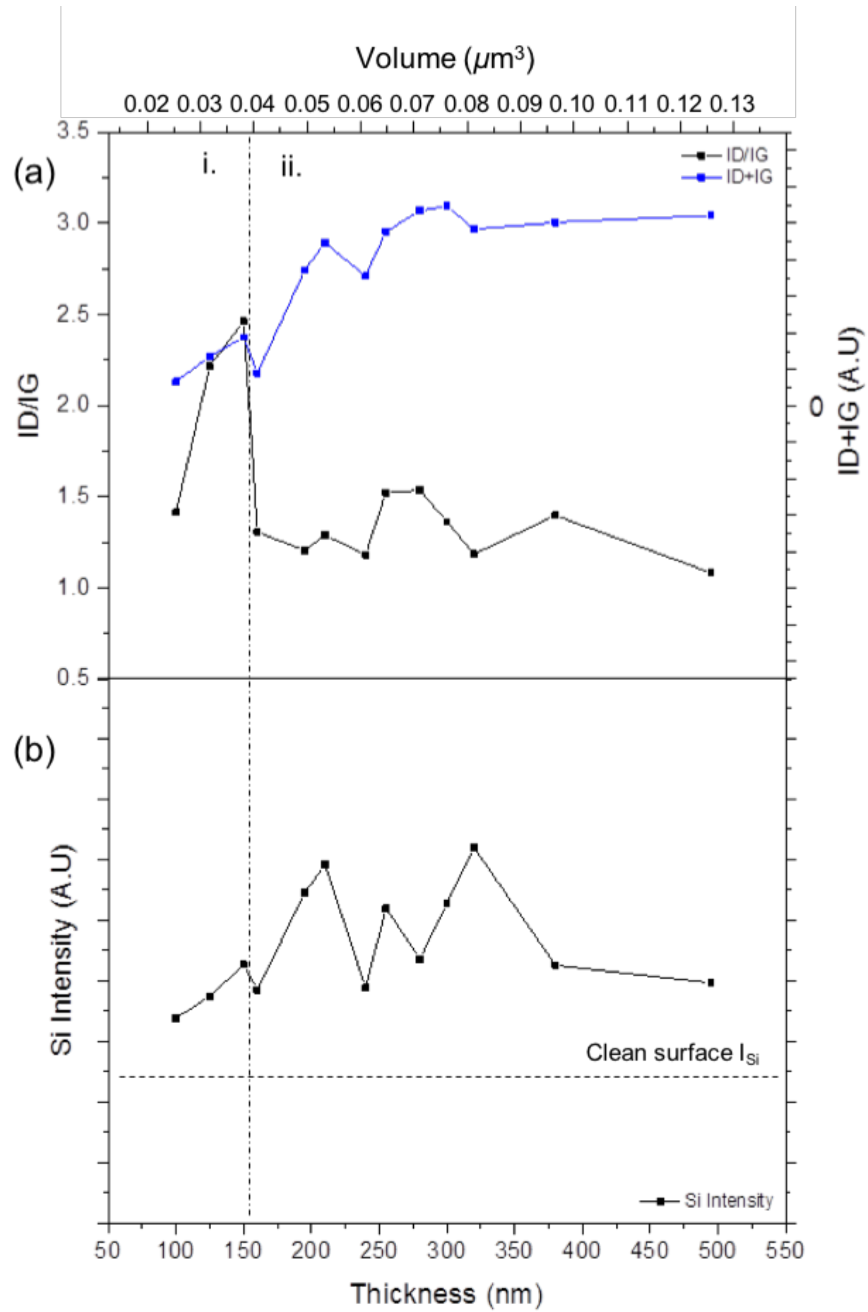

FIGURE 6.18: Carbon layers formed with 20 keV electron beam energy. (a) The relationship between carbon peak intensity ratio (I_D/I_G) and the sum of the carbon peaks ($I_D + I_G$) as a function of increasing carbon volume. (b) The variation in Si Raman shift (I_{Si}) observed for the increase in layer thickness. Fluctuation of the measured scattered light accounts for a ± 10% maximum variation in the carbon and Si Raman intensity values.

at ~260 nm returning to its initial value. With a further increase in thickness, I_{Si} falls back towards the level of the clean surface.

In phase (i) as the carbon volume increases the I_D/I_G ratio peaks at 2.2 for a volume of ~42 μm^3 after which it declines. The average I_D/I_G ratio for this phase is ~1.9. The $I_D + I_G$ also increases with the increase in carbon volume, reaching a distinctive peak at ~0.042 μm^3 and after which it also declines. The rate of decline in $I_D + I_G$ is less than that of the I_D/I_G ratio. I_{Si} decreases with the increase in carbon volume and reaches a minimum value for a layer thickness of ~225 nm. In this phase the decline I_{Si} is due to the decline in the I_D/I_G ratio. $I_D + I_G$ does decline in this phase however the centre region of this decline is levelled off. In phase (ii) as the carbon volume increases the I_D/I_G ratio continues its decline over the remainder of the volume range. The average I_D/I_G ratio for this phase is ~1.6. The $I_D + I_G$ increases with the increase in carbon volume, it reaches a peak at ~0.08 μm^3 and subsequently declines. I_{Si} increases and peaks for a thickness of ~263 nm. After this peak, I_{Si} decreases rapidly and reaches a minimum value - just above the intensity of the clean surface - at ~375 nm. In this phase the drop in I_D/I_G ratio causes the initial increase in I_{Si} however, as the layer thickness increases beyond ~263 nm attenuation commences and I_{Si} declines rapidly.

From the results displayed in Figure 6.20, the carbon layer generated with 30 keV electron beam energy has an enhancing effect on the Si Raman shift from the underlying specimen across its entire thickness range of 140 – 375 nm (0.035 – 0.094 μm^3). A maximum enhancement of 50% occurs twice within the layer at 140 and 260 nm (0.035 and 0.065 μm^3). Beyond the second enhancement peak the carbon layer begins to attenuate the Raman shift from the specimen resulting in a reduced enhancement of 8% for a layer thickness of 375 nm.

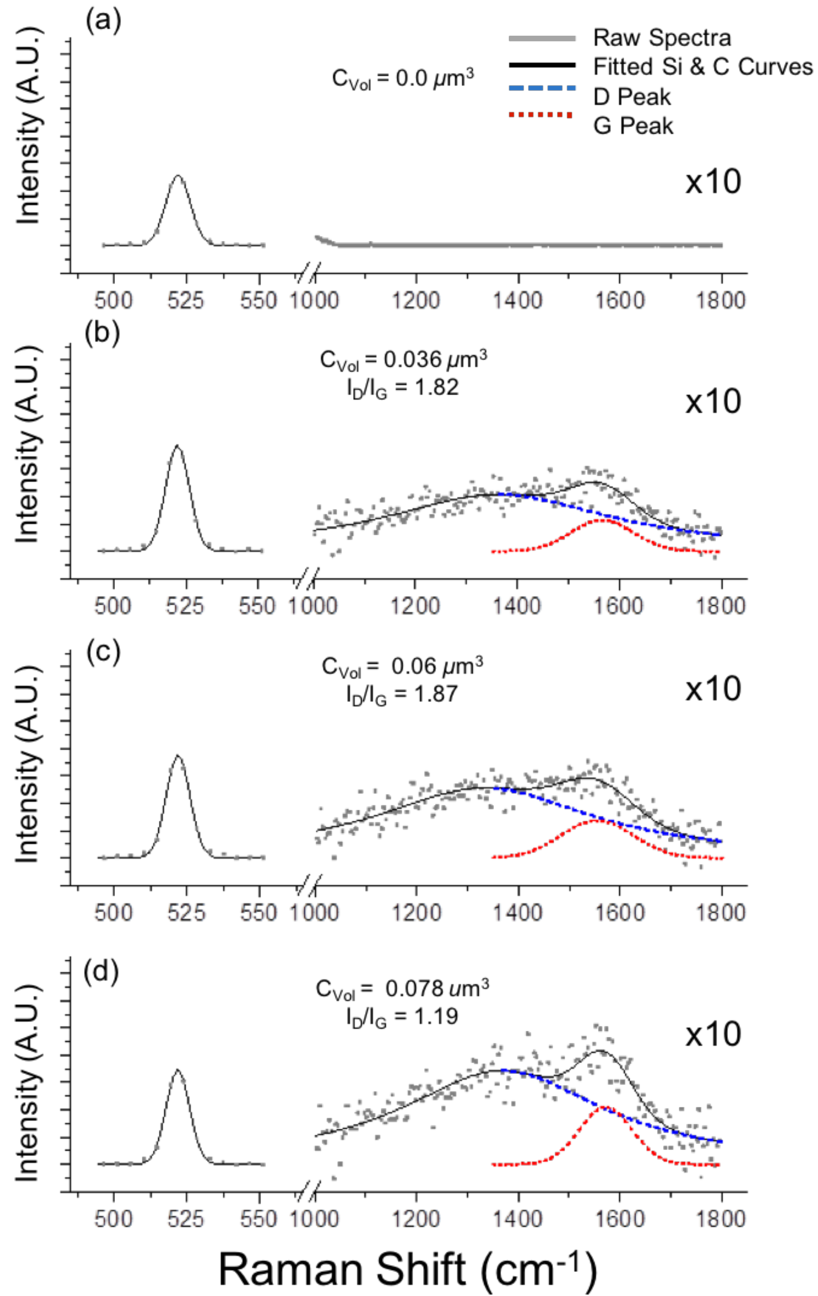

FIGURE 6.19: Raman spectra of Si specimen which had previously been contaminated in a scanning electron microscope by a 30 keV electron beam. Raman spectra shows the Si and carbon Raman shift present in an uncontaminated region of the specimen (a), and contaminated regions of the specimen with increasing volume in (b – d).

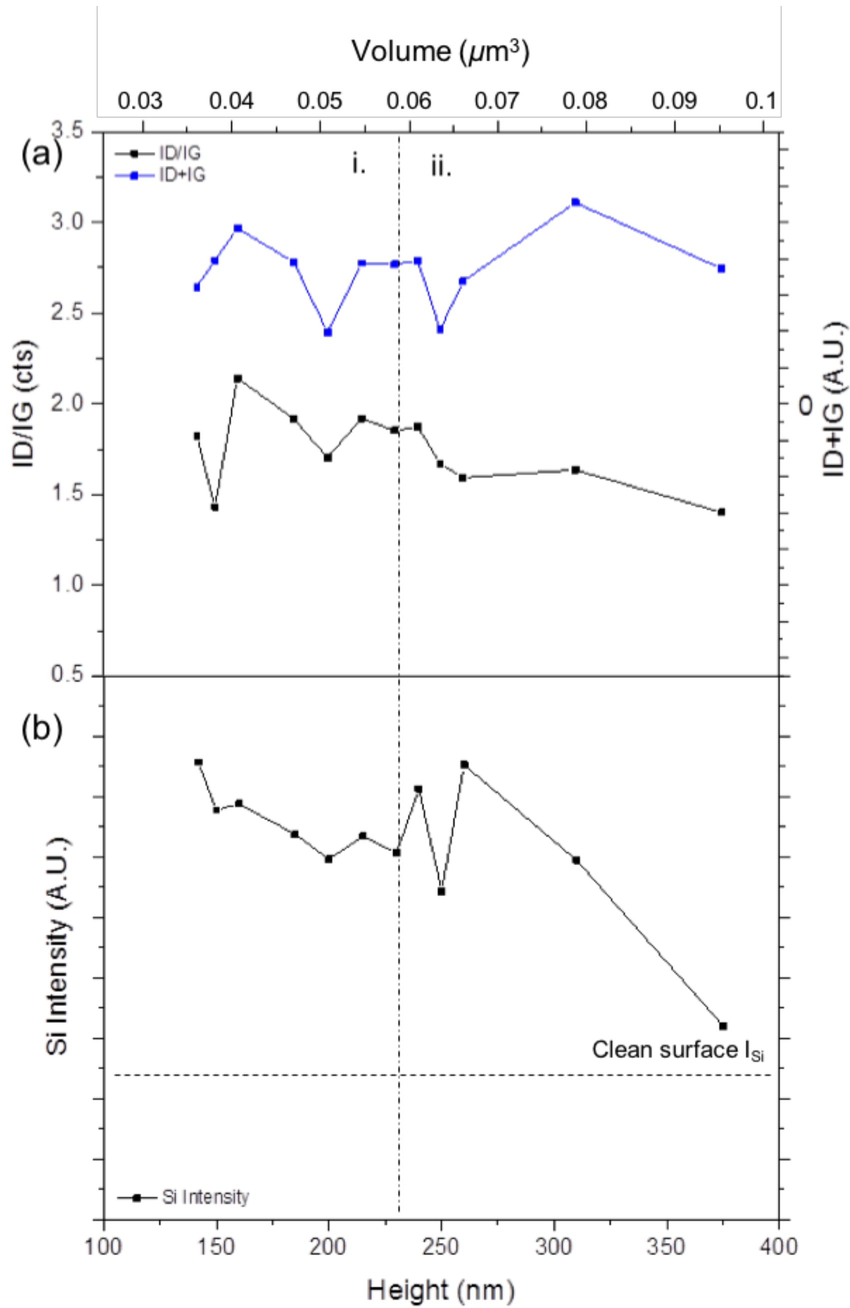

FIGURE 6.20: Carbon layers formed with 30 keV electron beam energy. (a) The relation between carbon peak intensity ratio (I_D/I_G) and the sum of the carbon peaks (I_D+I_G) as a function of increasing volume of contamination volume. (b) The variation Si Raman shift (I_{Si}) observed for the increase in contamination layer thickness. Fluctuation of the measured scattered light accounts for a $\pm$ 10% maximum variation in the carbon and Si Raman intensity values.

6.4 Exploring the mechanisms of enhancement

6.4.1 The effect of excitation energy

Differences in the Raman enhancing effect of the carbon layers have been observed for different laser excitation energies. In Figure 6.21, Raman maps of a typical carbon layer, deposited with electron beam energy of 3 keV and an applied dose of 5 nC·μm^{-2}, are shown for excitation energies of 532 nm and 633 nm, in (b) and (e), respectively. Centred in each map is the carbon layer. The intensity of the characteristic Si Raman peak observed across the layer was referenced to the intensity of Si Raman peak observed from the clean region of the specimen, surrounding the layer. This allowed a qualitative comparison of the enhancing characteristics of the carbon layer, upon irradiation by both laser excitation energies.

The enhancement of the characteristic Si Raman peak emitted from the left edge of the layer as a function of layer thickness (120 – 180 nm), is displayed in Figure 6.21 (a) and (d) for excitation energies of 532 nm and 633 nm, respectively. The enhancement generated by 532 nm excitation is significantly diminished across the layer edge, with the greatest reduction occurring at the thicker outer regions. In comparison, higher values of enhancement are observed across the layer edge for 633 nm excitation, with the central region displaying a greater levels than the outer regions. In Figure 6.21 (c) the height profile and the 532 nm enhancement profile of the right edge of the carbon layer is displayed. A layer thickness of 60 – 80 nm serves to enhance the Si Raman peak from the underlying specimen, with the magnitude of enhancement being proportional to layer thickness. Figure 6.21 (f) shows the height profile and the 633 nm enhancement profile of the right edge. Similar to that observed for 532 nm excitation, enhancement is proportional to layer thickness, however the outer regions of the edge display a further increase in enhancement.

Further analysis of the enhancement of the characteristic Si Raman peak observed at the edges of the carbon layer, as a function of layer thickness for both excitation energies, is given in Figure 6.22. For a thickness range of 60 – 80 nm, the intensity is observed to increase linearly with the increase in layer thickness. In this range similar levels of intensity are observed for both excitation energies. For layer thickness's above ~100 nm, the enhancement of the Si Raman peak varies significantly

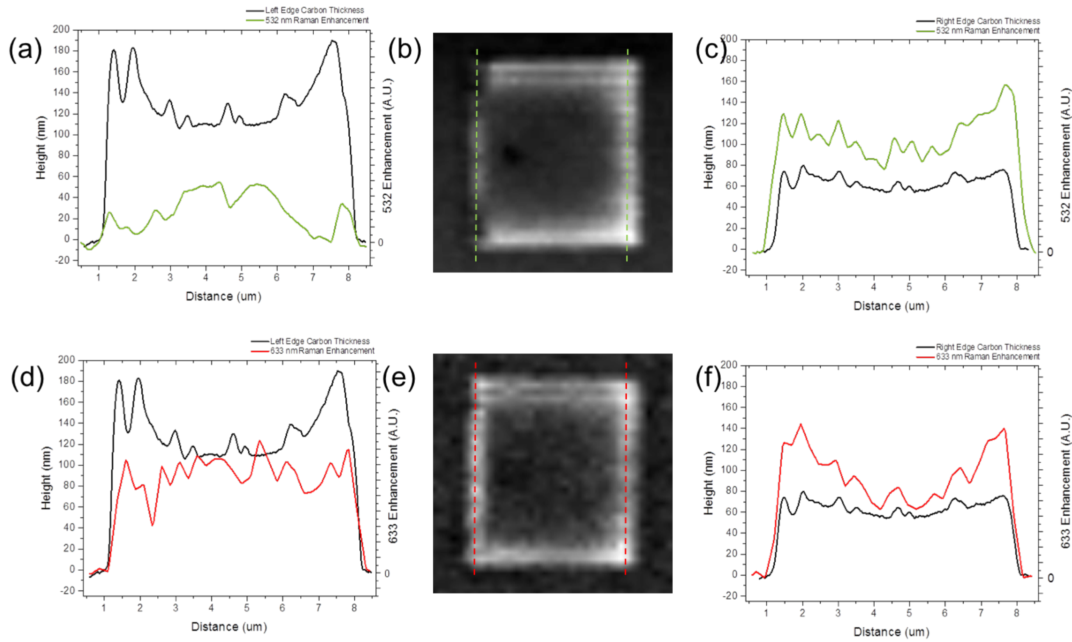

FIGURE 6.21: The Raman enhancing characteristics of a carbon layer, produced with electron beam energy of 3 keV and an applied dose of 5 nC$\cdot\mu$m^{-2}, excited with laser energies of 532 nm and 633 nm. Intensity maps of the characteristic Si Raman peak, generated from the carbon layer and referenced to the clean region of the specimen in each image, are displayed in (b) for 532 nm and in (e) 633 nm excitation. The enhancement of the Si Raman peak observed along the left edge of the layer, relative to its height profile, is displayed in (a) for 532 nm and in (d) for 633 nm excitation. The enhancement of the Si Raman peak observed along the right edge of the layer, relative to its height profile, is displayed in (c) for 532 nm and in (f) 633 nm excitation.

between both excitation energies. For 532 nm excitation, enhancement is initially reduced by ∼65% relative to its peak at ∼80 nm, and decreases further with the increase in thickness. For 633 nm excitation the Si Raman enhancement is initially reduced by ∼25% relative to its peak at ∼80 nm, however with further increase in thickness enhancement plateaus with a similar levels being observed up to ∼190 nm.

Previous analysis of the carbon layers produced with 3 keV electron beam energy, (Figure 6.14), revealed that layer thicknesses above 150 nm attenuated the intensity of the Si Raman peak. In this range the I_D/I_G ratio present in the layer reached a saturation value of ∼0.75. According to the Beer-Lambert law there is a linear relationship between absorbance and the concentration of an absorbing

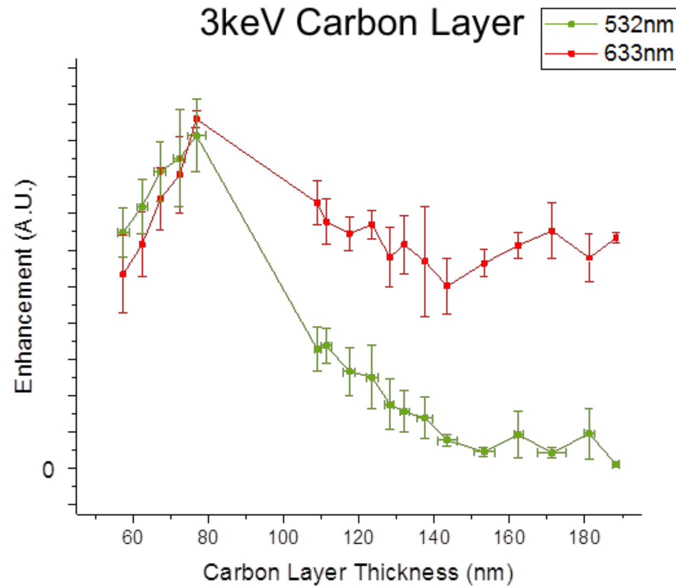

FIGURE 6.22: Thickness-dependent Raman enhancement observed from the 3 keV carbon layers excited with laser energies of 532 nm and 633 nm.

species. Written as,

$$A = a(\lambda) \times b \times c \tag{6.1}$$

where A is the measured absorbance, $a(\lambda)$ is the wavelength-dependent absorption coefficient, b is the path length and c is the analyte concentration. As the saturated I_D/I_G ratio present in the carbon layer represents a fixed concentration of the absorbing species, the path length of the light travelling through the layer is therefore inversely proportional to its wavelength. The Beer-Lambert law explains why the intensity of the Si Raman peak generated with 532 nm laser excitation can be attenuated to a greater extent, by a 3 keV carbon layer of 120 – 180 nm in thickness, in comparison to the intensity of the Si Raman peak generated with 633 nm excitation.

Also revealed in the previous analysis of the 3 keV carbon layer (Figure 6.14), a thickness range of 60 – 80 nm significantly enhanced the intensity of the Si Raman peak. In this range the I_D/I_G ratio present in the layer fluctuated between 1.2 – 1.4. As similar levels of enhancement are observed for excitation energies of 532 nm and 633 nm (Figure 6.22), the concentration of the absorbing species in the layer over this thickness range is not sufficient to attenuate the Si Raman peak for either excitation energy.

The observed differences in the excitation energy dependent Raman enhancing effect of the carbon layers, induced with electron beam energies of 1, 5, 12, 20 and 30 keV, are displayed in Figure 6.23 to Figure 6.32.

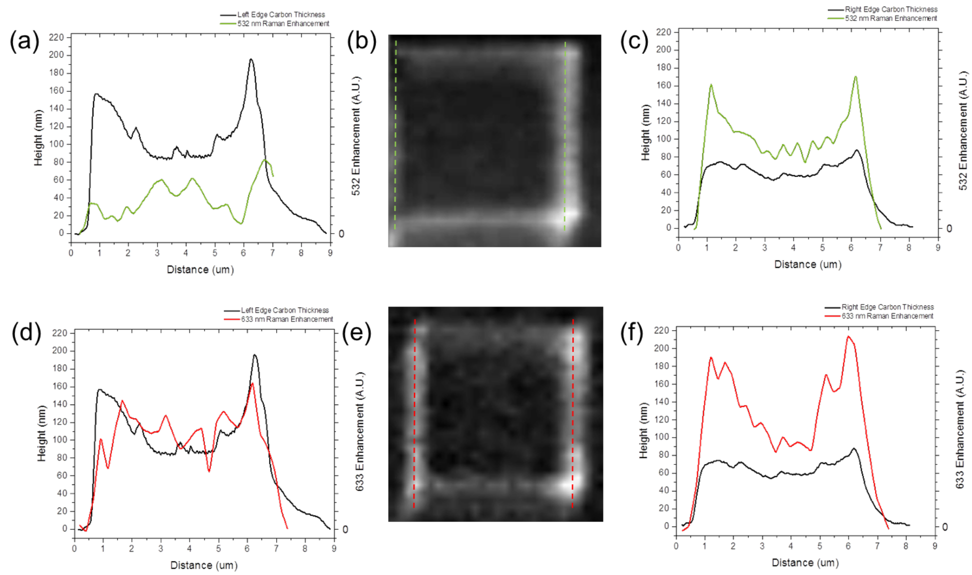

FIGURE 6.23: The enhancement properties of a carbon layer produced with electron beam energy of 1 keV and an applied dose of 5 nC·μm^{-2} and excited with laser energies of 532 nm and 633 nm. Intensity maps of the characteristic Si Raman peak, generated from the carbon layer and normalised to the clean region of the specimen, are displayed for 532 nm and 633 nm in (b) and (e) respectively. The enhancement of the Si Raman peak observed along the left edge of the layer, relative to its height profile, is displayed in (a) and (d) for 532 nm and 633 nm excitation energy, respectively. The enhancement of the Si Raman peak observed along the right edge of the layer, relative to its height profile, is displayed in (c) and (f) for 532 nm and 633 nm excitation energy, respectively.

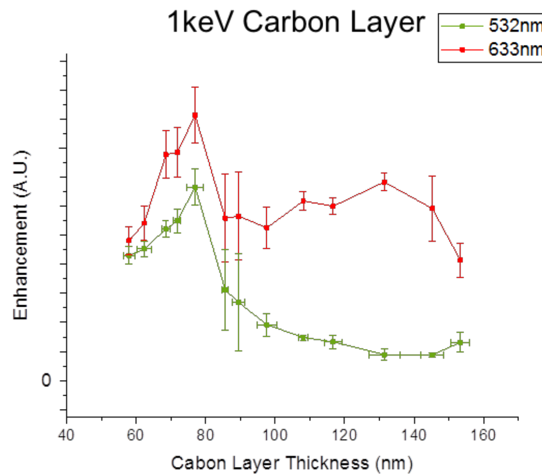

FIGURE 6.24: Thickness-dependent Raman enhancement observed from the 1 keV carbon layers excited with laser energies of 532 nm and 633 nm.

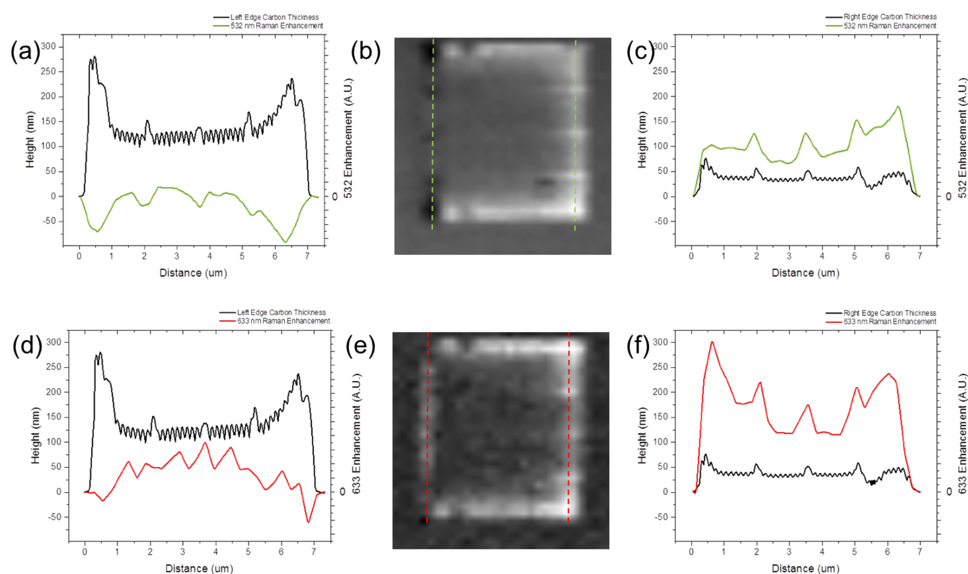

FIGURE 6.25: The enhancement properties of a carbon layer produced with electron beam energy of 5 keV and an applied dose of 5 nC$\cdot\mu$m^{-2} and excited with laser energies of 532 nm and 633 nm. Intensity maps of the characteristic Si Raman peak, generated from the carbon layer and normalised to the clean region of the specimen, are displayed for 532 nm and 633 nm in (b) and (e) respectively. The enhancement of the Si Raman peak observed along the left edge of the layer, relative to its height profile, is displayed in (a) and (d) for 532 nm and 633 nm excitation energy, respectively. The enhancement of the Si Raman peak observed along the right edge of the layer, relative to its height profile, is displayed in (c) and (f) for 532 nm and 633 nm excitation energy, respectively.

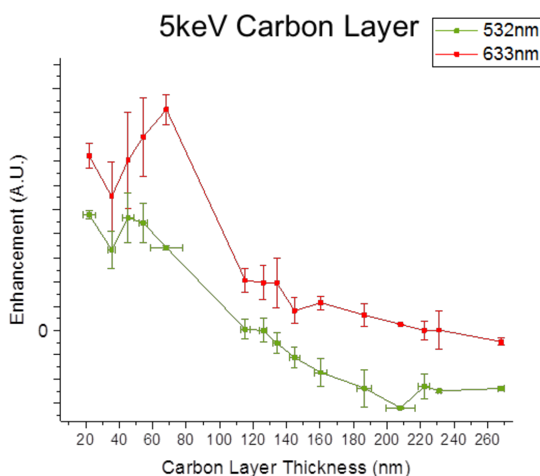

FIGURE 6.26: Thickness-dependent Raman enhancement observed from the 5 keV carbon layers excited with laser energies of 532 nm and 633 nm.

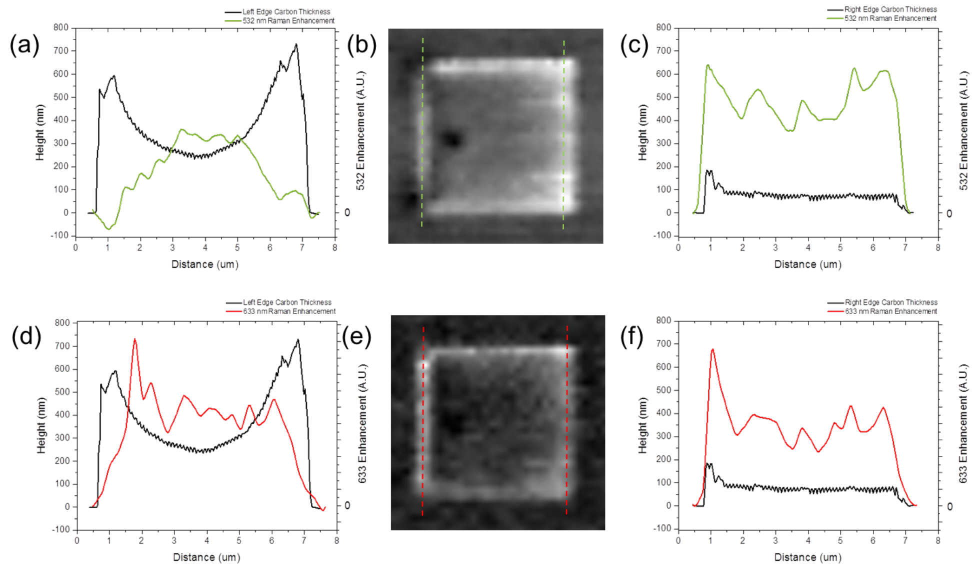

FIGURE 6.27: The enhancement properties of a carbon layer produced with electron beam energy of 12 keV and an applied dose of 5 nC$\cdot\mu$m^{-2} and excited with laser energies of 532 nm and 633 nm. Intensity maps of the characteristic Si Raman peak, generated from the carbon layer and normalised to the clean region of the specimen, are displayed for 532 nm and 633 nm in (b) and (e) respectively. The enhancement of the Si Raman peak observed along the left edge of the layer, relative to its height profile, is displayed in (a) and (d) for 532 nm and 633 nm excitation energy, respectively. The enhancement of the Si Raman peak observed along the right edge of the layer, relative to its height profile, is displayed in (c) and (f) for 532 nm and 633 nm excitation energy, respectively.

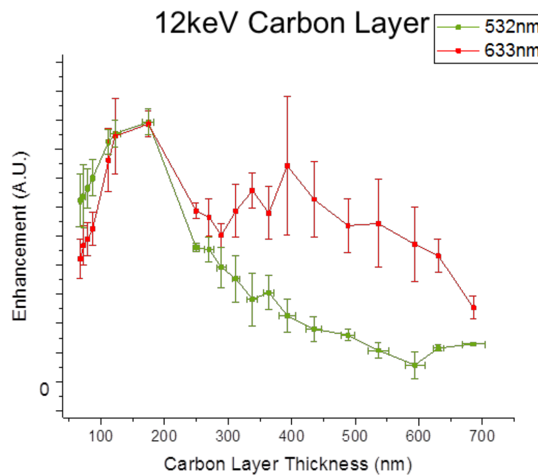

FIGURE 6.28: Thickness-dependent Raman enhancement observed from the 12 keV carbon layers excited with laser energies of 532 nm and 633 nm.

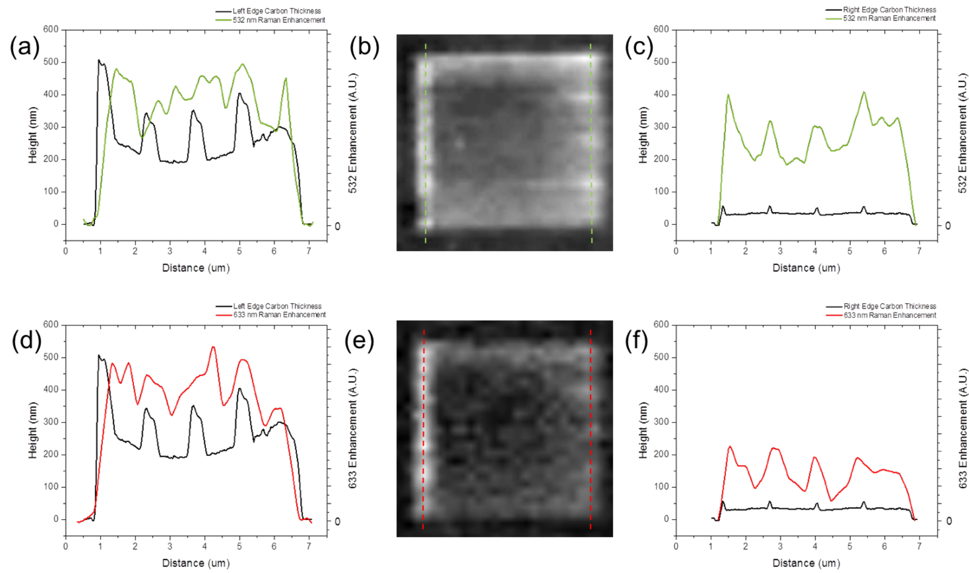

FIGURE 6.29: The enhancement properties of a carbon layer produced with electron beam energy of 20 keV and an applied dose of 5 nC$\cdot\mu$m^{-2} and excited with laser energies of 532 nm and 633 nm. Intensity maps of the characteristic Si Raman peak, generated from the carbon layer and normalised to the clean region of the specimen, are displayed for 532 nm and 633 nm in (b) and (e) respectively. The enhancement of the Si Raman peak observed along the left edge of the layer, relative to its height profile, is displayed in (a) and (d) for 532 nm and 633 nm excitation energy, respectively. The enhancement of the Si Raman peak observed along the right edge of the layer, relative to its height profile, is displayed in (c) and (f) for 532 nm and 633 nm excitation energy, respectively.

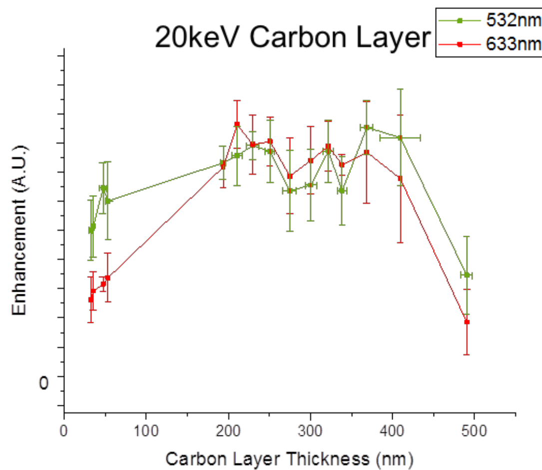

FIGURE 6.30: Thickness-dependent Raman enhancement observed from the 20 keV carbon layers excited with laser energies of 532 nm and 633 nm.

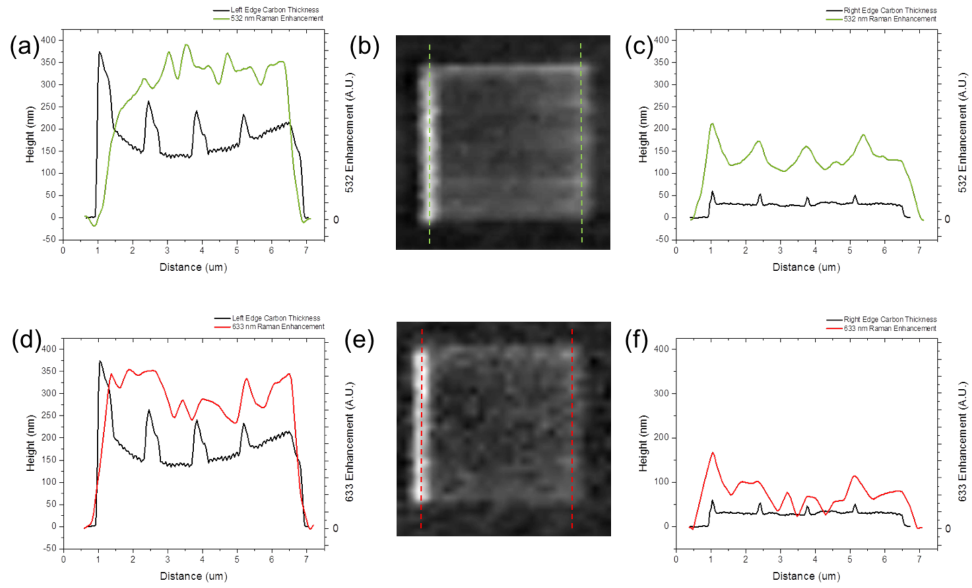

FIGURE 6.31: The enhancement properties of a carbon layer produced with electron beam energy of 30 keV and an applied dose of 5 nC·μm^{-2} and excited with laser energies of 532 nm and 633 nm. Intensity maps of the characteristic Si Raman peak, generated from the carbon layer and normalised to the clean region of the specimen, are displayed for 532 nm and 633 nm in (b) and (e) respectively. The enhancement of the Si Raman peak observed along the left edge of the layer, relative to its height profile, is displayed in (a) and (d) for 532 nm and 633 nm excitation energy, respectively. The enhancement of the Si Raman peak observed along the right edge of the layer, relative to its height profile, is displayed in (c) and (f) for 532 nm and 633 nm excitation energy, respectively.

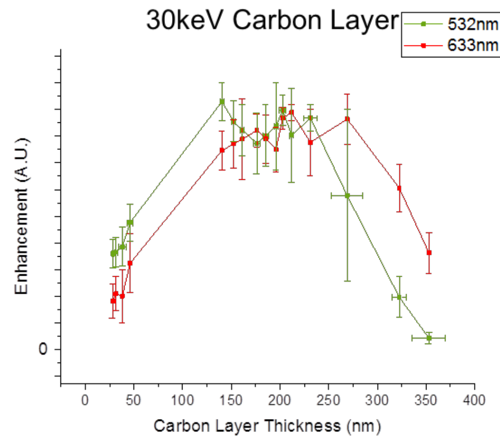

FIGURE 6.32: Thickness-dependent Raman enhancement observed from the 30 keV carbon layers excited with laser energies of 532 nm and 633 nm.

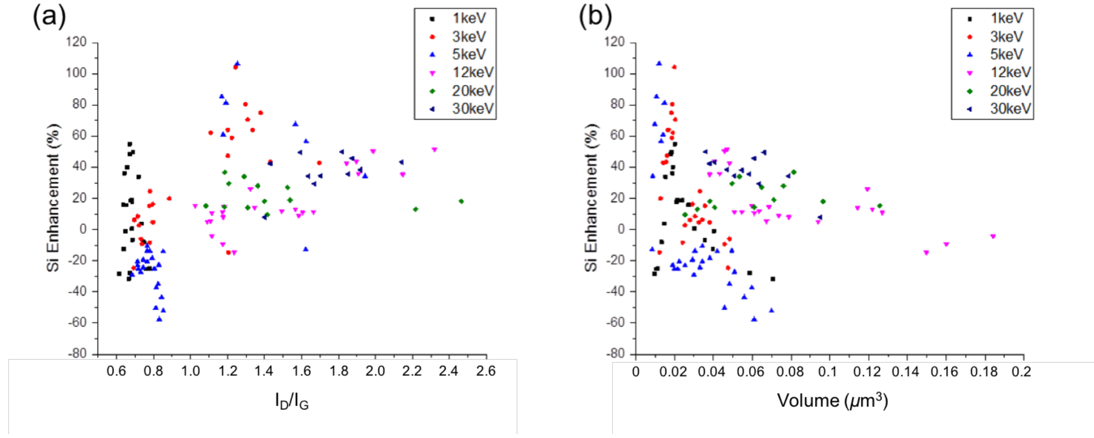

FIGURE 6.33: Enhancement of the Si Raman peak observed from carbon layers generated with an electron beam energy range of 1 – 30 keV is displayed as a function of I_D/I_G ratio in (a) and layer volume in (b).

6.4.2 The influence of deposition energy

The finite intensity values for the Si Raman shift observed across the carbon layers, as displayed in Figure 6.9 to Figure 6.20, were converted to enhancement values and are displayed in Figure 6.33. This was achieved by using the intensity of the Si Raman peak from a clean region of the Si specimen (I_{Si}) as a reference for the enhancing effect. The enhancement, given as a percentage of the reference, is determined using Equation 6.2, where I_C is the intensity of the Si Raman peak collected from the carbon and I_{Si} is the reference intensity.

$$Si_{Enh} = \left(\frac{I_C - I_{Si}}{I_{Si}} \right) \times 100\% \tag{6.2}$$

Figure 6.33 (a) shows the relationship between enhancement and I_D/I_G ratio present in the carbon layers generated with 1 – 30 keV electron beam energy. Positive data points represent specific measured volumes of deposited carbon which enhance the Si Raman peak from the underlying region of the specimen. Negative points represent those that attenuate the intensity of Si Raman peak. Enhancement and attenuation is present for carbons generated at 1 – 12 keV however at 20 – 30 keV only enhancement is observed. For the carbon data points with an I_D/I_G ratio of less than 1.0, ∼40% are Raman enhancing and the remaining are

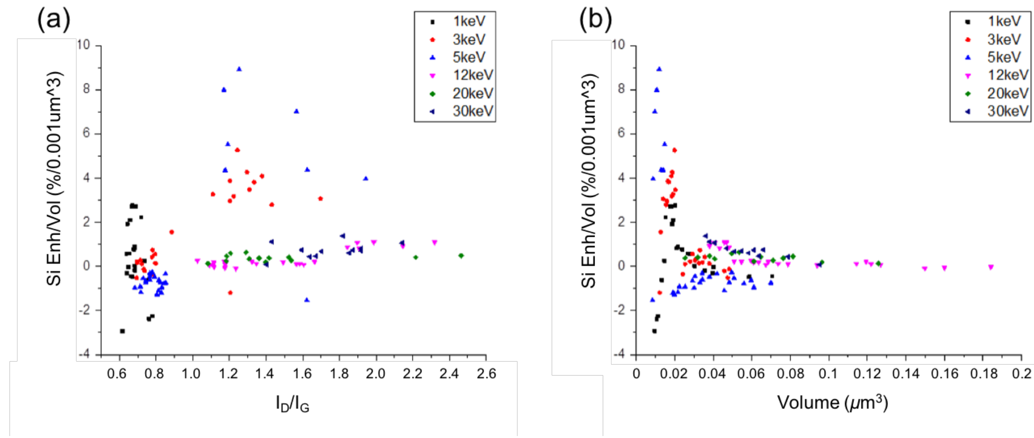

FIGURE 6.34: Volume normalised enhancement of the Si Raman peak observed from carbon layers generated with an electron beam energy range of 1 – 30 keV is displayed as a function of I_D/I_G ratio in (a) and layer volume in (b).

Raman attenuating. For those with an I_D/I_G ratio above 1.0, ~90% are Raman enhancing.

Figure 6.33 (b) shows the enhancement observed with the increase in carbon volume. Maximum enhancement occurs for minimum values of carbon volume generated at low beam energies (< 5 keV). The same values of enhancement are observed at varying carbon volumes, across the range of e-beam energies. In order to compare the enhancement effect, as a function of electron beam energy, all data points were normalised to their individual volumes. The relationships between volume normalised enhancement, as a function of I_D/I_G ratio and carbon volume, are displayed in Figure 6.34.

Figure 6.34 (a) shows the volume normalised Si Raman enhancement as a function I_D/I_G ratio. Low energy carbon (1 - 5 keV) is up to ~8 times more enhancing than high energy carbon (12 – 30 keV). Peak enhancement occurs at for 5 keV when the I_D/I_G ratio ranges between 1.1 – 1.5. An increase in the rate of volume normalised enhancement for high energy carbon is observed with the increase in I_D/I_G ratio. Figure 6.34 (b) shows the volume normalised Si Raman enhancement, for the increase of carbon layer volume generated across the 1 - 30 keV deposition energy range. As the volume increases the enhancement immediately peaks at ~0.02 μm^3 for low energy carbon, however with further increase in volume the enhancement decreases at an exponential rate.

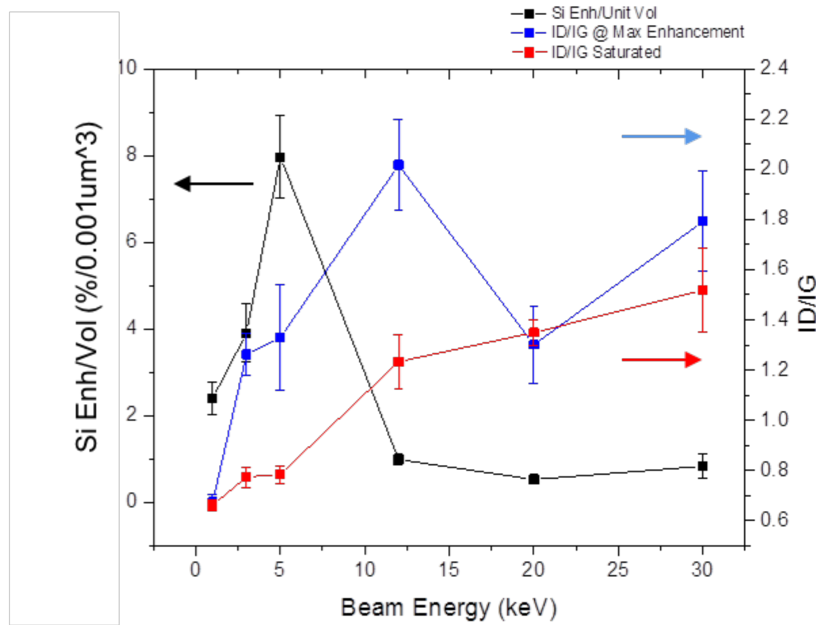

FIGURE 6.35: Maximum normalised Si Raman enhancement occurring at each electron beam deposition energy, with the I_D/I_G ratio present at max enhancement and the saturated I_D/I_G ratio.

The volume normalised Si Raman enhancement reaches a maximum at each beam energy, for a given volume of deposited carbon. These maxima can be used to directly compare the effect of deposition energy on the enhancement properties of the carbon layers. Presented in Figure 6.35 are the volume normalised Si Raman enhancements for each beam energy, along with their corresponding I_D/I_G ratios. Also given are the saturated I_D/I_G ratios occurring within the carbon layers generated at each beam energy. For low energy carbon (1 – 5 keV), maximum volume normalised enhancement increases with the increase in electron beam energy. This peaks at 5 keV and coincides with a maximum I_D/I_G ratio of ∼1.3. In contrast to low energy carbon, the maximum volume normalised enhancement observed for high energy carbon (12 – 30 keV) is significantly reduced. In this range the I_D/I_G ratio remains high and peaks at a value of ∼2.0 for 12 keV carbon. It then drops to ∼1.3 for 20 keV carbon and increases again to ∼1.8 for 30 keV carbon. The observed enhancement appears to be directly correlated to I_D/I_G ratio at each deposition energy. Greatest enhancement is observed at 12 keV (I_D/I_G ∼2.0), a reduction is observed at 20 keV and coincides with a drop I_D/I_G (∼1.3). At 30 keV enhancement increases with the increase in I_D/I_G ∼1.8 but to a level just

below that observed at 12 keV.

The I_D/I_G ratio for the carbon produced at each beam energy reaches a saturated value, for a given deposition volume. As displayed in Figure 6.35, I_D/I_G *Saturated* increases with increase in electron beam energy. For low energy carbon it has a value below 1.0 and for high energy carbon it has a value above 1.0. The saturated I_D/I_G ratio at each beam energy gives an indication of the optical gap present in each layer, i.e. its ability to transmit incident and scattered light.

6.4.3 Discussion on the mechanisms of enhancement

For a given laser excitation energy (532 nm), enhancement of the characterisic Si Raman peak (520 cm^{-1}) as a function of electron beam deposition energy is dependent upon carbon layer thickness (or deposited volume). The effect can be explained as follows. Layers produced with low electron beam energy (1 – 5 keV) generate a maximum volume normalised enhancement for a layer thickness of ∼60 – 80 nm (∼0.01 – 0.02 μm^3). This enhancement is greatest for high I_D/I_G ratios and is directly correlated to the concentration of aromatic sp^2 carbon bonds present within the excited volumes. As the thickness (or volume) increases beyond the point of maximum enhancement, the intensity of the Si Raman peak is attenuated and the enhancement is diminished. The attenuation of the Si Raman peak is due to the final arrangement of the carbon bonds, which is given by the saturated I_D/I_G ratios (< 1.0). A reduced I_D/I_G ratio indicates a lower concentration of aromatic carbon bonds, i.e. a lower level of disorder within the excited volume, which results in a lower optical gap. This in turn reduces the optical transmission ability of the low energy carbon layers to their thinnest regions, from where the enhancement can be observed.

Carbon layers produced with high electron beam energy (12 – 30 keV) generate a maximum volume normalised enhancement at a layer thickness of ∼180 – 250 nm (∼0.05 – 0.065 μm^3). The observed enhancement in this energy range is also directly correlated to the concentration of aromatic sp^2 carbon bonds within the excited volumes, exemplified by the high I_D/I_G ratios present at the maximum volume normalised enhancements. In contrast to the low energy carbon layers, the higher saturated I_D/I_G ratios of the high energy layers indicates greater carbon bond disorder, which in turn produces an opening of the optical gap. As a result,

incident and scattered light can transition through the carbon layers at increased thicknesses, across which the enhancement of the Si Raman peak can be observed.

The effect of excitation energy on the enhancement characteristics of the carbon layers, was studied by comparing the observed enhancement effect using laser energies of 532 nm and 633 nm. For the regions of the layers that contained the saturated I_D/I_G ratio, enhancement of the Si Raman signal was observed over a greater carbon thickness for 633 nm excitation, than for 532 nm excitation. This effect can be explained by applying the the *Beer-Lambert* law. As the saturated I_D/I_G ratio represents a fixed concentration of the absorbing species, the path length is therefore inversely proportional to excitation wavelength. Excitation by 633 nm thus enabled the transmission of the characteristic Si Raman peak over larger distances within the carbon layer. In the enhancing phase of the carbon layers, those produced at 1 and 5 keV revealed a greater level of enhancement for 633 nm than for 533 nm. At 3 keV both excitation energies revealed similar levels of enhancement. However the carbon layers produced at high electron beam energies revealed the opposite effect. This can be explained by the differences in thickness and optical gap. For low e-beam energy deposits (1 - 5 keV), the thickness of the enhancing phase is $\sim$60 – 80 nm and although the concentration of the absorbing species (i.e. I_D/I_G ratio) varies significantly, the low optical gap associated with these deposits results in more absorption for the higher excitation energy in comparison to that for the lower excitation energy. This results in an increased level of excitation and enhancement of the underlying Si by the lower excitation energy. For high e-beam energy deposits (12 - 30 keV), the enhancing phase is between $\sim$100 - 250 nm and the I_D/I_G ratio varies to a lesser extent. The higher optical gap associated with these deposits results in relatively less absorption of the 532 nm excitation energy in this thickness range, giving the higher excitation energy a greater ability to excite and enhance the underlying Si.

The differences in the optical properties of the carbon layers can explain how the intensity of the Si Raman peak changes with thickness (or volume) at each deposition energy and over the range of deposition energies. However, it does not explain how the deposited carbon species enhances the Raman signals from the underlying Si specimen. As the energy of the characteristic Si Raman scattered light, 2.27 eV, is significantly greater than the energies associated with the aromatic, 0.167 eV (D peak) and linear, 0.196 eV (G peak) carbon bonds, it is unlikely that an electro magnetic enhancement mechanism - as a result of excited oscillating carbon bonds

- is responsible for the observed enhancement. Also unlikely is enhancement by direct chemical bonding between the carbon and Si atoms at the layer-substrate interface. This is because the band gap of adjoining sp^2 carbon bonds (linear or aromatic) is significantly greater than the electron affinity of the Si atoms in substrate.

The results of the EELS analysis, presented in section 6.1.2, show a 3% difference in the sp^2 bond concentration for carbon layers deposited at 3 and 30 keV, with the lower energy carbon having the relatively higher concentration. Even though the EELS result do not definitively indicate that the increase electron beam deposition energy influences the resultant sp^3 concentration, the electrical measurement data, presented in section 6.1.3, gives direct evidence to indicate that the band gap of the layers is influenced by deposition energy.

In the cluster model for amorphous carbon structures, the band gap per sample is given by the average band gap per cluster, with average band gap per cluster being proportional to cluster disorder, i.e. number of rings per cluster [130]. The optical gap of an amorphous carbon structure depends on the configuration of the sp^2 sites, which may or may not vary with of its sp^3 content [130]. The sp^2 sites have a lower band gap than the sp^3 sites, due to the energy differences between $\pi - \pi^*$ and $\sigma - \sigma^*$ transitions. In an amorphous carbon structure the sp^3 sites can act as a tunnel barrier between the sp^2 clusters, so as the sp^3 content increases in the structure its optical gap increases likewise [130]. The overall band gap and optical gap of an amorphous carbon structures (including electron beam induced carbon layers) is therefore determined by both the sp^2 ordering and the sp^2:sp^3 ratio.

For all carbon volumes analysed in this data set, enhancement is observed when the I_D/I_G ratio is greater than the saturated I_D/I_G ratio. As the saturated I_D/I_G ratio has been observed to increase with the increase in beam energy, beam energy therefore is the major factor influencing the final distribution of the sp^2 bonds, i.e. aromatic vs. linear. It is this distribution that determines the optical gap present within the layers and their Raman enhancing capability. These results explain the optical properties of the electron beam induced carbon layers, as a function of laser excitation energy, electron beam deposition energy and deposited carbon volume. The source of the enhancement of the Si Raman peak has however yet to be determined.

6.5 Summary of Raman enhancement properties of electron-beam induced carbon layers.

The Raman enhancing properties of electron beam induced layers have been observed to depend upon deposition volume and deposition energy. Formed on an intrinsic 100 Si substrate from residual hydrocarbons - in a SEM with a deposition energy range of 1 - 30 keV and a dose range of 1 - 5 pC$\cdot\mu$m^{-2} - the deposition process employed resulted in the formation of highly topographic layered structures. Morphology characterisation revealed variations in layer thickness of $\sim$50 nm - $\sim$1 μm. EDX analysis did not reveal the presence of Si from within the layers. EELS analysis revealed a 3% increase in sp^2 concentration, between low (3 keV) and high (30 keV) beam energy depositions. Electrical characterisaion revealed a 400% increase in resistivity (0.25 - $\sim$ 10MΩ cm), between low and high electron beam deposition energies. Raman mapping analysis, conducted at excitation energies of 532 nm and 633 nm, revealed the intensity distribution of the Si Raman and Carbon Raman signals present within the layers, relative to the Raman intensity of the uncontaminated region of the specimen. The presence of the D and G carbon Raman bands confirmed the amorphous nature of the deposited layers. Raman intensity maps, generated at 532 nm, were precisely correlated to AFM thickness profiles. From this correlation a systematic analysis of Si Raman peak intensity, as a function of layer sp^2 configuration (I_D/I_G ratio) and contamination volume, was conducted. From this analysis the observed variations in Raman intensity were first converted to enhancement values. These enhancement values where then normalised to deposited carbon volume, which enabled a comparison of the observed enhancement as a function of deposition energy. For low energy carbon (1 – 5 keV), maximum normalised enhancement and I_D/I_G increased with the increase in electron beam energy, both peaking at 5 keV (I_D/I_G $\sim$1.3). For high energy carbon (12 – 30 keV), maximum normalised enhancement was significantly reduced and the I_D/I_G fluctuated between $\sim$1.3 - $\sim$2.0. The I_D/I_G ratio of the carbon produced at each beam energy reaches a saturation value, once a given deposition volume is reached. The saturated I_D/I_G ratio is observed to increase monotonically with the increase in electron beam energy, with values below and above 1.0 for low and high energy carbon, respectively.

Chapter 7

Conclusion and future work

To conclude this work, firstly, detailed summaries of each sub-section in the comparative SE study and a discussion their findings is given. This is followed by a conclusion and further discussion on the results for the Raman enhancement effect of electron beam induced carbon layers. Lastly, a section on future work outlines the open research questions remaining from this work, and the experimental and theoretical approaches required to clarify them.

7.1 Conclusion for the comparative SE study.

The formation and effect of He^+ beam-induced contamination.

Summary: The formation and effect of He^+ beam-induced contamination in a HIM has been assessed in relation to specimen properties and beam parameters. The pre-exposed environments determine the level of hydrocarbons on the specimen surface. The 'cleaned' specimens showed a higher SE intensity with an approximate difference of ~250% from the "un-cleaned" specimens. The correlation between the beam dose and the contamination profile has been investigated. When the He^+ dose increased from 0.7 to 22.4 pC·μm^{-2}, a decrease in the SE signal and an increase in the contamination height profile was observed. As the dose exceeded 22.4 pC·μm^{-2} the height of the contamination first dropped off and then increased again. The SE intensity from the most irradiated region is observed to have abnormally increased.

For SEM, beam conditions were selected as to generate an approximately equal number of SEs for inducing the contamination. The observed SE intensities from electron-induced contamination profiles decreased with the increase of electron dose, accompanied by an increase in the average height of the profile. SE intensity

is also saturated at higher doses. Unlike HIM, specimen cleaning did not significantly affect the contamination formation in SEM. The specimens in the HIM are also not subjected to the same level of additional hydrocarbon absorption as in the SEM, due to its design (a load port which keeps the chamber at a constant optimum vacuum). The drop and subsequent rise in measured height of the HIM contamination profiles can be explained in terms of ion sputtering and implantation respectively. Substrate swelling in Si is known to occur at this highest dose regime and the observed increase in SE intensity confirms that it is not a contamination profile [175].

Discussion: In the low He^+ ion dose regime, the contrast for the induced contamination correlated positively with dose. This was observed for both the cleaned and un-cleaned Si specimens and indicated that an increase in layer thickness was due to an increase in applied dose. For each He^+ ion dose (in this regime), a significant reduction in contrast was observed between the un-cleaned and the cleaned specimens. This suggested a lower amount of contamination being built on the cleaned sample and indicated a higher degree of cleanliness within the HIM chamber. The contrast from the cleaned and un-cleaned Si specimens was also observed to saturate, i.e. a weak increase in contrast with the increase in He^+ dose. For the cleaned sample, contrast saturation appeared at a lower dose. This also indicating a reduced supply of hydrocarbons for the contamination formation process. These observations indicate that contamination formation in the HIM is hydrocarbon limited and their supply is mainly due to the adsorbed molecules present on the sample surface prior to irradiation.

In SEM, cleaning the Si specimens had little effect on the contamination formation, as no change in the dose dependent SE contrast was observed, for either the cleaned or un-cleaned specimens. This indicated that the SEM environment dominated the supply of hydrocarbons and the limiting parameter for the contamination formation was the electron dose.

In the low dose regimes for HIM and SEM, the average height of the contamination layers formed in both microscopes show similar values. The likely cause for this similarity is the generation of an equivalent number SEs during the irradiation process, in combination with sufficient hydrocarbon concentrations. This observation confirms the significance of the SE signal in the contamination process. SE yield - a function of beam dose and material type - must therefore be taken into consideration when promoting or minimising contamination formation

in HIM. Further investigation on the correlation between the beam dose, SE yield and the contamination profile is required, to clarify the characteristics of the He^+ ion irradiation in the contamination formation process.

Comparative study of image contrast in SEM and HIM.

Summary: Amorphous Ga-implanted Si regions were prepared on a Si substrate by using Ga^+ FIB irradiation. The Ga atomic density in each 30-nm-thick implanted region varies from $9.1 \times 10^{20}\ cm^{-3}$ to $8.1 \times 10^{21}\ cm^{-3}$. Images of the regions were collected by using the InLens, ET, EsB detectors in a SEM as well as MCP and ET detectors in a HIM. The SEM-EsB and ET images show materials contrast which linearly depends on the Ga density and is attributed to the Z-dependence of the backscattered electron yield. The HIM-MCP images do not show material contrast due to the low yield of backscattered ions but the visibility of the implanted regions in the images may be due to the de-channeling effects of the top amorphous layer. HIM-ET and SEM-InLens images bear the most similarity and the dominant signal of the two types of imaging is SE1. In both cases, the contrast decreases linearly with increasing the Ga density and for each implanted region the contrast increases with dwell time. The modification of the SE yield due to the Ga implantation as well as the dynamic charging effect are responsible for the dependence of the SEM-InLens contrast on the imaging parameters, while charge diffusion may be the key factor that causes the observed contrast reversal in the HIM ET images.

Discussion: The Ga implantation reduced work function of the implanted regions and gave them an insulator-like behaviour. In SEM, this resulted in a change to SE yield profile of these regions, relative to that of the crystalline Si. The insulating properties of the layers scaled with Ga density such that, as Ga density increased a narrowing of the SE yield profile and a reduction in the primary electron beam energy for maximum SE intensity occured. As a result, for a given e-beam energy and fixed dwell time, the contrast of the implanted regions scaled in accordance with the difference between the SE yield of the implanted regions and the SE yield of the crystalline Si. Also, when the SE yield of the implanted regions was above either above or below that of the crystalline Si, positive or negative contrast were observed, respectively.

The effects of dynamic charging on SE contrast in SEM, were more apparent for low primary e-beam energy (0.5 keV). This was due to the restriction of the

electron-specimen interaction within the Ga implantation depth (∼30 nm). At a short dwell time (0.54 s), the SE yield of the high density Ga was lower than that of the crystalline Si, and SE yield of the low density Ga was higher than that of the crystalline Si. As the dwell time increased, charging within the implanted regions increased. This forced the landing energy of primary electrons to a lower value, thus increasing SE yield. The magnitude of charging effect scaled with dwell time therefore the contrast observed from each implanted region increased with the increase in dwell time.

In HIM, the observed changes in SE contrast, are explained as follows. As the He^+ ions penetrated the insulator-like layers, positive charges began to accumulate therein. This reduced the SE emission below that of the crystalline Si and produced negative contrast. With the increase in dwell time, the number of positive charges in the layers reduced. This was attributed to diffusion of the charges to the underlying Si. As a result, the intensity of each implanted region appeared less dark as dwell time increased. In low density Ga the the effects of diffusion were more significant, due to a lower degree of damage induced by the implantation process. In high density Ga the effects of diffusion were less apparent. Contrast reversal for each of the implanted regions was also observed however the dwell time at which it occurred was dependent upon Ga density. The SE contrast observed from the implanted regions in HIM was therefore dependent upon, the magnitude of positive charging and the rate of charge diffusion.

SE yield was therefore the critical factor in determining image contrast in this comparative study. It is influenced by primary particle type, specimen work function and the band-structure of the specimen within entire beam-specimen interaction volume. The effects of imaging parameters and sample charging on HIM contrast have lacked detailed exploration to date, therefore this work may be of benefit to further development of quantitative SE imaging techniques for semiconductor metrology and analysis.

High throughput secondary electron imaging of organic residues on a graphene surface.

Summary: In this work we have demonstrated the visibility of nanoscale PMMA residues on a graphene surface in secondary electron imaging. Artefacts have been attributed to the finite probe size and the varying nature of the beam-sample interaction at different beam conditions. In terms of imaging fidelity, HIM is superior to SEM, since HIM provides a sub-nanometer probe and increases surface sensitivity. The low-energy SEM images however demonstrate higher contrast. Other features such as folds, ridges and ruggedness could also be observed in the SE imaging.

Discussion: For both imaging techniques, feature size directly correlated to probe size i.e., the smaller the probe the greater the fidelity between the features presented in the images to those present on the graphene surfaces. The varying nature of the beam-sample interactions determined the SE contrast. In SEM, images produced at a low beam energy revealed high contrast. This was due to the majority of the interaction occurring within the top $\sim$12 nm of the specimen. The images produced at a high beam energy portrayed a reduced overall contrast and a higher degree of translucency. This was due to a reduced primary electron scattering cross-section within the available depth of the specimen. In HIM, image contrast was determined by the SE emission associated with the increased stopping power of the He^+ ions in the specimen, and image sensitivity by the localisation of the beam-specimen interaction.

SE emission and the finite size of the probe ultimately determined the spatial resolution and fidelity of the graphene specimens analysed in this study. The experimental methodology followed provides a quantitative approach to readily obtain the physical size of the features present on a graphene surface, with HIM being the superior SE imaging technique.

Quantitative SE imaging for work function extraction at atomic level and layer identification of graphene.

Summary: In this work we established a method to quantitatively analyse SE images of graphene on SiO_2/Si substrates. We have demonstrated that the SE contrast exhibits a universal visibility of few-layer graphene. Graphene with layer

numbers of less than ten can be determined from the SE contrast. Besides the quantification of graphene layer thickness, the work function of few-layer graphene can also be quantified by extracting the SE attenuation contributions from the layer-dependent SE contrast.

Discussion: The work function of few-layer 2D materials (e.g. graphene) is primarily determined by layer thickness (i.e. layer number). As SEs need to overcome the surface potential in order to escape to vacuum, SE contrast in HIM and SEM can be used to determine layer thickness and work function of 2D materials. SE contrast can be affected by other factors, such as beam parameters, beam-induced contamination, specimen electric potential, SE collection efficiency, etc., the influence of which is required for quantitative SE analysis.

In this work, the SE contrast of graphene as a function of layer thickness was analysed. The SE contrast for each graphene layer was determined by accounting for all of the invididual contributions to the overall SE signal. These were identified as, the SEs emitted from the graphene excited by the primary beam, the SEs emitted from the graphene excited by BS particles exiting the supporting substrate, and the SEs emitted from the substrate which diffused through the graphene. For the experiments conducted in both microscopes, a rapid decrease in contrast was observed for layers 1 - 4, a linear decrease for layers 4 - 12, and contrast saturation at 14 layers and above. The contribution of the substrate SEs in the overall SE signal was the major factor determining the graphene SE contrast. The initial rapid decrease is explained by a reflection coefficient parameter for the substrate SEs. An exponential function - dependent upon layer thickness (nm) as a fraction of the SE IMFP - it's greatest influence was observed between layers 1 - 4. Between layers 4 - 12 the influence of the reflection coefficient was reduced and the SE intensity attenuated linearly in accordance with the mean free path of the substrate SEs in the graphene. Above the 12th layer, the combined layer thickness (nm) approached that of the IMFP and as a result, the majority of the substrate SEs were attenuated from the overall SE signal. In this case graphene contrast was determined by the SE signals excited from within in the layer.

As the SE yield of graphene is determined by work function, work function can be directly extracted from the observed contrast. Quantification of graphene layer work function (up to 4 layers) was determined by extracting the SE attenuation contributions from the layer-dependent SE contrast. This was conducted for SE

contrast measurements acquired in SEM and HIM, with the results revealing a $< 1\%$ difference between both excitation sources.

In comparison to the techniques which have previously demonstrated the characterisation of graphene work function [88–90, 95], the results presented in this work provide a simple method to detect the work function of graphene - with high speed and atomic level accuracy - unhindered by environmental, throughput and specimen interactions factors. It also extends the application fields of SE contrast to quantitative analysis.

Fabrication and application of a SE energy filter in HIM and SEM

Summary: A *High-Pass* energy filter device was designed and fabricated for use in HIM and SEM. When placed directly over a specimen region of interest, a retarding field was generated between the device and specimen, on the application of a negative bias to the device. The retarding field limited the kenitic energy (eV) of the SEs delivered to the detector enabling the generation of SE energy distributions (spectra) and energy filtered SE images.

The EF device was initially evaluated in the HIM. The retarding field was assessed as being homogeneous with unity SE filtering efficiency, (i.e. $\Delta V_{GRID} : \Delta E_K =$ 1:1). The influence of specimen bias and He^+ ion beam energy on the operation of the device were evaluated. Specimen bias did not influence filtering efficiency, however the fine details in the spectral were impacted. Changes to He^+ ion beam energy did not influnce filtering efficiency or spectral information. The EF device was evaluated in SEM and its SE filtering efficiency was not 1:1. However on application of the appropriate correction factor, reliable SEM SEED data was generated.

The EF device was used to generate SE energy spectra from HOPG and graphene specimens. The HOPG specimen was analysed in HIM with SEEDs generated from three types of surface regions. The spectral data in the initial SEEDs from two surface regions show good alignment with the expected SE energy peaks. The third revealed a distinctively different initial SEED, suggesting that the surface conditions prior to He^+ ion irradiation in this region were significantly different. Continued irradiation on all regions resulted in changes to the SEED profiles, with damage inducing doses (≥ 6 pC$\cdot\mu$m^{-2}) changing the visible appearance of

the specimen. The spectra associated with the damaged regions were comparable to the SE energy profile of glassy carbon, indicating the occurrence of material conversion by the high dose He^+ ion irradiation. SE spectra of graphene were generated in SEM and HIM. These were used to determine the work function monolayer and multi-layer (2 - >10) graphene specimens. The accuracy of fit of the extracted SE spectral data, to the expected work function values, was the method used to confirm correlation between SE energy spectral profile and layer thickness.

Discussion: In the HIM energy filtered work completed by Petrov and Mikhailovskii et al. [27, 28, 59], a fixed hemi-spherical retarding grid was used, in conjunction with the specimen bias function of the microscope, to filter specimen SEs. This arrangement enabled successful implementation of their work however their design was not optimised in terms of specimen analysis, microscope operation and retarding field homogeneity. For optimum adaptation to the Carl Zeiss HIM instruments (Orion Plus and Orion Nano Fab), and an arbitrary SEM, significant changes to this basic design were required. The final design of the EF device in this work had a high degree of flexibility - in terms of placement over and above the specimen surface - and produced a homogeneous retarding field without obscuring the specimen region of interest in the image FOV. It did this with minimum impact on microscope operation and maximum specimen throughput.

The key advantage of the EF device is its ability to elicit specimen information pertaining to the SE emission process, i.e. peak SE energy and spectral profile. From this information specimen work function can be derived. The spectral (or SEED) data generated by the device can be used to finger print, or characterise changes to, a particular material. A study on characterising the SE emission from HOPG by He^+ ion irradiation reported clear peaks at 1 eV and 3 eV associated with its electronic structure [60]. Further studies on characterising electron beam induced SE emission from HOPG reported peaks at 4.3 and 5.4eV [197]. In the energy filter work presented in this thesis, these peaks are clear in the SEEDs generated from pristine surface regions. As HOPG is quickly damaged by prolonged irradiation, these peaks shifted in energy and droped in intensity as the overall He^+ ion dose increased. An EF device with the ability to select a predefined SE energy range would have the potential to over come this barrier and effectively characterise beam sensitive specimens based on their SE emission properties.

The SE device also enables the microscope to overcome the effects of beam-induced contamination. Characterisation of the SE emission profile of a contaminated region of a specimen, relative to an uncontaminated region, reveals the SE energy range (0 eV – X eV) most impacted by the contamination. By using the EF to retard the SEs below X eV, specimen images can be produced with minimum impact from the deposited contamination species. An example of this can be found in [59].

Finally, the EF device can also be used for generating SE images with a known energy range. To do this with the current set-up, a minimum of two images are required along with a *post-process* image overlay and pixel subtractive technique. In the future work section of this chapter a proposal for an advanced EF device is outlined. This improved design incorporates a second retarding mesh for the purpose of accurately controlling the SE energy range (eV + ΔeV) received at the detector during a single imaging scan. This enhanced design would increase the effectiveness of the imaging and characterisation functions of the device, especially for beam sensitive specimens.

7.2 Conclusion for the Raman enhancement of electron-beam induced carbon layers.

Summary: The Raman enhancing properties of electron beam induced layers have been observed to depend upon deposition volume and deposition energy. Formed on an intrinsic 100 Si substrate from residual hydrocarbons - in a SEM with a deposition energy range of 1 - 30 keV and a dose range of 1 - 5 pC$\cdot\mu$m^{-2} - the deposition process employed resulted in the formation of highly topographic layered structures. Morphology characterisation revealed variations in layer thickness of ~50 nm - ~1 μm. EDX analysis did not reveal the presence of Si from within the layers. EELS analysis revealed a 3% increase in sp^2 concentration, between low (3 keV) and high (30 keV) beam energy depositions. Electrical characterisaion revealed a 400% increase in resistivity (0.25 - ~ 10MΩ cm), between low and high electron beam deposition energies. Raman mapping analysis, conducted at excitation energies of 532 nm and 633 nm, revealed the intensity distribution of the Si Raman and Carbon Raman signals present within the layers, relative to the Raman intensity of the uncontaminated region of the specimen. The presence of the D and

G carbon Raman bands confirmed the amorphous nature of the deposited layers. Raman intensity maps, generated at 532 nm, were precisely correlated to AFM thickness profiles. From this correlation a systematic analysis of Si Raman peak intensity, as a function of layer sp^2 configuration (I_D/I_G ratio) and contamination volume, was conducted. From this analysis the observed variations in Raman intensity were first converted to enhancement values. These enhancement values where then normalised to deposited carbon volume, which enabled a comparison of the observed enhancement as a function of deposition energy. For low energy carbon (1 – 5 keV), maximum normalised enhancement and I_D/I_G increased with the increase in electron beam energy, both peaking at 5 keV (I_D/I_G ~1.3). For high energy carbon (12 – 30 keV), maximum normalised enhancement was significantly reduced and the I_D/I_G fluctuated between ~1.3 - ~2.0. The I_D/I_G ratio of the carbon produced at each beam energy reaches a saturation value, once a given deposition volume is reached. The saturated I_D/I_G ratio is observed to increase monotonically with the increase in electron beam energy, with values below and above 1.0 for low and high energy carbon, respectively.

Discussion: From the results presented, enhancement as a function of beam energy is directly correlated to deposited carbon volume (or layer thickness). Low beam energy deposits are significantly enhancing however their enhancement is limited to their thinner regions and varies significantly with beam energy. High beam energy deposits, although still enhancing, show little variation with beam energy. The saturated I_D/I_G ratio at each beam energy gives an indication of the optical gap present in each layer, i.e. its ability to transmit incident and scattered light. The EELS data and the variation in Raman I_D/I_G ratio, at the saturated and at the volumes of maximum enhancement, give clear indication that the configuration and concentration of oscillating sp^2 carbon bonds present in the layers plays a significant role in the enhancement effect. However further investigation into the exact source of enhancement and the influence of optical gap is required. The results of the electrical characterisation reveal higher conductivity in the layers generated at lower beam energies. The nature of this reduction is unknown, however upon further investigation, and clarification of the hydrogen content in the layers, a correlation between conductivity, sp^2 ratio and optical band gap could be determined.

7.3 Future work

Based on the work reported in this thesis, the future work I propose to do is outlined as follows.

SE spectroscopy and energy filtered imaging

Fristly, in order continue with the fundamental understanding of He^+ ion induced SE energy spectroscopy, I propose the generation of image based SEEDs from a comprehensive set of standard samples. This work would be conducted under a variety of beam and specimen biasing conditions. Each sample in the set will have a predefined SE energy profile generated via an alternative spectral collection method. If possible, a SE spectrum analyser should be mounted within the HIM chamber. This would enable the generation of SE energy profiles from the standard samples, via the spectrum analyser, and simultaneous comparison to those generated from the energy filtered imaging method.

Secondly, the design of the SE energy filter device can be improved upon by incorporating a second retarding mesh, for the purpose of accurately controlling the energy of the SEs received at the detector. So far this work has determined that generating SEEDs with fine spectral detail requires a high number of energy filtered images, each having a small separation in SE energy (eV). This process can result in significant degradation of the analysed specimen properties, due to extensive He^+ ion irradiation. The new design would require the use of both attractive and repulsive components, therefore careful simulation of their associated fields, as well as the tracking of the primary and secondary charged particles, is required. In the implementation phase of this new design I propose the use of the COSMOL simulation software package, to generate an SE energy filter device whose component geometry, placement within the beam path, and SE energy filtering efficiency, is optimised. Successful implementation of this new design would enable the generation of specimen images with a predefined SE energy range. This enhancement would be particularly useful for the imaging of beam sensitive (organic or biological) materials, where the SE emission characteristics of a specimen could be revealed with a single high-resolution imaging scan. The application of the device could be further extended to the generation of single-pass energy filtered images of semi-conductor devices. Such imaging would enable preferential selection the SEs associated with certain device features and also minimise the formation of effect

of beam-induced contamination in the acquired image. Both of these attributes could aid the current critical dimension measurements techniques, especially as minimum feature size approach the few nm range. The device could also be used as a qualitative screening method to characterise device features based on their SE emission properties, when applied to variety of in-line SEM instruments. Prior to conducting further applications work with the re-designed energy filter device, first-principle calculations on the SE generation and emission properties of the proposed organic and semiconductor experimental specimens, by He^+ ion irradiation, would be conducted.

Raman enhancement of beam-induced carbon layers

For the continuation of the work on characterising the observed Raman enhancement effect of electron bean induced carbon layers, I first propose continuing the exploration of the fundamental knowledge of the effect by conducting further experiments to characterise the morphology of a new set of carbon layers deposited on Si specimens. To do this, UV-Raman spectroscopy (and mapping), will be utilised to directly probe layer sp^3 content, in conjunction with a further EELS study focusing on layers generated at e-beam energies not characterised to date. Also, *μ-Fourier transform infra-red* (FTIR) spectroscopy and UV-VIS (NIR) spectroscopy will be employed to determine hydrogen content and optical gap of the layers, respectively. The proposed future work will include theoretical simulation of the field enhancement at the carbon-surface interface (i.e. finite element simulation) and an understanding of the propagation and attenuation of the light within the amorphous carbon layers.

Other work has reported the enhancement of the carbon Raman signal (G peak) by the deposition of electron beam induced carbon layers [42], however this is the first reporting of enhancement of the Raman scattered light from other substances as a result of deposited carbonaceous species. To address the possibility of applying the carbon layers for use as optical bio-sensors in cancer research, their Raman enhancing effect on the spectra generated from elements such as, Sr, Ca, Fe, Zn, P, K, Cu, and As needs to be clarified. Depending on the type and nature of a cancer cell, these elements have been found to exist in significantly less quantities, in comparison to their quantity in non-cancerous cells [201]. The advantage of this technique, over work in this field which couples types of enhancing media to a particular analytic (e.g. [202]), the carbon layers may have the potential to simultaneously, and indiscriminately, enhance the Raman signal of these elements

- which are typically difficult to characterise by non-enhanced Raman spectroscopy - when both cell types are treated to the appropriate deposition of electron beam induced carbon layers and comparisons of element type and concentration in each are drawn. Prior to conducting further work on developing the applications of the effect, simulation on the Raman enhancement of these elements within the confines of biological detection will be explored. This will be done using the excitation energies that produce the strongest scattering for non-enhanced Raman.

Appendix A

TEM lamella preperation

In order for the chemical analysis of the carbon layers to be completed, lamella specimens ($\sim$ 60 nm) of the 3 and 30 keV carbon layers were required. This was completed by in-situ FIB lift out and thinning.

To protect the carbon layers during the lamella preperation, a series of protective layers were deposited over them. The first layer ($\sim$ 100 nm AuPd), was evaporated of over the entire specimen using a Cressington 108 thermal evaporator. The second layer ($\sim$ 150 nm Pt), was deposited over a 10 μm $\times$ 2 μm region on top to the 3 and 30keV carbon layers, by electron beam induced deposition. The third layer ($\sim$ 1 μm Pt), was selectively deposited in the same 10 μm $\times$ 2 μm region, by Ga^+ ion beam induced deposition. The second and third layers were deposited in the FEI Strata DB-235 instrument. The first AuPd protective layer is not required for standard FIB lamella preparation, however in this case the amorphous carbon layers needed to be clearly distinguished, from the carbon containing electron beam induced Pt layer, in the TEM analysis. The Ga^+ ion beam induced Pt layer provides the primary protection to the specimen during the lamella thinning process. Ga^+ ions can damage specimens during layer deposition, however this was prevented by the e-beam Pt layer. Images of the protective layers deposited on the 3 and 30 keV carbon layers are shown Figure A.1.

The second step in the lamella process was the in-situ FIB lift-out. This commenced immediately after the protective layering process. The protective Pt layer covering the 3 keV carbon layer was used to set the specimen stage to the point of electron and ion beam coincidence. The stage was tilted to 52°, so that the specimen surface was incident to the Ga^+ beam. Deep trenches ($\sim$ 10 μm) were then milled into the specimen immediately above, below and to the right of the Pt layer. This action removed the majority of the bulk material surrounding the Pt protective layer and left behind a $\sim$ 2 μm thick lamella, supported by the bulk specimen on its left side. The specimen stage was then tilted to 0° and a lift-out

needle, attached to a micro-manipulator (Kelindeik MM3A), was positioned in close proximity to the lamella. The lift-out needle was bonded to the lamella by the deposition of a Pt strap and the lamella cut from the specimen using the Ga^+ ion beam. As soon as the cutting was complete, the lift-out needle was retracted and the lamella freed from the specimen.

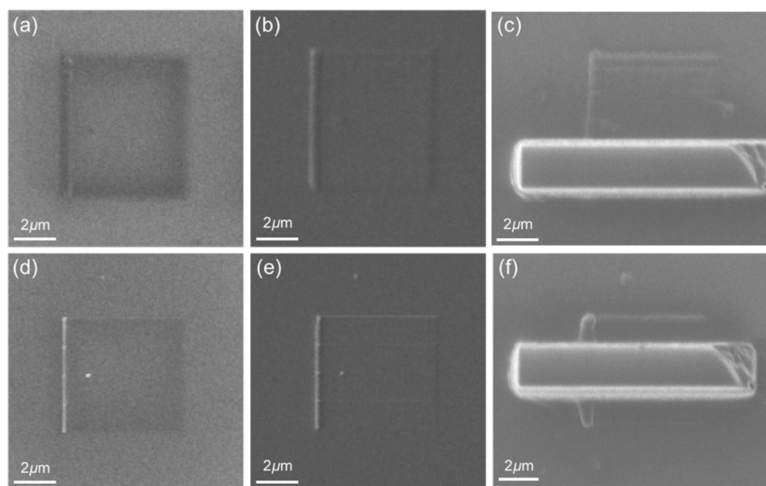

FIGURE A.1: SEM images of the 3 keV carbon layer, (a) uncoated , (b) post ~100 nm Au-Pd coating and (c) post ~100 nm SEM Pt and ~1 μm FIB Pt coatings. The same coatings for the 30 keV carbon layer are displayed in (d - f).

The lift-out needle, with the lamella attached, was moved to a safe position and a TEM lamella-grid was centred in the FOV, at the beam coincidence point. Using fine movements of the micro-manipulator, the lamella was carefully brought in contact with the grid and bonded to it with a connecting Pt strap. The lamella was then freed from the lift-out needle by cutting the connecting Pt strap. Once freed, the needle was retracted and moved to a safe position. To secure the lamella firmly to the grid, the specimen stage was rotated 180° and an additional Pt strap was placed between the gird and the back side of the lamella. A lamella for the 30 keV carbon layer was generated by the same process but mounted to a separate TEM grid. Images of the mounted lamellae for the 3 and 30 keV carbon layers are shown in Figure A.2.

Once on the TEM grid(s), the lamellae were thinned to the final desired thickness by coarse thinning, fine thinning and a polishing step. The coarse thinning step was conducted in the FEI Strata at 30 keV, using Ga^+ ion beam currents of 500,

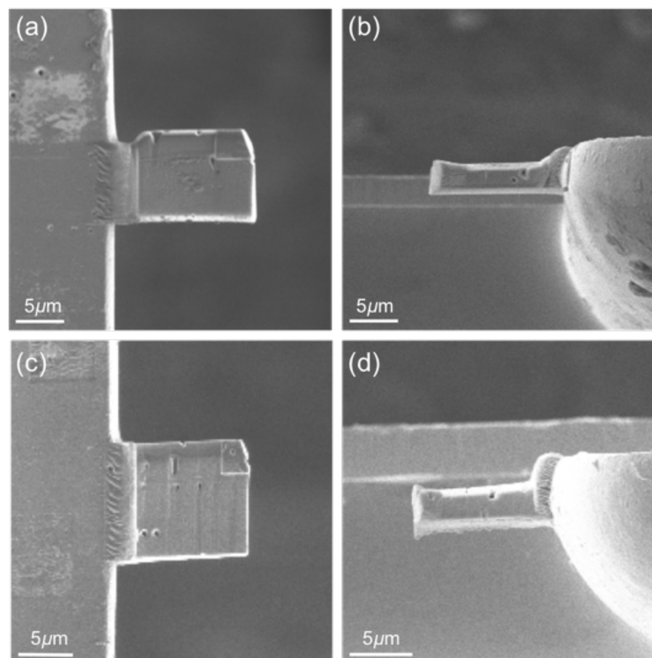

FIGURE A.2: TEM lamellae of the 3 and 30 keV carbon layers as observed from the Ga^{+} ion beam (a, c) and electron beam (b, d). The images were acquired in the FEI DB-235 dual FIB/SEM instrument immediately post lift-out and attachment to TEM lamella grids (specimen stage tilt set to at 0°).

100 and 50 pA. The lamellae specimens where then moved to a Carl Zeiss Auriga FIB/SEM instrument, where the fine thinning was conducted at 30 keV, 20 pA, and the final polishing step at 3 keV, 20 pA. In the coarse thinning, the lamellae were brought to a thickness of ∼200 nm by alternate cross-sectional milling on each side. During this sectioning the glancing angle of the ion beam varied $\pm\ 5^{o}$ from normal. This process was repeated in the fine thinning step however a lower beam current was used to bring the specimen to electron transparency (∼ 100 nm). The polishing step was required to remove lateral amorphorisation caused by the 30 keV thinning. This resulted in a final cross-sectional carbon layer depth of ∼ 60 nm. Images of the lamellae after final preparation are shown in Figure A.3.

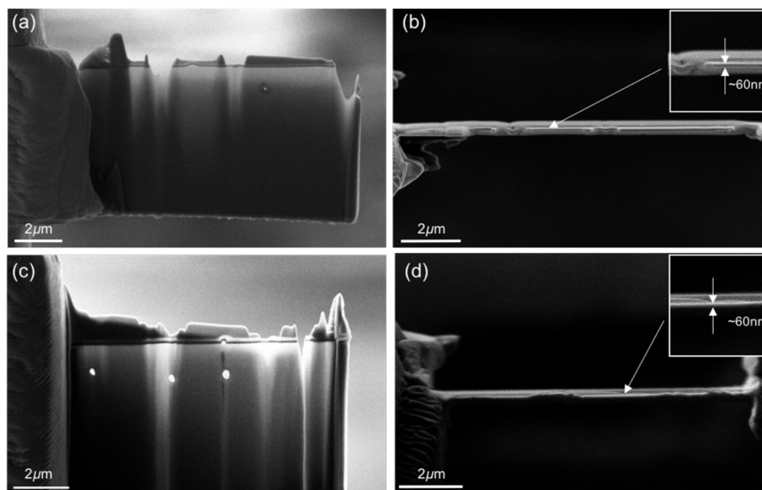

FIGURE A.3: TEM lamellae of the 3 and 30 keV carbon layers post final thinning. (a) SEM image of the 3 keV carbon layer lamella, specimen stage tilt 54°. (b) SEM image of the 3 keV carbon layer lamella, specimen stage tilt 0° with inset showing the final polished thickness. (c) SEM image of the 30 keV carbon layer lamella, specimen stage tilt 54°. (d) SEM image of the 30 keV carbon layer lamella, specimen stage tilt 0° with inset showing the final polished thickness.

BIBLIOGRAPHY

[1] A. Hashimoto, K. Suenaga, A. Gloter, K. Urita, and S. Iijima. Direct evidence for atomic defects in graphene layers. *Nature*, 430(7002):870–873, 2004. ISSN 0028-0836. doi: 10.1038/nature02817.

[2] The international technology roadmap for semiconductors. `http://www.itrs2.net/`, 2017. Accessed: 2017-09-23.

[3] J. Notte, B. Ward, N. Economou, R. Hill, R. Percival, L. Farkas, and S. McVey. *An introduction to the helium ion microscope*, volume 931 of *Aip Conference Proceedings*, pages 489–496. Amer Inst Physics, Melville, 2007. ISBN 0094-243X 978-0-7354-0441-0.

[4] S. Kostinski and N. Yao. Rutherford backscattering oscillation in scanning helium-ion microscopy. *Journal of Applied Physics*, 109(6), 2011. ISSN 0021-8979. doi: 10.1063/1.3549016.

[5] R. Hill and Fhmf Rahman. Advances in helium ion microscopy. *Nuclear Instruments & Methods in Physics Research Section a-Accelerators Spectrometers Detectors and Associated Equipment*, 645(1):96–101, 2011. ISSN 0168-9002. doi: 10.1016/j.nima.2010.12.123.

[6] L. Scipioni, C. A. Sanford, J. Notte, B. Thompson, and S. McVey. Understanding imaging modes in the helium ion microscope. *Journal of Vacuum Science & Technology B*, 27(6):3250–3255, 2009. ISSN 1071-1023. doi: 10.1116/1.3258634.

[7] D. Bazou, G. Behan, C. Reid, J. J. Boland, and H. Z. Zhang. Imaging of human colon cancer cells using he-ion scanning microscopy. *Journal of Microscopy*, 242(3):290–294, 2011. ISSN 0022-2720. doi: 10.1111/j.1365-2818.2010.03467.x.

[8] D. Fox, Y. B. Zhou, A. O'Neill, S. Kumar, J. J. Wang, J. N. Coleman, G. S. Duesberg, J. F. Donegan, and H. Z. Zhang. Helium ion microscopy of graphene: beam damage, image quality and edge contrast. *Nanotechnology*, 24(33):7, 2013. ISSN 0957-4484. doi: 10.1088/0957-4484/24/33/335702.

[9] Y. B. Zhou, D. S. Fox, P. Maguire, R. O'Connell, R. Masters, C. Rodenburg, H. C. Wu, M. Dapor, Y. Chen, and H. Z. Zhang. Quantitative secondary electron imaging for work function extraction at atomic level and layer identification of graphene. *Scientific Reports*, 6:8, 2016. ISSN 2045-2322. doi: 10.1038/srep21045.

[10] Y. B. Zhou, R. O'Connell, P. Maguire, and H. Z. Zhang. High throughput secondary electron imaging of organic residues on a graphene surface. *Scientific Reports*, 4, 2014. ISSN 2045-2322. doi: 10.1038/srep07032.

[11] A. J. Pearson, S. A. Boden, D. M. Bagnall, D. G. Lidzey, and C. Rodenburg. Imaging the bulk nanoscale morphology of organic solar cell blends using helium ion microscopy. *Nano Letters*, 11(10):4275–4281, 2011. ISSN 1530-6984. doi: 10.1021/nl202269n.

[12] C. Rodenburg, X. Liu, M. A. E. Jepson, Z. Zhou, W. M. Rainforth, and J. M. Rodenburg. The role of helium ion microscopy in the characterisation of complex three-dimensional nanostructures. *Ultramicroscopy*, 110(9):1178–1184, 2010. ISSN 0304-3991. doi: 10.1016/j.ultramic.2010.04.009.

[13] Y. Chakk and D. Horvitz. Contribution of dynamic charging effects into dopant contrast mechanisms in silicon. *Journal of Materials Science*, 41 (14):4554–4560, 2006. ISSN 0022-2461. doi: 10.1007/s10853-006-0086-8.

[14] M. M. El-Gomati, T. C. R. Wells, I. Mullerova, L. Frank, and H. Jayakody. Why is it that differently doped regions in semiconductors are visible in low voltage sem? *Ieee Transactions on Electron Devices*, 51(2):288–292, 2004. ISSN 0018-9383. doi: 10.1109/ted.2003.821884.

[15] M. Itakura, N. Kuwano, K. Sato, and S. Tachibana. Variations in contrast of scanning electron microscope images for microstructure analysis of si-based semiconductor materials. *Journal of Electron Microscopy*, 59:S165–S173, 2010. ISSN 0022-0744. doi: 10.1093/jmicro/dfq044.

[16] C. P. Sealy, M. R. Castell, and P. R. Wilshaw. Mechanism for secondary electron dopant contrast in the sem. *Journal of Electron Microscopy*, 49(2): 311–321, 2000. ISSN 0022-0744.

[17] Mark Jepson, Xiong Liu, David Bell, David Ferranti, Beverley Inkson, and Cornelia Rodenburg. Resolution limits of secondary electron dopant contrast

in helium ion and scanning electron microscopy. *Microscopy and Microanalysis*, 17(4):637–642, 2011. ISSN 1431-9276. doi: 10.1017/s1431927611000365.

[18] M. A. E. Jepson, B. J. Inkson, C. Rodenburg, and D. C. Bell. Dopant contrast in the helium ion microscope. *Epl*, 85(4), 2009. ISSN 0295-5075. doi: 10.1209/0295-5075/85/46001.

[19] M. A. E. Jepson, B. J. Inkson, Xiong Liu, L. Scipioni, and C. Rodenburg. Quantitative dopant contrast in the helium ion microscope. *Epl*, 86(2), 2009. ISSN 0295-5075. doi: 10.1209/0295-5075/86/26005.

[20] Kensuke Inai, Kaoru Ohya, and Tohru Ishitani. Simulation study on image contrast and spatial resolution in helium ion microscope. *Journal of Electron Microscopy*, 56(5):163–169, 2007. ISSN 0022-0744. doi: 10.1093/jmicro/dfm024.

[21] David C. Bell. Contrast mechanisms and image formation in helium ion microscopy. *Microscopy and Microanalysis*, 15(2):147–153, 2009. ISSN 1431-9276. doi: 10.1017/s1431927609090138.

[22] P. Hirsch, M. Kassens, M. Puttmann, and L. Reimer. Contamination in a scanning electron-microscope and the influence of specimen cooling. *Scanning*, 16(2):101–110, 1994. ISSN 0161-0457.

[23] A. Vladar and M. Postek. Electron beam-induced sample contamination in the sem. *Microscopy and microanalysis : the official journal of Microscopy Society of America, Microbeam Analysis Society, Microscopical Society of Canada*, 11 Suppl 2:764–5, 2005. ISSN 1435-8115. doi: 10.1017/s1431927605507785.

[24] R. F. Egerton, P. Li, and M. Malac. Radiation damage in the tem and sem. *Micron*, 35(6):399–409, 2004. ISSN 0968-4328. doi: http://dx.doi.org/10.1016/j.micron.2004.02.003.

[25] S. Kwitnewski, E. Ptasinska-Denga, and C. Szmytkowski. Relationship between electron-scattering grand total and ionization total cross sections. *Radiation Physics and Chemistry*, 68(1-2):169–174, 2003. ISSN 0969-806X. doi: 10.1016/s0969-806x(03)00275-5.

[26] H Seiler. Secondary electron emission in the scanning electron microscope. *Journal of Applied Physics*, 54(11):R1–R18, 1983. doi: doi:http://dx.doi.org/10.1063/1.332840.

[27] V. Yu. Mikhailovskii, Yu. V. Petrov, and O. F. Vyvenko. Energy filtration of secondary and backscattered electrons by the method of the retarding potential in scanning electron and ion microscopy. *Journal of Surface Investigation. X-ray, Synchrotron and Neutron Techniques*, 9(1):196–202, 2015. ISSN 1819-7094. doi: 10.1134/s1027451014060378.

[28] Y. V. Petrov, O. F. Vyvenko, and A. S. Bondarenko. Scanning helium ion microscope: Distribution of secondary electrons and ion channeling. *Journal of Surface Investigation-X-Ray Synchrotron and Neutron Techniques*, 4(5): 792–795, 2010. ISSN 1027-4510. doi: 10.1134/s1027451010050186.

[29] A E Ennos. The origin of specimen contamination in the electron microscope. *British Journal of Applied Physics*, 4(4):101, 1953. ISSN 0508-3443.

[30] R. L. Patterson and C. M. Wayman. Study of contamination rates in an electron microscope. *Review of Scientific Instruments*, 34(11):1213–&, 1963. ISSN 0034-6748. doi: 10.1063/1.1718179. URL `<GotoISI>://WOS:A19632610C00025`.

[31] J. J. Hren. Specimen contamination in analytical electron-microscopy - sources and solutions. *Ultramicroscopy*, 3(4):375–380, 1978. ISSN 0304-3991. doi: 10.1016/s0304-3991(78)80057-6.

[32] D. Joy and B. Griffin. Microanalysis with a low energy helium ion beam. *Microsc Microanal*, 13(Suppl 2):1398CD–1399CD, 2007.

[33] Robert C. Masters, Andrew J. Pearson, Tom S. Glen, Fabian-Cyril Sasam, Letian Li, Maurizio Dapor, Athene M. Donald, David G. Lidzey, and Cornelia Rodenburg. Sub-nanometre resolution imaging of polymer–fullerene photovoltaic blends using energy-filtered scanning electron microscopy. *Nature Communications*, 6:6928, 2015. doi: 10.1038/ncomms7928.

[34] D. C. Joy and B. J. Griffin. Is microanalysis possible in the helium ion microscope? *Microscopy and Microanalysis*, 17(4):643–649, 2011. ISSN 1431-9276. doi: 10.1017/s1431927611000596.

[35] M. S. Joens, C. Huynh, J. M. Kasuboski, D. Ferranti, Y. J. Sigal, F. Zeitvogel, M. Obst, C. J. Burkhardt, K. P. Curran, S. H. Chalasani, L. A. Stern, B. Goetze, and J. A. J. Fitzpatrick. Helium ion microscopy (him) for the imaging of biological samples at sub-nanometer resolution. *Scientific Reports*, 3, 2013. ISSN 2045-2322. doi: 10.1038/srep03514.

[36] K.I. Schiffmann. Investigation of fabrication parameters for the electron-beam-induced deposition of contamination tips used in atomic force microscopy. *Nanotechnology*, 4(3):163–9, 1993.

[37] T. Djenizian, L. Santinacci, and P. Schmuki. Factors in electrochemical nanostructure fabrication using electron-beam induced carbon masking. *Journal of the Electrochemical Society*, 151(3):G175–G180, 2004. ISSN 0013-4651. doi: 10.1149/1.1643744.

[38] M. Castagne, M. Benfedda, S. Lahimer, P. Falgayrettes, and J. P. Fillard. Near field optical behaviour of c supertips. *Ultramicroscopy*, 76(4):187–194, 1999. ISSN 0304-3991. doi: 10.1016/s0304-3991(98)00075-8.

[39] A. N. Broers, W. W. Molzen, J. J. Cuomo, and N. D. Wittels. Electron-beam fabrication of 80-a metal structures. *Applied Physics Letters*, 29(9): 596–598, 1976. ISSN 0003-6951. doi: 10.1063/1.89155.

[40] A. Bezryadin and C. Dekker. Nanofabrication of electrodes with sub-5 nm spacing for transport experiments on single molecules and metal clusters. *Journal of Vacuum Science & Technology B*, 15(4):793–799, 1997. doi: 10. 1116/1.589411.

[41] W. Ding, D.A. Dikin, X. Chen, R.d. Piner, R.S. Ruoff, and E. Zussman. Mechanics of hydrogenated amorphous carbon deposits from electron-beam-induced deposition of a paraffin precursor. *Journal of Applied Physics*, 98 (1):014905, 2005.

[42] D. Lau, A. E. Hughes, T. H. Muster, T. J. Davis, and A. M. Glenn. Electron-beam-induced carbon contamination on silicon: Characterization using raman spectroscopy and atomic force microscopy. *Microscopy and Microanalysis*, 16(1):13–20, 2010. ISSN 1431-9276. doi: 10.1017/s1431927609991206.

[43] J. Morgan, J. Notte, R. Hill, and B. Ward. An introduction to the helium ion microscope. *Microscopy Today*, 14(4):24–31, 2006.

[44] R. Hill, J. Notte, and B. Ward. The alis he ion source and its application to high resolution microscopy. *Physics Procedia*, 1:135–141, 2008.

[45] B. J. Griffin. A comparison of conventional everhart-thornley style and in-lens secondary electron detectors-a further variable in scanning electron microscopy. *Scanning*, 33(3):162–173, 2011. ISSN 0161-0457. doi: 10.1002/sca.20255.

[46] A. G. Cid, R. Rosenkranz, and E. Zschech. Optimization of the sem working conditions: Esb detector at low voltage. *Advanced Engineering Materials*, 18(2):185–193, 2016. ISSN 1438-1656. doi: 10.1002/adem.201500161.

[47] David C. Joy. *Introduction to Helium Ion Microscopy*, pages 1–3. Springer New York, New York, NY, 2013. ISBN 978-1-4614-8660-2. doi: 10.1007/978-1-4614-8660-2_1.

[48] W. Jiang BW Arey, V. Shutthanandan. Helium ion microscopy versus scanning electron microscopy. *www.microscopy.org*, 2010.

[49] C. Legressus, F. Valin, M. Gautier, J. P. Duraud, J. Cazaux, and H. Okuzumi. Charging phenomena on insulating materials - mechanisms and applications. *Scanning*, 12(4):203–210, 1990. ISSN 0161-0457.

[50] D. C. Joy, M. S. Prasad, and H. M. Meyer. Experimental secondary electron spectra under sem conditions. *Journal of Microscopy-Oxford*, 215:77–85, 2004. ISSN 0022-2720. doi: 10.1111/j.0022-2720.2004.01345.x.

[51] C. Schonjahn, C. J. Humphreys, and M. Glick. Energy-filtered imaging in a field-emission scanning electron microscope for dopant mapping in semiconductors. *Journal of Applied Physics*, 92(12):7667–7671, 2002. ISSN 0021-8979. doi: 10.1063/1.1525862.

[52] M. Buzzo, M. Ciappa, M. Stangoni, and W. Fichtner. Two-dimensional dopant profiling and imaging of 4h silicon carbide devices by secondary electron potential contrast. *Microelectronics Reliability*, 45(9-11):1499–1504, 2005. ISSN 0026-2714. doi: 10.1016/j.microrel.2005.07.069.

[53] P. Kazemian, S. A. M. Mentink, C. Rodenburg, and C. J. Humphreys. Quantitative secondary electron energy filtering in a scanning electron microscope and its applications. *Ultramicroscopy*, 107(2-3):140–150, 2007. ISSN 0304-3991. doi: 10.1016/j.ultramic.2006.06.003.

[54] J. Jatzkowski, M. Simon-Najasek, and F. Altmann. Novel techniques for dopant contrast analysis on real ic structures. *Microelectronics Reliability*, 52(9-10):2098–2103, 2012. ISSN 0026-2714. doi: 10.1016/j.microrel.2012.06.113.

[55] C. Rodenburg, M. A. E. Jepson, E. G. T. Bosch, and M. Dapor. Energy selective scanning electron microscopy to reduce the effect of contamination layers on scanning electron microscope dopant mapping. *Ultramicroscopy*, 110(9):1185–1191, 2010. ISSN 0304-3991. doi: 10.1016/j.ultramic.2010.04.008.

[56] D. Tsurumi, K. Hamada, and Y. Kawasaki. Energy-filtered imaging in a scanning electron microscope for dopant contrast in inp. *Journal of Electron Microscopy*, 59:S183–S187, 2010. ISSN 0022-0744. doi: 10.1093/jmicro/dfq046.

[57] D. Tsurumi, K. Hamada, and Y. Kawasaki. Highly reproducible secondary electron imaging under electron irradiation using high-pass energy filtering in low-voltage scanning electron microscopy. *Microscopy and Microanalysis*, 18(2):385–389, 2012. ISSN 1431-9276. doi: 10.1017/s1431927611012852.

[58] Augustus K. W. Chee and Stuart A. Boden. Dopant profiling based on scanning electron and helium ion microscopy. *Ultramicroscopy*, 161:51–8, 2016. doi: 10.1016/j.ultramic.2015.10.003.

[59] Yu Petrov and O. Vyvenko. Secondary electron emission spectra and energy selective imaging in helium ion microscope. *Scanning Microscopies 2011: Advanced Microscopy Technologies for Defense, Homeland Security, Forensic, Life, Environmental, and Industrial Sciences*, 8036, 2011. ISSN 0277-786X. doi: 10.1117/12.886347.

[60] J. Ferron, R. A. Vidal, N. Bajales, L. Cristina, and R. A. Baragiola. Role of hopg density of empty electronic states above vacuum on electron emission spectra induced by ions and uv photons. *Surface Science*, 622:83–86, 2014. ISSN 0039-6028. doi: 10.1016/j.susc.2013.12.010.

[61] K. Ohya, T. Yamanaka, K. Inai, and T. Ishitani. Comparison of secondary electron emission in helium ion microscope with gallium ion and electron microscopes. *Nuclear Instruments & Methods in Physics Research Section*

B-Beam Interactions with Materials and Atoms, 267(4):584–589, 2009. ISSN 0168-583X. doi: 10.1016/j.nimb.2008.11.003.

[62] M. S. Chung and T. E. Everhart. Simple calculation of energy-distribution of low-energy secondary electrons emitted from metals under electron-bombardment. *Journal of Applied Physics*, 45(2):707–709, 1974. ISSN 0021-8979. doi: 10.1063/1.1663306.

[63] H. Kanter. Slow-electron mean free paths in aluminum, silver, and gold. *Phys. Rev. B*, 1:522–536, Jan 1970. doi: 10.1103/PhysRevB.1.522.

[64] J. F. Ziegler, M. D. Ziegler, and J. P. Biersack. Srim - the stopping and range of ions in matter (2010). *Nuclear Instruments & Methods in Physics Research Section B-Beam Interactions with Materials and Atoms*, 268(11-12):1818–1823, 2010. ISSN 0168-583X. doi: 10.1016/j.nimb.2010.02.091.

[65] K. S. Novoselov, A. K. Geim, S. V. Morozov, D. Jiang, Y. Zhang, S. V. Dubonos, I. V. Grigorieva, and A. A. Firsov. Electric field effect in atomically thin carbon films. *Science*, 306(5696):666–669, 2004. ISSN 0036-8075. doi: 10.1126/science.1102896.

[66] A. H. Castro Neto, F. Guinea, N. M. R. Peres, K. S. Novoselov, and A. K. Geim. The electronic properties of graphene. *Reviews of Modern Physics*, 81(1):109–162, 2009. ISSN 0034-6861. doi: 10.1103/RevModPhys.81.109.

[67] A. K. Geim and K. S. Novoselov. The rise of graphene. *Nature Materials*, 6 (3):183–191, 2007. ISSN 1476-1122. doi: 10.1038/nmat1849.

[68] Long Ju, Baisong Geng, Jason Horng, Caglar Girit, Michael Martin, Zhao Hao, Hans A. Bechtel, Xiaogan Liang, Alex Zettl, Y. Ron Shen, and Feng Wang. Graphene plasmonics for tunable terahertz metamaterials. *Nature Nanotechnology*, 6(10):630–634, 2011. ISSN 1748-3387. doi: 10.1038/nnano.2011.146.

[69] Jiyu Fan, J. M. Michalik, L. Casado, S. Roddaro, M. R. Ibarra, and J. M. De Teresa. Investigation of the influence on graphene by using electron-beam and photo-lithography. *Solid State Communications*, 151(21):1574–1578, 2011. ISSN 0038-1098. doi: 10.1016/j.ssc.2011.07.028.

[70] K. S. Novoselov, V. I. Fal'ko, L. Colombo, P. R. Gellert, M. G. Schwab, and K. Kim. A roadmap for graphene. *Nature*, 490(7419):192–200, 2012. ISSN 0028-0836. doi: 10.1038/nature11458.

[71] Masa Ishigami, J. H. Chen, W. G. Cullen, M. S. Fuhrer, and E. D. Williams. Atomic structure of graphene on sio2. *Nano Letters*, 7(6):1643–1648, 2007. ISSN 1530-6984. doi: 10.1021/nl070613a.

[72] Zengguang Cheng, Qiaoyu Zhou, Chenxuan Wang, Qiang Li, Chen Wang, and Ying Fang. Toward intrinsic graphene surfaces: A systematic study on thermal annealing and wet-chemical treatment of sio2-supported graphene devices. *Nano Letters*, 11(2):767–771, 2011. ISSN 1530-6984. doi: 10.1021/nl103977d.

[73] A. Pirkle, J. Chan, A. Venugopal, D. Hinojos, C. W. Magnuson, S. McDonnell, L. Colombo, E. M. Vogel, R. S. Ruoff, and R. M. Wallace. The effect of chemical residues on the physical and electrical properties of chemical vapor deposited graphene transferred to sio2. *Applied Physics Letters*, 99(12), 2011. ISSN 0003-6951. doi: 10.1063/1.3643444.

[74] A. M. Goossens, V. E. Calado, A. Barreiro, K. Watanabe, T. Taniguchi, and L. M. K. Vandersypen. Mechanical cleaning of graphene. *Applied Physics Letters*, 100(7), 2012. ISSN 0003-6951. doi: 10.1063/1.3685504.

[75] Yung-Chang Lin, Chun-Chieh Lu, Chao-Huei Yeh, Chuanhong Jin, Kazu Suenaga, and Po-Wen Chiu. Graphene annealing: How clean can it be? *Nano Letters*, 12(1):414–419, 2012. ISSN 1530-6984. doi: 10.1021/nl203733r.

[76] Guannan Yu, Xinfeng Liu, Guichuan Xing, Shi Chen, Chin Fan Ng, Xiangyang Wu, Edwin Kok Lee Yeow, Wen Siang Lew, and Tze Chien Sum. Spatially-resolved ultrafast optical spectroscopy of polymer-grafted residues on cvd graphene. *The Journal of Physical Chemistry C*, 118(1):708–713, 2014. ISSN 1932-7447. doi: 10.1021/jp406675r.

[77] Y. Sano, I. Kawayama, M. Tabata, K. A. Salek, H. Murakami, M. Wang, R. Vajtai, P. M. Ajayan, J. Kono, and M. Tonouchi. Imaging molecular adsorption and desorption dynamics on graphene using terahertz emission spectroscopy. *Scientific Reports*, 4:6046, 2014. doi: 10.1038/srep06046https://www.nature.com/articles/srep06046#supplementary-information.

[78] C. Rodenburg, P. Viswanathan, M. A. E. Jepson, X. Liu, and G. Battaglia. Helium ion microscopy based wall thickness and surface roughness analysis of polymer foams obtained from high internal phase emulsion. *Ultramicroscopy*, 139:13–19, 2014. ISSN 0304-3991. doi: 10.1016/j.ultramic.2014.01.004.

[79] Vidya Kochat, Atindra Nath Pal, E. S. Sneha, Arjun Sampathkumar, Anshita Gairola, S. A. Shivashankar, Srinivasan Raghavan, and Arindam Ghosh. High contrast imaging and thickness determination of graphene with in-column secondary electron microscopy. *Journal of Applied Physics*, 110 (1), 2011. ISSN 0021-8979. doi: 10.1063/1.3608062.

[80] Hongxuan Guo, Jianhua Gao, Nobuyuki Ishida, Mingsheng Xu, and Daisuke Fujita. Characterization of two-dimensional hexagonal boron nitride using scanning electron and scanning helium ion microscopy. *Applied Physics Letters*, 104(3), 2014. ISSN 0003-6951. doi: 10.1063/1.4862819.

[81] Kai Yan, Di Wu, Hailin Peng, Li Jin, Qiang Fu, Xinhe Bao, and Zhongfan Liu. Modulation-doped growth of mosaic graphene with single-crystalline p-n junctions for efficient photocurrent generation. *Nature Communications*, 3, 2012. ISSN 2041-1723. doi: 10.1038/ncomms2286. URL `<GotoISI>://WOS:000316356700047`.

[82] Jacques Cazaux. Calculated dependence of few-layer graphene on secondary electron emissions from sic. *Applied Physics Letters*, 98(1), 2011. ISSN 0003-6951. doi: 10.1063/1.3534805.

[83] H. Yang, J. Heo, S. Park, H. J. Song, D. H. Seo, K. E. Byun, P. Kim, I. Yoo, H. J. Chung, and K. Kim. Graphene barristor, a triode device with a gate-controlled schottky barrier. *Science*, 336(6085):1140–1143, 2012. ISSN 0036-8075. doi: 10.1126/science.1220527.

[84] J. Janata and M. Josowicz. Conducting polymers in electronic chemical sensors. *Nature Materials*, 2(1):19–24, 2003. ISSN 1476-1122. doi: 10.1038/nmat768.

[85] Z. A. Page, Y. Liu, V. V. Duzhko, T. P. Russell, and T. Emrick. Fulleropyrrolidine interlayers: Tailoring electrodes to raise organic solar cell efficiency. *Science*, 346(6208):441–444, 2014. ISSN 0036-8075. doi: 10.1126/science.1255826.

[86] H. Zhang, J. Tang, J. Yuan, J. Ma, N. Shinya, K. Nakajima, H. Murakami, T. Ohkubo, and L. C. Qin. Nanostructured lab6 field emitter with lowest apical work function. *Nano Letters*, 10(9):3539–3544, 2010. ISSN 1530-6984. doi: 10.1021/nl101752z.

[87] Bae Sukang, Kim Sang Jin, Shin Dolly, Ahn Jong-Hyun, and Hong Byung Hee. Towards industrial applications of graphene electrodes. *Physica Scripta*, 2012(T146):014024, 2012. ISSN 1402-4896.

[88] H. Hibino, H. Kageshima, M. Kotsugi, F. Maeda, F. Z. Guo, and Y. Watanabe. Dependence of electronic properties of epitaxial few-layer graphene on the number of layers investigated by photoelectron emission microscopy. *Physical Review B*, 79(12), 2009. ISSN 1098-0121. doi: 10.1103/PhysRevB.79.125437.

[89] Y. J. Yu, Y. Zhao, S. Ryu, L. E. Brus, K. S. Kim, and P. Kim. Tuning the graphene work function by electric field effect. *Nano Letters*, 9(10): 3430–3434, 2009. ISSN 1530-6984. doi: 10.1021/nl901572a.

[90] Vishal Panchal, Ruth Pearce, Rositza Yakimova, Alexander Tzalenchuk, and Olga Kazakova. Standardization of surface potential measurements of graphene domains. *Scientific Reports*, 3:2597, 2013. doi: 10.1038/srep02597.

[91] Y. M. Shi, K. K. Kim, A. Reina, M. Hofmann, L. J. Li, and J. Kong. Work function engineering of graphene electrode via chemical doping. *Acs Nano*, 4(5):2689–2694, 2010. ISSN 1936-0851. doi: 10.1021/nn1005478.

[92] J. Park, W. H. Lee, S. Huh, S. H. Sim, S. B. Kim, K. Cho, B. H. Hong, and K. S. Kim. Work-function engineering of graphene electrodes by self-assembled monolayers for high-performance organic field-effect transistors. *Journal of Physical Chemistry Letters*, 2(8):841–845, 2011. ISSN 1948-7185. doi: 10.1021/jz200265w.

[93] S. M. Choi, S. H. Jhi, and Y. W. Son. Effects of strain on electronic properties of graphene. *Physical Review B*, 81(8), 2010. ISSN 1098-0121. doi: 10.1103/PhysRevB.81.081407.

[94] M. M. Giangregorio, W. Jiao, G. V. Bianco, P. Capezzuto, A. S. Brown, G. Bruno, and M. Losurdo. Insights into the effects of metal nanostructuring and oxidation on the work function and charge transfer of metal/graphene

hybrids. *Nanoscale*, 7(30):12868–12877, 2015. ISSN 2040-3364. doi: 10.1039/C5NR02610E.

[95] C. Mathieu, N. Barrett, J. Rault, Y. Y. Mi, B. Zhang, W. A. de Heer, C. Berger, E. H. Conrad, and O. Renault. Microscopic correlation between chemical and electronic states in epitaxial graphene on sic(000(1)over-bar). *Physical Review B*, 83(23), 2011. ISSN 1098-0121. doi: 10.1103/PhysRevB.83.235436.

[96] J. Goldstein, D.E. Newbury, D.C. Joy, C.E. Lyman, P. Echlin, E. Lifshin, L. Sawyer, and J.R. Michael. *Scanning Electron Microscopy and X-ray Microanalysis*. Springer US, 2003.

[97] R. Ramachandra, B. Griffin, and D. Joy. A model of secondary electron imaging in the helium ion scanning microscope. *Ultramicroscopy*, 109(6): 748–757, 2009. ISSN 0304-3991. doi: 10.1016/j.ultramic.2009.01.013.

[98] A. A. Suvorova and S. Samarin. Secondary electron imaging of sic-based structures in secondary electron microscope. *Surface Science*, 601(18):4428–4432, 2007. ISSN 0039-6028. doi: 10.1016/j.susc.2007.04.142.

[99] J. Cazaux. Material contrast in sem: Fermi energy and work function effects. *Ultramicroscopy*, 110(3):242–253, 2010. ISSN 0304-3991. doi: 10.1016/j.ultramic.2009.12.002.

[100] H. Hiura, H. Miyazaki, and K. Tsukagoshi. Determination of the number of graphene layers: Discrete distribution of the secondary electron intensity stemming from individual graphene layers. *Applied Physics Express*, 3(9), 2010. ISSN 1882-0778. doi: 10.1143/apex.3.095101.

[101] S. Gupta, E. Heintzman, and J. Jasinski. Secondary electron intensity contrast imaging and friction properties of micromechanically cleaved graphene layers on insulating substrates. *Journal of Electronic Materials*, 43(9):3458–3469, 2014. ISSN 0361-5235. doi: 10.1007/s11664-014-3277-0.

[102] William Thompson, Lewis Stern, Dave Ferranti, Chuong Huynh, Larry Scipioni, John Notte, and Colin Sanford. Techniques for improving material fidelity and contrast consistency in secondary electron mode helium ion microscope (him) imaging. *Scanning Microscopy 2010*, 7729, 2010. ISSN 0277-786X. doi: 10.1117/12.861488.

[103] Konrad Rykaczewski, William B. White, and Andrei G. Fedorov. Analysis of electron beam induced deposition (ebid) of residual hydrocarbons in electron microscopy. *Journal of Applied Physics*, 101(5), 2007. ISSN 0021-8979. doi: 10.1063/1.2437065.

[104] K. Rykaczewski, A. Marshall, W. B. White, and A. G. Fedorov. Dynamic growth of carbon nanopillars and microrings in electron beam induced dissociation of residual hydrocarbons. *Ultramicroscopy*, 108(9):989–992, 2008. ISSN 0304-3991. doi: 10.1016/j.ultramic.2008.04.006.

[105] G. Love, V. D. Scott, N. M. T. Dennis, and L. Laurenson. Sources of contamination in electron-optical equipment. *Scanning*, 4(1):32–39, 1981. ISSN 0161-0457.

[106] H. W. Conru and P. C. Laberge. 15-oil contamination with sem operated in spot scanning mode. *Journal of Physics E-Scientific Instruments*, 8(2): 136–138, 1975. ISSN 0022-3735. doi: 10.1088/0022-3735/8/2/021.

[107] P. Roediger, H. D. Wanzenboeck, G. Hochleitner, and E. Bertagnolli. Evaluation of chamber contamination in a scanning electron microscope. *Journal of Vacuum Science & Technology B*, 27(6):2711–2717, 2009. ISSN 1071-1023. doi: 10.1116/1.3244628.

[108] K.I. Schiffmann. Investigation of fabrication parameters for the electron-beam-induced deposition of contamination tips used in atomic force microscopy. *Nanotechnology*, 4(3):163–9, 1993.

[109] Edgar R. Stephens and Frank R. Burleson. Distribution of light hydrocarbons in ambient air. *Journal of the Air Pollution Control Association*, 19 (12):929–936, 1969. ISSN 0002-2470. doi: 10.1080/00022470.1969.10469359.

[110] Ted Pella Inc. Conductive adhesives and specimen preperation adhesives for scanning electron microscopy. URL `http://www.tedpella.com/SEMmisc_html/SEMadhes.htm`.

[111] M. Amman, J. W. Sleight, D. R. Lombardi, R. E. Welser, M. R. Deshpande, M. A. Reed, and L. J. Guido. Atomic force microscopy study of electron beam written contamination structures. *Journal of Vacuum Science & Technology B*, 14(1):54–62, 1996. ISSN 1071-1023. doi: 10.1116/1.588429.

[112] K. Mitsuishi, M. Shimojo, M. Tanaka, and K. Furuya. Nano-fabrication using electron-beam-induced deposition combined with low energy ion milling. *Nuclear Instruments & Methods in Physics Research Section B-Beam Interactions with Materials and Atoms*, 242(1-2):244–246, 2006. ISSN 0168-583X. doi: 10.1016/j.nimb.2005.08.022.

[113] E. I. Rau. The effect of contamination of dielectric target surfaces under electron irradiation. *Applied Surface Science*, 254(7):2110–2113, 2008. ISSN 0169-4332. doi: 10.1016/j.apsusc.2007.08.076.

[114] M. T. Postek. An approach to the reduction of hydrocarbon contamination in the scanning electron microscope. *Scanning*, 18(4):269–274, 1996. ISSN 0161-0457.

[115] A. E. Vladar, M. T. Postek, and R. Vane. *Active monitoring and control of electron beam induced contamination*, volume 4344 of *Proceedings of the Society of Photo-Optical Instrumentation Engineers (Spie)*, pages 835–843. SPIE 4344, 2001. ISBN 0277-786X 0-8194-4030-2. doi: 10.1117/12.436724.

[116] Neal Sullivan, Tung Mai, Scott Bowdoin, and Ronald Vane. A study of the effectiveness of the removal of hydrocarbon contamination by oxidative cleaning inside the sem. *Microscopy and Microanalysis*, 8(SupplementS02): 720–721, 2002. ISSN 1435-8115. doi: doi:null.

[117] Ronald Vane. Immobilization and removal of hydrocarbon contamination using the evactron® de-contaminator. *Microsc Microanal*, 12(2), 2006. doi: 10.1017/S1431927606066803.

[118] Charles Soong, Patrick Woo, and David Hoyle. Contamination cleaning of tem/sem samples with the zone cleaner. *Microscopy Today*, 20(06):44–48, 2012. ISSN null. doi: doi:10.1017/S1551929512000752.

[119] N. Miura, A. Yamada, and M. Konagai. Fabrication of sub-micron tungsten carbide (wcx) amorphous carbon (a-c) stacked junction by beam-induced reaction processes. *Japanese Journal of Applied Physics Part 2-Letters*, 36 (9AB):L1275–L1278, 1997.

[120] P. Kumar and M. Kar. Effect of structural transition on magnetic and optical properties of ca and ti co-substituted bifeo3 ceramics. *Journal of Alloys and*

Compounds, 584:566–572, 2014. ISSN 0925-8388. doi: 10.1016/j.jallcom.2013.09.107.

[121] P. Jain and P. Arun. Influence of grain size on the band-gap of annealed sns thin films. *Thin Solid Films*, 548:241–246, 2013. ISSN 0040-6090. doi: 10.1016/j.tsf.2013.09.089.

[122] V. M. Dzhagan, M. Y. Valakh, A. G. Milekhin, N. A. Yeryukov, D. R. T. Zahn, E. Cassette, T. Pons, and B. Dubertret. Raman- and ir-active phonons in cdse/cds core/shell nanocrystals in the presence of interface alloying and strain. *Journal of Physical Chemistry C*, 117(35):18225–18233, 2013. ISSN 1932-7447. doi: 10.1021/jp4046808.

[123] B. Choudhury and A. Choudhury. Lattice distortion and corresponding changes in optical properties of ceo2 nanoparticles on nd doping. *Current Applied Physics*, 13(1):217–223, 2013. ISSN 1567-1739. doi: 10.1016/j.cap.2012.07.014.

[124] G. Vaccaro, S. Agnello, G. Buscarino, and F. M. Gelardi. Thermally induced structural modification of silica nanoparticles investigated by raman and infrared absorption spectroscopies. *Journal of Physical Chemistry C*, 114 (33):13991–13997, 2010. ISSN 1932-7447. doi: 10.1021/jp103565a.

[125] R. Zhang, P. G. Yin, N. Wang, and L. Guo. Photoluminescence and raman scattering of zno nanorods. *Solid State Sciences*, 11(4):865–869, 2009. ISSN 1293-2558. doi: 10.1016/j.solidstatesciences.2008.10.016.

[126] V. Swamy, D. Menzies, B. C. Muddle, A. Kuznetsov, L. S. Dubrovinsky, Q. Dai, and V. Dmitriev. Nonlinear size dependence of anatase tio(2) lattice parameters. *Applied Physics Letters*, 88(24), 2006. ISSN 0003-6951. doi: 10.1063/1.2213956.

[127] M. Fernandez-Garcia, X. Q. Wang, C. Belver, A. Iglesias-Juez, J. C. Hanson, and J. A. Rodriguez. Ca doping of nanosize ce-zr and ce-tb solid solutions: Structural and electronic effects. *Chemistry of Materials*, 17(16):4181–4193, 2005. ISSN 0897-4756. doi: 10.1021/cm050265i.

[128] C. V. RAMAN and K. S. KRISHNAN. A new type of secondary radiation. *Nature*, 121:501–502, Mar 1928. doi: 10.1038/121501c0.

[129] Shu-Lin Zhang. *Basic Knowledge of Raman Spectroscopy*, pages 1–17. John Wiley & Sons, Ltd, 2012. ISBN 9781119961659. doi: 10.1002/9781119961659.ch1.

[130] J. Robertson. Diamond-like amorphous carbon. *Materials Science & Engineering R-Reports*, 37(4-6):129–281, 2002. ISSN 0927-796X. doi: 10.1016/s0927-796x(02)00005-0.

[131] D. S. Knight and W. B. White. Characterization of diamond films by raman-spectroscopy. *Journal of Materials Research*, 4(2):385–393, 1989. ISSN 0884-2914. doi: 10.1557/jmr.1989.0385.

[132] R. J. Nemanich and S. A. Solin. 1st-order and 2nd-order raman-scattering from finite-size crystals of graphite. *Physical Review B*, 20(2):392–401, 1979. ISSN 0163-1829. doi: 10.1103/PhysRevB.20.392.

[133] B. S. Elman, M. Shayegan, M. S. Dresselhaus, H. Mazurek, and G. Dresselhaus. Structural characterization of ion-implanted graphite. *Physical Review B*, 25(6):4142–4156, 1982. ISSN 0163-1829. doi: 10.1103/PhysRevB.25.4142.

[134] A. C. Ferrari and J. Robertson. Interpretation of raman spectra of disordered and amorphous carbon. *Physical Review B*, 61(20):14095–14107, 2000. ISSN 1098-0121. doi: 10.1103/PhysRevB.61.14095.

[135] K. Sato, R. Saito, Y. Oyama, J. Jiang, L. G. Cancado, M. A. Pimenta, A. Jorio, Ge G. Samsonidze, G. Dresselhaus, and M. S. Dresselhaus. D-band raman intensity of graphitic materials as a function of laser energy and crystallite size. *Chemical Physics Letters*, 427(1-3):117–121, 2006. ISSN 0009-2614. doi: 10.1016/j.cplett.2006.05.107.

[136] F. Tuinstra and J. L. Koenig. Raman spectrum of graphite. *Journal of Chemical Physics*, 53(3):1126–&, 1970. ISSN 0021-9606. doi: 10.1063/1.1674108.

[137] P. Lespade, R. Aljishi, and M. S. Dresselhaus. Model for raman-scattering from incompletely graphitized carbons. *Carbon*, 20(5):427–431, 1982. ISSN 0008-6223. doi: 10.1016/0008-6223(82)90043-4.

[138] J. Schwan, S. Ulrich, V. Batori, H. Ehrhardt, and S. R. P. Silva. Raman spectroscopy on amorphous carbon films. *Journal of Applied Physics*, 80(1):440–447, 1996. ISSN 0021-8979. doi: 10.1063/1.362745.

[139] T. Kohler, T. Frauenheim, and G. Jungnickel. Stability, chemical bonding, and vibrational properties of amorphous-carbon at different mass densities. *Physical Review B*, 52(16):11837–11844, 1995. ISSN 1098-0121. doi: 10.1103/PhysRevB.52.11837.

[140] S. Prawer, K. W. Nugent, Y. Lifshitz, G. D. Lempert, E. Grossman, J. Kulik, I. Avigal, and R. Kalish. Systematic variation of the raman spectra of dlc films as a function of sp(2):sp(3) composition. *Diamond and Related Materials*, 5(3-5):433–438, 1996. ISSN 0925-9635. doi: 10.1016/0925-9635(95)00363-0.

[141] C. Casiraghi, A. C. Ferrari, and J. Robertson. Raman spectroscopy of hydrogenated amorphous carbons. *Physical Review B*, 72(8), 2005. ISSN 1098-0121. doi: 10.1103/PhysRevB.72.085401.

[142] M. A. Tamor and W. C. Vassell. Raman fingerprinting of amorphous-carbon films. *Journal of Applied Physics*, 76(6):3823–3830, 1994. ISSN 0021-8979. doi: 10.1063/1.357385.

[143] J. Robertson. Gap states in diamond-like amorphous carbon. *Philosophical Magazine B-Physics of Condensed Matter Statistical Mechanics Electronic Optical and Magnetic Properties*, 76(3):335–350, 1997. ISSN 0141-8637. doi: 10.1080/01418639708241098.

[144] J. Robertson and E. P. Oreilly. Electronic and atomic-structure of amorphous-carbon. *Physical Review B*, 35(6):2946–2957, 1987. ISSN 0163-1829. doi: 10.1103/PhysRevB.35.2946.

[145] T. Bret, S. Mauron, I. Utke, and P. Hoffmann. Characterization of focused electron beam induced carbon deposits from organic precursors. *Microelectronic Engineering*, 78-79:300–306, 2005. ISSN 0167-9317. doi: 10.1016/j.mee.2005.01.006.

[146] P. Lemoine, S. S. Roy, J. P. Quinn, P. D. Maguire, and J. A. D. McLaughlin. Carbon nanostructures grown with electron and ion beam methods. *Applied Physics a-Materials Science & Processing*, 86(4):451–456, 2007. ISSN 0947-8396. doi: 10.1007/s00339-006-3806-7.

[147] M. Fleischmann, P. J. Hendra, and McQuilla.Aj. Raman-spectra of pyridine adsorbed at a silver electrode. *Chemical Physics Letters*, 26(2):163–166, 1974. ISSN 0009-2614. doi: 10.1016/0009-2614(74)85388-1.

[148] M. D. Sonntag, E. A. Pozzi, N. Jiang, M. C. Hersam, and R. P. Van Duyne. Recent advances in tip-enhanced raman spectroscopy. *Journal of Physical Chemistry Letters*, 5(18):3125–3130, 2014. ISSN 1948-7185. doi: 10.1021/jz5015746.

[149] R. Zhang, Y. Zhang, Z. C. Dong, S. Jiang, C. Zhang, L. G. Chen, L. Zhang, Y. Liao, J. Aizpurua, Y. Luo, J. L. Yang, and J. G. Hou. Chemical mapping of a single molecule by plasmon-enhanced raman scattering. *Nature*, 498 (7452):82–86, 2013. ISSN 0028-0836. doi: 10.1038/nature12151.

[150] E. C. Le Ru, E. Blackie, M. Meyer, and P. G. Etchegoin. Surface enhanced raman scattering enhancement factors: a comprehensive study. *Journal of Physical Chemistry C*, 111(37):13794–13803, 2007. ISSN 1932-7447. doi: 10.1021/jp0687908.

[151] Taka-aki Yano, Yasushi Inouye, and Satoshi Kawata. Nanoscale uniaxial pressure effect of a carbon nanotube bundle on tip-enhanced near-field raman spectra. *Nano Letters*, 6(6):1269–1273, 2006. ISSN 1530-6984. doi: 10.1021/nl060108y.

[152] D. Roy, J. Wang, and C. Williams. Novel methodology for estimating the enhancement factor for tip-enhanced raman spectroscopy. *Journal of Applied Physics*, 105(1):6, 2009. ISSN 0021-8979. doi: 10.1063/1.3056155.

[153] M. Moskovits. Surface-enhanced raman spectroscopy: a brief retrospective. *Journal of Raman Spectroscopy*, 36(6-7):485–496, 2005. ISSN 0377-0486. doi: 10.1002/jrs.1362.

[154] A. Campion and P. Kambhampati. Surface-enhanced raman scattering. *Chemical Society Reviews*, 27(4):241–250, 1998. ISSN 0306-0012. doi: 10.1039/a827241z.

[155] J. R. Lombardi, R. L. Birke, T. H. Lu, and J. Xu. Charge-transfer theory of surface enhanced raman-spectroscopy - herzberg-teller contributions. *Journal of Chemical Physics*, 84(8):4174–4180, 1986. ISSN 0021-9606. doi: 10.1063/1.450037.

[156] Paul L. Stiles, Jon A. Dieringer, Nilam C. Shah, and Richard P. Van Duyne. Surface-enhanced raman spectroscopy. *Annual Review of Analytical Chemistry*, 1(1):601–626, 2008. doi: 10.1146/annurev.anchem.

1.031207.112814. URL `https://doi.org/10.1146/annurev.anchem.1.031207.112814`. PMID: 20636091.

[157] J. R. Lombardi and R. L. Birke. A unified approach to surface-enhanced raman spectroscopy. *Journal of Physical Chemistry C*, 112(14):5605–5617, 2008. ISSN 1932-7447. doi: 10.1021/jp800167v.

[158] M. G. Albrecht and J. A. Creighton. Anomalously intense raman-spectra of pyridine at a silver electrode. *Journal of the American Chemical Society*, 99 (15):5215–5217, 1977. ISSN 0002-7863. doi: 10.1021/ja00457a071.

[159] M. Moskovits. Surface-enhanced spectroscopy. *Reviews of Modern Physics*, 57(3):783–826, 1985. ISSN 0034-6861. doi: 10.1103/RevModPhys.57.783.

[160] H. X. Lin, J. M. Li, B. J. Liu, D. Y. Liu, J. X. Liu, A. Terfort, Z. X. Xie, Z. Q. Tian, and B. Ren. Uniform gold spherical particles for single-particle surface-enhanced raman spectroscopy. *Physical Chemistry Chemical Physics*, 15(12):4130–4135, 2013. ISSN 1463-9076. doi: 10.1039/c3cp43857k.

[161] R. A. Tripp, R. A. Dluhy, and Y. P. Zhao. Novel nanostructures for sers biosensing. *Nano Today*, 3(3-4):31–37, 2008. ISSN 1748-0132. doi: 10.1016/s1748-0132(08)70042-2.

[162] A. M. Schwartzberg and J. Z. Zhang. Novel optical properties and emerging applications of metal nanostructures. *Journal of Physical Chemistry C*, 112 (28):10323–10337, 2008. ISSN 1932-7447. doi: 10.1021/jp801770w.

[163] K. H. Cho and S. W. Joo. Tautomerism of cytosine on silver, gold, and copper: Raman spectroscopy and density functional theory calculation study. *Bulletin of the Korean Chemical Society*, 29(1):69–75, 2008. ISSN 0253-2964.

[164] N. A. Abu Hatab, J. M. Oran, and M. J. Sepaniak. Surface-enhanced raman spectroscopy substrates created via electron beam lithography and nanotransfer printing. *Acs Nano*, 2(2):377–385, 2008. ISSN 1936-0851. doi: 10.1021/nn7003487.

[165] P. J. Tarcha, J. DeSaja-Gonzalez, S. Rodriguez-Llorente, and R. Aroca. Surface-enhanced fluorescence on sio2-coated silver island films. *Applied Spectroscopy*, 53(1):43–48, 1999. ISSN 0003-7028. doi: 10.1366/0003702991945443.

[166] T. Dorfer, M. Schmitt, and J. Popp. Deep-uv surface-enhanced raman scattering. *Journal of Raman Spectroscopy*, 38(11):1379–1382, 2007. ISSN 0377-0486. doi: 10.1002/jrs.1831.

[167] M. S. Anderson. Locally enhanced raman spectroscopy with an atomic force microscope. *Applied Physics Letters*, 76(21):3130–3132, 2000. ISSN 0003-6951. doi: 10.1063/1.126546.

[168] R. M. Stockle, Y. D. Suh, V. Deckert, and R. Zenobi. Nanoscale chemical analysis by tip-enhanced raman spectroscopy. *Chemical Physics Letters*, 318 (1-3):131–136, 2000. ISSN 0009-2614. doi: 10.1016/s0009-2614(99)01451-7.

[169] Duo Lin, Shangyuan Feng, Hao Huang, Weisheng Chen, Hong Shi, Nenrong Liu, Long Chen, Weiwei Chen, Yun Yu, and Rong Chen. Label-free detection of blood plasma using silver nanoparticle based surface-enhanced raman spectroscopy for esophageal cancer screening. *Journal of Biomedical Nanotechnology*, 10(3):478–484, 2014. ISSN 1550-7033. doi: 10.1166/jbn.2014.1750.

[170] Elena Bailo and Volker Deckert. Tip-enhanced raman spectroscopy of single rna strands: Towards a novel direct-sequencing method. *Angewandte Chemie-International Edition*, 47(9):1658–1661, 2008. ISSN 1433-7851. doi: 10.1002/anie.200704054.

[171] C. Chen, N. Hayazawa, and S. Kawata. A 1.7 nm resolution chemical analysis of carbon nanotubes by tip-enhanced raman imaging in the ambient. *Nature Communications*, 5, 2014. ISSN 2041-1723. doi: 10.1038/ncomms4312.

[172] KH Ong, JCH Phang, and JTL Thong. A robust focusing and astigmatism correction method for the scanning electron microscope. *Scanning*, 19(8): 553–563, 1997. ISSN 1932-8745.

[173] D. Teweldebrhan and A. A. Balandin. Modification of graphene properties due to electron-beam irradiation. *Applied Physics Letters*, 94(1), 2009. ISSN 0003-6951. doi: 10.1063/1.3062851.

[174] W. K. Yi, T. Jeong, S. G. Yu, J. Lee, S. W. Jin, J. Heo, and J. M. Kim. Study of the secondary-electron emission from thermally grown sio2 films on si. *Thin Solid Films*, 397(1-2):170–175, 2001. ISSN 0040-6090. doi: 10.1016/s0040-6090(01)01492-4.

[175] R. Livengood, S. Tan, Y. Greenzweig, J. Notte, and S. McVey. Subsurface damage from helium ions as a function of dose, beam energy, and dose rate. *Journal of Vacuum Science & Technology B*, 27(6):3244–3249, 2009. ISSN 1071-1023. doi: 10.1116/1.3237101.

[176] D. Drouin, A. R. Couture, D. Joly, X. Tastet, V. Aimez, and R. Gauvin. Casino v2.42 - a fast and easy-to-use modeling tool for scanning electron microscopy and microanalysis users. *Scanning*, 29(3):92–101, 2007. ISSN 0161-0457. doi: 10.1002/sca.20000.

[177] M. A. Stevens-Kalceff and D. P. Kruss. Focused ion beam induced local modifications of the contact potential difference of n- and p-doped silicon. *Journal of Physics D-Applied Physics*, 42(14), 2009. ISSN 0022-3727. doi: 10.1088/0022-3727/42/14/145117.

[178] H. Gnaser, A. Brodyanski, and B. Reuscher. Focused ion beam implantation of ga in si and ge: fluence-dependent retention and surface morphology. *Surface and Interface Analysis*, 40(11):1415–1422, 2008. ISSN 0142-2421. doi: 10.1002/sia.2915.

[179] G. Hlawacek, M. Jankowski, H. Wormeester, R. van Gastel, H. J. W. Zandvliet, and B. Poelsema. Visualization of steps and surface reconstructions in helium ion microscopy with atomic precision. *Ultramicroscopy*, 162:17–24, 2016. ISSN 0304-3991. doi: 10.1016/j.ultramic.2015.11.009.

[180] M. Dapor, M. A. E. Jepson, B. J. Inkson, and C. Rodenburg. The effect of oxide overlayers on secondary electron dopant mapping. *Microscopy and Microanalysis*, 15(3):237–243, 2009. ISSN 1431-9276.

[181] J. Cazaux. Charging in scanning electron microscopy "from inside and outside". *Scanning*, 26(4):181–203, 2004. ISSN 0161-0457.

[182] J. Cazaux. On some contrast reversals in sem: Application to metal/insulator systems. *Ultramicroscopy*, 108(12):1645–1652, 2008. ISSN 0304-3991. doi: 10.1016/j.ultramic.2008.06.005.

[183] C. I. Ukah, R. V. Kruzelecky, D. Racansky, S. Zukotynski, and J. M. Perz. Insitu work function measurements in evaporated amorphous-silicon. *Journal of Non-Crystalline Solids*, 103(1):131–136, 1988. ISSN 0022-3093. doi: 10.1016/0022-3093(88)90425-5.

[184] M. Morita, T. Ohmi, E. Hasegawa, M. Kawakami, and M. Ohwada. Growth of native oxide on a silicon surface. *Journal of Applied Physics*, 68(3):1272–1281, 1990. ISSN 0021-8979. doi: 10.1063/1.347181.

[185] T. Ishitani, T. Yamanaka, K. Inai, and K. Ohya. Secondary electron emission in scanning ga ion, he ion and electron microscopes. *Vacuum*, 84(8):1018–1024, 2010. ISSN 0042-207X. doi: 10.1016/j.vacuum.2009.12.010.

[186] Xuesong Li, Weiwei Cai, Jinho An, Seyoung Kim, Junghyo Nah, Dongxing Yang, Richard Piner, Aruna Velamakanni, Inhwa Jung, Emanuel Tutuc, Sanjay K. Banerjee, Luigi Colombo, and Rodney S. Ruoff. Large-area synthesis of high-quality and uniform graphene films on copper foils. *Science*, 324(5932):1312–1314, 2009. ISSN 0036-8075. doi: 10.1126/science.1171245.

[187] P. Blake, E. W. Hill, A. H. Castro Neto, K. S. Novoselov, D. Jiang, R. Yang, T. J. Booth, and A. K. Geim. Making graphene visible. *Applied Physics Letters*, 91(6):3, 2007. ISSN 0003-6951. doi: 10.1063/1.2768624.

[188] G. Q. Teo, H. M. Wang, Y. H. Wu, Z. B. Guo, J. Zhang, Z. H. Ni, and Z. X. Shen. Visibility study of graphene multilayer structures. *Journal of Applied Physics*, 103(12):6, 2008. ISSN 0021-8979. doi: 10.1063/1.2938840.

[189] K. A. Peterson, M. B. Zimmt, S. Linse, R. P. Domingue, and M. D. Fayer. Quantitative-determination of the radius of gyration of poly(methyl methacrylate) in the amorphous solid-state by time-resolved fluorescence depolarization measurements of excitation transport. *Macromolecules*, 20(1): 168–175, 1987. ISSN 0024-9297. doi: 10.1021/ma00167a028.

[190] Bo Peng, Ernest van der Wee, Arnout Imhof, and Alfons van Blaaderen. Synthesis of monodisperse, highly cross-linked, fluorescent pmma particles by dispersion polymerization. *Langmuir*, 28(17):6776–6785, 2012. ISSN 0743-7463. doi: 10.1021/la301288r.

[191] Z. H. Ni, H. M. Wang, J. Kasim, H. M. Fan, T. Yu, Y. H. Wu, Y. P. Feng, and Z. X. Shen. Graphene thickness determination using reflection and contrast spectroscopy. *Nano Letters*, 7(9):2758–2763, 2007. ISSN 1530-6984. doi: 10.1021/nl071254m.

[192] A. Reina, H. B. Son, L. Y. Jiao, B. Fan, M. S. Dresselhaus, Z. F. Liu, and J. Kong. Transferring and identification of single- and few-layer graphene on

arbitrary substrates. *Journal of Physical Chemistry C*, 112(46):17741–17744, 2008. ISSN 1932-7447. doi: 10.1021/jp807380s.

[193] M. P. Seah and W. A. Dench. Quantitative electron spectroscopy of surfaces: A standard data base for electron inelastic mean free paths in solids. *Surface and Interface Analysis*, 1(1):2–11, 1979. ISSN 1096-9918. doi: 10.1002/sia.740010103.

[194] A. C. Ferrari, J. C. Meyer, V. Scardaci, C. Casiraghi, M. Lazzeri, F. Mauri, S. Piscanec, D. Jiang, K. S. Novoselov, S. Roth, and A. K. Geim. Raman spectrum of graphene and graphene layers. *Physical Review Letters*, 97(18): 4, 2006. ISSN 0031-9007. doi: 10.1103/PhysRevLett.97.187401.

[195] T. Filleter, K. V. Emtsev, T. Seyller, and R. Bennewitz. Local work function measurements of epitaxial graphene. *Applied Physics Letters*, 93(13):3, 2008. ISSN 0003-6951. doi: 10.1063/1.2993341.

[196] D. Ziegler, P. Gava, J. Guttinger, F. Molitor, L. Wirtz, M. Lazzeri, A. M. Saitta, A. Stemmer, F. Mauri, and C. Stampfer. Variations in the work function of doped single- and few-layer graphene assessed by kelvin probe force microscopy and density functional theory. *Physical Review B*, 83(23): 7, 2011. ISSN 1098-0121. doi: 10.1103/PhysRevB.83.235434.

[197] A. Hoffman. Fine-structure in the secondary-electron emission-spectrum as a spectroscopic tool for carbon surface characterization. *Diamond and Related Materials*, 3(4-6):691–695, 1994. ISSN 0925-9635. doi: 10.1016/0925-9635(94)90250-x.

[198] S. Banerjee, M. Sardar, N. Gayathri, A. K. Tyagi, and B. Raj. Conductivity landscape of highly oriented pyrolytic graphite surfaces containing ribbons and edges. *Physical Review B*, 72(7):7, 2005. ISSN 2469-9950. doi: 10.1103/PhysRevB.72.075418.

[199] K. Ueno, T. Kumihashi, K. Saiki, and A. Koma. Characteristic secondary-electron emission from graphite and glassy-carbon surfaces. *Japanese Journal of Applied Physics Part 2-Letters*, 27(5):L759–L761, 1988. doi: 10.1143/jjap.27.l759.

[200] J. J. Cuomo, J. P. Doyle, J. Bruley, and J. C. Liu. Sputter deposition of dense diamond-like carbon-films at low-temperature. *Applied Physics Letters*, 58 (5):466–468, 1991. ISSN 0003-6951. doi: 10.1063/1.104609.

[201] Yongpeng Tong, Yongping Zhang, Yaoliang Xu, Jingyi Rui, Minqian Li, Cuiying Shen, Zhongming Xiao, and Jinxin Hong. Determination of eight elements in six human cancer cell lines and two human normal cell lines by pixe. *Biological Trace Element Research*, 29(1):31–34, 1991. ISSN 1559-0720. doi: 10.1007/bf03032671.

[202] Jichun Zhu, Jing Zhou, Jianyu Guo, Weiying Cai, Bo Liu, Zugeng Wang, and Zhenrong Sun. Surface-enhanced raman spectroscopy investigation on human breast cancer cells. *Chemistry Central Journal*, 7(1):37, 2013. ISSN 1752-153X. doi: 10.1186/1752-153x-7-37.